RECENT ADVANCES IN TITANIUM ALLOY EXTRUSIONS FOR AEROSPACE APPLICATIONS

Sesh Tamirisakandala[1], Matthew Dahar[1], Derek Ramirez[2], Martin Davey[3]

1 Howmet Aerospace, 1000 Warren Ave., Niles OH 44446 USA.
2 Howmet Aerospace, 7600 S. Santa Fe Drive, Bldg. C, Houston, TX 77061 USA.
3 Howmet Aerospace, Brighouse Road, Bradford, Low Moor, BD12 0QL, UK.

The extrusion method of manufacturing is ideally suited to produce long members of constant or nearly constant cross-section bars and shapes. Titanium alloy extrusion technology evolved over the past seven decades with advanced process designs and effective manufacturing process controls, leading to widespread use of Ti extrusions as aircraft structural parts that require high quality surfaces and tight dimensional tolerances. Engineering and design data generated led to the creation of specifications that cover various Ti alloys, different heat treat conditions, and different section thickness gauge breaks. Improvements in producibility and design efficiencies led to significant cost reductions of extruded Ti parts and increased product reliability. The application of Ti extrusions received significant boost in new composite-centric aircraft models to meet significant lightweighting and cost reduction demands. In certain locations of aircraft, Ti was found to be the only choice due to galvanic corrosion resistance and compatibility with carbon fiber materials. The extrusion method was found to be attractive compared to other alternatives to justify replacement of less expensive aluminum incumbents to overcome composite incompatibility issues. Post-extrusion hot stretch forming of near-net shapes enables production of contoured structural members of modern aircrafts to minimize the material needs for final machining. Howmet's vertically integrated Ti alloy extrusion product offerings provide unique design and cost benefits. This paper provides an overview of advances in Ti alloy extrusions, opportunities to achieve buy-to-fly cost reductions, and some challenges unique to extrusion producibility.

Keywords: Ti 6Al-4V, Extrusion, Durability, Damage Tolerance, Aerostructure parts, Transformed beta microstructure.

1. Evolution of Titanium Extrusions for Aerospace

The extrusion method of manufacturing is ideally suited to produce long members of constant or nearly constant cross-section bars and shapes. Difficulties associated with extruding Ti alloys compared to Al alloys were well recognized in the early years of shaped extrusion manufacturing development [1]. Based on early evaluations and assessments, two distinct aircraft markets for Ti extrusions were identified. Aircraft engines employ massive shapes that are subsequently machined all over to produce finished parts. Hence, surface and dimensional tolerance requirements of as-extruded parts were not so rigid. Extrusions of Ti alloys were first used in jet engines for parts such as nonrotating spacers, rings, and flanges of uniform and simple cross-section. Formed extrusions are flash welded into circular shapes, and fully machined to final dimensions to produce these parts. Airframe part shapes, on the other hand, required high quality surfaces and tight dimensional tolerance specifications. Major need of airframe parts demanded simple "alphabetic" shapes ("L", "T", "Z" are the most common) with the size of a circumscribing-circle (the diameter of the smallest circle that will completely enclose the cross section of the shape) of ~150-mm (6") diameter and minimum section thicknesses in the range 1–3 mm (0.040–0.125"). Though Ti has high strength, the modulus of elasticity is relatively low, hence Ti extruded shape requirements are relatively large with thin web thicknesses. Critical roles of billet heating, extrusion temperature and pressure, press speed, die material, die design, and lubricants on the producibility, quality, and cost of Ti alloy shaped extrusions were extensively studied under various government sponsored research efforts for military as well as commercial use [2-6]. It was concluded that "net" extrusions similar to Al are not feasible in Ti due to a combination of properties of titanium that make extrusion process difficult. Envelopes (excess material), as shown in Figure 1, are necessary to allow for manufacturing, dimensional, and machining tolerances.

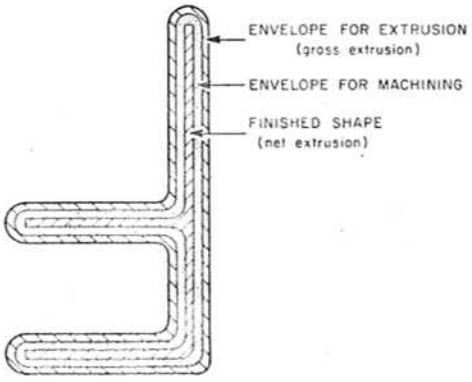

Figure 1. An example Ti alloy aerospace net extrusion cross-section illustrating the envelopes added to meet manufacturing, dimensional, and machining tolerances.

Titanium extrusions are very expensive (on the order of 10×) compared to Al extrusions, primarily due to higher material cost and significant machining cost. High extrusion ratios (area of billet divided by area of extrusion, as high as 20:1) are typically used in high-speed horizontal presses with near-net shape profiles to achieve maximum benefits. The force required to push the extrusion increases exponentially with increase in extrusion ratio. Hence, Ti billets are heated to high

temperatures above the beta transus. High ram speeds (100-200 mm/s or 4–8 inch/s) must be used to avoid billet galling and chilling and also to minimize front-to-rear variations in critical to quality metrics. Adiabatic temperature rise in the core due to high strain rate deformation must be carefully managed to avoid microstructural failures. Application of molten glass lubricant to billet and thermal barrier coating to die became standard practices to reduce the friction and die erosion caused by hot metal as it passes through the die. The lubricants greatly assist in extrusion process but result in dimensional deviations and rougher striated surfaces. These complexities create 100% machining requirements to make Ti extrusions suitable for structural use. Reduction of envelopes on net extrusions is a continuous improvement activity to balance producibility and cost.

Titanium alloy extrusion technology evolved over the past 7 decades with advanced process designs and effective manufacturing process controls (frozen processes and matured specifications), leading to widespread use of Ti extrusions as aircraft structural parts [1-6]. The importance of beta-worked microstructure on the engineering data development for use in aerospace design was well recognized in the early years (1960s) of titanium alloy extrusion introductions [2]. Property uniformity in the section, in length, and directionality (texture) were found to be acceptable. Reliability and uniformity of properties within the individual extruded shapes were established. Extensive testing programs generated tensile, compression, shear, bearing, fracture toughness, impact, delayed failure, creep and stress rupture, and axial fatigue data. Limited axial fatigue and fracture toughness data obtained generally indicated that extruded Ti shapes could be utilized in the same manner as materials produced by other methods such as rolling or forging. Experience with evaluations under FAA supersonic transport program proved that Ti 6Al-4V (Ti 6-4) extrusions are not nearly equivalent to that of beta annealed plate [5]. Characterization testing demonstrated variability in mechanical, fracture, and metallurgical properties. Engineering and design data generated under various funded projects led to the creation of the military specification MIL-T-81556, first issued in March 1968, Rev A published in January 1983 [7]. This specification covers various Ti alloys (CP Ti, Ti 5Al-2.5Sn, extra-low interstitial ELI Ti 5Al-2.5Sn, Ti 8Al-1V-1Mo, Ti 6Al-4V, ELI Ti 6Al-4V, Ti 6Al-6V-2Sn, and Ti 6Al-2Sn-4Zr-2Mo), different heat treat conditions (annealed, duplex annealed, solution treat plus age), and different section thickness gauge breaks. Design allowables for extruded Ti bars and shapes are published in the Metallic Materials Properties Development and Standardization (MMPDS) Handbook (current Version 17, July 2022) [8], a joint effort of government, industrial, educational, and international aerospace organizations. Industry aerospace material specification AMS 4935 [9] for Ti 6-4 (first issued in 1959, Revision M 2022-08) covers extrusions and flash welded rings, beta processed and annealed in the range 1300–1400°F. Parts made to AMS 4935 for section sizes ≤ 75-mm (3") are most widely used. Specification for another heat treat condition, AMS 4934 [10], Ti 6-4 Extrusions and Flash Welded Rings, Solution Heat Treated and Aged (first issued in 1975, Revision H 2019-06), is also active. Higher strengths and complex residual stress profiles of water quenched STA extrusions add complexity during machining compared to annealed. Due to these reasons, STA Ti 6-4 extrusions usage is limited. ELI Ti 6-4 extrusions are used for parts designed with higher fracture toughness requirement that experience stress corrosion cracking issues in sea water [11]. Significant knockdown in fracture toughness when exposed to saltwater was identified due to the presence of short-range ordering (Al atoms occupying specific locations of Ti lattice forming Ti_3Al α_2 phase).

Improvements in producibility and design efficiencies led to significant cost reductions of extruded Ti parts and increased product reliability. The application of Ti extrusions significantly boosted in new composite-centric (graphite-reinforced organic-matrix) models and their derivatives to meet significant lightweighting and cost reduction demands [12, 13]. In certain locations of the aircraft, Ti was found to be the only choice due to galvanic corrosion resistance compatibility with graphite. Significant collaboration engineering efforts became necessary for Ti extruded parts substitutions or introductions to fully realize the performance benefits that justify significant lifecycle cost savings although the acquisition costs are very high compared to the baseline. Post-extrusion hot stretch forming was found to be an enabler for producing contoured structural members of modern commercial aircrafts to minimize the material needs for final machining [14]. Howmet Aerospace's vertically integrated Ti alloy extrusion product offerings demonstrated unique design and cost benefits.

2. State-of-the-Art of Ti Alloy Extrusions

Currently, Ti alloy extrusions use is limited to static loaded parts only due to limitations on their performance and knowledgebase under dynamic loading conditions. Transformed beta microstructures (typical macro and microstructure features of Ti 6-4 AMS 4935

extrusion presented in Figure 2) created due to high-speed processing above the beta transus restrict microstructural engineering opportunities in single-step extrusions to moderate-strength static components.

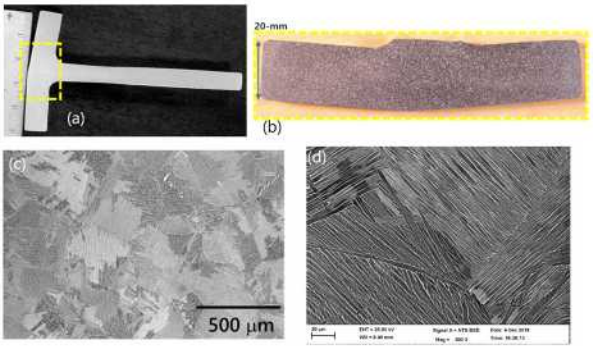

Figure 2. Macro (a, b) and microstructural (c, d) features of a typical tee-shaped Ti 6-4 extrusion produced to the specification AMS 4935. Fine and uniform macrostructure (macro level 10), fine prior beta grain size, colony size, alpha lath thickness, and thin grain boundary alpha layer thickness observed are typical.

Property combinations in other wrought products such as plates and forgings can be easily controlled via multi-step thermomechanical processing sequences above and below β transus to produce any class of microstructure, (fully equiaxed, fully lamellar, or duplex, Figure 3) in a controlled manner under production settings. Complex interplay between size, morphology, volume fraction, and orientation of lamellar colony microstructural features at different length scales (prior beta grain size, colony size, alpha lath thickness, grain boundary alpha layer thickness) controls various static and dynamic property combinations (Figure 4) achievable in a repeatable and reproducible manner. It is well known that fine lamellar microstructures in β processed Ti extrusions provide higher tensile strength and fatigue strength at the expense of debits in fracture toughness and fatigue crack growth resistance (damage tolerance) due to reduced contributions from crack path tortuosity and roughness [15]. Coarsening the microstructural features via controlled post-extrusion heat treatment is feasible, as illustrated in Figure 5, to improve damage tolerance of Ti alloy extrusions. An assessment of performance of various Ti 6-4 extrusions produced under controlled production conditions was made to understand capability and suitability Ti extrusions for fatigue-rated applications [16]. Comparisons were made with α+β rolled plate subjected to beta anneal to produce lamellar microstructures.

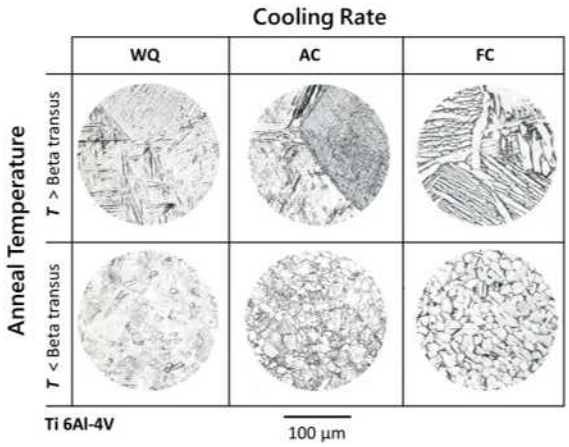

Figure 3. Different microstructural classes achievable in Ti 6-4 wrought products such as plates and forgings via controlled thermo-mechanical processing.

Figure 4. Illustration of strength, durability, and damage tolerance combinations in Ti 6-4 damage-critical aerospace parts.

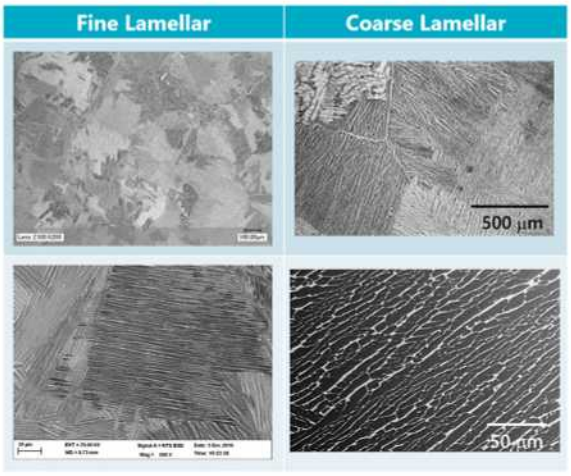

Figure 5. Comparison of two microstructural variants generated in Ti 6-4 extrusion, fine lamellar (left) and coarse lamellar (right). Optical micrographs on the top show the colony and prior beta grain characteristics. Backscattered electron images at the bottom show alpha lath and beta matrix characteristics of these two variants.

Room temperature tensile properties (0.2% offset tensile yield strength, tensile ultimate strength, and tensile elongation) of Ti 6-4 extrusions produced to the specification AMS 4935 are presented in Figure 6. This dataset includes release data on various extruded shapes,

sizes, section thicknesses, finishing operations, final heat treat conditions, and testing directions1. These box plots demonstrate excellent statistical process control (SPC) of Ti 6-4 annealed extrusions to meet design minimum tensile requirements. Tensile strength distribution plots of Ti 6-4 extrusion are similar to those of beta annealed plate, confirming their equivalency for substitution. Coarse lamellar microstructure variant of extrusion shows minor debits in tensile strength compared to fine lamellar extrusion, which is as expected due to reduced contribution of boundary/interface strengthening component [15]. Tensile elongation of fine lamellar extrusions is much superior compared to coarse lamellar variant or beta annealed plate.

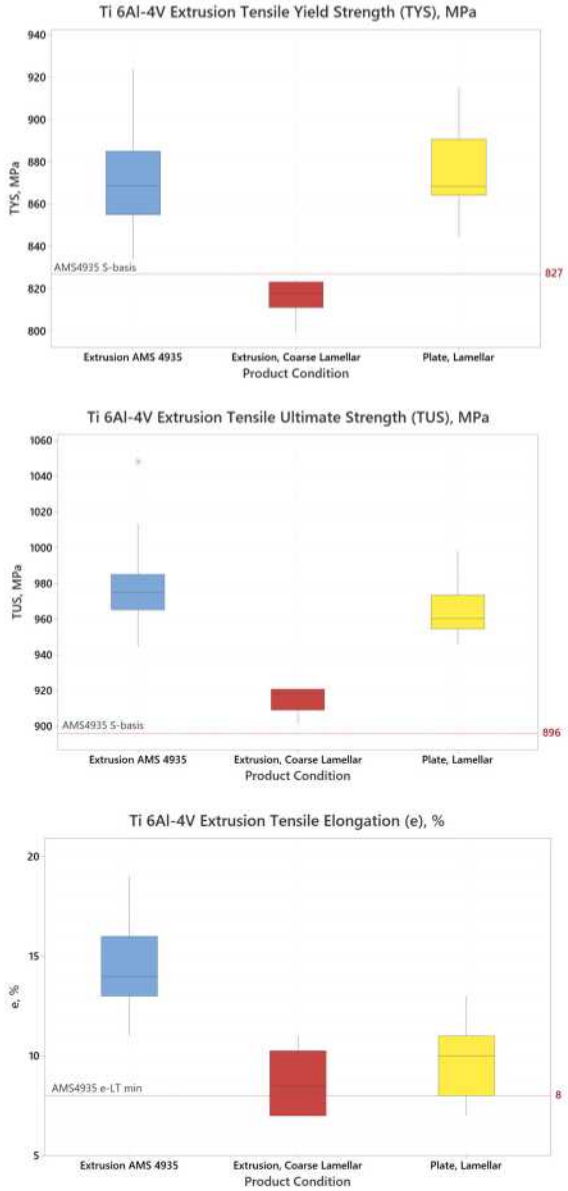

Figure 6. Tensile yield strength (0.2% offset), ultimate strength, and elongation of Ti 6-4 AMS 4935 extrusions. Properties of beta annealed plate and coarse lamellar variant of extrusion are also shown for comparison.

The high cycle fatigue (HCF) strength (resistance to crack nucleation) of Ti 6-4 AMS 4935 extrusions is presented in Figure 7 in the form of stress-cycles to failure (*S-N*) curves generated on flat open-hole specimens with a stress concentration factor K_t=2.3 under tension-tension (stress ratio R=0.1) loading conditions. The stress-life of extrusions is similar to that of beta annealed plate, with HCF strength of ~200 MPa for 3 million cycles run out (RO). Based on these comparisons, notch HCF strength is relatively insensitive to product form and structure variations within lamellar class. For reference, *S-N* curve of Ti 6-4 plate with equiaxed microstructure class produced to AMS 4911 specification [16] is also shown in Figure 7, which exhibits superior HCF strength of ~275 MPa for the same RO.

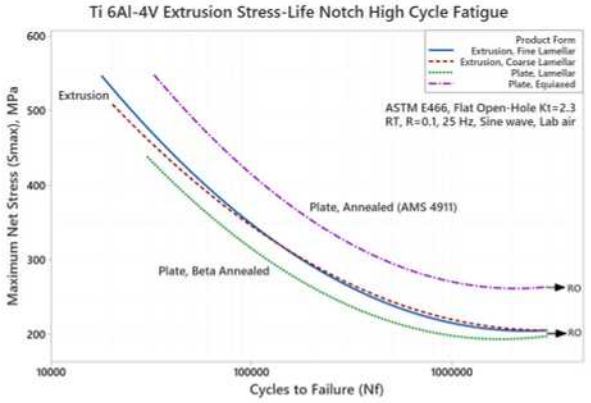

Figure 7. Stress-life notch HCF *S-N* curves of Ti 6-4 extrusion compared to plate. Run out (RO) is defined as 3 million cycles.

Fracture toughness (ability to absorb energy by localized plastic deformation rather than by crack propagation or fracture, particularly in the presence of notches or other stress concentrators) data generated on Ti 6-4 extrusions produced to AMS 4935 specification is presented in Figure 8. The plane-strain fracture toughness (K_{Ic}) dataset shows a very broad distribution, with low values corresponding to smaller/thinner extrusions and higher values corresponding to larger/thicker extrusions, all within the specification. Fine macro and microstructure features created during high-speed extrusion above the beta transus and cooling rate variations in different sections explain the wide KIc range. Beta annealed plate, on the other hand, shows higher fracture toughness and tighter distribution, as a result of significant alpha+beta rolling work followed by controlled heat treatment above the beta transus. Coarse lamellar variant of extrusion shows significant improvement in fracture toughness compared to fine lamellar variant. Fracture capability similar to beta annealed plate is achievable in extrusions via structure coarsening, which enhances geometric contribution of fracture resistance in this microstructure class [15].

Typical long fatigue crack growth rate behavior (crack growth rate da/dN vs. stress intensity factor range ΔK) of Ti 6-4 extrusions produced to AMS 4935 is presented in Figure 9. Faster crack growth rates were

noted at lower ΔK values (Paris law regime) compared to beta annealed plate. This is attributed to reduced crack path tortuosity and crack front roughness contributions in fine lamellar microstructures [15]. Coarse lamellar variant of extrusion, on the other hand, shows crack growth resistance similar to that of beta annealed plate, demonstrating the ability to improve damage tolerance of extruded products in the Paris law regime. Fatigue crack growth behavior at higher ΔK values is insensitive product form and structure variations within the product form of lamellar class.

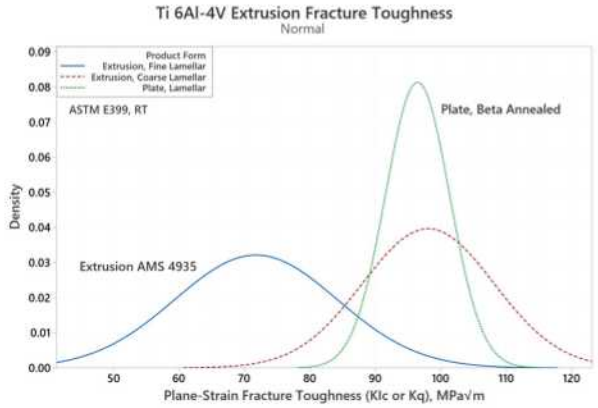

Figure 8. Fracture toughness of Ti 6-4 extrusion in two different microstructure conditions (fine lamellar AMS4935 and coarse lamellar) compared to beta annealed plate.

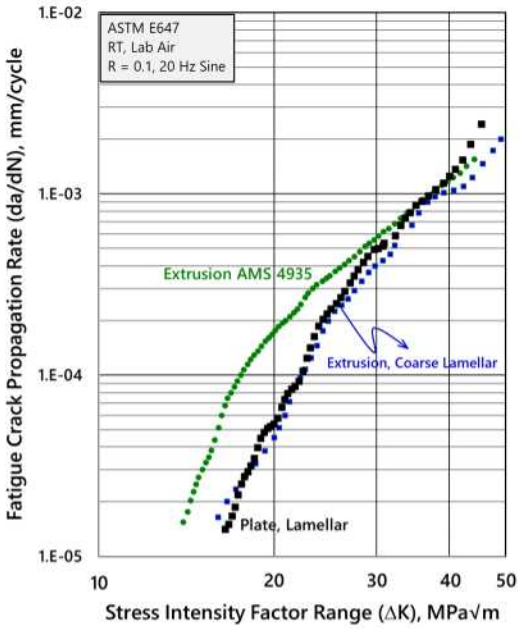

Figure 9. Fatigue crack growth rate curves of Ti 6-4 extrusion in two different microstructure conditions (fine lamellar AMS4935 and coarse lamellar) compared to beta annealed plate.

3. Summary and Conclusions

Although titanium alloy extrusion technology dates back to early 1950s and cost reduction advantages were well recognized, the use of Ti extrusions in aerospace is limited to statically-loaded secondary and tertiary structures only due to process constraints, lack of dynamic performance data, and perceived risks. A comprehensive assessment of Ti 6Al-4V (Ti 6-4) extrusions was performed to develop an understanding of the technology and manufacturing readiness levels to consider their use for primary structures with durability and damage tolerance (DADT) requirements. The following conclusions are drawn based on critical analyses of metallurgical and mechanical characteristics.

i) Ti 6-4 extrusions produced to AMS 4935 (most common industry specification for statically loaded components) exhibit good balance of static and dynamic properties. Beta processing followed by air cooling of thin extrusion sections results in finer structures at all length scales (prior beta grain size, alpha colony size, and alpha lath thickness) compared to beta annealed Ti 6-4 plate. Superior tensile strength and ductility, moderate fracture toughness, good high cycle fatigue strength, and moderate fatigue crack propagation resistance combinations were observed. As expected, finer alpha colony size in annealed extrusions does lead to faster macrocrack propagation rates under fatigue at low stress intensity factor range (Paris Law regime) due to reduced crack tortuosity and crack front roughness profile contributions.

ii) Coarsening of microstructure features at different length scales is feasible via post-extrusion heat treatment to improve damage tolerance similar to that of other beta annealed wrought products with minor debits in tensile strength and ductility.

4. Acknowledgements

The authors appreciate support and contributions provided by various Howmet Aerospace Niles, Houston, and Low Moor production team members.

5. References

1. Extrusion of New Titanium Alloys, US Air Force Contract No. AF 33 (600) – 28322, Harvey Aluminum, Sep 1954 – Oct 1957, Final Report November 1957.
2. R.M. Brockett, J.A. Gottbrath, Lockheed-California Company, Development of Engineering Data on Titanium Extrusions for Use in Aerospace Design, AFML-TR-67-189, July 1967.
3. Extrusion of titanium alloy shapes, O.S. Mironov et al., in Titanium Alloys for Modern Technology by N.P. Sazhin et al., NASA Technical Translation F-596 of "Titanovyye splavy dlya novoy tekhniki", p. 301, "Nauka" Press, Moscow, 1968.
4. Extruding titanium and titanium alloys, Paul Loewenstein, Society of Manufacturing Engineers, International Engineering Conference

and Tool Exposition, Philadelphia PA, Apr 1971, Paper MF 71-139.

5. Titanium alloy 6Al-4V Extrusions, W.F. Spurr, The Boeing Company, Commercial Airplane Group, FAA Super Sonic Technology Follow-on Program, Phase I, Report No. FAA-SS-72-06, July 1972.
6. T.G. Byerer et al., Design Guide for the Use of Structural Shapes in Aircraft Applications, AFML-TR-73-211, Battelle Report, September 1973.
7. Military Specification MIL-T-81556A, Titanium and Titanium Alloys, Extruded Bars and Shapes, Aircraft Quality, 31 January 1983
8. Metallic Materials Properties Development and Standardization MMPDS-17, July 2022.
9. Aerospace Material Specification AMS 4935 Titanium Alloy Extrusions and Flash Welded Rings, 6Al-4V, Annealed, Beta Processed, Rev M 2022-08, SAE International.
10. Aerospace Material Specification AMS 4934 Titanium Alloy Extrusions and Flash Welded Rings, 6Al-4V, Solution Heat Treated and Aged, Rev H 2019-06, SAE International.
11. R. Briggs, Stress Corrosion Cracking Threshold of Ti-6Al-4V Extrusions, AEROMAT 2013 Presentation, The Boeing Company.
12. Near-Net-Shape Titanium Alloy Extrusions, R.R. Boyer, E.R. Barta, and J.W. Henderson, JOM, March 1989, pp. 36 – 39.
13. R.J. Tisler, R.S. Addison, AEROMAT 2002 Presentation, Titanium Extrusions for Aerospace Applications
14. A. Keskar, K. Minakawa, Hot stretch forming of titanium 6Al-4V alloy extrusions, Ti-2007 Science and Technology, Conference Proceedings, The Japan Institute of Metals (2007) pp. 1275-1278.
15. G. Lutjering and J.C. Williams, Titanium, Springer, 2007, pp. 218-227.
16. U.G. Goranson, Fatigue issues in aircraft maintenance and repairs, Intl. J. Fatigue, Vol. 20, No. 6, 1997, pp. 413-431.
17. Aerospace Material Specification AMS 4911 Titanium Alloy, Sheet, Strip, and Plate, 6Al-4V, Annealed, Rev. R 2019-12, SAE International.

TECHNOLOGY CAPABILITY STUDY OF LASER POWDER BED FUSION TO PRODUCE LARGE CRITICAL AEROSPACE STRUCTURES IN Ti-6Al-4V

M. Bodie[1], M. Mani[1], S. Milward[1], T. Garcia[1], R. Martinez-Ramos[1], F. Kassim[2]

1 GKN Aerospace, Taurus Road, Patchway, Filton, Bristol, United Kingdom
2 The University of Bath, Claverton Down, Bath, United Kingdom

In aerospace manufacturing there are very few large conventional suppliers that can produce complex aero engine components. Laser Powder Bed Fusion (L-PBF), an additive manufacturing technology, has been identified as a possible substitute technology to diversify the supply chain. L-PBF could also be used to produce parts for the next generation of aero engines. L-PBF manufacturing can offer advantages over conventional manufacture. Such advantages include; improved buy to fly ratio, reduced waste, properties on demand, rapid component development, and complex design capability.

The study presented in this article compared the production capability of two multi-laser L-PBF systems to produce a large critical aero engine component from Ti-6Al-4V. In previous work large thermal gradients and rapid cooling during solidification in L-PBF was shown to generate high tensile residual stresses. These stresses, even after stress relief heat treatment, were shown to cause heavy distortion and ultimately the failure of the part. Multi-laser L-PBF systems have been shown to reduce these residual stresses and distortions. In this article, the component selected had a complex geometry that posed significant challenges for the technology; features such as overhangs, vanes, thin to thick wall transitions and holes were present. The mechanical properties, laser stitching effect, and geometric conformance are assessed and discussed.

Keywords: Ti-6Al-4V, Additive Manufacturing, Mechanical Property Characterisation, Laser Stitching, Geometric Conformance

1. Introduction

A key design consideration for material selection in the aerospace industry is weight minimisation. Titanium alloys, with excellent strength to weight ratio, high temperature tolerance, and fatigue strength, are extensively employed. However, the supply chain for the fabrication of complex titanium parts for the aerospace industry in general and aero engine components in particular is very limited. Additive manufacture, a layer-by-layer manufacturing process, is a potential alternative to conventional manufacturing processes. The components produced are near-net shape and titanium components have been produced with complex geometries at a reduced buy-to-fly ratio (3-12:1 cf. 12-25:1 for traditional titanium aerospace manufacturing methods) [1-4].

Laser Powder Bed Fusion (L-PBF) additive manufacturing has been developed and evaluated by GKN Aerospace for a number of years. GKN Aerospace believe this alternative technology has potential and can be substituted for traditional manufacturing methods. L-PBF could also enable more novel component designs to be considered for the next-generation of aero engines.

The input powder quality for L-PBF can have a significant impact on the printability and performance of parts. The more spherical powders have been shown to pack more efficiently which yield higher density; they possess improved flowability, produce an improved surface finish and are more dimensionally accurate. Packing density has been shown to be influenced by particle size distribution (PSD). If the PSD has an insufficient distribution of fine particles there is an increased the risk of porosity. In addition, fine particles increase laser absorption and result in denser builds. Therefore, a well distributed PSD and high apparent density in L-PBF systems are desirable [9-12].

In the case of Ti-6Al-4V alloys, strength and ductility are strongly influenced by oxygen content, consequently the oxygen content of the powders used in L-PBF are tightly controlled. Each L-PBF system maintains different oxygen levels in the process chamber and therefore the rate of oxygen infusion differ. If oxygen levels in the powder exceeds specification, a whole batch could need to be disposed. Hence, powders in L-PBF are tested to ensure compliance with specification prior to parts being built [13].

Unwanted L-PBF defects such as porosity are deleterious to the structural integrity and durability of additive manufactured components, particularly for fatigue strength where premature failure is primarily controlled by the defect. Porosity in L-PBF can form in a number of ways namely; keyhole porosity, lack of fusion porosity, or gas porosity. Keyhole pore formations are typically process parameter dependent and characteristic of high power, low velocity regions. These pores correspond to instabilities in deep keyholes during the lasing process that can pinch off and form a pore. Lack of fusion pore formation can be related to either process parameters or the systems gas flow. Parameter dependent lack of fusion pores form when insufficient overlaps between melt pools are used or within low power, high speed regions. Whereas gas flow lack of fusion pores form when the gas flow is

insufficient and ejected “spatter” from the melt pool is not removed. This spatter may land on the powder bed and not be fully melted during subsequent lasing. Similarly, if the gas flow does not remove small condensate particles in the vapour plume ejected from a keyhole it can result in laser scattering and limited laser penetration, which likewise results in lack of fusion. Gas pores are formed from entrapped gas within individual powder granules which is not removed during the lasing process. Characterisations of unwanted defects, such as porosity, can be used to determine the capability and performance of L-PBF systems [15-16].

Most L-PBF suppliers have started to incorporate multiple lasers within their system to enhance productivity by reducing interlayer times. It has been shown that if two or more laser incident points encounter each other during the build, a large number of keyhole defects can occur which affect the integrity of the component. It is therefore necessary for the systems software to ensure that interactions of different laser incident points are avoided. For the manufacture of large components, a series of overlap regions must be arranged and there is a higher propensity for defect formation. To the best of the authors’ knowledge studies into this area are limited [14].

Previous work completed by GKN Aerospace found that large thermal gradients and rapid cooling during solidification of large Ti-6Al-4V parts manufactured with L-PBF generate high tensile residual stresses. After stress relief heat treatment heavy distortion and failure can still occur. Common methods to reduce residual stresses include the utilisation of multi-laser systems to reduce the interlayer time, higher baseplate temperatures, or improved thermal control of the process chamber. The work reported here compares the capability of two multi-laser systems to produce a large critical aero engine component from Ti-6Al-4V. Input material feedstock, bulk material properties, and geometric conformance are assessed and discussed.

1.0 Experimental Procedure

The input powder used in this experiment was tested in accordance with GKN Aerospace’s internal manufacturing specification. The alloy powder compositions used were aligned with technical requirements of ASTM F2924, AMS7017 for Ti-6Al-4V ELI or AMS7015 for Ti-6Al-4V Grade 5 [6-8].

All the chemical compositions were tested by Element Materials Technology with bulk reactive and non-reactive elements, except Carbon, determined in accordance with ASTM E539 or ASTM E2371. Oxygen and Nitrogen were determined in accordance with ASTM E1409, Hydrogen in accordance with E1447 and Carbon in accordance with ASTM E1941 [21-25].

Hall flow rate and apparent density of the input powders were tested at GKN Aerospace using a Hall Flowmeter Funnel to ASTM B213 and ASTM B212 respectively. PSD were tested by Carpenter Additive using light scattering in accordance with ASTM B822. Powder morphologies were assessed at GKN Aerospace using a Hitachi Table Top TM3030Plus SEM [18-20].

The L-PBF system used by Supplier 1 comprised 3 500W fibre lasers emitting coherent light at 1070nm. The L-PBF system used by Supplier 2 employed 4 1kW fibre lasers that also emitted at 1070nm. Two L-PBF builds from Ti-6Al-4V were completed for each multi-laser system, the first builds were coupons used to establish mechanical properties, microstructure, and porosity from each system; an example build is presented in Figure 1. The second builds, presented in Figure 2, were a notional geometry based on a section of a large critical aero engine component used to evaluate the printability and geometric performance of each system.

Both coupon and component builds received a stress relief heat treatment after manufacture to reduce the likelihood of the part cracking when cooled. Heat treatments were carried out in a vacuum at 720°C in accordance with AMS2801B and cooled under vacuum, in Argon or Nitrogen to 200°C [5].

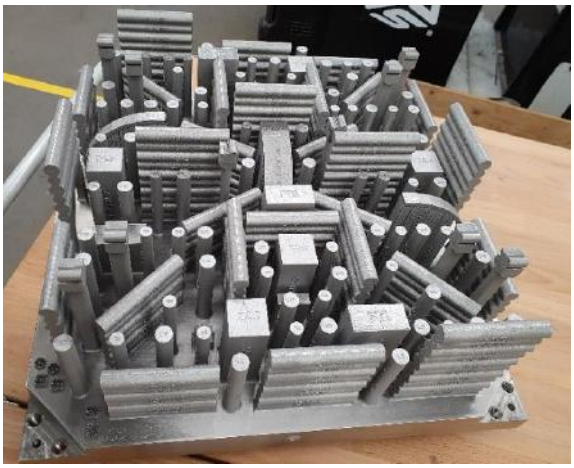

Figure 1: Supplier 1 coupon build used to establish mechanical properties, microstructure and porosity

Figure 2: Supplier 2 section of a large critical aero engine component used to evaluate the system's printability

The microstructure and porosity of metallographic samples taken from coupon builds were assessed at GKN Aerospace by optical microscopy and a Hitachi Table Top TM3030Plus Scanning Electron Microscopy (SEM).

Post stress relief samples from coupon builds were machined into test pieces for tensile tests carried by Element Materials Technology in accordance to ASTM E8. Both vertical and horizontal tensile properties were evaluated against ASTM F2924 [8, 17].

The component builds were scanned, after stress relief, using a high precision 3D optical scanner and compared with the original CAD models to assess geometric conformance.

2. Results and Discussion

The rheological properties and chemical composition of the input powders are reported in Tables 1 and 2. The flow rates achieved correlated with the powder morphologies seen in Figure 3. The powders with more spherical morphology flowed at a greater volumetric rate through the funnel due to lower surface friction and mechanical interlocking. The apparent density tests also correlated with the powder morphologies observed. The greatest packing density was exhibited by the powders with the greater spherical morphology. The input powders chemical compositions, flow rates and apparent densities were within the specification of AMS7017, AMS 7015 and ASTM F2924.

Table 1: Hall flow and apparent density measurements for input powders tested in accordance with ASTM B213 and ASTM B212 [19-20]

Test	**Supplier 1**	**Supplier 2**	**AMS7017 AMS7015**
Flow Rate (sec/50g)	25.0	27.5	Max 30
Apparent Density (g/cm^3)	2.49	2.44	Min 2.30

Table 2: Chemistry specification from ASTM F2924, Standard Specification for Additive Manufacturing Titanium-6 Aluminum-4 Vanadium with Powder Bed Fusion [8]

Element	**Min**	**Max**	**Supplier 1**	**Supplier 2**
Aluminium	5.50	6.75	6.50	6.40
Vanadium	3.50	4.50	4.10	4.00
Iron	-	0.30	0.23	0.20
Oxygen	-	0.2	0.11	0.13
Carbon	-	0.08	0.01	0.01
Nitrogen	-	0.05	0.01	0.01
Hydrogen	-	0.015	0.0045	0.0028
Yttrium	-	0.005	0.001	0.001
Other elements, each	-	0.10	0.09	0.01
Other elements, total	-	0.40	0.14	0.02
Titanium	remainder			

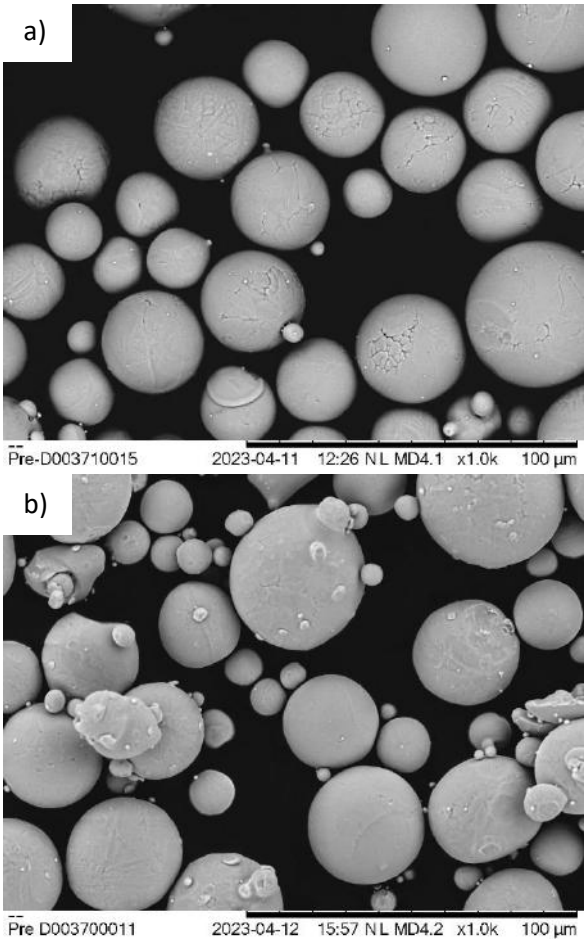

Figure 3: Powder morphology of input powders for both multi-laser systems a) Supplier 1 b) Supplier 2

Analysis of the PSDs of input powder, presented in Table 3, showed that both batches had comparable size distributions. The powder used by Supplier 1 had a marginally narrower distribution that shifted towards fine particles. However, both input

powders PSD were within GKN Aerospace's internal powder manufacturing specifications.

Table 3: PSD measurements for input powders tested by light scattering in accordance with ASTM B822 [18]

	D_v10 (µm)	D_v50 (µm)	D_v90 (µm)
Supplier 1	23.4	34.3	49.9
Supplier 2	24.8	38.2	57.5

Optical micrographs taken from metallographic samples within the coupon builds in the stress relieved condition and swab etched with Kroll's reagent are presented in Figure 4. The samples from Supplier 2 showed columnar prior-β grains parallel to the build direction. This is typical for Ti-6Al-4V additive manufactured parts that are rapidly cooled with large directional thermal gradients. Conversely, Supplier 1's samples showed prior-β grains with a significantly more equiaxed morphology. This indicated that Supplier 1 achieved superior thermal control within the process chamber that reduced directional thermal gradients.

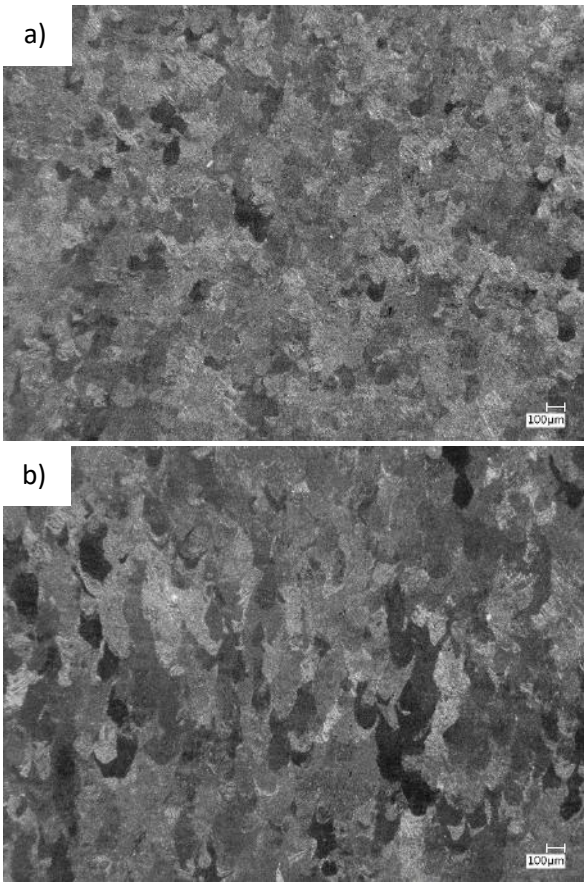

Figure 4: Microstructures from metallographic samples for each multi-laser system taken at x100 magnification a) Supplier 1 b) Supplier 2

The porosity measurements were taken from metallographic samples within coupon builds from various locations with respect to the gas flow outlet. These samples were assessed to determine the effectiveness of each system's gas flow to reduce defect formation. Porosity levels and maximum defect size were measured; the results are presented in Figures 5 and 6. No clear relationship was observed for either multi-laser systems, this indicated that the gas flow was consistent across the powder bed for both systems.

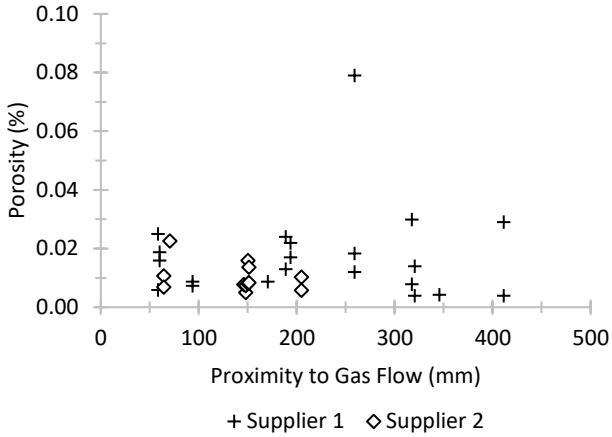

Figure 5: Porosity levels in metallographic samples with proximity from the gas flow outlet for both multi-laser systems

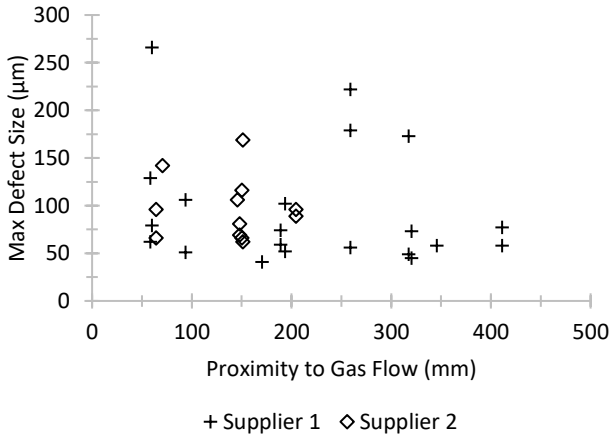

Figure 6: Maximum defect size in metallographic samples with proximity from the gas flow outlet for both multi-laser systems

The porosity morphology of the metallographic samples from Supplier 1, presented in Figure 7a, were predominantly spherical pores which are indicative of keyhole porosity or entrapped gas porosity. As previously discussed, keyhole pores are typically process parameter dependent rather than system related. Conversely, the porosity observed from Supplier 2, Figure 7b, showed mostly irregular pores that are indicative of lack of fusion pores that could be either process parameter dependent or related to insufficient gas flow.

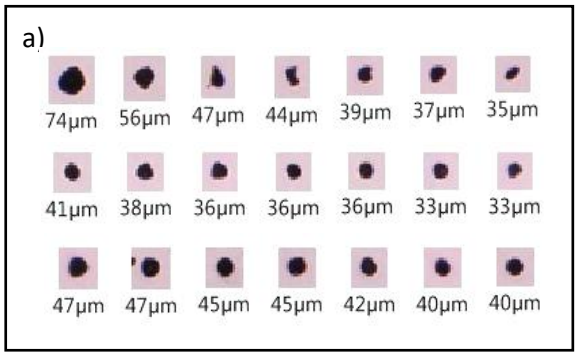

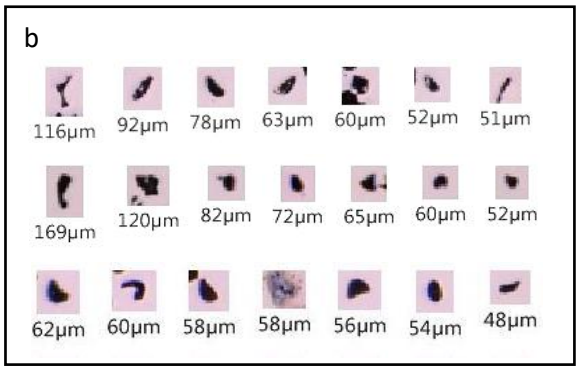

Figure 7: Pores observed from metallographic samples for each multi-laser system a) Supplier 1 b) Supplier 2

The tensile properties of stress relieved samples from the coupon builds are presented in Figures 8 and 9. The yield strength and 4D elongation of multi-laser tensile samples were comparable to, or slightly higher than that of the single laser material. This indicated that if different laser incident points are avoided there are no deleterious impacts corresponding to the laser stitching region and both systems were effective at mitigating this phenomenon.

The tensile results of Supplier 2 showed greater variability than Supplier 1. In addition, two of the samples produced by Supplier 2 had elongation values below ASTM F2924. These are thought to be related to the lack of fusion porosity as observed in the metallographic samples. Whereas the higher tensile strength results achieved by Supplier 2 are likely associated with the marginally higher oxygen content of the input powder.

A geometric scan taken of the notional geometry based on a section of a large critical aero engine component from Supplier 2 is presented in Figure 10. The scans were used to evaluate the printability performance of both systems and measure the extent of distortion or shrinkage that occurred during part manufacture.

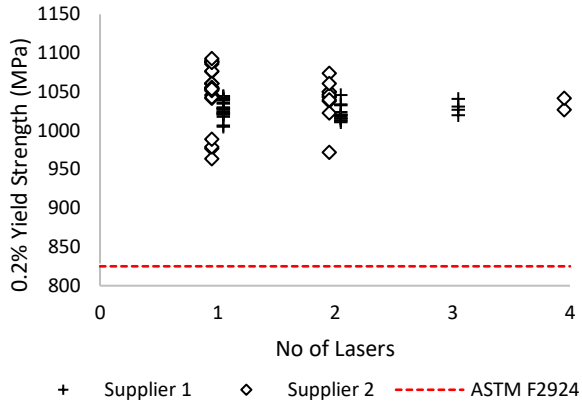

Figure 8: Yield strength of samples produced by multiple and single lasers for both multi-laser systems

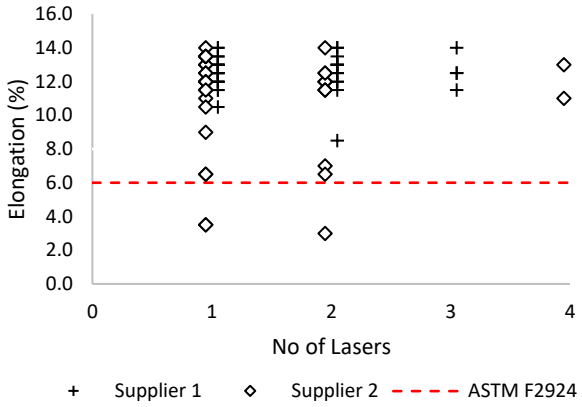

Figure 9: Elongation results of samples produced by multiple and single lasers for both multi-laser systems

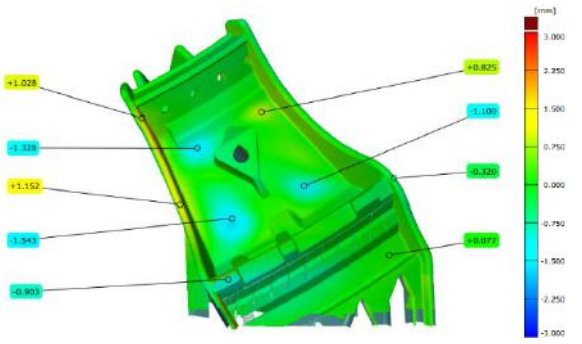

Figure 10: High precision 3D optical scan of component build completed by Supplier 2

Geometric conformance was measured in seven equivalent locations on the two component builds. A comparison of conformance is presented in Figure 11. The component manufactured by Supplier 1 had better conformance to the original CAD geometry. This was taken as a measure of process thermal control that resulted in lower inherent residual stresses and therefore less distortion. This conclusion is consistent with the microstructures observed earlier.

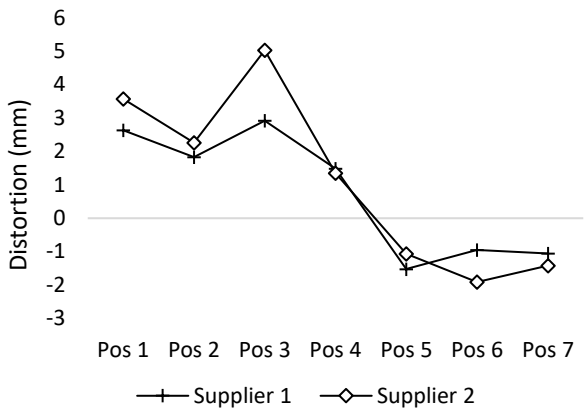

Figure 11: Comparison of distortion observed across seven key features on component builds

3. Conclusions

The powder batches utilised within both multi-laser system builds were assessed for their flowability, chemical composition, PSD, and apparent density. The results showed that all powders were within specification prior to manufacture. Slight variations in rheological properties and apparent density were related to differences in the powder morphology. Similarly, minor variations in oxygen content resulted in higher yield strength in some tensile samples produced by Supplier 2.

There were no clear trends in porosity level and maximum defect size with the proximity to the gas flow for either multi-laser systems. This showed that the gas flow was consistent across the powder bed for both systems.

The morphology of pores observed between the two multi-laser systems were different, with Supplier 1 showing spherical pores consistent with keyhole or gas pores. Whereas Supplier 2's morphology showed lack of fusion pores. These lack of fusion pores are thought to be correlated with the greater variability of tensile results and several below ASTM F2924 elongation values.

Both systems were effective at mitigating different laser incident points. The yield strength and 4D elongation results of the multi-laser tensile samples were comparable to that of single laser material.

The prior β-grain morphology of metallographic samples and geometric conformance of the component build indicated that Supplier 1 had achieved improved process thermal control with lower inherent residual stresses. Overall Supplier 1 demonstrated the more stable process for manufacturing large critical aero engine components from Ti-6Al-4V.

4. References

1. M.Bodie et al, "Effect of microstructure and cooling rate on the fatigue performance of TIMETAL®575," Conf. Proc. of the 14th World Titanium Conference, 2019.
2. Rugg et al, *J Strain Anal*, Vol. 42, 2007.
3. Thomas et al. "TIMETAL 575: A Novel High Strength Forgeable α/β Titanium Alloy," Conf. Proc. of the 13th World Titanium Conf, 2016.
4. Yung C. Shin et al, *Materials & Design*, Vol. 164, 2019, 107552, ISSN 0264-1275.
5. AMS2801B, 2014, Heat Treatment of Titanium Alloy Parts, SAE.
6. AMS7017, 2022, Ti-6Al-4V Powder for Addit. Manuf. Extra Low Interstitial, SAE.
7. AMS 7015, 2022, Ti-6Al-4V Powder for Addit. Manuf., SAE.
8. ASTM F2924, October 2021, Standard Specification for Addit. Manuf Ti-6Al-4V with Powder Bed Fusion.
9. S.Brika et al, Addit. Manuf. 31, 100929, 2020.
10. C.Lu et al, J. of Mat Research and Tech., Vol. 18, 2022, 2292-2309.
11. M.Bonesso et al. *Berg Huettenmaenn Monatsh* 166, 256-262 (2021).
12. K.Riener et al, *Addit. Manuf*. 34, 101286, 2020.
13. M.Schafnitzel et al, Euro PM2020 Virtual Congress, November 2020.
14. K.Wei et al, *Materials Science & Engineering A*, Volume 802, 2021, 140644.
15. J.Gordon et al, Addit. Manuf. 36, 2020, 101552.
16. J.Reijonen et al, Addit. Manuf. 32, 2020, 101030.
17. ASTM E8-04, 2010, Standard Test Methods for Tension Testing of Metallic Materials.
18. ASTM B822, 2020, Standard Test Method for Particle Size Distribution of Metal. Powders and Related Compounds by Light Scattering
19. ASTM B213, 2021, Standard Test Methods for Flow Rate of Metal Powders Using the Hall Flowmeter Funnel.
20. ASTM B212, 2021, Standard Test Method for Apparent Density of Free-Flowing Metal Powders Using the Hall Flowmeter Funnel.
21. ASTM E539, 2029, Standard Test Method for Analysis of Ti Alloys by Wavelength Dispersive X-Ray Fluorescence Spectrometry.
22. ASTM E2371, 2022, Standard Test Method for Analysis of Ti and Ti Alloys by Direct Current Plasma and Inductively Coupled Plasma Atomic Emission Spectrometry.
23. STM E1409, 2022, Standard Test Method for Determination of O and N in Ti and Ti Alloys by Inert Gas Fusion.
24. ASTM E1941, 2016, Standard Test Method for Determination of Carbon in Refractory and Reactive Metals and their Alloys by Combustion Analysis.
25. ASTM E1447, 2022, Standard Test Method for Determination of Hydrogen in Reactive Metals and Reactive Alloys by Inert Gas Fusion with Detection by Thermal Conductivity or Infrared Spectrometry.

TENSILE DUCTILITY AT ROOM TEMPERATURE IN HIGH-TEMPERATURE TITANIUM ALLOYS USED FOR AEROENGINE APPLICATIONS

Ramachandra Canumalla[1], Tanjore V. Jayaraman[2]

1 Weldaloy Specialty Forgings, Warren, MI 48089, USA.
2 Department of Mechanical Engineering, United States Air Force Academy, CO 80840, USA.

Alpha (α) /beta (β) and near-α high-temperature titanium alloys are used in compressor parts in jet engines. Some of these alloys show very low ductility at room temperature. Efforts have been made to understand this aspect. It is attempted to comprehensively put together the findings in the literature on this aspect of low ductility at room temperature. Al, Sn, Zr, Hf, Si, and some other elements are added to titanium to exhaust the solid solubility to improve the high-temperature properties. Silicides and/or Ti_3Al (α_2) are precipitated in these alloys depending upon the composition, thermomechanical treatments, thermal processing, and exposures during service. These precipitates have been reported to cause low ductility in these alloys. However, it is unclear whether the low ductility at room temperature is due to silicides or α_2 or both or some other reason like surface oxidation, texture effects, or a combination of all the factors. Further, it was also observed that the low ductility is severe in the lamellar microstructures compared to bimodal microstructures of the matrix when silicides and/or α_2 or both occur. The tensile ductility is not affected very much when the α_2 precipitates selectively in the primary α in the bimodal microstructures and small ($\leq$ ~6 nm). The low tensile ductility could be mitigated by alloy design, optimizing heat treatment processes by appropriately controlling the size, volume fraction, and location of the embrittling phases, namely silicides and/or α_2, texture, and protective coatings. Alloys with replacing Zr with Hf and other elements like Ge showed better room temperature ductility. This is a direction to investigate. It is important to mention that low ductility has consequences in aspects of low-cycle fatigue like two slope behaviour in Coffin -Mason plots and Cold Dwell Fatigue as evidenced in the literature. The study revealed that there is a need for more investigations in the areas of alloy design and thermo-mechanical processing to optimize microstructure, texture/microtextured regions, and coatings.

Keywords: titanium alloys; silicides; Ti_3Al; ductility, microstructure, alpha case, embrittlement, coatings

1. Introduction

Conventional high temperature titanium alloys with their excellent strength to weight ratio, elevated temperature properties, good corrosion resistance, weldability, fabricability have entered aeroengine components around the year 1950 and their proportion increased to more than 30% of the compressor and many other parts [1-7]. The evolution of the alloys since 1950 is shown in Figure 1. The development of these conventional high temperature titanium alloys has been presented earlier [1-7]. The design philosophy is based mainly in exhausting the limits of solid solubility (for Al, Sn, Zr, Si) to improve their high temperature capability while conforming to Rosenberg's [8] empirically defined aluminium equivalence to be less than 9 wt.%. It is surmised that by honoring the aluminum equivalence condition, the precipitation of the embrittling ordered Ti_3Al (α_2) phase is avoided. However, the coherent α_2 phase has been reported in titanium alloys [7-12] in some thermomechanical conditions, even on obeying the above aluminium equivalence of Rosenberg. It is necessary to point out that Zr is a weak β stabilizer [13] and thus elimination of the Zr factor from the above empirical relation for aluminium equivalence may be an appropriate approach. Small amounts of Silicon are added to these alloys to improve their high temperature properties like creep. The mechanism of improving creep resistance by silicon being in solid solution or in the form of silicides has been a subject of investigations and other properties with various other microstructural and textural manifestations [3-27].

The current advanced conventional near alpha titanium alloys namely IMI 834 and Ti1100 are used for applications up to temperatures of about 1100°F (~600°C). Several research findings [26, 27] show that these alloys have low ductility at room temperature under some thermomechanical processing conditions or up on long exposures during service. This aspect of low ductility at room temperature in these alloys was reviewed by Ramachandra [26] in the year 2020.

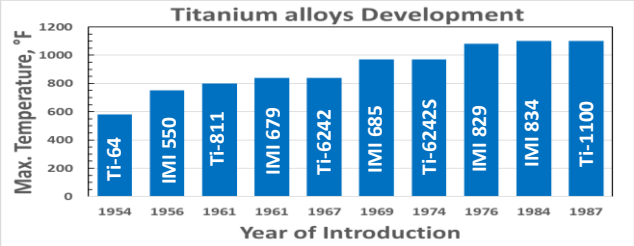

Figure 1. Evolution of conventional Ti alloys with aluminium equivalent values of 6, 4.33, 8, 6.5, 7.5, 6.8, 7.4, 7.2, 8.1, 8.2 for alloys Ti64, IMI550, Ti811, IMI679, Ti6242, IMI685, Ti6242S, IMI829, IMI834, Ti1100 respectively. Interstitials were not included in the calculation of Al. Eq. using Rosenber's empirical relationship Al + 1/3 Sn + 1/6 Zr + 10 (O+C+2N)

Very recently, the authors [27] have examined the available data on these conventional high temperature titanium alloys for selection for applications in compressor parts of an aeroengine using a decision science-based approach and have observed more insights

into these alloys. The room temperature ductility in these high temperature titanium alloys along with texture effects resulting from the thermomechanical processing could cause some serious effects in the Low Cycle Fatigue (LCF) behaviour like two slope behaviour [28-35] in the Coffin-Manson (CM) plots and the Cold Dwell Fatigue or CDF [36-38]. Thus, it is the objective of this paper to bring out the insights of these observations and point out the directions for further improvements of these alloys for use in aeroengines.

2. Low Ductility at Room Temperature

Ramachandra [26] has reviewed the literature in 2020 and has comprehensively presented the findings. It is pointed out that a small amount of silicon is added to these titanium alloys to improve their creep resistance and other properties either silicon in solid solution or in the form of silicides or both [1-15]. It was also found that as pointed out there is precipitation of the embrittling phase α_2 despite the design of these alloys to obey the Rosenberg's aluminium equivalence criterion [8] to avoid the precipitation of the embrittling phase. It was also a subject of several investigations [19-20] to delineate the effects of silicides and α_2 in these alloys. The review [26] clearly brought out that the factors of silicides, silicides aided by α_2, α_2 aided by silicides, α_2/Short Range Order (SRO) and Oxidation as major factors in lowering the room temperature tensile ductility in the conventional high temperature titanium alloys and has been summarised in Figure 2.

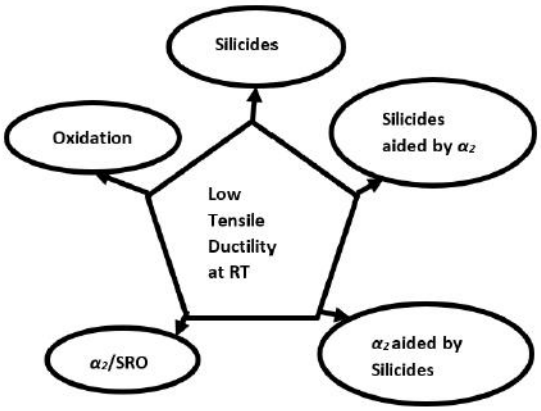

Figure 2. Silicides: IMI685 [26] with planar slip – faceted fracture, No Ti3Al (α_2), IMI829 [26] - planar slip – dislocations interacting with silicides- ductility dropped from 8% to ~2.5%; Silicides aided by α_2: IMI829 [18] - Interaction of slip bands with silicides, α_2 ppts are very fine <6nm. [26]- ductility dropped from ~9.6% to ~3%; α_2 aided by Silicides: [20,26] – ductility dropped from 5.5% to 0.18%; Short Range Order (SRO) [9] α_2 [26] – ductility dropped from ~18% to ~5%; Oxidation: is another factor that causes lowering the ductility (can go to very low values) and coatings will mitigate the reduction in ductility [26]. [RT: Room Temperature]

It was noted [26] that there is a general agreement that reduction in ductility at room temperature in lamellar microstructures is higher than that in bimodal microstructures. The controlling of silicides, α_2 and their combination and protection from oxidation is expected to mitigate the lowering of tensile ductility at room temperature. It was observed [26] that a new alloy KIMS (Ti-6.5Al-3Sn-4Hf-0.2Nb-0.4Mo-0.4Si-0.1B) is very close to the current advanced near alpha Ti alloys and showed [21] improvement in tensile ductility at room temperature. The major difference is that Zr is replaced with Hf. It can be seen that KIMS-I condition has both α_2 and silicides and the ductility is lower at 4% (Figure 3). However, aging at above the critical temperature of 1292°F (700°C) for the dissolution of the ordered α_2 phase left only the silicides in KIMS-II condition and the ductility is quite good at 16.9%. Thus, elimination of α_2 substantially improved the ductility (Figure 3). Further, it is important to point out that silicides showed only 4 at.% Hf (and no Zr) in this KIMS-II condition of the alloy as against 30 at.% Zr in the current alloys IMI834 and Ti-1100 and this shows that the retention of Hf in solid solution contributed to the strength both at room and elevated temperatures.

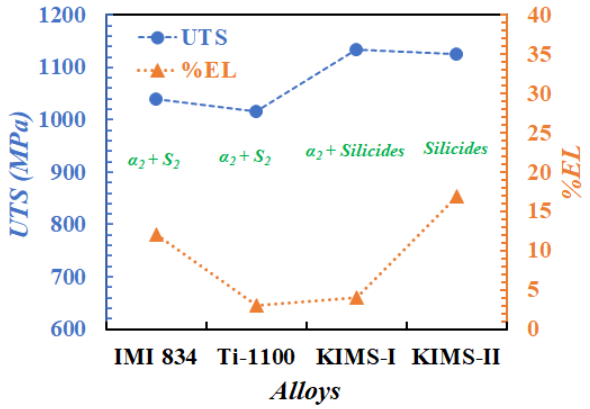

Figure 3. Room temperature tensile properties for Alloys IMI834 (Ti-5.5Al-4Sn-4Zr-0.3Mo-1Nb-0.5Si-0.06C – Al. Eq of 8.1), Ti1100 (Ti-6Al-2.75Sn-4Zr-0.4Mo-0.45Si-Al. Eq. 8.2), and KIMS (Ti6.5Al-3Sn-4Hf-0.2Nb-0.4Mo-0.4Si-0.1B- Al. Eq. 8.1) respectively. The heat treatments for IMI834, Ti1100, KIMS-I, and KIMS-II, respectively, are (α+β) ST-2Hr-OQ-1292°F(700°C)-2Hr-AC; β-ST-0.5Hr-AC-1100°F(593°C)-175Hr-AC; (α+β) ST-1Hr-WQ-1202°F(650°C)-5Hr-AC; (α+β) ST-1Hr-WQ-1292°F (700°C)-5Hr-AC; (AC: Air Cooling, OQ: Oil Quenching; WQ: Water Quenching)

3. Insights from the decision Science driven selection of the Conventional titanium alloys and the tensile ductility

During February 2023, the authors [27] have examined literature data of 105 variants of 19 distinct near-α conventional high temperature titanium alloys from around 1980 till the current time to rank the alloys for use in aeroengine applications based on the room

temperature properties 0.2%YS, UTS and % Elongation using decision science driven approach. The analysis has provided eight top ranked alloys namely (alloy designations are indicated in parentheses), Ti-6.7Al-1.9Sn-3.9Zr-4.6Mo-0.96W-0.23Si (WJZTi-2 and WJZTi-1) [22, 27], Ti-4.8Al-2.2Sn-4.1Zr-2Mo-1.1Ge (TKT-2) [24, 27], Ti-6.6Al-1.75Sn-4.12Zr-1.91Mo-0.32W-0.1Si (TA19-2 & TA19-1) [23, 27], Ti-4.9Al-2.3Sn-4.1Zr-2Mo-0.1Si-0.8Ge, (TKT-6) [24, 27] Ti-4.8Al-2.3Sn-4.2Zr-2Mo (TKT-1) [24, 27], Ti-6.5Al-3Sn-4Hf-0.2Nb-0.4Mo-0.4Si-0.1B (KIMS-II) [21, 27], Ti-5.8Al-4Sn-3.5Zr0.7Mo-0.35Si-0.7Nb-0.06C (IMI834-2) [17, 27], and Ti-6Al-3.5Sn-4.5Zr-2.0Ta-0.7Nb-0.5Mo-0.4Si (PC-IMDF4) [25, 27]. These top ranked alloys suggest either bimodal matrix (primary α + transformed β) together with the aluminium equivalent preferably up to 8, or the above combination with nano crystalline precipitates of α_2, germanides, and/or silicides to provide good 0.2%YS, UTS and % Elongation at room temperature. These findings make metallurgical sense.

4. The effects of low tensile ductility on the important LCF behaviour.

Two important aspects of LCF behaviour that were observed in the literature that is of direct relevance to low tensile ductility are two slope behaviour and the Cold Dwell Fatigue (CDF) and have been presented below.

4.1. Two slope behaviour in the CM plots

First, some background about LCF [28]. Components which are subjected to alternating/cyclic loads can fail at stresses well below the material's ultimate tensile stress. When the applied stress value is high around the yield strength of the material, some amount of plastic deformation occurs in each cycle, the material fails in a very low number of cycles and is termed as LCF and designated in the schematic in Figure 4. A commonly used equation that describes the behavior of LCF is the CM relation which is strain-based approach.

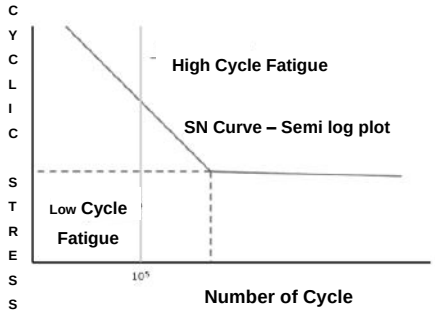

Figure 4. Cyclic Stress vs Number of cycles.

Log – log plot of $(\Delta\varepsilon_p/2)$ vs $2N_f$ is the CM plot where $\Delta\varepsilon_p/2$ is the plastic strain amplitude and $2N_f$ is the number of reversals to failure.

This can be correlated to the fracture strain in a tensile test and refers to the tensile ductility of the material [28]. In general, the higher the ductility, the higher is the LCF resistance [28].

In the (α+β) titanium alloy VT9 in the beta treated conditions with lamellar microstructures, two aspects need to be highlighted about LCF resistance from the CM plots [30] shown in Figure 5.

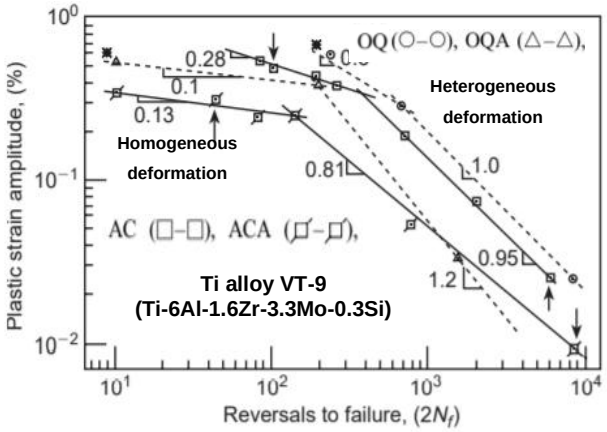

Figure 5. Plastic strain amplitude vs reversals to failure (or CM plots) for β Solution treated (ST) namely OQ & AC and ST & aged (1292°F/700°C) OQ-A & AC-A conditions at Room Temperature for lamellar microstructures in alloy VT-9. OQ: Oil quenching, AC: Air cooling (adapted from [30])

The first observation is that the relative positions of the CM plots for the aged conditions OQA and ACA are placed lower than their respective solution treated conditions OQ and AC and this reduction in fatigue life is attributed to the precipitation of silicides in the aged conditions. The higher position of the CM plots for the OQ conditions compared to the respective AC conditions is due to the crack path tortuosity in the OQ conditions because of criss-cross basketweave structure and thus higher fatigue life compared to the AC conditions.

The second observation is that there is two slope behavior in all the four conditions (Figure 5). The fatigue life in the region of the low strain amplitude is much lower than that expected from extrapolation of the data of high strain amplitude. Extrapolation of high strain amplitude fatigue data to obtain fatigue life at lower strain amplitudes for any design purposes is dangerous.

It is shown that while heterogeneous planar slip was observed in the lower strain amplitude, there is homogeneous slip/deformation at the higher strain amplitude via TEM examination [30]. Similar observations were noted in alloys IMI685 in the lamellar

microstructures [33] and in IMI834 in bimodal microstructures [31, 32, 34, 35].

Cold reduction to as low as 2.5% eliminated the two-slope behaviour in the bimodal microstructure of IMI834 [32, 35]. This is attributed to the strengthening of the surface grains of soft orientation and promoting crack branching and tortuosity and consequent inhibition of planarity of slip and the study says texture is not a factor. Thus, ductility and planarity of slip seem to play a role in the two-slope behaviour. Planar slip indicates role of texture and could be examined. More studies are needed in this direction.

4.2. Cold Dwell Fatigue

Reduction in fatigue life of a part due to a constant high mean stress of the fatigue cycle up to temperatures of 572°F (300°C) is called Cold Dwell Fatigue (CDF) [36-38]. Table 1 shows the historic failures due to CDF in these high temperature titanium alloys used in compressor parts of an aeroengine.

Table1: Historical failures due to CDF [36]

Incident dt.	**Route/place of accident**	**Aircraft/ Engine/Material**
Fan Hub or disks -- CDF		
1973	Défense	Lockheed Tristar/ RB211/IMI685
1985, 91, 93, 95	Dakar, Seol, LA, Bangkok	GE CF6-50/Ti6242
30Sept.2017 [36]	Air France-Paris to Los Angeles	A380/GP7270*/Ti64
Fan Blades -- 2018 & 2019 are CDF, and the 2020 & 2021 are suspected to be CDF		
13Feb.2018	UA1175-SFCo Honolulu (Hawaii)	B777/PW4077/Ti64
10Mar.2019	AF703 -Abidjan Airport (Ivory Coast)	A380/GP7270/Ti64
4Dec. 2020	Japan airlines-Okinawa to Tokyo	B777/PW4074/Ti64
20Feb. 2021	UA328-Denver to Honolulu	B777/PW4077/Ti64

*designed to last a minimum of 15K cycles but failed at 3534 cycles

The decades old CDF issue (since about 1973) has drawn attention with the 2017 first occurrence of civil airplane failure (Table 1) and has been thoroughly investigated [36]. At the time of the certification of GP7200 engines, the scientific community, industry and the certification authorities considered the (α+β) Ti64 insensitive to CDF. However, this understanding is contrary to this failure. It is important to mention that there was one failure of Ti64 component every year since 2018. The concept of design of the parts in the early years seems to be expensive conservative life calculations and supported by intermittent regular field inspections like UT and Eddy current and pulling out the parts that showed critical cracks in the near alpha alloy Ti6242. This is because non-conservative and aggressive approaches are not acceptable as the consequences are dangerous.

The investigation (2017 failure) has determined the cause for the initiation of the CDF crack as due to the millimetric size Micro Textured Regions (MTRs) causing the faceted fracture on the basal pane and consequent drastic reduction in fatigue life [36] and explained with Stroh's model and the hypothesis draws support from transmission electron microscopy evidence for this mechanism [36-38]. The questions that arise are what the historical data on these kinds of failures was, and if that data existed, how was this addressed etc. in the design of the components. The faceted fracture on the basal plane due to planarity of slip and the associated low tensile ductility has been noted in the literature for a few decades and very well referenced in articles [16, 29]. The MTRs are thus connected with the CDF. There is no way to quantify or classify the MTRs and relate it to CDF as of today [36]. Efforts are being made to develop and establish models [37] to find the relationship between the macro-zones (MTRs) and the CDF in alloys Ti64 and Ti6242. The models are to predict the influence of a macro-zone's characteristics on the fatigue life.

Questions like whether the heterogeneous deformation dominated by planar slip under the two-slope behavior is also a manifestation of CDF need to be understood. Ways are being considered to avoid or reduce the size of the millimetric MTRs to homogenize the slip by proper TMP, additive manufacturing and any other that could help, determine, and define the safe size for these MTRs [36-38].

5. Summary

The existing compositions of the near alpha alloys with small variations could be thermomechanically processed to optimize the microstructure to be bimodal with fine nanometer size α_2 precipitation within the primary alpha and finer silicides and thus improve tensile ductility. It was observed that new alloys designed and as ranked and listed in section 3 have good tensile ductility along with strength properties and are promising for development. The two-slope behaviour and the CDF effects require more data and understanding. After a thorough understanding, manufacturing of parts is to be done using properly evaluated manufacturing methodologies with appropriate thermomechanical processing to address the size of the MTRs, tensile ductility and dispersing or randomizing slip to avoid two slope behaviour as well as CDF.

6. Acknowledgements

The authors R. Canumalla and T. V. Jayaraman thank respectively the Weldaloy Specialty Forgings management and the United States Air Force Academy for all their support.

7. References

1. Titanium USA 2018- Executive Summary, *34th Annual Int. Conf. and exhibition*, Oct. 7-10, 2018, Bellagio Resort, Las Vegas organized and sponsored by Int. Ti Association.
2. M. Thomas, S. Murray, D. Furrer, *7th International Symposium on Superalloy 718 and Derivatives*, TMS, 2010.
3. D. Eylon, S. Fujishiro, P.J. Postans, F.H. Froes, *Journal of Metals* 1 (1984) 55-62.
4. C. Ramachandra, V. Singh, P. Rama Rao, *Defence Science Journal* 36 (1986) 207-220.
5. A.K. Gogia, *Defence Science Journal* 55 (2005) 149–173.
6. M. Nageswara Rao, Book *on Advances in Gas Turbine Technology*, intechopen.com. (2011) 293 - 314.
7. J. Foltz, M. Gram, *ASM Handbook, Volume 4E, Heat Treating of Nonferrous Alloys* G.E. Totten and D.S. MacKenzie, (Eds.) (2016)
8. H.W. Rosenberg, *The Science, Technology and Application of Titanium*, R.I. Jaffee and N.E. Promisel (Eds.), Pergamon Press, New York, (1970) 851-859.
9. D. Banerjee, D. Mukherjee, R.L. Saha, K. Bose, *Metallurgical Transactions A* 14 (1983) 413-420.
10. C. Ramachandra, V. Singh V, *Scripta Metallurgica* 20 (1986) 509-512.
11. C. Ramachandra, A.K. Singh, G.M.K. Sarma (1993) *Metallurgical Transactions A* 24 (1993) 1273-1280.
12. C. Ramachandra, A.K. Singh, *Metallurgical Transactions A* 24 (1993) 763-765.
13. F.H. Froes, J.C. Chesnutt, J.C. Rhodes, J.C. William, *ASTM STP-651* (1978) 115-53.
14. M.W. Mahoney, N.E. Paton, *Metallurgical Transactions A* 9 (1978) 1497-1501.
15. A.T.K. Assadi, H.M. Flower, D.R.F. West, *Metals Technology* 6 (1979) 8-15.
16. C. Ramachandra, V. Singh, *Metallurgical Transactions A* 16 (1985) 227–231.
17. M. Peters, Y.T. Lee, K.J. Grundhoff, H. Schurmann, G. Welsch, *Proceedings of the Minerals and Metals Society Fall Meeting*, Detroit, MI, USA, 7–11 October 1991; 533–548.
18. A.P. Woodfield, P. Postans, M. Loretto, R. Smallman, *Acta Metallurgica* 36 (1988) 507–515.
19. A. Madsen, H. Ghonem, *Journal of Materials Engineering & Performance* 4 (1995) 301-307,
20. A. Madsen, H. Ghonem, *Materials Science & Engineering A* 177 (1994) 63–73,
21. P. Narayana, S.W. Kim, J.K. Hong, N. Reddy, J.T. Yeom, *Materials Science & Engineering A* 718 (2018) 287–291.
22. W.J. Zhang, X.Y. Song, S.X. Hui, W. J. Ye, Y. Yu, Y.F. Li, *Rare Metals* 40 (2019) 3261–3268.
23. M. Luo, T. Lin, L. Zhou, W. Li, Y. Liang, M. Han, Y. Liang, *Materials* 14 (2021) 3380.
24. T. Kitashima, K.S. Suresh, Y. Yamba-Mitarai, *Materials Science & Engineering A* 597 (2014) 212–218.
25. C.J. Zhang, C.X. Guo, S.Z. Zhang, H. Feng, C.Y. Chen, H.Z. Zhang, P. Cao, *Materials Science & Engineering A* 771 (2020) 138569.
26. R. Canumalla, SCIREA *Journal of Metallurgical Engineering* V 4, Iss.2 (2020) 16-51.
27. R. Canumalla, T.V. Jayaraman, *MDPI Aerospace*, 10, 211 (2023) 1-22.
28. Deformation and Fracture Mechanics of Engineering Materials, Richard Hertzberg. 1976
29. C. Ramachandra and V. Singh, *Scripta Metallurgica* 21, 5 (1987), 633-636.
30. G. S. Nanjundaswamy, C. Ramachandra, P. K. Sengupta, B. Chatterji, H. V. Sudhakar Nayak, and A. K. Singh, *Journal of Materials Science Letters*,1 7 (1998) 993-997.
31. Nidhi Singh, Gouthama, Vakil Singh, *Materials Science and Engineering A* 325 (2002) 324–332.
32. K.V. S. Srinadh and V. Singh, *Metallurgical & Materials Transactions A*, 38, (2007) 1868-71.
33. A. K. Nag, K.V. U. Praveen and V. Singh, *Bulletin of Materials. Science* 29, 3 (2006) pp. 271-275.
34. N. Singh, Gouthama and V. Singh, *International Journal of Fatigue* 29 (2007) 843-851.
35. M.K. Tripathi, N.C. Santhi Srinivas and V. Singh, *International Journal of Research in Engineering. and Technology* V02, Iss 8, (2013) 345-348.
36. Investigation Report *(Accident to the Airbus A380-861 equipped with Engine Alliance GP7270 engines registered F-HPJE on 30Th Sept 2017)*, BEA2017-0568.en/September 2020, 85 pages
37. V. Venkatesh, R. Noraas, A. Pilchak, S. Tamirisakandala, K. Calvert, A. Salem, T. Broderick, M. Glavicic, I. Dempster, V. Saraf, *MATEC Web of Conferences, 321, 11091, 14th World Conference on Titanium*, 2020.
38. Y. Xu, S. Joseph, P. Karamched, K. Fox, D. Rugg, F.P.E. Dunne, D. Dye, *Nature communications,* (2020) 11:5868 K.S. Chan, M.P. Enright and R.C. McClung, Southwest Research Institute, San Antonio, TX 78238, *Cold Dwell Fatigue Workshop, Dayton*, OH, April 18-19, 2016.

COMPETITOR TITANIUM-CONTAINING HIGH ENTROPY ALLOYS TO HAYNES 230 ALLOY FOR AEROENGINE APPLICATIONS

Tanjore V. Jayaraman[1], Ramachandra Canumalla[2]

1 Department of Mechanical Engineering, United States Air Force Academy, Colorado 80840, USA.
2 Weldaloy Specialty Forgings, Warren, Michigan 48089, USA.

Haynes 230 alloy, which combines excellent oxidation resistance, up to ~1150°C, high-temperature strength, and good forming capabilities, is ubiquitous in aeroengine applications. The relatively lightweight Ti-containing high-entropy alloys (Ti-HEAs), having distinctly high elevated- and ambient-temperature properties, are potential competitors to Haynes 230 alloy, specifically as thermal protection sheets/static sheets in aeroengines. We evaluated the Ti-HEAs data in the literature by combining multiple attribute decision making (MADM), principal component analysis (PCA), and hierarchical clustering (HC) to find the probable competitors to Haynes 230 in aeroengine applications. The ranks assigned by the MADMs including WEDBA (weighted Euclidean distance-based approach), SAW (simple additive weighting), ROVM (range of value method), OCRA (operational competitiveness ratio), MEW (Multiplicative exponent weighing), and ARAS (additive ratio assessment), were concordant. While MADM identified similar top-ranked alloys, PCA consolidated the MADM ranks, and HC clustered the alloys. The analyses identify the Ti-HEAs having properties significantly superior to Haynes 230 alloy and reveal their potential to substitute as thermal protection sheets/static sheets in aeroengines. The analyses also provide possible directions for developing Ti-HEAs.

Keywords: Ti-containing high entropy alloys, Haynes 230, material selection, multiple attribute decision making.

1. Introduction and Background

Haynes 230 alloy—a Ni-Cr-W-Mo alloy for elevated-temperature applications in aeroengines and power generation industries—combines outstanding oxidation resistance, excellent high-temperature strength, premier resistance to oxidizing environments, and long-term stability, and good forming capabilities [1-2]. The application of conventional titanium alloys—pronounced for their good forgeability, good corrosion resistance, suitable mechanical properties (at elevated and ambient temperatures), and notably low density—has gone up in aeroengine parts from about 0% to beyond 30% in the last several decades [3]. The Ti-containing high-entropy alloys (Ti-HEAs) have introduced scope for replacing the relatively heavier Ni-based alloys in aeroengine parts [4].

Ti-HEAs have an excellent combination of basic properties reported extensively in the current literature, including density, yield strength at room and elevated temperatures, a good structure that meet the thermal stability requirements, and great potential for elevated temperature applications [4]. For the aeroengine applications, where density is a crucial parameter for weight reductions, among other properties, it is apt to focus on Ti-HEAs in the current literature and compare them with Haynes 230 [2, 4-5]. Ti-HEAs are limited in the contemporary literature, and it is imperative to devise a methodology to rank the available Ti-HEAs using their basic room-temperature and high-temperature properties, such as density and yield strengths. Once the alloys are ranked, the focus could be shifted to a few top-ranked Ti-HEAs with similar properties compared to Haynes 230 and, subsequently, generate extensive data of various other properties, viz., stress rupture, creep, fracture toughness, thermal stability, etc., based on the application requirements. Such an approach is likely to save time, effort, and cost compared to generating extensive data for numerous alloys. Similar approaches were adopted for (i) selection and ranking of conventional high temperature Ti alloys for compressor parts [6], and (ii) identifying Ti-containing refractory high entropy alloys that are competitor to superalloys 718 and their derivatives [7-8].

Material selection is selecting an optimal material from an inventory; it typically involves adjustment between various attributes, viz., carbon footprints, cost, properties, and so forth [9]. Multiple attribute decision making (MADM) is favourably adopted in construction, logistics, manufacturing, and transportation; it involves choice decisions over the alternatives defined by normally inconsonant properties/attributes [9-12].

We applied MADM coupled with principal component analysis (PCA) and hierarchical clustering (HC) to rank the Ti-HEAs and identify the competitors to Haynes 230 for elevated temperature aeroengine applications. The investigation (i) ranks the Ti-HEAs by MADM, (ii) consolidates the ranks from diverse MADMs by applying mean-based and principal component analysis (PCA)-based techniques, (iii) assesses the relative similarities among the Ti-HEAs and Haynes 230 by hierarchical clustering (HC), and (iv) identifies the top competitor Ti-HEAs to Haynes 230 in aeroengines.

2. Materials and Methodology

The data-driven methods for identifying competitor Ti-HEAs to Haynes 230 consisted of the following routines: (i) literature data, (ii) ranking—

applies six MADM methods, viz., WEDBA (weighted Euclidean approach), SAW (simple additive weighting), etc., and (iii) analyses that consolidates ranks and identifies the competitor Ti-HEAs to Haynes 230. The flow diagram for data-driven identification of competitor Ti-HEAs to Haynes 230 is presented in Fig. 1.

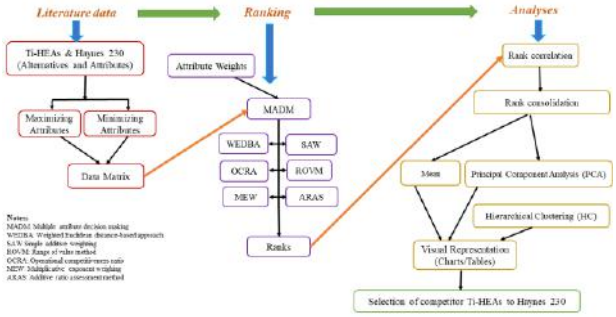

Figure 1. The flow diagram of data-driven identification of competitor Ti-HEAs to Haynes 230

The Ti-HEAs for the investigation are taken from the most recent literature [4, 7-8]. The properties of yield strength at 800ºC (*0.2% YS-800ºC*), yield strength at room temperature (*0.2% YS-RT*), and density (ρ) of Ti-HEAs and Haynes 230 formed the data matrix, which is compiled elsewhere [4, 7-8]. A combination of high yield strengths at elevated and ambient temperatures and low density is desirable. Hence *0.2% YS-800*ºC and *0.2% YS-RT* are beneficial (maximizing) attributes, while ρ is a non-beneficial (minimizing) attribute. Additionally, subjective attribute weights were assigned to the properties—0.10 each for ρ, 0.10 for *0.2% YS-RT*, and 0.80 for *0.2% YS-800°C*). The six MADMs methods applied to the data matrix were Weighted Euclidean distance-based approach (WEDBA) [13], Simple additive weighting (SAW) [14], Range of value method (ROVM) [15], Operational competitiveness ratio (OCRA) [16], Multiplicative exponent weighting (MEW) [17], and Additive ratio assessment method (ARAS) [18]. The MADMs were soft coded in Microsoft Excel.

The similarities among the ranks from the six MADMs were quantified by evaluating Spearman's correlation coefficients (S_ρ) [19]. The ranks were consolidated by averaging (mean) the ranks and by reducing the dimensionality by orthogonal transformation (PCA) [20]. The relative similarities among Haynes 230 and Ti-HEAs were evaluated by hierarchical clustering (HC) [21]. The commercial software Minitab® 20.3 was used for carrying out statistical analyses.

3. Results and Discussion

The alloys' ranks evaluated by the six MADMs are presented in Figure 2. The alloys ranked #1, #2, etc., are the preferred or top-ranked alloys. The ranks evaluated by the MADMs deviated since each applied a specific mathematical model to rank the alloys. For example, the rank evaluated by the various MADMs for TKT-HESA1-FCC-Ti5.8, ONS-BCC-Ti26.7, and NDS-BCC-Ti25.1 (shaded in red) differs significantly. On the contrary, all the MADMs ranked ONS-BCC-Ti20, EF-BCC-V20-Ti20, EF-BCC-Cr20-Ti20, and ONS-BCC-Ti17.8 (shaded in green) #4, #3, #2, and #1, respectively.

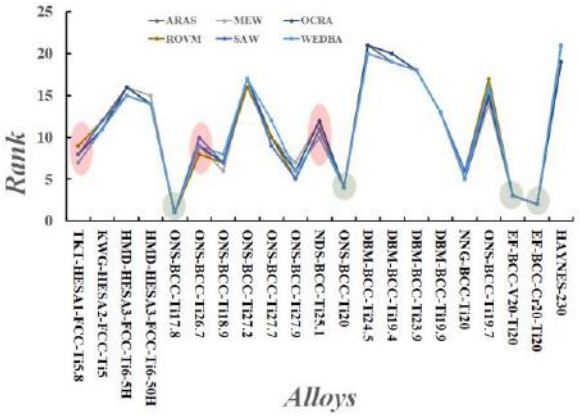

Figure 2. The ranking of the data matrix (Haynes 230 and Ti-HEAs) was evaluated by the MADM methods.

The S_ρ quantifies the rank disparities evaluated by the six MADMs is presented in Table 1. Among the 15 combinations, all of them have $S_\rho > 0.95$! Such a strong correlation of ranks elicits rank consolidation from various MADMs.

Table 1: The S_ρ of ranks of the data-matrix (Haynes 230 and Ti-HEAs) evaluated by the MADM methods.

	WEDBA	*SAW*	*ROVM*	*OCRA*	*MEW*
SAW	0.986				
ROVM	0.990	0.983			
OCRA	0.991	0.997	0.988		
MEW	0.996	0.992	0.991	0.996	
ARAS	0.995	0.982	0.990	0.988	0.994

The rank consolidation of Haynes 230 and Ti-HEAs by taking the mean of the ranks from the six MADMs is presented in Figure 3. The combined rank of the alloys—solid yellow points and dashed green lines—is laid over the individual MADM ranks as in Fig. 2. Among the 21 alloys (20 Ti-HEAs and Haynes 230),

Haynes 230 is ranked 20th, and the alloy that is ranked lower to Haynes 230 is DBM-BCC-Ti24.5 (rank#21). Although the top three alloys are EF-BCC-V20-Ti20 (rank#3), EF-BCC-Cr20-Ti20 (rank#2), and ONS-BCC-Ti17.8 (rank#1), the three Ti-HEAs ONS-BCC-Ti27.2, DBM-BCC-Ti23.9, and DBM-BCC-Ti19.4 ranked ahead of Haynes 230, i.e., ranked #17, #18, and #19 respectively could be considered as appropriate competitors to Haynes 230.

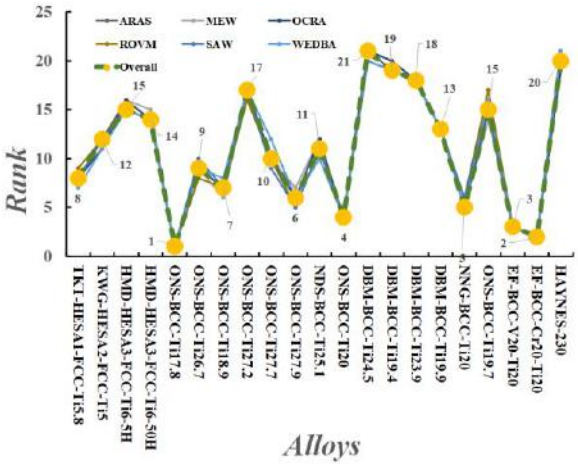

Figure 3. The mean-based rank consolidation (solid green points and lines/curves) of the data-matrix (Haynes 230 and Ti-HEAs) was evaluated by the MADM methods.

Consolidation by PCA is presented in Figure 4 (score plot). The plot presents the primary two components. The eigenvalues that capture the variation of the distribution of each principal component is presented in Table 2. The orthogonal axes capture ~100% of the original data variation.

Table 2: The eigenvalues PCA of the ranks of the data-matrix (Haynes 230 and Ti-HEAs) by the MADM methods.

	Eigenvalue	*Proportion*	*Cumulative*
PC1	5.953	0.992	0.992
PC2	0.026	0.004	0.996
PC3	0.013	0.002	0.998
PC4	0.005	0.001	0.999
PC5	0.003	0.000	1.000
PC6	0.002	0.000	1.000

The principal component *PC1* captures ~99% of the scatter in the original data, while the principal component *PC2* describes a meagre 0.4% of the scatter. Because *PC1* captures ~99% of the variation in the initial sets of ranks, it is the approximate combined ranks of the data-matrix. The three top-ranked alloys consolidated by PCA have uncanny similarity with the top-ranked alloys consolidated by taking the average (mean) of the ranks.

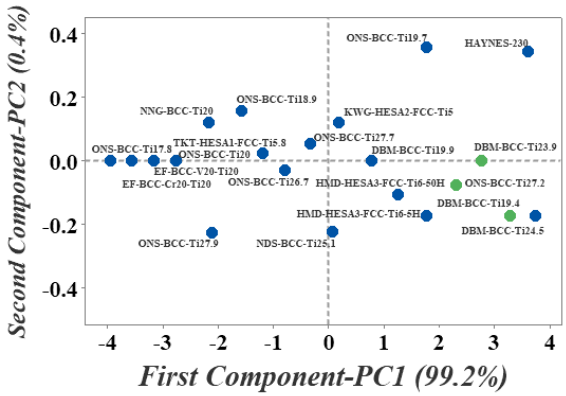

Figure 4. The rank consolidation by PCA of the data-matrix (Haynes 230 and Ti-HEAs) evaluated by the MADM methods.

The alloys ONS-BCC-Ti27.9 ($Al_{11.3}$-$Nb_{22.3}$-$Ta_{13.1}$-$Ti_{27.9}$-$V_{4.5}$-$Zr_{20.9}$), EF-BCC-Cr20-Ti20 (Ti_{20}-Zr_{20}-Hf_{20}-Nb_{20}-Cr_{20}), and ONS-BCC-Ti17.8 ($Al_{20.4}$-$Mo_{10.5}$-$Nb_{22.4}$-$Ta_{10.1}$-$Ti_{17.8}$-$Zr_{18.8}$) are the top three alloys #3, #2, and #1, respectively and are potential competitors to superalloy 718 [7,8]. The lowest ranked Ti-HEA alloy, ranked lower to Haynes 230, is DBM-BCC-Ti24.5 (rank#21) probably because it has a significantly lower *YS-800°C* (i.e., ~33%) in spite of being ~28% lighter and ~2.7 times higher *YS-RT* compared to Haynes 230.

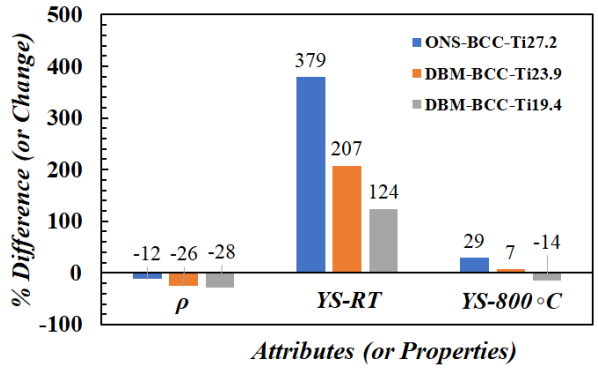

Figure 5. The percentage difference of the properties of Ti-HEAs ONS-BCC-Ti27.2, DBM-BCC-Ti23.9, and DBM-BCC-Ti19.4 compared to Haynes 230.

The Ti-HEAs ONS-BCC-Ti27.2 ($Al_{5.7}$-$Nb_{23.5}$-$Ta_{17.6}$-$Ti_{27.2}$-Zr_{26}), DBM-BCC-Ti23.9 ($Cr_{24.6}$-$Nb_{26.7}$-$Ti_{23.9}$-$Zr_{24.8}$), and DBM-BCC-Ti19.4 ($Nb_{22.6}$-$Ti_{19.4}$-$V_{37.2}$-$Zr_{20.8}$) are ranked #17, #18, and #19, respectively, just ahead of Haynes 230, which is similar to evaluated by mean-based consolidation. Both ONS-BCC-Ti27.2 and DBM-BCC-

Ti23.9 have superior combination of properties (low ρ, high *YS-RT*, and high *YS-800°C*) compared to Haynes 230. On the other hand, DBM-BCC-Ti19.4 though has *YS-800°C* lower than Haynes 230 by ~15%, its ρ and *YS-RT* are significantly superior ~28% lower and ~2.7 times higher, respectively, compared to Haynes 230 (Fig. 5).

If we include the current material cost (cost per unit weight) in the analyses, the HEAs ranked #1, #2, #3, #17, #18, #19 are ~$103, ~$372, ~$413, ~$134, ~$41, and ~$138, respectively [22]. Based on the material cost, the HEAs ranked #2 and #3 are prohibitively expensive and so they may not be competing well. Although the HEA ranked #1 is very competitive, the HEA ranked #18 stands out on the top both cost wise and meeting the *YS-RT* and *YS-800°C*. The HEAs ranked #1, #17, and #19 are more than double the cost compared to HEA ranked #18. Thus, the HEA ranked #18 (DBM-BCC-Ti23.9) is very good that meets the technical requirements and cost-effective.

The dendrogram from hierarchical clustering (HC) of the ranks of the data-matrix (Haynes 230 and Ti-HEAs) evaluated by the MADMs is presented in Fig. 6. The similarities among the top three Ti-HEAs (#1, #2, and #3) are ~64%. Apparently, the Ti-HEAs ranked #17, #18, and #19 ahead of Haynes 230 are ~62% similar to one another. On the other hand, both ONS-BCC-Ti27.2 and DBM-BCC-Ti23.9 are ~94% similar to each other. It appears that the Ti-HEAs ONS-BCC-Ti27.2 and DBM-BCC-Ti23.9 (ranked #17 and #18, respectively) are potential competitors to Haynes 230. The potential of the data-driven methodology could further be unearthed by aptly assigning weights of the properties based on the intended application in aeroengine parts.

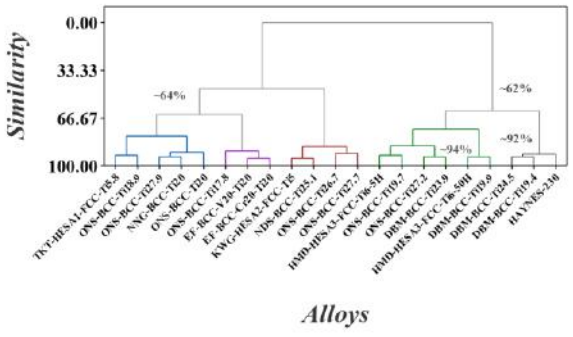

Figure 6. The hierarchical clustering (HC) of the data matrix (Ti-containing high entropy alloys and Haynes 230) evaluated by the multiple attribute decision making (MADM) methods.

The focus and objective of the present work has been to rank the available research alloys based on the limited available properties/attributes using the MADM methodology and then recommend extensive study and generation of desired data on the top-ranked alloys for the intended use effectively and efficiently saving time, effort and cost and has been demonstrated as a useful tool in this paper and iterations of this procedure could be done as more and more research data becomes available on the limited basic attributes on more research Ti-HEAs as discussed. Further work will include novel MADMs on a broader dataset and properties/attributes in the literature.

4. Summary and Conclusions

We applied multiple attribute decision making (MADM) coupled with principal component analysis (PCA) and hierarchical clustering (HC) to Ti-HEA literature data to identify competitor Ti-HEAs to Haynes 230 for elevated temperature applications in aeroengines. The ranks assigned by six MADMs (WEDBA, SAW, ROVM, OCRA, MEW, and ARAS,) were concordant. We consolidated the ranks evaluated by diverse MADMs by applying mean-based and principal component analysis (PCA)-based techniques and identified the following two Ti-HEAs: ONS-BCC-Ti27.2 ($Al_{5.7}$-$Nb_{23.5}$-$Ta_{17.6}$-$Ti_{27.2}$-Zr_{26}) and DBM-BCC-Ti23.9 ($Cr_{24.6}$-$Nb_{26.7}$-$Ti_{23.9}$-$Zr_{24.8}$), ranked #17, and #18, respectively, as potential competitors to Haynes 230 in aeroengines, although DBM-BCC-Ti23.9 is cost-effective (approx. one third the cost of ONS-BCC-Ti27.2).

5. Acknowledgments

The authors T. V. Jayaraman and R. Canumalla thank the Department of Mechanical Engineering, College of Engineering and Computer Science, University of Michigan-Dearborn, and Weldaloy Specialty Forgings, respectively, for all the support.

6. References

1. J.R. Davis, ASM International Handbook Committee. Nickel, Cobalt, and their alloys, ASM International 2000.
2. HAYNES® 230® Alloy Datasheet (2021), Haynes International
3. R. Canumalla, *SCIREA Journal of Metallurgical Engineering* 4(2) (2020), 16-51
4. D.B. Miracle, O.N. Senkov, *Acta Materialia* 122 (2017), 448-511
5. S. Chatterjee, *Ph.D. Thesis* (2010), University of Nevada, Las Vegas
6. R. Canumalla, T.V. Jayaraman, *Aerospace* 10(3) (2023), 211 1-22.
7. R. Canumalla, T.V. Jayaraman, *Materials Research* 26 (2023), e20220213.

8. T.V. Jayaraman, R. Canumalla, *TMS 2023 152nd Annual Meeting & Exhibition Supplemental Proceedings* (2023), 501-516
9. M.F. Ashby, *Materials and the Environmental Eco-informed Materials Choice* (2009), Elsevier
10. G.H. Tzeng, J.J. Huang, *Multiple attribute decision making methods and applications* (2011), CRC Press
11. A. Jahan, K.L. Edwards, M. Bahraminasab, *Multi-criteria decision analysis—for supporting and selection of engineering materials in product design*, (2016), Elsevier.
12. E.K. Zavadskas, Z. Turskis, S. Kildiene, *Technol. Econo. Dev. Economy* 20(1) (2014), 165-179
13. R.V. Rao, D. Singh, *International Journal of Risk Management* 3 (2012), 32-53
14. A. Afshari, M. Mojaahed, R.M. Yusuff, *International Journal o. Innovation, Management. and Technology.* 1(5) (2010), 511-515
15. M. Madic, M. Radovanovic, M. Manic, *Decision Science Letters*, 5 (2016), 245-254
16. S. Erdogan, S. Aydin, M.K. Balki, C. Sayin, *Renewable Energy* 151 (2020), 698-706
17. A.P. Windarto, A. Muhamad, *International Journal of Software Engineering Applications* 11(4) (2017), 69-90
18. S. Stanujic, R. Jovanovic, *Contemporary Issues in Business Management and Education*, 2012 (2012), 545-554
19. W. Navidi, *Statistics for Engineers and Scientists* (2010) McGraw Hill Science and Engineering
20. J. Cadima, I.T. Jolliffle, *Philosophical Transactions of Royal Society A* 374 (2014), 20150202
21. P. Arabie, L.J. Hubert, G De Soete, *Clustering and Classification* (1999) World Scientific
22. https://en.wikipedia.org/wiki/Prices_of_chemical_elements

ON THE MECHANISM AND PREDICTION OF FATIGUE CRACK INITIATION IN A NEAR-ALPHA TITANIUM ALLOY

Conghui Liu[1], Michael Preuss[1, 2], João Quinta da Fonseca[1]

1 Department of Materials, The University of Manchester, Manchester, M13 9PL, UK.
2 Department of Materials Science and Engineering, Monash University, Clayton, Vic-3800, Australia

This paper summaries some of the key findings from the PhD thesis of Conghui Liu [1], published in a pair of papers [2, 3]. First, we provide a review of fatigue crack initiation mechanisms in titanium alloys reported in the literature and illustrate the specific aims of our study, considering the controversy from the perspective of critical microstructural features influencing crack initiation and the crack facet formation process in terms of the degree of contribution of plastic slip versus cleavage. Then the workflow of experimental study is summarized including extensive time-lapse surface characterization in combination with high-resolution digital image correlation (HR-DIC) and post-mortem 3D-EBSD characterization techniques. This has enabled the quantitative assessment of cyclic strain accumulation at microstructural configurations, particularly grain boundaries and localised slip bands that favour fatigue crack initiation. Most importantly it has also provided the necessary crystallographic information of crack facets and grain neighbourhood effect, to better understand the facet formation mechanism beneath the surface. Based on the understanding above, two different mechanistically informed crack initiation criterion in relation to elastic, plastic and critical microstructural parameters are proposed to provide a precise prediction of fatigue crack initiation sites.

Keywords: Titanium alloy, Fatigue, Slip, Fatigue crack initiation, 3D EBSD, HR-DIC.

1. Introduction

Titanium alloys are widely used in aerospace applications including gas turbine engines owing to their superior mechanical properties and a relative low density. The alloy to be investigated here is TIMETAL®834, a near-α titanium alloy, which has been developed for high temperature (up to 600ºC) applications such as high-pressure compressor disks and blades of gas turbine engines [4]. During service, the high cycle fatigue (HCF) has proven to be the largest single cause of component failure. To obtain good mechanical properties and high fatigue strength, TIMETAL®834 is typically produced with a bimodal microstructure consisting of equiaxed primary alpha (α_p) grains located at the triple-point of the β grain boundaries, and secondary alpha (α_s) lamellae embedded in the β matrix. The volume fraction and grain size of α_p, thickness of α_s lamellae and size of α_s colonies are the most critical microstructural features for the control of mechanical properties. It is well established that increasing the volume fraction of α_p can deteriorate fatigue strength in the two-phase titanium alloys and 10-25 vol.% α_p is generally suggested for an optimum combination of fatigue and creep resistance [5]. Although certain microstructural parameters can be tailored by thermomechanical processing to extend fatigue life, significant variability in lifetime has been observed among a wide range of studies, some of which even pertain to the same material and microstructure type. This implies the complex impact of microstructural features on crack initiation, highlighting the need for a comprehensive understanding of the micro-mechanisms of fatigue crack initiation.

In the case of titanium alloys, with the absence of any carbides that act as pre-existing cracks, the evaluation of fatigue cracking is thought to be caused by highly localized slip activities [6]. It is, therefore, not surprising that several experimental and numerical studies have investigated the nature and distribution of active slip systems [7, 8]. Considering the activation of different slip modes in terms of the magnitude of the critical resolved shear stress, basal <a> and prismatic <a> slip are the major slip modes over pyramidal <c+a> slip for α-titanium [9]. However, if the difference in slip strength is subtler, for example basal and prismatic slip, in the low stress regime, grains well oriented for basal slip are expected to experience higher stresses owing to the local elastic anisotropy of α-titanium, which is consistent with the experimental observation of earlier onset and predominant basal slip activity [7]. This is closely associated with the frequent presence of localised basal slip involved in the fatigue crack initiation over a wide range of loading conditions including continuous cycling loading and dwell fatigue, although crack initiation on prismatic slip bands was occasionally reported in specific microstructures [6, 10]. While the formation of localised slip is well known to form stress concentrations to promote the formation of short cracks, prediction of fatigue crack initiation sites is still a significant challenge. The fundamental question is why do cracks form in certain grains but not in others in a polycrystalline aggregate when certain microstructural features and crystal orientations seem very similar. This requires quantitative assessment of strain field heterogeneities at the scale of slip bands to understand the contribution of local strain accumulation in relation to the critical

microstructural features to the overall plastic deformation.

A common observation of fatigue crack initiation sites in both near-α and α + β titanium alloys have revealed the presence of faceted features, which are α grains fractured in a transcrystalline and highly planar manner [11]. The transgranular crack facet formation is intrinsically attributed to the highly elastic and plastic anisotropy of hexagonal crystal structure of α-titanium. However, the exact conditions that are necessary for the occurrence of facet formation, and the mechanisms that control the facet formation process across several studies on titanium alloys are still controversial in terms of the extent of contribution of slip versus cleavage [11, 12]. Additionally, facets at crack initiation sites are characterised as coincident with certain crystallographic planes and limited research found that the potential plasticity during facet formation process can influence the facet characteristics, i.e., the crystallographic orientation and spatial distribution [13, 14]. However, in these previous studies, the existence of potential slip deformation was only determined by back tracing from the fracture surface, while lacking direct experimental observation of the facet formation process, especially by 3D characterisation. Recently, intergranular crack facet at the low angle (0001) twist grain boundary, a unique grain boundary configuration, has received particular attention under both fatigue and dwell-fatigue loading in α+β titanium alloys, but was only from a very limited amount of research [15, 16]. The insufficient understanding of the nature of intergranular cracking at this specific grain boundary configuration raises the demand for a systematic study from a micromechanical point of view.

A consequence of the current understanding of plasticity and crack nucleation in titanium alloys is that predicting the preferential crack site is still not possible. To this end, extensive surface characterisation including scanning electron microscopy (SEM) combined with electron backscatter diffraction (EBSD) have been used for the statistical analysis of early slip activities and crack initiation during interrupted four-point bending fatigue tests. High-resolution digital image correlation (HR-DIC) in combination with relative displacement ratio (RDR) analysis have been conducted to quantitatively assess the active slip system and localised strain distribution at the scale of slip bands. 3D-EBSD have been carried out to allow precise spatial visualization of the crack plane and expose the crystallography of the underlying fractured grain and its neighbours in 3D. The specific aims of this experimental work are listed below:

- Developing the correlation among microstructural variables, i.e., the critical slip characteristics, specific grain boundary configurations, and crystallographic alignment with neighbouring grains, and crack initiation sites on a quantitative and micromechanical basis.

- Proposing predictive models for fatigue crack initiation combining elastic, plastic and geometrical parameters as a means to identify susceptive locations.

- Assessing the impact of α_p volume fraction on the mechanism and prediction of fatigue crack initiation.

2. Experimental procedure

In this study, the relationship between plastic slip activity and fatigue crack initiation was investigated in a near-α titanium alloy using cyclic four-point bending at up to 90% of the proof stress. The workflow of entire experimental work carried out was summarized in Figure 1. Two parallel experimental routes were pursued consisting of crack monitoring and HR-DIC strain mapping, which require different sample surface treatments and interrupted fatigue cyclic numbers. For both routes, samples were prepared to a quality that EBSD data can be obtained, and micro-hardness indents were applied to the sample surface to allow the characterization of consistent regions of interest at each interrupted cyclic number. For route 1, the evolution from early slip activity to crack initiation was checked after every 1,000 cycles by optical microscopy. Once crack initiation was detected, BSE imaging in combination with EBSD orientation mapping of an area of 600 × 600 μm^2 was conducted encompassing each detected crack. The activated slip system was identified by using the EBSD-based slip trace analysis and crack types were differentiated using EBSD orientation maps. Following the 2D investigations of crack morphology on sample surface, detailed 3D analysis was conducted on different crack types. Confocal laser microscopy was applied to measure the slip induced surface roughness. 3D EBSD was used to expose the spatial orientation of crack plane and the crystallography of underlying fractured grain and its neighbours. For route 2, gold speckle patterns were applied to the sample surface after the marking by micro-hardness indents. SEM images for HR-DIC were acquired before deformation and after 10, 10^2, 10^3 and 10^4 loading cycles, respectively. The acquired images were imported to the DIC software (LaVision Davis 8.4) to generate the

displacement data and then further processed by a Python script (DefDap) in combination with the EBSD data for the HR-DIC strain mapping. The active slip system was finally identified by using relative displacement ratio (RDR) analysis.

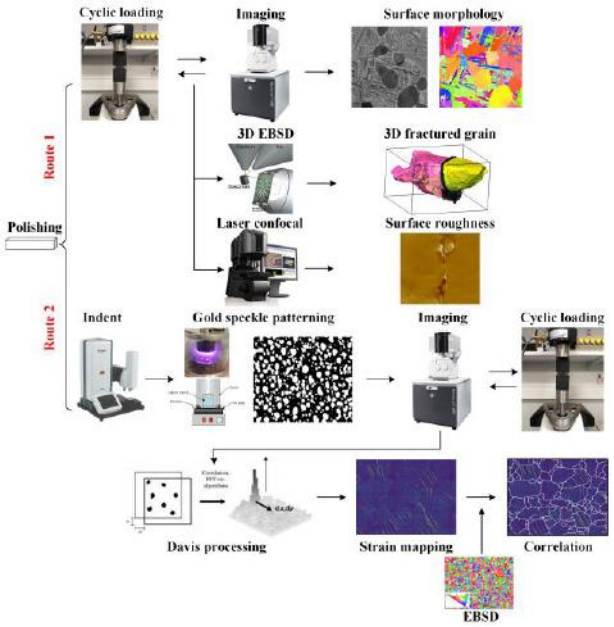

Figure 1. Workflow of entire experimental work carried out in this study.

3. Key results

3.1. Crack facet formation mechanism

Two types of cracking parallel to basal slip traces were observed in our study by surface characterizations, i.e., transgranular cracks across α_p grains (Figure 2 (a)) and intergranular cracks at the grain boundary between α_p grains having their c-axes aligned nearly parallel to each other but with mis-aligned prismatic planes (Figure 2 (b)). Accordingly, planar facets were formed on the basal plane when a crack formed along a surface slip band in both transgranular crack and intergranular crack. Detailed 3D analysis clarified two different crack facet initiation mechanisms depending on the presence of the local plasticity flow at the crack tip, although both crack types initiated from basal <a> slip bands on the sample surface, Figure 3. Transgranular cracks are preferential to initiate along slip bands with a more out-of-plane Burgers vector resulting in a greater slip step, which in turn induces the formation of micro-notch on the surface while a sufficiently high normal stress on the basal plane is necessary to enhance the driving force for the mode I crack opening (statistical analysis based on fractured grains distributed towards [0001] pole within the inverse pole figure, Figure 4). Accordingly, the transgranular crack facet develops in multi-steps at 6° away from the basal plane due to additional prismatic slip activation, resulting in a near-basal facet, Figure 3 (c). In comparison, intergranular cracks are related to basal <a> slip initiating from (0001) twisted grain boundaries even though the boundary is partially parallel to the slip trace. The special twist grain boundary can initially constrain both grains and therefore act as stress raiser leading eventually to the intense and localized slip activity (as confirmed by HR-DIC analysis, Figure 2 (c)) when the stress reaches a critical level, which promotes the intergranular cracking. The intergranular crack facet forms by an easy cleavage in one step and because the absence of additional slip activation at the crack tip keeps the crack facet flat and therefore parallel to the basal plane leading to a basal facet.

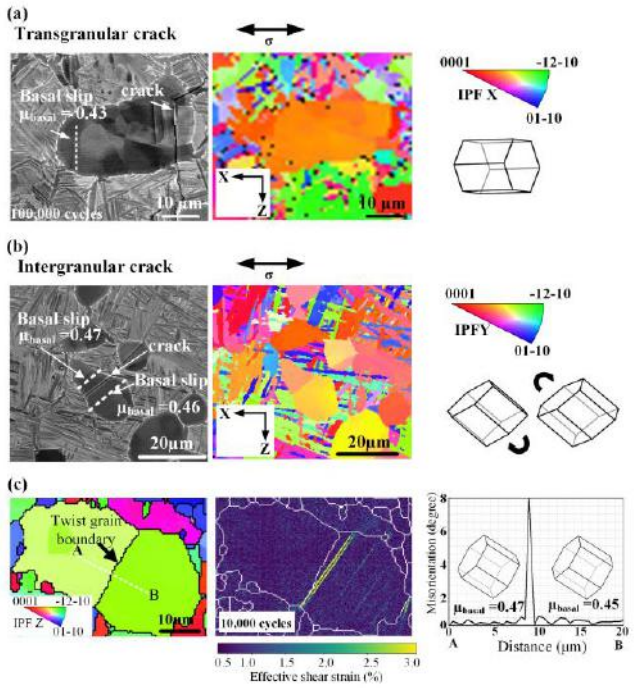

Figure 2. Surface characterization of the (a) transgranular and (b) intergranular cracks; (c) strain localisation at the (0001) twist grain boundary

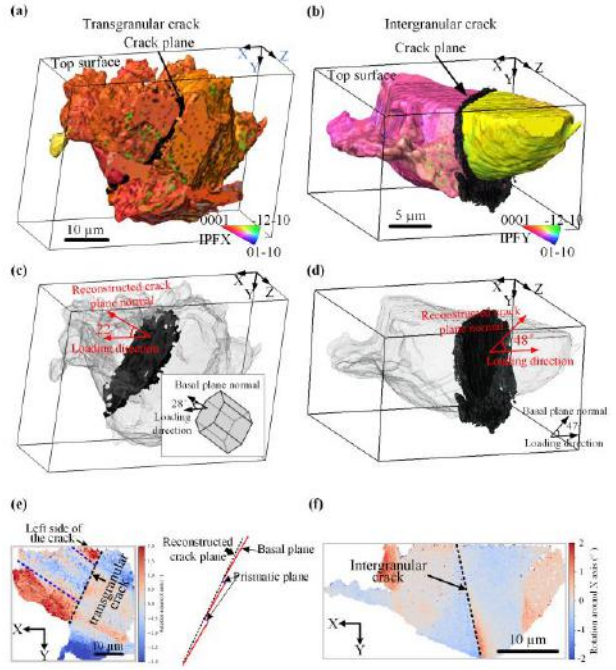

Figure 3. Reconstructed fractured grain and crack facet plane for transgranular crack (a) and (c), and intergranular crack (b) and (d); (e) and (f) illustrating the local plasticity at crack tip during facet formation in the trangranular and intergranular cracks, respectively.

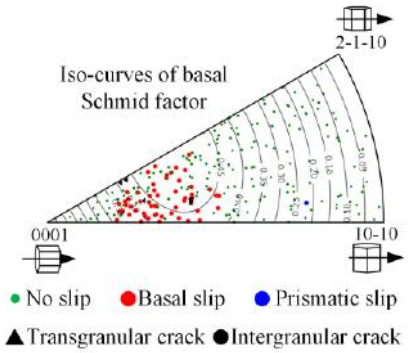

Figure 4. Crystallographic orientation of α_p grains with basal slip (red), prismatic slip (blue), transgranular crack (black triangle), intergranular crack (black circle) and without slip traces (green) after 60,000 cycles, plotted with iso-curves of basal Schmid factor. Crystal orientations are relative to the tensile axis.

3.2. *Fatigue crack initiation criteria*

Statistical investigation demonstrated transgranular cracking always occurred in grains with a moderately high Schmid factor for basal slip, high resolved tensile stress along the c-axis and the Burgers vector being orientated strongly out-of-surface plane, while intergranular crack initiated at the (0001) twist grain boundary, a unique grain boundary configuration. These observations were used to develop models that can predict transgranular and intergranular crack initiation sites using a F parameter for considering the critical slip characteristics and G parameter identifying the (0001) twist grain boundary, respectively, Figure 5, as follows:

$$F = \mu_{basal} \cdot cos\alpha \cdot sin\Omega \quad (1)$$

$$G = cos\beta \cdot cos\beta_{adj} \cdot cos\gamma \quad (2)$$

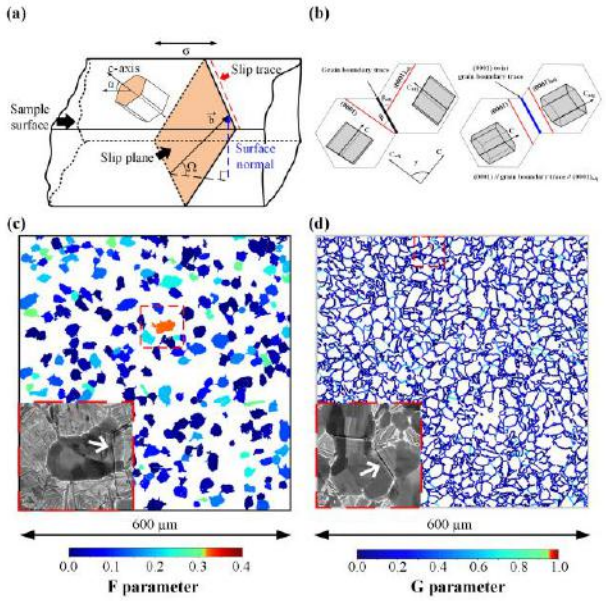

Figure 5. Schematic depiction of (a) F parameter and (b) G parameter; (c) F parameter and (d) G parameter maps of the region with transgranular and intergranular cracks, respectively.

In F parameter, the first term (μ_{basal}) is the maximum Schmid factor for an operating basal <a> slip of α_p grains, which identifies slip bands leading to the largest resolved shear stress; the second term ($cos\alpha$) refers to the strength of a mode I opening component at the slip planes, where α is the angle between tensile axis and basal plane normal; the third term ($sin\Omega$) describes the extent of out-of-plane shear direction of the basal plane where Ω is the angle between Burgers vector and sample surface. A large $sin\Omega$ indicates great slip-induced extrusion at the surface promoting the surface roughening-induced fatigue crack initiation mechanism.

In G parameter, β and β_{adj} refer to the deviation angles between the basal plane trace of the neighbouring α_p grains and grain boundary trace; γ identifies the declination angle between the c-axes of the α_p grain pair. The proposed G parameter quantifies the extent of alignment between the basal slip plane of neighbouring α_p grains and the grain boundary, with the value close to 1 indicating the presence of (0001) twist grain boundary. It should be addressed that intense slip very close to the twist grain boundary precedes crack initiation at the intense slip trace. Thus, a high basal slip Schmid factor filter (>0.35 [3]) should be applied as the prerequisite before identifying the (0001) twist grain boundary configuration to provide a robust criterion for the intergranular cracking.

These two parameters were then applied to a bimodal microstructure with random texture. Results show that a threshold value of F parameter at 0.3 can effectively differentiate the fractured grains from intact grains while a threshold value of 0.95 is assigned to the G considering in most cases the twist grain boundaries are only partially parallel to the basal slip trace. A high G parameter and the preference of neighbouring α_p grain pair for basal <a> slip (high basal <a> Schmid factor), are effective to predict vulnerable sites for intergranular cracking sites, Figure 5.

3.3. Validation of crack initiation criteria

Two intrinsically different fatigue crack initiation modes concurrently observed in a near-α titanium alloy, it is then interesting to discuss whether the proposed crack initiation criteria are effective in the microstructure with different levels of microtexture and α_p volume fractions ranging from 25% to 100%. The statistically analysis of 24 samples with studied region of around 30 mm^2 suggests that G parameter combined with high basal <a> Schmid factor is effective to predict the intergranular cracking sites regardless of the α_p volume fraction and the presence of macrozones, Figure 6.

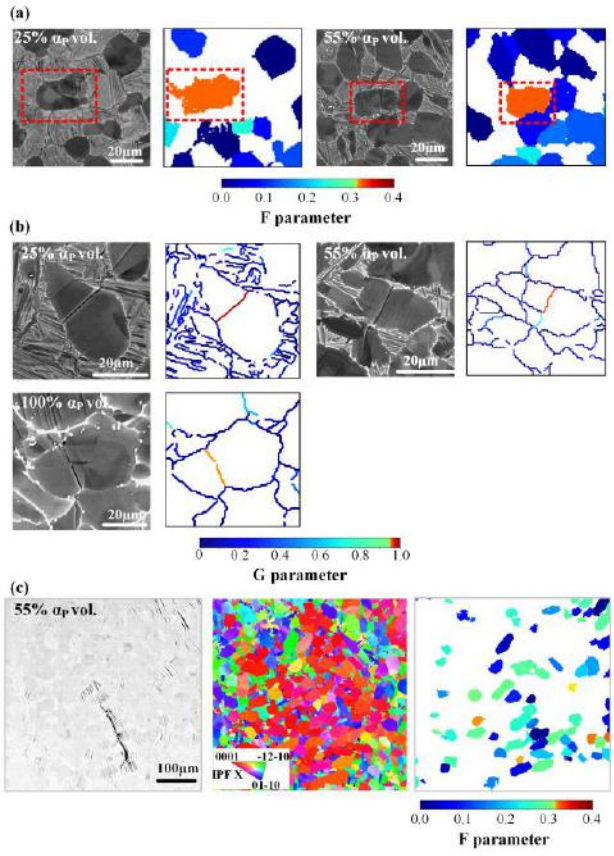

Figure 6. (a) F parameter and (b) G parameter maps of representative intergranular cracks in bimodal microstructures with α_p volume fraction ranging from 25% to 100%; (c) F parameter map showing the transgranular crack initiated in the microtextured region.

In contrast, the increasing α_p volume fraction and concomitant presence of macrozone reduce the reliability of the F parameter for the prediction of transgranular crack formation, Figure 5. This is because both microstructural features have the potential of increasing the apparent slip length arising from well-aligned grains in α_p clusters for easy slip transmission. This reduces the constraint imposed by neighbouring grains and therefore decreases the demand of out-of-plane shear to initiate a crack and potentially higher local stress. In addition, the competitive relation of initiation mechanisms restricts the applicability of F parameter in the microstructure with a higher α_p volume fraction. This is highly consistent with the phenomenon that intergranular crack initiation preceded transgranular crack initiation in all the microstructures and a distinct shift from transgranular to intergranular crack initiation with increasing α_p fraction even though some grains having high F parameter.

4. Conclusions

Technically, our study has demonstrated the capability of HR-DIC technique assisted by SEM in quantifying the heterogeneous strain fields resolved at the scale of localized plasticity, i.e. slip bands, in the nominally elastic stress regime. The direct correlation between HR-DIC and EBSD makes it possible to clarify the role of microstructural configurations that favour crack initiation, i.e., grain boundary, in strain accumulation, and better relate the local mechanical behaviour to the global loading conditions. Furthermore, advanced 3D EBSD characterization of the crack initiation sites provides rich 3D information of crack facets, e.g., crystallographic orientation and spatial morphology, allowing a comprehensive understanding of crack facet formation mechanisms.

From the material point of view, the relationship between critical microstructural features, e.g. slip characteristics and grain boundary configurations, and the crack formation process have been well established in the context of different α constituents in the bimodal microstructure. Consequently, the predictive models for identifying the crack initiation sites were proposed on the basis of physical and statistical analysis. This can provide additional insights into the fatigue variability behaviour that pertains to the same material and microstructure type, which in turn reduces the uncertainty in material life-cycle prediction and management.

5. Acknowledgements

C. Liu would like to acknowledge funding by President's Doctoral Scholar award from the University of Manchester. The author would also like to thank the Mechanics of Microstructures group at the University of Manchester to providing the data analyse code. J. Quinta da Fonseca acknowledges EPSRC funding for the LightForm programme grant (EP/R001715/1). M. Preuss also acknowledges EPSRC funding for the HEXMAT programme grant (EP/K034332/1). This work was supported by the Henry Royce Institute for Advanced Materials, funded through EPSRC grants EP/R00661X/1, EP/S019367/1, EP/P025021/1 and EP/P025498/1.

6. References

1. C. Liu, Understanding the slip deformation and crack initiation mechanism in a near-alpha titanium alloy during fatigue loading, University of Manchester, 2022.
2. C. Liu, R. Thomas, T. Sun, J. Donoghue, X. Zhang, T.L. Burnett, J.Q. da Fonseca, M. Preuss, Multi-dimensional study of the effect of early slip activity on fatigue crack initiation in a near-α titanium alloy, Acta Materialia 233 (2022).
3. C. Liu, X. Xu, T. Sun, R. Thomas, J.Q. da Fonseca, M. Preuss, Microstructural effects on fatigue crack initiation mechanisms in a near-alpha titanium alloy, Acta Materialia 253 (2023).
4. G. Lütjering, J.C. Williams, Titanium, Springer Science & Business Media2007.
5. G. Lütjering, Influence of processing on microstructure and mechanical properties of (α+ β) titanium alloys, Materials Science and Engineering: A 243(1-2) (1998) 32-45.
6. F. Bridier, P. Villechaise, J. Mendez, Slip and fatigue crack formation processes in an α/β titanium alloy in relation to crystallographic texture on different scales, Acta Materialia 56(15) (2008) 3951-3962.
7. S. Hémery, V.T. Dang, L. Signor, P. Villechaise, Influence of Microtexture on Early Plastic Slip Activity in Ti-6Al-4V Polycrystals, Metallurgical and Materials Transactions A (2018).
8. F. Bridier, P. Villechaise, J. Mendez, Analysis of the different slip systems activated by tension in a α/β titanium alloy in relation with local crystallographic orientation, Acta Materialia 53(3) (2005) 555-567.
9. H. Li, D.E. Mason, T.R. Bieler, C.J. Boehlert, M.A. Crimp, Methodology for estimating the critical resolved shear stress ratios of α-phase Ti using EBSD-based trace analysis, Acta Materialia 61(20) (2013) 7555-7567.
10. F. Briffod, A. Bleuset, T. Shiraiwa, M. Enoki, Effect of crystallographic orientation and geometrical compatibility on fatigue crack initiation and propagation in rolled Ti-6Al-4V alloy, Acta Materialia 177 (2019) 56-67.
11. S.K. Jha, C.J. Szczepanski, P.J. Golden, W.J. Porter, R. John, Characterization of fatigue crack-initiation facets in relation to lifetime variability in Ti–6Al–4V, International Journal of Fatigue 42 (2012) 248-257.
12. A.L. Pilchak, J.C. Williams, Observations of Facet Formation in Near-α Titanium and Comments on the Role of Hydrogen, Metallurgical and Materials Transactions A 42(4) (2010) 1000-1027.
13. P.O. Tympel, T.C. Lindley, E.A. Saunders, M. Dixon, D. Dye, Influence of complex LCF and dwell load regimes on fatigue of Ti–6Al–4V, Acta Materialia 103 (2016) 77-88.
14. A.L. Pilchak, A. Bhattacharjee, A.H. Rosenberger, J.C. Williams, Low ΔK faceted crack growth in titanium alloys, International Journal of Fatigue 31(5) (2009) 989-994.
15. S. Hémery, J.C. Stinville, F. Wang, M.A. Charpagne, M.G. Emigh, T.M. Pollock, V. Valle, Strain localization and fatigue crack formation at (0001) twist boundaries in titanium alloys, Acta Materialia 219 (2021).
16. C. Lavogiez, S. Hémery, P. Villechaise, On the mechanism of fatigue and dwell-fatigue crack initiation in Ti-6Al-4V, Scripta Materialia 183 (2020) 117-121.

LARGE-SCALE 3D ELECTRON BACKSCATTER DIFFRACTION STUDY OF α LATH MICROSTRUCTURES IN A TWO-PHASE TITANIUM ALLOY

Conghui Liu[1], Xun Zhang[1], Jack Donoghue[1], Tianzhu Sun[2], Tim L. Burnett[1], Bernadeta Karnasiewicz[1], João Quinta da Fonseca[1]

1 Department of Materials, The University of Manchester, Manchester, M13 9PL, UK.
2 Warwick Manufacturing Group (WMG), University of Warwick, Coventry CV4 7AL, UK

Titanium alloys often exhibit inherently complex multi-phase microstructures, characterised by characteristic 3D morphologies and specific orientation and geometrical relationships between α and β phases, which form during thermomechanical processing. The morphology of secondary α laths produced on cooling from the high temperature β phase is thought to be controlled by the nucleation and growth process within the prior β grain. The α lath often forms on a specific habit plane with its longest axis along the lattice invariant line. This constraint on the spatial orientation of α laths make it difficult to fully characterize their realistic morphology across large length scales in 2D. This study investigated the 3D microstructural characteristics, e.g., interconnectivity and habit plane of α laths, of a slow cooled two-phase α+β Ti-6Al-4V alloy using serial sectioning in Xe+ plasma FIB. The findings reveal that all α laths in the colony microstructure are highly interconnected by bridges or branching points, forming a single large, clustered domain. The habit plane of studied α laths is aligned with the prismatic plane, with the deviation angle ranging from 4°-16°, lying in the range of the two different views from literature. In addition, notable features of growth ledges or steps were characterised on the broad face of α laths. These 3D microstructural features provide significant insights into the complex branching phenomenon observed in different titanium microstructures and the accurate grain morphology allows for reliable plasticity modelling.

Keywords: Titanium alloys, 3D-EBSD, Habit plane, Interconnectivity

1. Introduction

Two phase α+β titanium alloys such as Ti-6Al-4V are widely used in the aerospace industry. Their microstructure can be tailored by different thermomechanical processing routes to achieve an optimal balance of mechanical properties combining specific strength, ductility, and fracture toughness. During thermomechanical processing, the allotropic transformation from the high temperature, bcc phase (β) to the low temperature hcp phase (α), can result in a wide range of spatial distributions, morphologies, volume fractions and length scales of individual phases, as well as the interactions between them. For instance, in the β heat-treated condition and a relatively slow cooling rates, α initially forms at grain boundaries of the prior β, and grows into the β grain as plates. These α plates may grow parallel and with nearly identical crystallographic orientation, separated by thin ribs of retained β, resulting in a colony type of microstructure. Alternatively, at higher cooling rates, many α plates can nucleate independently with different crystallographic orientations, leading to a basketweave type of microstructure.

As is well known, the transformation from β phase to α phase tends to follow the Burgers orientation relationship (BOR) with $\{110\}_\beta//\{0001\}_\alpha$ and $<111>_\beta//<1120>_\alpha$, i.e. the β and α phases align with their (110) and (0001) planes while on these planes, the $[\bar{1}11]_\beta//[\bar{1}\bar{1}20]_\alpha$ and the $[\bar{1}\bar{1}2]_\beta//[\bar{1}100]_\alpha$ directions also align [1]. This preference for maintaining the BOR also has a significant influence on the morphology of the α plates, that is controlled by the nucleation and growth of the α phase, although it is still not clear what the broad face (termed as habit plane) and growth directions of the α plate are [1-3] and how they change with cooling rate, for example. Furuhara et al. [2] determined the habit plane normal with respect to the β plates of both coarse and thin α plates in a Ti-Cr alloy to be $[\bar{1}\bar{1}\ 11\ 13]_\beta$, but since α and β plates are parallel to each other, the habit plane normal of the α plate was further calculated by Tong et.al [3] to be approximately $[11\ \bar{2}0\ 9\ 0]_\alpha$ assuming BOR is maintained, Figure 1 (b). The ledged nature of the α and β plates were also reported in [4, 5], where the ledge terrace faces are $\{10\bar{1}0\}_\alpha//\{112\}_\beta$ and the ledge step planes are $\{11\bar{2}0\}_\alpha//\{111\}_\beta$ as illustrated in Figure 1 (c). The presence of a ledged terrace face leads to the macroscopic broad face (actual habit plane) deviated from the terrace plane by about 14.4°. However, Lütjering and Williams [1] proposed a different habit plane of $\{10\ \bar{1}\ 0\}_\alpha//\{112\}_\beta$ in a much coarser, colony type microstructure in Ti-6Al-4V. Figure 1 summarises the two different views of interface structures and crystallographic relationships between α and β plates from Furuhara et al. [2] , and Lütjering and Williams [1] separately.

The structure of the α/β interface in these studies was investigated by using high resolution transmission electron microscopy (HR-TEM), in which only a small section of the interface has been studied and thus it may not be representative of the average orientation of habit

plane. More recently, electron backscatter diffraction (EBSD) - based habit plane trace analysis was proposed [3] to verify the habit plane orientation for each α variant in a bimodal Ti-6242. The method compares the normal directions of the major axis of the α plate measured from either EBSD or electron micrographs, representing the projection of habit plane normal in the sample sectioned plane, with each potential habit plane normal acquired from the stereographic projection of the candidate habit planes in pole figures, i.e. $\{11\ \overline{20}\ 9\ 0\}_\alpha // \{\overline{11}\ 11\ 13\}_\beta$ for Furuhara et al. and $\{10\overline{1}0\}_\alpha // \{112\}_\beta$ for Lütjering and Williams and the exact habit plane orientation is determined from the best match. However, the habit plane analysis can be ambiguous in some cases due to the increase uncertainty in the determination of the major axis of α plate using the sectioning plane, leading to the measured habit plane fitting both theories for different alpha laths.

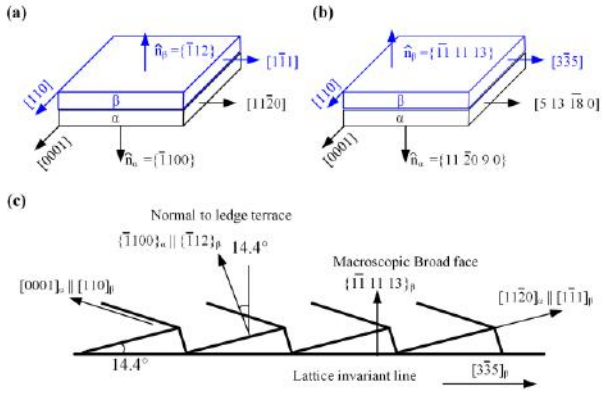

Figure 1. Schematic diagram showing the growth directions and habit planes of the α/b phases proposed by (a) Lütjering and Williams [1] and (b) Furuhara et al. [2] when a Burgers orientation relationship is maintained; (c) the ledge terrace structure of the α/β interface reported by Furuhara et al.

Even with the most sophisticated stereological methods, 2D characterisation techniques alone cannot reveal the complex 3D morphologies and orientation of α plates including their interconnectivity, the extent of branching, and the effective habit plane orientation. Specifically, to understand the terraced nature of habit plane of the α plates in a colony structure from hundreds of microns to millimetres in width consisting of parallel plates with width of ~10 μm as the case of present study, the collection of large volume 3D datasets at high resolution is required. Through serial sectioning with focused ion beam scanning electron microscope (FIB SEM) combined with EBSD it is possible resolve morphological and crystallographic features down to tens of nanometres.

Plasma Xe^+ FIB (PFIB) allows the collection of large volumes up to ~300 μm^3 at milling speed 60 × faster than conventional Ga^+ FIB, while producing a good quality surface indicative of low damage milling for EBSD characterisation [6]. Recently, the integration of femtosecond laser (fs-laser) into PFIB SEM, in a system termed Tri Beam, has improved the trade-off between fast preparation of statistically valid volumes of material volumes larger than 1 mm^3, whilst ensuring sufficient spatial resolution of the following serial sectioning [7]. Coupled with a new EBSD camera using a Symmetry series detector that enables rapid EBSD data collection [8], it becomes possible to bridge the length scales needed to characterise the fine terraced nature of habit plane at the same time as the morphology and interconnectivity of the coarse colony structure.

In this study we perform an 3D microstructural investigation of two-phase Ti-6Al-4V alloy using serial sectioning in Tri-Beam system. We first provide a practical procedure to prepare large volume sample, ~300 μm in length in a reasonably short milling time for the subsequent 3D EBSD, without the need for a lift-out step. We then visualize the reconstructed 3D morphology and crystallography of α/β laths in a colony microstructure, and compares the reconstructed habit plane of the α laths with the two reported models in the literature [1, 2]. This provides critical insights into two important gaps in the state of the art: first, the realistic orientation of habit plane was revealed using 3D characterization methods for the first time to the best of the authors' knowledge, and second the complex 3D morphology of two-phase microstructure will be demonstrated, which can directly inform a more accurate prediction of local deformation history.

2. Material

The material investigated in this study is forged Ti-6Al-4V provided by TIMET, UK Ltd. In order to create a colony type microstructure consisting ideally of only one α variant within a single β grain, a block of material ~ 5 cm^3 was first solution heat treated above β-transus at 1540 °C for 33 hours, followed by slow cooling rate at 2°C to the ambient temperature, to yield large prior β grains >1.5 cm in size, coarsen α laths and supress the formation of multi-variant basketweave microstructure.

3. 3D-EBSD collection

3.1. Sample geometry and volume of interest

A small slice, ~5 × 5 × 1 mm^3, was cut using electrical discharge machining from the centre of heat-treated block. The slice was then ground to first remove the recast layer and then to thinned to ~300 μm, followed by polishing for 20 minutes in a solution of 4:1 colloidal-silica to hydrogen peroxide. This process produced a

clean surface suitable for SEM characterisation and is necessary for locating the region of interest (ROI) on the top surface and produces a small slice of approximately the desired thickness (250 µm) for subsequent 3D EBSD via FIB sectioning. The sliced sample was then mounted on to the flat side of the specially prepared SEM stub, with the edge of the sample near the ROI manually aligned with the flat contour of the stub but at an offset of ~2 mm, Figure 2 (a). This improved procedure simplifies the subsequent preparation of the required small block without the need for conventional lift-out and reduced the depth of milling during slicing.

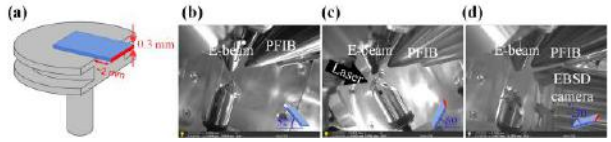

Figure 2 (a) Schematic representation of the geometry of the sample mount on the special designed SEM stub; the Helios Laser-PFIB chamber showing the relative sample positions for (b) PFIB sectioning, (c) laser slicing and (d) EBSD mapping.

A Thermo Scientific Helios 5 Laser P-FIB Tri-Beam system with an ultra-fast Oxford Instruments Symmetry EBSD detector was used to prepare the initial small block and subsequently perform the 3D slicing with automated data acquisition. Figure 2 (b)-(d) illustrate the sample position for laser milling, PFIB slicing and EBSD mapping, respectively. The sample was mounted on a 36° pre-tilted holder in order to minimise the tilt movements between the position of milling and EBSD scan. To start, the position of the sample holder was adjusted in the vertical direction so that the working distances for both PFIB and laser milling positions were kept at 4 mm. The stage tilt was maintained at 16° to have the surface of ROI perpendicular to the milling position with a total tilt of 52°. For laser milling, the sample holder was rotated 180° around the central axis and the stage was tilted at -24°, which brought the ROI to be perpendicular to the laser beam.

Figure 3 outlines the preparation of the small block in the ROI. Firstly, A ROI of 250 µm by 250 µm was selected in BSE mode, with the criteria that all α laths are almost parallel to each other (the colony microstructure transformed from the same prior β grain), and protected with ion beam assisted deposition of platinum. The initial bulk milling operations were performed on each side and underside of the ROI to leave a block of ~ 280 µm × 280 µm × 280 µm using the 515 nm wavelength laser at relatively high (0.735 W) power and a box pattern with 30 pass raster configurations. For deeper cuts, this was repeated with the laser focus moved in a few 200 µm each time to maintain the objective focal position at the base of the trench and ensure the optimal ablation rate. The milling takes only less than 2 minutes for each of the initial large trenches. After that, wider trenches were milled away from the position of previous trenches, Figure 3 (e), to avoid any potential shadowing of the EBSD detector. This block was then further trimmed down to its final dimensions of ~ 250 µm × 250 µm × 250 µm using the PFIB at 30 kV and a high probe current (1.3 nA). Finally, a cross-shaped fiducial marker was milled at the top surface of the block for registering the milling and EBSD position during serial sectioning.

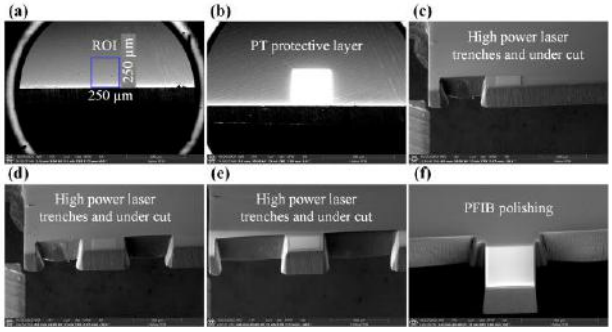

Figure 3 (a) –(f) Procedures for 3D EBSD sample preparation assisted by the laser and PFIB.

3.2. PFIB serial sectioning procedure and data processing

Serial sectioning was carried out using PFIB at an accelerating voltage of 30 kV and a beam current of 0.5 µA, and EBSD scans were performed at an operating voltage of 20 kV, a current of 22 nA and a step size of 0.4 µm. For EBSD mapping, the sample holder was rotated 180° around the central axis from the PFIB milling position, which brought the cross-section of the ROI to an inclination of 70° with respect to the electron beam for EBSD analysis. The serial sectioning and EBSD acquisition were completed using Auto slice & view software. A total of 1415 slices were collected with 200 nm removed for each new slice and the EBSD data was gathered for every other slice using a lateral 0.4 µm step size, leading to a voxel size of 0.4 µm (X) × 0.4 µm (Y) × 0.4 µm (Z) for the 3D EBSD dataset.

3.3. 3D-EBSD data processing

The 3D data visualization was conducted by utilising the FEI Avizo visualization and analysis software package. Stacks of IPF coloured maps and band contrast images acquired from the EBSD scan were aligned using the 'Align Slices' module by a least squares algorithm before being converted to greyscale maps for the following segmentation of α and β phases based on different greyscale values. The semi-automated approach used watershed segmentation to label the two different phases. A surface mesh and constrained smoothing were

subsequently applied to the α laths and β regions to create the visualisations.

4. Results and discussion

The reconstructed and cropped volume used for analysis is a rectangular prism of ~200 × 200 × 250 μm^3, Figure 4. The α colony microstructure consists of α laths with the same orientation, aligned perpendicular to the top surface (XZ plane) and thin β layers separating the α laths. Apparent branching was observed from cross-section surfaces (XY plane and YZ plane). Although parallel α laths look to be separated by continuous layers from XY plane, it is clear that neighbouring α laths are interconnected when viewed in the XZ plane.

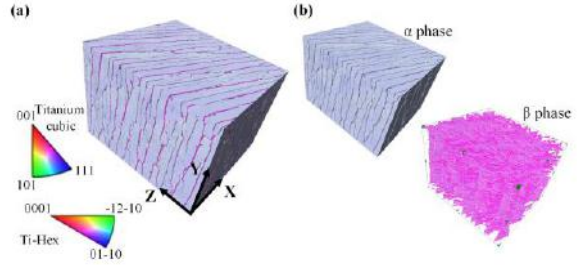

Figure 4 (a) The reconstructed 3D dataset coloured by IPFX colour; (b) segmented dataset in α and β phase.

4.1. Interconnectivity and segmentation of α colony

To examine the potential existence of interconnectivity between α laths and quantify the individual volume of all isolated domains, 'Label Analysis' was first performed in the segmented α phase using Avizo. The volume size distribution of all detected domains is plotted in Figure 5 (c), where the largest one has the volume of ~1.32×10^{16} nm^3, 10^6 orders of the magnitude larger than the second. After visualisation of the largest domain by performing 'Volume Rendering', Figure 5 (a), it was found that the colony microstructure was segmented as single large cluster, evidence that all the α laths were interconnected in 3D. This makes it challenging to analyse the shape, spatial and crystallographic orientation of individual α lath segments, which are generally considered as the fundamental unit of the titanium microstructure. In particular, the habit plane of α laths that reveals the preferential growth and morphological relationship between α and β phases [9] is not well defined. The sub-segmentation of these interconnected α laths is required to allow better visualisation of the interconnectivity behaviour, e.g., number of α laths in each cluster and number of branching points, and to reveal the broad face topography of the laths.

To sub-segment the interconnected α laths, we used the 'Separate Object' modules in Avizo, which are based on a combination of watershed, distance transform and numerical reconstruction algorithms. In this operation, the split of α colony is conducted based on the criterion that any voxel having at least one common vertex with the neighbouring voxel is identified to be connected. Figure 5 (b) shows the sub-segmentations where 738 domains, labelled and differentiated in colour. Although some adjacent domains may have the same colour due to the use of cyclic coloured scale, they are identified as individual domains following segmentation.

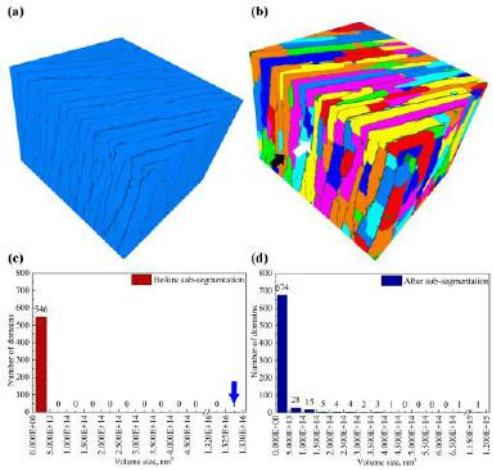

Figure 5 Visualisation of α phase (a) before and (b) after sub-segmentation, with the volume size distribution summarized in (c) and (d) respectively. Note that cyclic colour scale was used in (a) and (b), and only one large domain in (a) was labelled in blue, corresponding to the peak at 1.32e+16 nm^3.

Representative sub-segmentations of single α laths are shown individually in Figure 6. Observation in multiple directions reveals the presence of notches along the broach face of α lath (Figure 6 (d)), which would appear, in a 2D section (YX plane), as discrete grains (Figure 5 (b) as addressed by white arrow), showing how the topographically complex nature of α laths can be seen more readily in 3D. Among all cases, the notable features of growth ledges or steps on the broad face of α laths were characterised, providing the indication of the growth mechanism of α/β phases. The recent phase field simulation by Shi et al. [9] demonstrates that the presence of growth ledges could provide a source for the branching, i.e., the ledged structure provides a pre-existing perturbation to initiate an instability. Their comparative study shows that a lower growth ledge height delays the onset of branching, indicating a critical ledge height exists for branching to occur. Figure 7 shows the representative sub-segmentations of clustered α laths. The significant branching of intragranular α laths during growth leads to the formation of a cluster of parallel α laths of the same variant, resulting in a highly interconnected colony type microstructure as seen in the present study and exacerbating the topographical complexity of α laths. The

branching phenomenon is clearly visible in Figure 7 (d), where and multiple α laths are connected by branching points and bridges as indicated by arrows. The colony type microstructure, same-orientated α laths arranged in parallel and highly interconnected without the block of β phases, can provide extended mean free path for slip transmission, acting as single crystal, which has a great impact on the fatigue behaviour of titanium alloys [10]. In addition, the use of realistic 3D microstructures (e.g., geometry and connectivity) can help improve the prediction of local deformation history during thermomechanical processing by many studies [11-13]. For example, Chatterjee et al. [13] suggests that the connectivity of elements by only a node allows the ligament allows the ligament to exist to higher loads and thus indicates a higher yield stress in Ti-6Al-4V alloys by using crystal plasticity finite element modelling. The ledged surface feature and interconnectivity behaviour in the colony microstructure of titanium alloys has been rarely reported and is crucial to inform plasticity modelling and microstructural evolution.

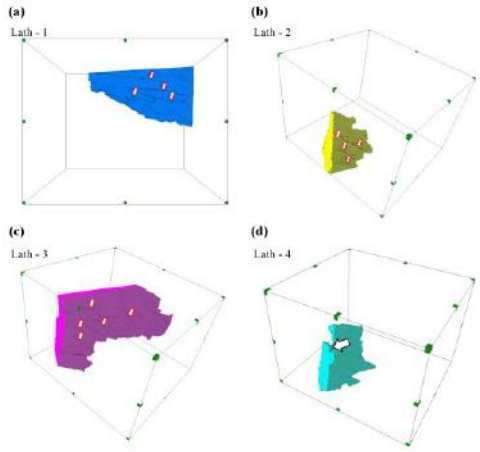

Figure 6. (a)-(d) showing the representative single α lath, where the features including growth ledge and notch were indicated by arrows.

4.2. The verification of Burgers orientation relationship

In a two-phase titanium alloy, the preference for maintaining the BOR has a significant impact on the crystallographic relationships between α and β phases and morphology of the α/β laths [1]. If the BOR is obeyed, once the habit plane normal with respect to the α lath is determined, the habit plane normal for the β lath is unambiguously defined since α and β laths are parallel to each other. Figure 8 shows the method of verifying the orientation relationship between α and β phases from pole figures [3]:

(1) Identify an α variant and its parent β grain in the EBSD IPF map and their corresponding stereographic projections on the $\{0001\}_\alpha$, $\{110\}_\beta$, $<11\bar{2}0>_\alpha$, $<111>_\beta$ pole figures separately. In the present study, it is not necessary to specify the location of the α/β grains on the IPF map since all the α laths share the same orientation and there is only one prior β grain.

(2) Overlay the $\{0001\}_\alpha$ and $\{110\}_\beta$ pole figures. The parallel $\{0001\}_\alpha$ and $\{110\}_\beta$ planes must overlap in the same orientation position on both pole figures, as indicated by red circle.

(3) Overlay the $<11\bar{2}0>_\alpha$ and $<111>_\beta$ pole figures. There should be one $<11\bar{2}0>_\alpha$ direction that exactly overlaps with one $<111>_\beta$ direction, as indicated by green circle.

(4) If each α variant and its parent β grain follows the convention (2)-(3), the two phases are verified to maintain the BOR.

Following the procedures above, the α and β phases in the present study has been verified to obey BOR.

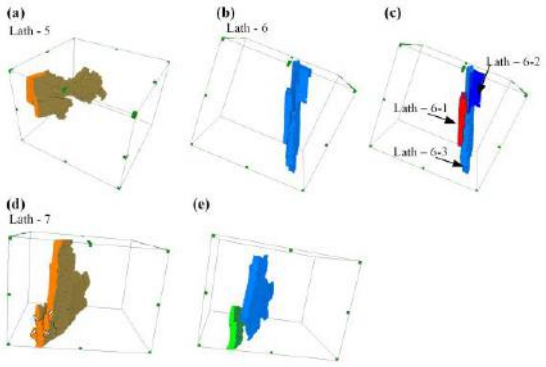

Figure 7. (a), (b) and (d) showing the representative clustered α laths; (c) and (e) visualising the local sub-segmentation of lath-6 and lath-7, respectively.

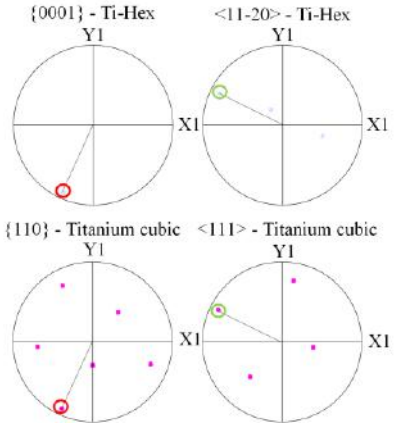

Figure 8. Method of verifying the BOR between α and β phases using stereographic analysis [3].

4.3. Habit plane of α/β laths

In this study, the meshed surface of each lath was first generated, and the coordinates of all vertexes were then used to fit a polynomial surface of degree 1 in both X and Y directions, using the least-square method. The deviation angle between the fitted habit plane and the prismatic plane was determined and listed in Table 1. Results show that all the studied α laths were aligned with the prismatic plane, with the deviation angle ranging from 4°-16°. Bhattacharyya et al. [5] reported the habit plane of α lath is misoriented 15.6° from $\{10\bar{1}0\}_\alpha$ about $[0001]_\alpha$ based on the model proposed by Furuhara et al. [2] due to

the ledged nature of α/β interface, while in the Lütjering and Williams model [1] the habit plane of α lath is identified to be $\{10\,\bar{1}\,0\}_\alpha$. The discrepancy of the alignment of α lath between current study and [1-2, 5] can be attributed to two facts. Technically, the habit plane of α lath in these studies [1-2, 5] was determined by HRTEM and results may deviate from the actual orientation as only a small section of the phase interface is characterised. Additionally, the irregular nature of α/β interface, as visualised in Figure 6 and Figure 7, results in the variation of the orientation of the habit plane in a certain range, not only among different single α laths but also between the branches of α lath (e.g., lath-7-1) and the overall clustered laths (e.g., lath-7). Revealing the irregular nature of α/β interface is important to understand the crystallographic texture evolution in titanium alloy during thermomechanical processing that is critically dependent on the morphology, size and spatial distribution of the α phase in the β matrix [14]. The ledged nature and irregular notches on the broad surface of α laths could lead to the penetration of β phase through the α laths during the α/β phase transformation at elevated temperature in order to minimize the surface energy and resultantly the break-up of α laths, forming highly spaced distribution of α phase (figure 9 (b)), rather than the dense distribution of α phase (figure 9 (c)) developed by the uniform growth of β phase. In the case of figure 9 (b), the soft β phase around hard α phase at high temperature is expected to cause the α phase rotation during hot rolling/forging, which potentially explains the strengthening of the transverse α texture component (0002//TD) during hot-working [1].

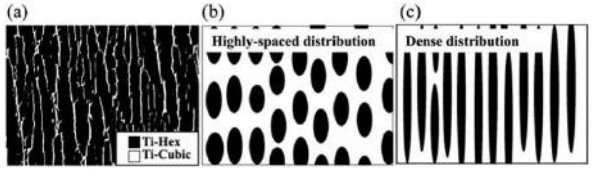

Figure 9. Schematic diagram illustrating the potential spatial distribution of α and β phase: (a) distribution at RT, (b) highly-spaced distribution at elevated T developed by the penetration of β phase through the α laths, and (c) dense distribution at high T developed by uniform growth of β phase.

Table 1 A summary of the deviation angle between the fitted habit plane and the prismatic plane, where lath -1 to lath - 4 refer to the single α lath shown in Figure 6, and lath – 5 to lath 7 refer to the clustered α lath shown in Figure 7.

Grain ID	Lath - 1	Lath - 2	Lath - 3
Deviation angle （°）	7.69	16.26	6.28
Grain ID	Lath - 4	Lath - 5	Lath - 6
Deviation angle （°）	7.69	13.34	7.25
Grain ID	Lath - 6 - 1	Lath - 6 - 2	Lath - 6 - 3
Deviation angle	9.24	7.69	4.43
Grain ID	Lath - 7	Lath - 7 - 1	Lath - 7 - 2
Deviation angle （°）	12.04	4.44	7.69

5. Conclusions

This study demonstrates the complex 3D morphology of colony type microstructure in β heat-treated Ti-6Al-4V using Laser P-FIB Tri-Beam system assisted 3D EBSD characterisation, which allows for the large-volume analysis of habit plane and interconnectivity of α laths. It is revealed that the coarse α laths in the colony microstructure are highly interconnected, forming a single large, clustered domain. There are notable features of growth ledges or steps on the broad face of α laths, that could provide as morphological instability for branching during the growth of α phase. In addition, the actual alignment of coarse α laths is different from the two models available in the literature. These 3D microstructural features provide significant insights into the complex branching phenomenon observed in different titanium microstructures and the accurate grain morphology allows for a more reliable plasticity modelling and texture prediction.

6. Acknowledgements

The author would like to acknowledge EPSRC funding for the LightForm programme (EP/R001715/1). This work was supported by the Henry Royce Institute for Advanced Materials, through EPSRC EP/R00661X/1, EP/S019367/1, EP/P025021/1 and EP/P025498/1.

7. References

1. G. Lütjering, J.C. Williams, Titanium, Springer Science & Business Media2007.
2. T. Furuhara, J. Howe, H. Aaronson, *Acta met* 39(11) (1991) 2873-2886.
3. V. Tong, S. Joseph, A.K. Ackerman, D. Dye, T.B. Britton, J. *Microscopy* 267(3) (2017) 318-329.
4. Y. Zheng, R.E.A. Williams, G.B. Viswanathan, W.A.T. Clark, H.L. Fraser, *Acta Mater* 150 (2018) 25-39.
5. D. Bhattacharyya, G.B. Viswanathan, R. Denkenberger, et al., *Acta Mater* 51(16) (2003) 4679-4691.
6. T.L. Burnett, R. Kelley, B. Winiarski, L. Contreras, M. Daly, A. Gholinia, M.G. Burke, P.J. Withers, *Ultramicroscopy* 161 (2016) 119-129.
7. M.P. Echlin, T.L. Burnett, A.T. Polonsky, T.M. Pollock, P.J. Withers, *Current Opinion in Solid State and Materials Science* 24(2) (2020).
8. A. Garner, J. Donoghue, R. Geurts, Y. Al Aboura, B. et al, *Mater Character* 188 (2022).
9. R. Shi, D. Choudhuri, A. Kashiwar, S. Dasari, Y. Wang, et al, *Phil. Mag* 102(5) (2021) 389-412.
10. S. Joseph, I. Bantounas, T.C. Lindley, D. Dye, *Int. Int. J. Plast* 100 (2018) 90-103.
11. C. Zhang, H. Li, P. Eisenlohr, W. Liu, C.J. Boehlert, M.A. Crimp, T.R. Bieler, *Int. J. Plast* 69 (2015) 21-35.
12. Y. Liu, Y. Wei, *Int. J. Plast* 55 (2014) 80-93.
13. K. Chatterjee, M.P. Echlin, M. Kasemer, P.G. Callahan, T.M. Pollock, P. Dawson, *Acta Mater* 157 (2018) 21-32.
14. S. Roy, R. Madhavan, S. Suwas, *Phil. Mag.* 94(4) (2013) 358-380.

SELECTIVE LASER MELTING PROCESS CHAIN FOR DEVELOPMENT OF A Ti6Al4V(ELI) NOSE WHEEL FORK OF A LIGHT AIRCRAFT

Lehlohonolo Francis Monaheng[1], Willie Bouwer du Preez[2], Claudia Polese[3&4]

1 Department of Mechanical and Mechatronics Engineering, Faculty of Engineering, Built Environment and Information Technology, Central University of Technology Free State, Bloemfontein 9300, South Africa,
2 Centre for Rapid Prototyping and Manufacturing, Faculty of Engineering, Built Environment and Information Technology, Central University of Technology Free State, Bloemfontein 9300, South Africa,
3 School of Mechanical, Industrial and Aeronautical Engineering, University of the Witwatersrand, Johannesburg 2050, South Africa
4 DSI-NRF Centre of Excellence in Strong Materials, University of the Witwatersrand, Johannesburg 2050, South Africa.

Components produced through selective laser melting (SLM), particularly for mission-critical components, are not yet fully qualified and accepted in the aviation industry. As a result, the benefits of this technology, such as increased design freedom, change from multi-part assemblies to monolithic components, and reduced buy-to-fly ratio, are forfeited in aeronautical metal structures. In this study, the utilisation of an SLM process for production of the Ti6Al4V(ELI) nose wheel fork of an aircraft was investigated. Topology optimisation was applied during the redesign to create a Ti6Al4V(ELI) nose wheel fork that would have an acceptable strength-to-weight ratio as compared to an aluminium alloy fork manufactured through a conventional method. Thereafter, a scaled-down version of the nose wheel fork was produced as an experimental prototype together with mechanical test specimens. Subsequently, the scaled-down nose wheel fork was tested for fit-for-purpose. It was concluded that the AHRLAC nose wheel fork which is 20% lighter in weight as compared to the one manufactured from the traditional processes, can be produced in Ti6Al4V(ELI) through SLM, provided that the defects such as the surface roughness can be eliminated or reduced.

Keywords: Topology optimisation design, Additive manufacturing, Ti6Al4V(ELI), Aircraft landing gear.

1. Introduction

The Advanced High-Performance Reconnaissance Light Aircraft (AHRLAC) is a two-person cockpit pusher propeller plane designed by the South African engineering company Aerosud and manufactured by Paramount Group and its partners in AHRLAC holdings [1]. As part of its production strategy, the AHRLAC company wanted to explore the use of additive manufacturing (AM) [1] due to its excellent buy-to-fly (BTF) ratio [2]. While the Ti6Al4V(ELI) alloy is commonly used for production of aircraft components based on its good mechanical and fatigue properties, the potential to manufacture some of the components through AM in this alloy was recognised [3]. An agreement was reached between the Central University of Technology (CUT) and the AHRLAC company to investigate the feasibility of manufacturing the nose wheel fork of the AHRLAC in the high-speed selective laser melting (HS-SLM) machine (Aeroswift). Aeroswift has a build volume of 2000 mm x 600 mm x 600 mm, which would allow the production of this structural component through HS-SLM in Ti6Al4V(ELI) [4]. It was expected that the mechanical properties of this component would be comparable to those of components built through commercially available SLM systems [5].

Through topology optimisation design for additive manufacturing (TO-DfAM), a complex shaped light-weight Ti6Al4V(ELI) nose wheel fork was redesigned that could be produced through SLM [6][7]. However, SLM has not yet been qualified for the production of mission-critical components of aircraft, such as the AHRLAC nose wheel fork [8][9]. Therefore, in this study, the feasibility of producing a nose wheel fork through SLM in Ti6Al4V(ELI) that would meet the design requirements of this component was researched.

2. Materials and methods

In Figure 1, the methodology followed to develop the Ti6Al4V(ELI) nose wheel fork is shown.

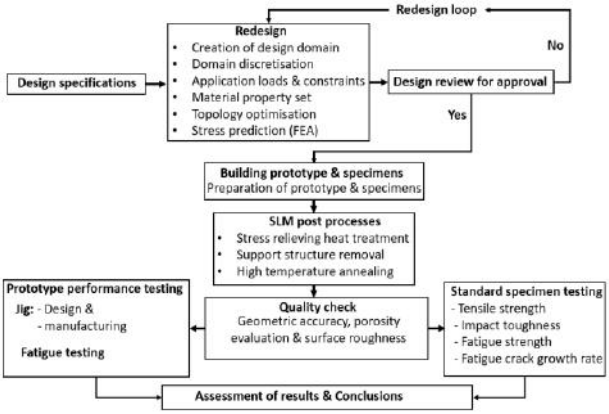

Figure 1. The SLM process chain followed to produce the nose wheel fork of the AHRLAC.

In the following sections, the key processes in this production chain are outlined.

2.1. Redesign of nose wheel fork

As presented in a previous paper [6], the redesign process began with the design specifications such as loads and constraints, and a computer aided design (CAD) model of the current conventional nose wheel fork, that were provided by the AHRLAC company. The volume of the actual nose wheel fork was slightly enlarged for creation of the design domain CAD model. However, the top contour and bushes of the design domain were kept the same as those of the existing nose wheel fork to avoid interference between the new design and other parts of the aircraft. The Ti6Al4V(ELI) material properties and the boundary conditions were

assigned to the optimisation model. A total of 16 load cases were applied to the design domain during the optimisation. In Figure 2 the schematic overview of the TO-DfAM process is given. The Altair SolidThinking Inspire® software was used for the TO-DfAM process.

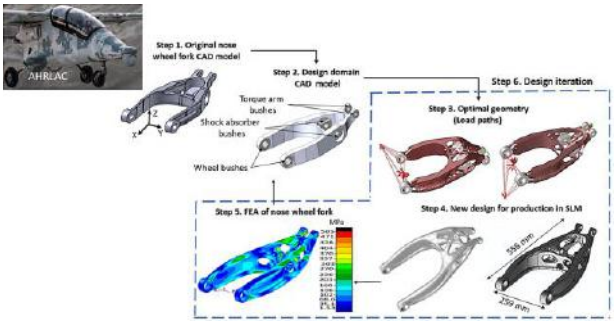

Figure 2. Schematic overview of the TO-DfAM of the SLM Ti6Al4V(ELI) nose wheel fork of the AHRLAC.

The optimised design was then submitted to finite element analysis (FEA) to evaluate the stress field. Using the von Mises safety criteria, the optimised design was reviewed and further refined. Once the safety factor was found to be 1.5 or more the design was accepted. To prepare the design for building an experimental prototype in the AM machine of CUT, the optimal design of the nose wheel fork was scaled down using a constant scale factor of 0.4.

2.2. Building of prototype and test specimens

A Ti6Al4V(ELI) powder that was supplied by TLS Technik GmbH & Co Spezialpulver KG (Bitterfeld-Wolfen, Germany) was used to build the prototype (scaled-down nose wheel fork) and all test specimens. This spherical powder had a particle size distribution of less than 45 μm. In Table 1 the chemical composition of the Ti6Al4V(ELI) powder is shown and compared with ASTM F3001-14 [10].

Table 1: Chemical composition of the supplied Ti6Al4V(ELI) powder and the composition required in the ASTM F3001-14 standard.

Chemical composition (wt %)	**TLS Technik powder**	**ASTM F3001-14** [10]
Titanium (Ti)	90.30	Balance
Aluminium (Al)	5.56	5.5–6.5
Vanadium (V)	4.02	3.5–4.5
Iron (Fe), max	0.23	0.25
Oxygen (O), max	0.12	0.13
Nitrogen (N), max	0.04	0.05

An EOSINT M290 machine (EOS GmbH, Germany), with the parameter set provided by the supplier, was used to build the experimental prototype scaled-down nose wheel fork and three cylindric bars on the same substrate. These bars were machined to create standard tensile test witness specimens to confirm the quality of the build process. In Figure 3, the dimensions and orientation of the prototype nose wheel fork and the cylindrical bars are shown.

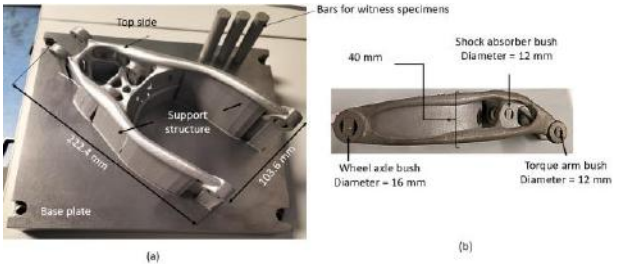

Figure 3. Images (a) of the SLM Ti6Al4V(ELI) scaled-down nose wheel fork with the cylindrical bars for machining standards tensile test specimens, (b) dimensions on the side view of the nose wheel fork.

On a separate build platform, a total of 9 Charpy impact toughness test specimens with as-built surface roughness and V-notch, 21 high cycle fatigue (HCF), also with as-built surface roughness, and 9 polished fatigue crack growth rate (FCGR) test specimens were built from the Ti6Al4V(ELI) powder.

The build orientation of the impact toughness, HCF, and FCGR test specimens are illustrated in Figure 4. For each orientation (XY, YX and Z) of the impact toughness specimens, triplicate specimens were built [11]. For the HCF, 7 specimens were built along the X-, Y-, and Z-directions [12]. Finally, the three specimens for FCGR determination were built in the XZY-, YXZ- and ZXY-orientations.

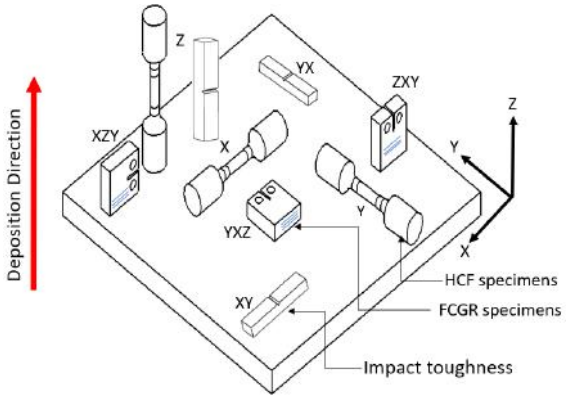

Figure 4. Illustration of the build orientation of the impact toughness, HCF, and FCGR test specimens.

2.3. SLM post processing

The scaled-down nose wheel fork with inherent SLM surface roughness and all specimens were submitted to a two-stage heat treatment. Firstly, while the scaled-down nose wheel fork and the test specimens were still secured on the base plate through the support structure, they were stress relieved by heating to 650 ℃ at a rate of 3.6 ℃/min, soaked at that temperature for 3 h, followed by furnace cooling to room temperature. Thereafter, the scaled-down nose wheel fork and test specimens were cut from the base plate through electric discharge wire cutting and the support structures were manually removed from them. Subsequently, the scaled-down nose wheel fork and all the test specimens were annealed by heating to 950 ℃ at a rate of 5.2 ℃/min, soaked at that temperature for 2 h, followed by furnace cooling to room temperature.

2.4. Characterisation of nose wheel fork

The quality of the SLM Ti6Al4V(ELI) prototype fork was evaluated using non-destructive tests, which included evaluation of the geometric accuracy, porosity determination using representative specimens, and surface roughness measurements.

2.4.1. Geometric accuracy

The dimensional accuracy of the SLM Ti6Al4V(ELI) nose wheel fork was measured through triangulation with a Kreon (Kreon GmbH Deutschland, Germany) 3D scanning coordinate measuring machine (CMM). With the maximum laser scanning speed of 600 points per second, data was captured over a length of 10 cm at an accuracy of 40 μm. To determine the deviation resulting from the post-process heat treatment, two scans were performed. Scan A was done after SLM, followed by stress-relieving heat treatment and support structure removal, whereas Scan B was performed after subsequent high temperature annealing (HTA). During the scanning process, the scaled-down nose wheel fork was virtually sectioned, and the scan data was auto-aligned on the CAD model to compute the geometric deviation using the Geomagic® software [13]. In Figure 5, the virtual sectioning of the CAD model of the nose wheel fork is shown.

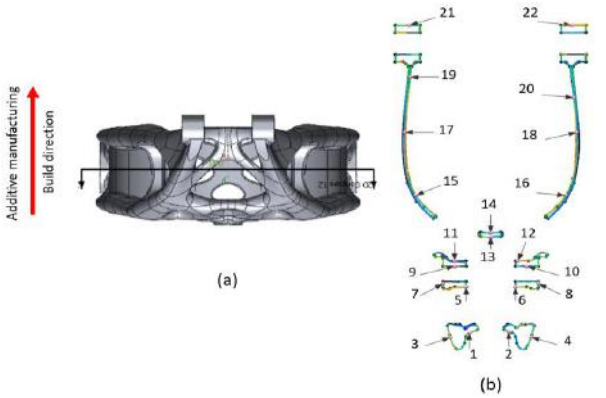

Figure 5. (a) A virtual section of the scaled-down nose wheel fork for geometric deviation evaluation, (b) illustration of 22 points during Scan A and Scan B.

A total of 22 points were selected for geometric deviation analyses. At each location point (1 to 22) the difference in millimetres between the CAD data and measured data was recorded at a tolerance of ± 0.1 mm. Finally, to determine how significant the difference between Scan A and Scan B was, a statistical significance F-test was performed for a significance level of 5%.

2.4.2. Porosity

Three SLM Ti6Al4V(ELI) specimens built along the X-, Y-, and Z-directions were used for porosity determination. The specimens had a length and diameter of 13 mm and 4.37 mm, respectively. A Nikon XTH 225 ST X-ray micro-computed tomography (Micro-CT) system (Nikon Corporation, Japan) was used for this testing. The test parameters were: scanning resolution of 8.2 µm, current of 200 µA, accelerating potential voltage of 185 kV, exposure period of 4 s per projection, and a total of 2 000 projections per specimen.

2.4.3. Surface roughness

The ZEISS Smartzoom 5 microscope (Carl Zeiss, Germany), equipped with D5x/0.3 FWD 30 mm objective, was used to capture high resolution digital images of the surface areas where the scaled-down nose wheel fork failed during performance testing. This was done to qualitatively characterise the surface roughness around a fatigue crack of the SLM Ti6Al4V(ELI) nose wheel fork.

2.5. Testing the standard test specimens

2.5.1. Tensile strength

The SLM Ti6Al4V(ELI) tensile specimens, built together with the nose wheel fork, were tested with a Model 43 MTS® Criterion™ tensile testing machine, following the ASTM E8 standard.

2.5.2. Impact toughness

Determination of the Charpy impact toughness of the SLM Ti6Al4V(ELI) specimens was done according to the ASTM E23 standard. An Instron 450MP2-J1 system (Instron, Norwood, US) with a maximum capacity of 300 J was used for these tests. All specimens were conditioned to a temperature of -50℃ by immersing them in ethanol solution followed by liquid nitrogen before testing them. This was done at the SecMet subsidiary of MegChem Holding (Pty) Ltd to evaluate impact toughness at a low temperature. The detailed methodology was presented in a previous study by the authors [11].

2.5.3. High cycle fatigue

A tension-tension fatigue test was performed on each SLM Ti6Al4V(ELI) specimen built in the X-, Y- and Z-orientations, following the ASTM E466 standard. A 50 kN Instron 1432 axial servo hydraulic machine (Instron, Norwood, US) was used for these HCF tests at a frequency of 10 Hz and a stress ratio R = 0.1. These axial force-controlled tests were performed at an environmental temperature of 20 $\pm$ 2℃. The run-out number of cycles (N) to failure was set at 5 million. The detailed methodology was presented in the study by Miya *et al*. [12].

2.5.4. Fatigue crack growth rate

The fatigue crack growth rate (FCGR) was determined with a 30 kN Instron 1342 servo-hydraulic testing machine (Instron, Norwood, US) in compliance with the ASTM E647 standard [14]. In Table 2 the pre-crack termination values and testing conditions are given. The pre-cracking was done under constant ΔK and the FCGR tests were performed under constant load while decreasing ΔK.

Table 2: The pre-crack termination values and FCGR test conditions used when testing the SLM Ti6Al4V(ELI) specimens.

Pre-crack termination values	
Final crack length (a_p)	6 mm
Stress intensity range (ΔK)	11 MPa·m$^{0.5}$
Force ratio	0.1
Cycle waveform	Sinusoidal
FCGR test conditions	
Environment and relative humidity	Air, 35~60%
Temperature	20±5 °C
Measurement interval of crack length (a)	0.25
Force frequency	15
Force ratio	0.1
Waveform	Sinusoidal
Initial stress-intensity range (ΔK_i)	11 MPa·m$^{0.5}$
Force	2 kN

2.6. Performance testing of the scaled-down nose wheel fork with as-built surface

The fatigue performance of the post-processed SLM Ti6Al4V(ELI) scaled-down prototype nose wheel fork was tested by using a custom-designed test jig [15]. For the performance testing, the X and Z components of the maximum landing load of the AHRLAC were selected. During testing, the X- and Z-loads were increased by 20% to determine the performance under higher loads. The X- and Z-loads applied were 6 000 N and 8 300 N, respectively. In each load case, the force was applied at a frequency of 3 Hz through the wheel shaft, while the torque arm and the shock absorber bushes were fixed by 12 mm high tensile strength bolts. In Figure 6, the experimental set up for fatigue performance testing of the SLM Ti6Al4V(ELI) nose wheel fork is shown.

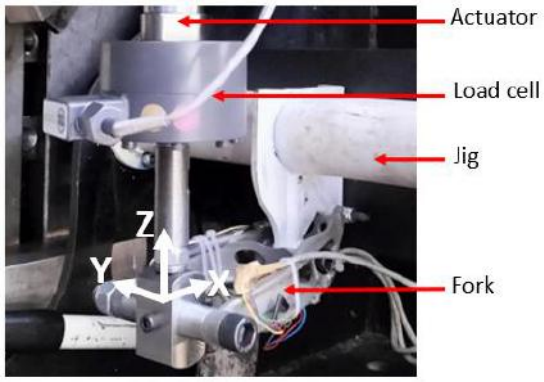

Figure 6: Set-up used in the performance testing of the SLM Ti6Al4V(ELI) nose wheel fork.

During the application of loads, strain values were measured on the nose wheel fork with strain gauges bonded to the areas of the fork anticipated to display high strain values. This was done by using two single grid strain gauges (6/350 LY4) (SG1 and SG2) and two rosette strain gauges (3/120 RY8) (SG3 and SG4) with an HBM Quantum X data acquisition system with 8 channels (HBK Inc, Marlborough, US). In Figure 7, the positions of the strain gauges on the SLM Ti6Al4V(ELI) nose wheel fork are shown.

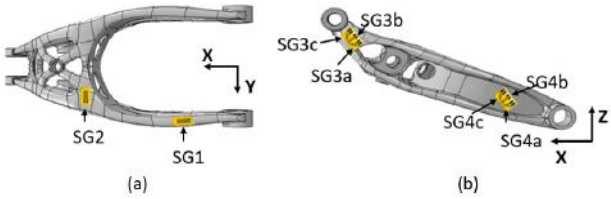

Figure 7: The positions of the strain gauges on the SLM Ti6Al4V(ELI) nose wheel fork: (a) single strain gauges, (b) rosette strain gauges.

3. Results and discussions

3.1. Characteristics of the SLM Ti6Al4V(ELI) scaled-down nose wheel fork

3.1.1. Dimensional accuracy

The geometric dimensional deviation distributions of the scaled-down nose wheel fork for Scan A and Scan B, as determined at the 22 data points shown in Figure 5, are presented in Figure 8.

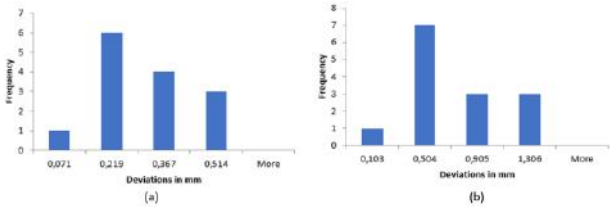

Figure 8: Histograms representing the deviation distributions between nominal CAD data and measured data of the SLM Ti6Al4V(ELI) nose wheel fork: (a) Scan A, (b) Scan B.

The calculated mean values and F factors are given in Table 3.

Table 3: F-test results of statistically significant evaluation of the geometric deviation between Scan A and Scan B.

	Scan A	**Scan B**
Mean	0.26 mm	0.31 mm
Standard deviation (SD)	0.20 mm	0.21 mm
Variance	0.04 mm	0.04 mm
Number of samples	22	22
Degrees of freedom	21	21
Calculated F value	**1.20**	
Critical F value	**2.08**	

Similar measurement accuracy was reported in a study by Rokicki *et al*. [16]. Since the calculated F value was lower than the critical F value, the geometric deviation between Scan A and Scan B was not statistically significant. Therefore, the heat treatment post-process had no significant effect on the geometric deviation of the scaled-down SLM Ti6Al4V(ELI) nose wheel fork.

3.1.2. Porosity

In Table 4 the porosity of the SLM Ti6Al4V(ELI) specimens built in three orthogonal directions is presented. Detail of this determination was

presented in Miya *et al.* [12]. Clearly, the specimens had a density > 99.99 %.

Table 4: Percentage porosity of the SLM Ti6Al4V(ELI) specimens as measured through micro-CT.

Specimen orientation	Porosity (%)
X	0.0029
Y	0.0033
Z	0.0011

3.2. Properties of SLM Ti6Al4V(ELI) specimens

3.2.1. Tensile properties

The tensile properties of the SLM Ti6Al4V(ELI) witness specimens, built with the nose wheel fork, are presented in Table 6. These conform to the ASTM F3001-14 standard [10]. Therefore, the build quality of the nose wheel fork was acceptable.

Property	Tensile Stress at Yield (Offset 0.2%) (MPa)	Ultimate Tensile Stress (MPa)	Elongation (%)
Witness Specimens	845	935	20
ASTM F3001-14	795	860	10

3.2.2. Impact toughness properties

Detailed impact toughness properties were presented in the previous study by Monaheng *et al.* [11]. Here, the impact toughness of the SLM Ti6Al4V(ELI) test specimens with as-built V-notch surface roughness is given in Table 6.

Table 6: Charpy impact toughness of SLM Ti6Al4V(ELI) specimens with as-built V-notch

Build orientation	Values (J/cm^2)			Mean (J/cm^2)	SD
XY	33	34	33	33	0.7
YX	35	35	34	35	0.7
Z	36	38	39	38	1.3

The measured impact toughness of all the SLM Ti6Al4V(ELI) specimens is larger than 26 J, which is recommended by the aviation industry [17]. Therefore, an acceptable impact toughness of the nose wheel fork was expected.

3.2.3. HCF properties

The fatigue strength of the SLM Ti6Al4V(ELI) test specimens with as-built surface roughness is summarised here, while the detailed fatigue properties were presented in the previous study by Miya *et al.* [12]. The fatigue strength of the SLM Ti6Al4V(ELI) specimens built in X-, Y- and Z-orientations are shown in Figure 9.

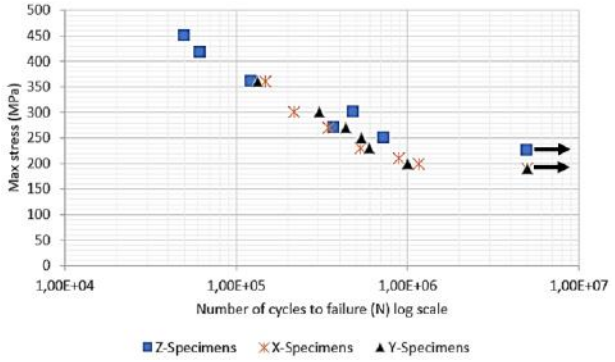

Figure 9: The fatigue strength of SLM Ti6Al4V(ELI) specimens with as-built surface roughness and built in the X-, Y- and Z-orientations.

It is clear from Figure 11 that the specimens built along the X- and Y-orientations had a lower fatigue strength of 190 MPa as compared to the Z-specimens with a fatigue strength of 225 MPa.

3.2.4. FCGR properties

The properties of the triplicate SLM Ti6Al4V(ELI) specimens for the build orientations XZY, YXZ, and ZXY, shown in Figure 4, are presented in Figure 10.

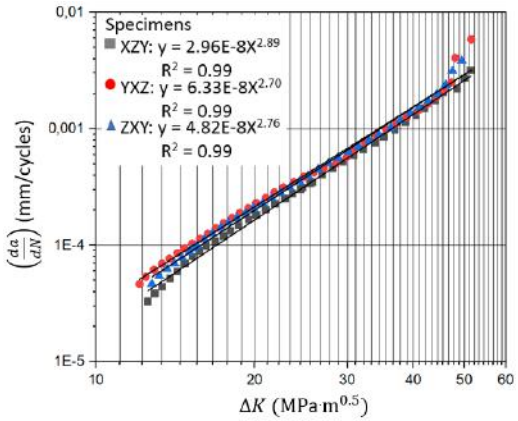

Figure 10: FCGR of SLM Ti6Al4V(ELI) specimens built in XZY-, YXZ- and ZXY-orientations.

The slopes of the FCGR ($\frac{da}{dN}$) versus stress intensity factor (ΔK) plots for various build orientations of the SLM Ti6Al4V(ELI) specimens are comparable. This slope has an average value of 2.78, indicating a good crack growth resistance behaviour. Therefore, the build orientation has no significant effect on the crack resistance of the SLM Ti6Al4V(ELI) components. Similar results were presented in a study by Cain *et al.* [18].

3.3. Performance of the scaled-down nose wheel fork

During the constant amplitude X-load test at 6 000 N and frequency of 3 Hz the SLM Ti6Al4V(ELI) nose wheel fork did not fail. The test was terminated after 101 609 cycles. However, at the same frequency, it failed

after 15 000 cycles under the Z-load case. The strain values recorded for the Z-load case are illustrated in Figure 11.

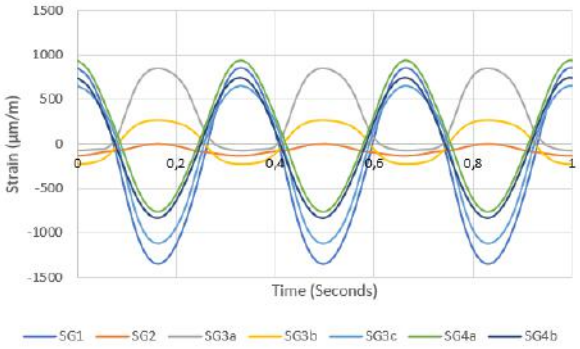

Figure 11: Strain values recorded during the constant amplitude Z-load fatigue testing of the scaled-down SLM Ti6Al4V(ELI) nose wheel fork.

Strain gauge SG1 detected the largest compressive strain values, whereas the SG4a gauge recorded the largest tensile strain. The SG3a gauge, which was bonded where the main crack was depicted, recorded a strain value that was comparable to that of SG4a. Along the surface of the SLM Ti6Al4V(ELI) nose wheel fork, the surface roughness varies, depending on the geometry of a particular area. In Figure 12 (a) and (b) the side surface is less rough than the top surface. In this case, the combination of tensile strain and surface roughness was the main cause of the fatigue cracking on the SLM Ti6Al4V(ELI) nose wheel fork.

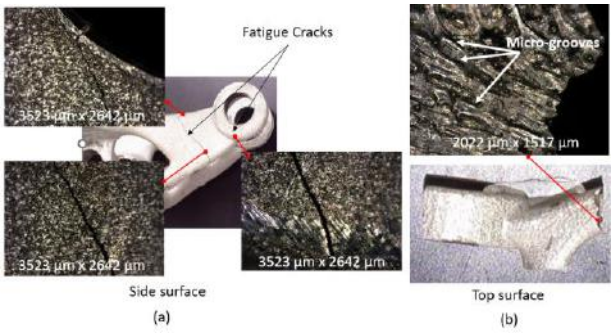

Figure 12: Images of the surface roughness and cracks on the SLM Ti6Al4V(ELI) nose wheel fork.

The high surface roughness acted as a stress riser on the surface of the SLM Ti6Al4V(ELI) scaled-down nose wheel fork. When the Z-load was applied, the stress was amplified to a stress level that supported crack initiation. Thereafter, the crack propagated throughout the nose wheel fork until final fracture.

4. Conclusions

Through this study on the scaled-down experimental prototype nose wheel fork, the feasibility of producing a full-scale nose wheel fork for the AHRLAC through SLM in Ti6Al4V(ELI) was confirmed. The SLM produced component would be 20% lighter than the conventionally manufactured part, however, post-process surface treatment would have to be done to achieve the required fatigue life of the nose wheel fork.

5. Acknowledgements

This research was supported financially by the South African Department of Science and Innovation through the Collaborative program in Additive Manufacturing [Contract No.: CSIR-NLC-CPAM-21-MOA-CUT-01]. Financial support from the Chair in Innovation and Commercialisation of Additive Manufacturing is also gratefully acknowledged.

6. References

1. J. Katzenellenbogen, *DefenceWeb*, (2017).
2. P.A. Kobryn, N.R. Ontko, L.P. Perkins, J.S. Tiley, In Cost Effective Manufacture via Net-Shape Processing, Meeting Proceedings RTO-MP-AVT-139 (2006), 1–14,
3. H.K. Rafi, N.V. Karthik, H. Gong, T.L. Starr, B. E. Stucker, A.A. Antonysamy, University of Manchester (2012) 1-135.
4. P. Middleton, *Crown Publications* (2018) 20–21.
5. L. Motibane, L. Tshabalala, N. Mathe, R. Knutsen, *RAPDASA Conference* (2019) 52–57.
6. L.F. Monaheng, W.B. Preez, N. Kotze, M. Vermeulen, *14th World Conference Titanium* 321 (2020) 1–11,
7. C.B Niutta, A. Tridello, G. Barletta, N. Gallo, A. Baroni, F. Berto, D.S. Paolino, *Engineering Failure Analysis* 142 (2022) 106737.
8. C. Dordlofva, P. Törlind, *Solid Freeform Fabrication* (2017) 2699–2712.
9. M. Roth, M. Yanishevsky, P. Beaudet, *Failure Analysis Techniques and Applications (Proceedings of the First International Conference on Failure Analysis)* (2019) 1–6.
10. ASTM F2924-14, *ASTM International* (2012) 1–9.
11. L.F. Monaheng, W.B. Du Preez, C. Polese, *Metals* 11 (2021) 1–12.
12. H.P. Miya, W.B. du Preez, L.F. Monaheng, *South African Journal of Industrial Engineering* 32 (2021) 248–257.
13. "Geomagics Control X", *3D-Systems*, 8 December 2016.
14. ASTM E647, *ASTM International* (2016) 1-8.
15. H.P. Miya, W.B. Du Preez, L.F. Monaheng, *Central University of Technology* 2023 1-143.
16. P. Rokicki, G. Budzik, K. Kubiak, T. Dziubek, *Aircraft Engineering and Aerospace Technology* 88 (2016) 374–381.
17. "Titanium Ti6Al4V (Grade 5) ELI annealed", *ASM Aerospace Specification Metals Inc*, 29 June 2021.
    V.E.M. Cain, L. Thijs, J. Van Humbeeck, B. Van Hooreweder, R. Knutsen, *Additive Manufacturing* 5, (2015) 68–76.

ADDITIVE MANUFACTURING OF TITANIUM AEROSPACE AND SPACE COMPONENTS

Christoph Leyens[1,2], Christoph Wilsnack[2], Robin Willner[2], Jakob Schneider[1,2], Elena López[2], Frank Brückner[2,3]

1 Technische Universität Dresden, Institute of Materials Research, Dresden, Germany.
2 Fraunhofer Institute for Material and Beam Technology IWS, Dresden, Germany.
3 Department of Engineering Sciences and Mathematics, Luleå University of Technology, Luleå, Sweden.

Additive manufacturing (AM) of metals is currently paving its way into industrial applications at high pace. While in medical applications there is already a widespread use of AM for customized solutions, the strongest innovation boost in AM is coming from aviation industry, followed by the energy sector, automotive industry, space and toolmaking industry. The focus of this lecture is on aerospace and space applications that have recently attracted major attention, some of them already being in series production. Using powder bed-based and nozzle-based (wire and powder) AM processes a large variety of customized solutions is feasible, ranging from micrometre-size parts with filigree features to the meter scale of large-size components. With regard to the processing requirements either high accuracy or high productivity can be achieved, whereas a combination is difficult. Among others, examples of industrialized solutions of micro-AM structures for aero engine use will be presented as well as a demonstrator component for space applications with a total diameter of about 3 meters.

The presentation will highlight recent developments in AM related to different processes, titanium alloys and part sizes/geometries. Unlike any other manufacturing technology, AM of high quality parts requires an in-depth understanding of the close relationship between the AM process, the material and the resulting component properties. As a matter of fact, customized hardware, online diagnostics and control systems are required for robust processing of AM parts. Moreover, the effects of defects on part quality shall be studied in detail.

Keywords: laser metal deposition, Ti-6Al-4 V, Agent-3D, Additive Manufacturing Center Dresden.

1. Realization and verification of a compliant mechanism for space applications [1]

The recent developments in Additive Manufacturing (AM) have attracted the interest of mechanism engineering with a particular emphasis on the realization of Compliant Mechanisms (CM) for space applications. Compliant mechanisms are defined as moveable mechanical assemblies that achieve their desired motion, force, or displacement by means of the elastic deflection of flexible members [2]. Distinct advantages of CM over traditional mechanisms include weight reduction, increased precision, reduced friction and the elimination of lubricants, ease of miniaturisation and integration of functions into fewer components – all of which can substantially impact the performance of space mechanisms.

The kinematic architecture, design and optimization of the CM require the definition of a specific end-to-end manufacturing process with verification methods for thin, flexible and dynamically loaded elements. In a joint project with RUAG Space Germany GmbH and the European Space Research and Technology Centre – ESTEC, we evaluated and verified the material properties and geometrical capabilities of the titanium alloy Ti-6Al-4 V manufactured by Laser Powder Bed Fusion (L-PBF) and highlight how those results impacted the design maturation of a Compliant Rotation Reduction Mechanism (CRRM). The kinematic architecture consists of an input rotation axis, a co-axial output rotation axis and the CM which performs the motion reduction function of the actuation Degree of Freedom (DoF), while constraining all the other directions (fig. 1). Furthermore, the influence of thermal and surface post processing (plasma polishing, flow grinding) on fatigue properties of thin structures was evaluated. Conclusively, the breadboard model was tested to verify the critical functions, resistance against space environment and lifetime performance. As a result, the gained knowledge can serve as a basis for further innovative designs, where high performance with monolithic designs reducing machining costs and integration efforts can be achieved.

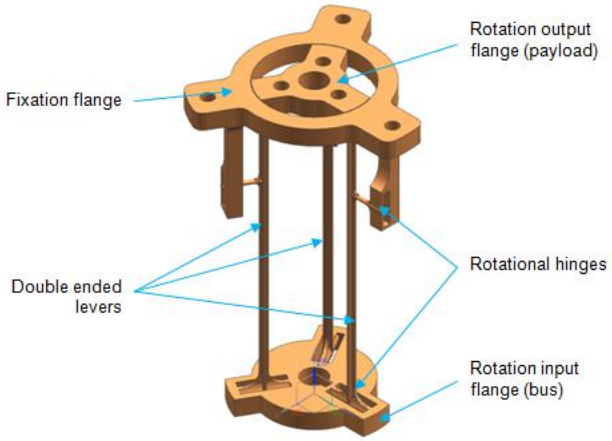

Figure 1. Design of the Compliant Rotation Reduction Mechanism (CPRM) as derived from the kinematic architecture.

1.1. *Manufacturing Process*

Based on the process and design boundaries as well as the desired material properties of the monolithic CMs, Laser Powder Bed Fusion (L-PBF) was chosen. For the manufacturing of the functional demonstrator a process chain including a complementary quality assurance in dependence with the ECSS-draft standard was developed. The quality assurance consists of the feedstock powder characterization and the characterization of the parallel processed material witness samples (tensile samples, density cubes). The manufacturing process was prepared with Materialize Magics 23.1. The remaining supporting structures beside the contactless support and the positioning of the parts were chosen based on experiences within the geometry study. After L-PBF manufacturing and disassembling from the machine the chain succeeded with the post processing of the parts. The parts were scanned via computer tomography (CT) and structural and dimensional measured sequentially and no porosity of the breadboard was detected. The target/actual-comparison of the CT-scanned parts show a good overall dimensional accuracy. The functional breadboard model (fig. 2) was submitted to MAIT-testing within the therefore designed testing facility and testing campaign.

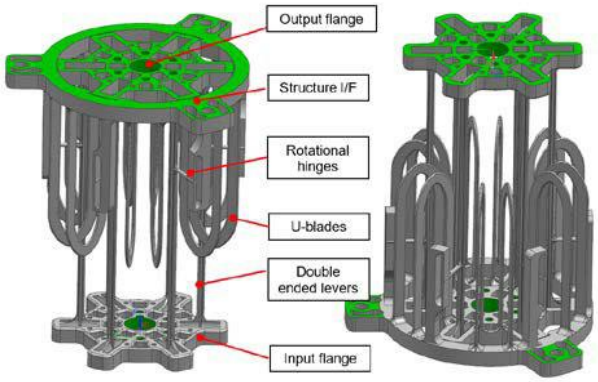

Figure 2. CPRM detailed design and breadboard model.

1.2. *MAIT Testing*

The test campaign was conducted to assess the compliance of the breadboard towards the requirements and the predicted performances. Overall, the breadboard model performed remarkably well, especially regarding nominal performance and repeatability. Some issues came however to light during the test campaign. The measured stiffness was lower than predicted. The test predictions were updated with the Young's Modulus values acquired from the witness samples, but the variations in the mechanical properties of the material did not fully explain the measured lower stiffness. It is assumed that local variations in the lever thickness and notching effect due to the roughness caused by the manufacturing process may be the cause of this deviation. During the testing, deformations were noticed at the output I/F, which have not been detected during the quality control. A deeper inspection of the CT images showed a shifting of the output with respect to the structure I/F (fig. 3), causing a misalignment to the hard-stops which were designed to prevent out-of-range rotations. As a result, the output motion range was limited, but the transmission ratio performance was as predicted 8:1. The breadboard was subjected to environmental testing including vibration, shock test and thermal tests. To test for endurance, 100'000 load cycles (+/- 5°) were applied without any visible deviation in repeatability and transmission ratio. Despite all tests conducted during the campaign, the performance could be retained, which proves that the CM breadboard offers a great base of knowledge for the design of future compliant mechanisms based on additive manufacturing.

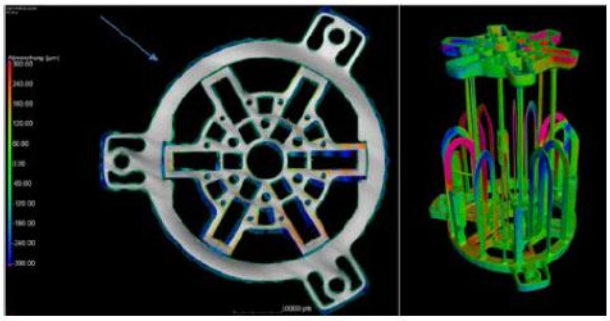

Figure 3. CT variance analysis for asymmetry evaluation.

1.3. *Conclusion*

Within this project, a process chain to manufacture a Titanium-based compliant mechanism for space applications was successfully developed. The breadboard model was manufactured by L-PBF, thermal treated, hiped, flow grinded and plasma polished. Afterwards it was tested under relevant environments and underwent a lifetime test to validate its fatigue resistance (100'000 cycles) without performance loss. The potential improvements of CM design based on the unique possibilities of additive manufacturing were further highlighted setting the scene for new innovations of space components.

2. Topology optimization of spacecraft structures [3]

Support structures for space applications consist of different types of carbon fibre reinforced polymers (CFRP) components, which are connected via corresponding metallic brackets to the interface of the satellite. While conventional subtractive manufacturing approaches set stark restrictions on the structure design, this study focused on the potential of topology optimization (TO) for metallic tertiary structures of spacecrafts produced by Laser Powder Bed Fusion (L-PBF). Based on a screening of existing conventionally manufactured products the benefits of a redesign concerning product performance and the associated economic impact were evaluated. As a result, a titanium mounting bracket made was selected. This reference structure was redesigned by TO taking into consideration the AM process constraints. The optimized structural parts were then manufactured from Ti-6Al-4 V and tested on qualification level.

2.1. Process design approach

To prepare the implementation of an additively manufactured tertiary structure several actions were considered (fig. 4). First, a list of representative tertiary space structures was prepared, while the AM requirement specifications were defined. The requirements were then applied to the list and the reviewed structures were characterized and analysed in terms of their potential for TO and AM. From the screening, three relevant structures emerged. A material validation and characterization process was performed in parallel to the TO on the selected structure. The process verification and part qualification was developed to ensure the processability of the AM structures. The proposed approach includes definition of witness samples. An iterative redesign process for AM was performed on the selected structure. Thus, manufacturing constraints and know-how was used from the early beginning, which resulted in few iterations and a printable structure right from the start.

The topology-optimized structure was manufactured and the part performance was tested in a campaign that included NDI, thermal cycling, and static as well as dynamic mechanical testing. The tests results and lessons learned were fed back into an update of the trade-off methodology and the impact analysis which was carried out at the beginning of the project. This approach gathers all the information needed for the preliminary design and analysis phase, ensures the process quality in order to prevent defects and increases the TRL from three up to five.

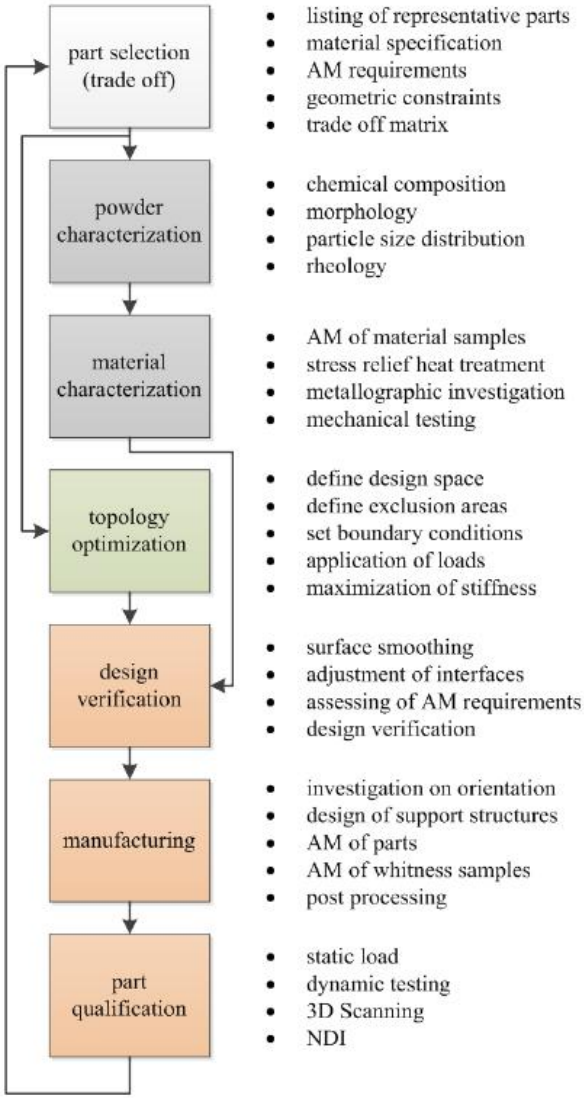

Figure 4. Workflow of the manufacturing approach.

2.2. Experimental approach

The optimized bracket was manufactured on an AM400 L-PBF machine from Renishaw. The laser was an ytterbium fiber laser with a wavelength of 1064 nm and a maximum power of 400 W. The beam diameter was 70 µm on the powder bed surface. For the transmission and scanning of the laser beam a f-θ-optic and scanner of the type Intelliscan 14 of the company Scanlab was used. During the build process, the building chamber was filled with the inert gas argon. The argon cross jet was applied above the powder bed to avoid the deposition of fume and sparks on the unmolten powder. The cross jet streamed into a fine particle air filter. The recoating mechanism was based on a silicone lip wiper. Latter was used to deploy the next powder layer on top of the previous layer via translational movement. The excess powder fell into two overflow shafts and into powder bottles. This powder could be reconditioned and reused through sieving into

the demanded particle fraction. The process boundaries like scanning parameter set and machine settings were defined from available information and common knowledge for the processing of Ti-6Al-4 V. The parameter set and the applied process boundary conditions are listed in Table 1.

Table 1: Process parameters for Ti-6Al-4 V L-PBF processing.

Property	Value
Powder description	Heraeus Ti-6Al-4 V Grade 5
Particle size fraction	10-45 µm
Layer thickness	30 µm
Laser power	200 W
Scan Strategy	Stripes, 67° rotation
Hatch distance	105 µm
Scan speed	1100 mm/s
Substrate plate heating	170 °C
Build rate	9355.5 mm^3/h
Atmosphere	Argon
Oxygen threshold	< 400 ppm

For the reduction of the process immanent residual stresses a stress relief heat treatment according to ASTM B348 – 13 (550°C, 180 min, Ar-atmosphere, furnace cooling) was performed after each build job.

2.3. Redesign and analysis

The redesign of the bracket was made with respect to a topological optimization of the part and its capability to be manufactured by AM methods. A structural goal of mass decrease ($\Delta m \geq -30$ %) and stiffness increase of (+30 %) was targeted. The main load was a tensile/compressive force to its interface applied in the axis on the contact surface. An FE analysis was conducted on the original part as reference for later comparison. The factor of safety of the original part was calculated to 2.9. The minimum allowable factor of safety is defined by ECSS-EST-32-10 to FOSU = 1.25. To cover uncertainties in the use of LPBF as a still new manufacturing process the target factor of safety for the topological optimized bracket was defined to 2.5.

2.4. Conclusion

Within this contribution the trade-off, the topology optimization, the manufacturing as well as the qualification for a titanium spacecraft bracket were presented. The part performance was verified in a test campaign that included NDI, thermal cycling, and static as well as dynamic mechanical testing. The additively manufactured test specimens passed all tests and partly excelled. The test results and lessons learned were fed back into an update of the trade-off methodology and the impact analysis. With the part qualification campaign TRL 5 was achieved. A qualification of the total, assembled structure of the built-in part would be capable to reach TRL 7. Nevertheless, the qualification is a vital part and with the path described herein a qualification up to TRL 7 is feasible.

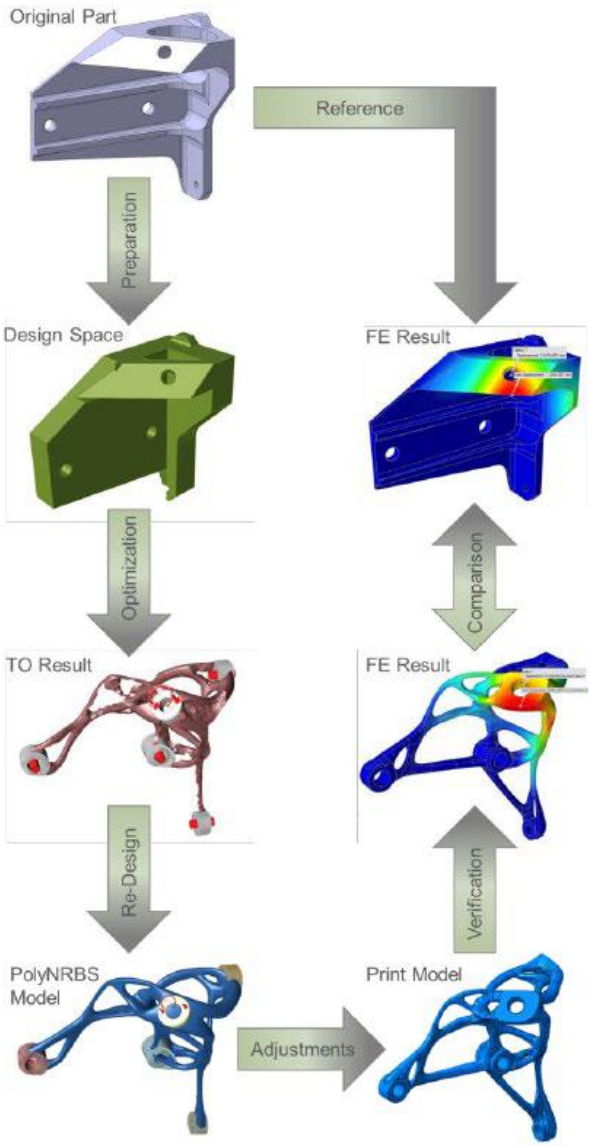

Figure 5. Redesign workflow.

3. Additive Manufacturing of a metallic optical bench for the ESA science mission ATHENA [4]

With the large-class science mission ATHENA, the European Space Agency (ESA) aims at exploring the hot and energetic universe with advanced X-Ray technology. As a central component of the telescope, hundreds of silicon pore optic (SPO) modules will be assembled in an optical bench with a diameter of about 2.5 m. In cooperation with ESA, the Fraunhofer IWS is currently investigating the manufacturing of the optical bench made from Ti-6Al-4 V by means of Additive Manufacturing using Laser Metal Deposition (LMD) followed by subtractive finishing. Within the scope of this presentation, a general overview is given about the project related developments, achievements, and flanking activities for solving various challenges. The suitability of the developed technologies and workflows are now being evaluated through the manufacture of a representative, large-scale breadboard.

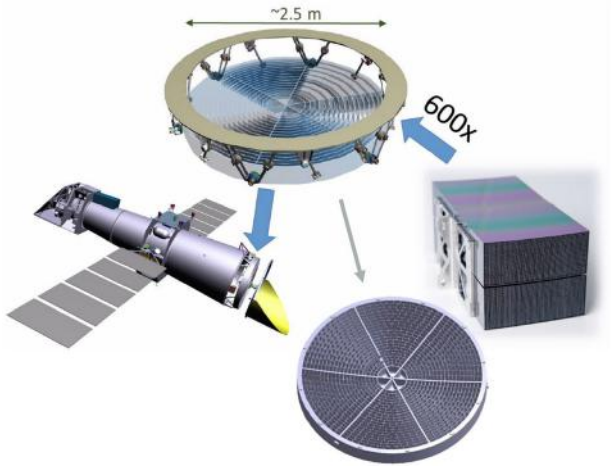

Figure 6. Schematic structure of the ATHENA telescope showing the mirror modules, optical bench and the supporting structure.

3.1. Manufacturing approach

Due to the general shape of the supporting structure, with its high aspect ratio resulting from narrow pocket widths combined with high pocket depths, and the limited accessibility for post-processing of specific areas in the fully build-up state, a stepwise alternating hybrid manufacturing approach was initially applied as the end-to-end manufacturing strategy. This strategy comprised the combination of Additive Manufacturing and subtractive machining in a step-by-step alternating production scheme. For the Additive Manufacturing technology, LMD, also known as Laser Powder-Based Direct Energy Deposition (DED-LB), was selected. The main benefits of this technology includes the production of dense layers with low porosity, small heat-affected areas and less distortion via highly localized heat inputs, and good scalability in terms of achievable resolution and deposition rates. Cryogenic milling with carbon dioxide as a coolant was identified as a suitable technology for the intermediate finishing. The capability of this technology for machining difficult materials like Ti-6Al-4 V compared to dry machining and machining with conventional lubricants has been demonstrated before. It is a very clean process and the nearly complete evaporation of the coolant results in less residual contaminations on the machined surfaces, making it especially suitable for usage in this alternating manufacturing approach.

3.2. System engineering and process development

Additive Manufacturing with Ti-6Al-4 V is challenging due to the high affinity of the material to gases in the ambient atmosphere, mainly nitrogen and oxygen, resulting in oxidation and inward diffusion into the bulk material at elevated temperatures leading to structural embrittlement. Due to the size of the supporting structure and to maintain acceptable accessibility and flexibility during production, global shielding did not appear to be feasible in the specific case. Alternatively, a novel shielding nozzle for local shielding called “COAXshield” was developed. The system enables a shielding of only the hot areas close to the fusion zone where severe oxidation can appear. Therefore a protective gas cone is created coaxially around the powder nozzle. Using this methodology, the residual oxygen content can be effectively lowered to about 100 ppm in the shielded areas.

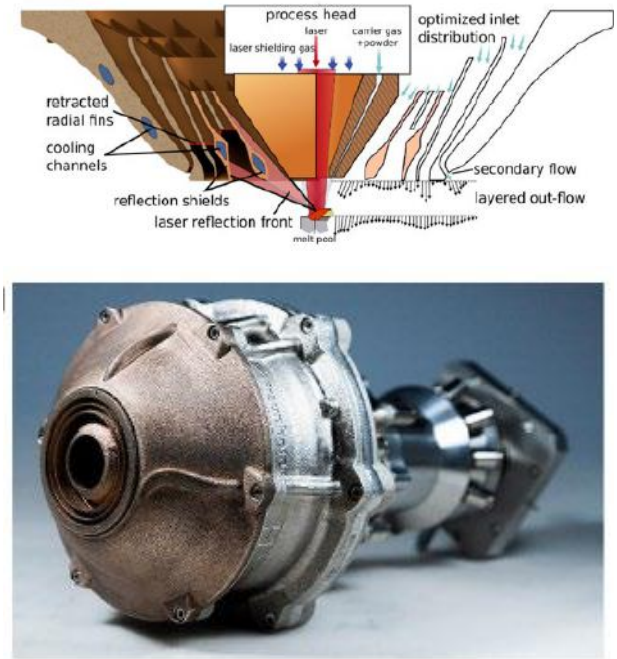

Figure 7. COAXshield nozzle for local gas shielding for LMD.

3.3. Material characterization

For the functionality of the optical bench, a particular focus was placed on determining the project-specific requirements which includes the mechanical strength and stiffness as well as various thermo-physical properties. Therefore, the microstructure and mechanical performance of the AM parts were evaluated by performing a comprehensive test campaign. This included destructive testing for the evaluation of the mechanical properties, non-destructive testing for the evaluation of the structural integrity, and the measurement of thermophysical material properties. Tensile tests were carried out according to ASTM E8 / E8M-16a. For the identification of possible mechanical anisotropies, different orientations and positions of the test specimens in the demonstrator were considered. The results were in good consistency with the requirements, and only minor mechanical anisotropy could be identified. However, the recorded ductility of around 8% was lower than expected which is unfavourable for the general machinability. The obtained microstructure can be classified as typical for LMD processed Ti-6Al-4 V. The main features are columnar prior β grains epitaxial grown across several layers oriented along the heat flow during solidification. The substructure can be characterized as columnar dendritic with α lath in a β matrix arranged in a Widmanstatten like grid morphology. The prior β grain boundaries are highlighted by grain boundary α and surrounding colony structures consisting of arranged α lath. No significant changes in the microstructure depending on the build height could be recognized. To further improve the ductility, it is planned to use a longer solution heat treatment time which is expected to allow the martensitic phase to decompose resulting in the creation of a basket wave α + β substructure.

3.4. Conclusion

In this project, a general framework for AM of large parts using Laser Metal Deposition coupled with different approaches to finishing has been demonstrated by manufacturing of a large optical bench for the ATHENA mission. The traditional manufacturing approach of machining the support structure from solid wrought material is unsuitable for manufacturing. This is largely due to the high costs associated with the procurement of large titanium forgings and extensive amount of machining. By changing the process route to AM, the application is expected to become technologically profitable, even for large component production. Extensive development work has been performed starting at the system engineering level, followed by an evaluation of an overall end-to-end manufacturing approach. A number of valuable lessons have been learned. Firstly, it must be stressed that the sheer size of the component places enormous demands on the production. To be able to design the shown manufacture approach in an attractive manner from a production point of view, a general scaling on the process level is required to reduce the production times whilst delivering a high degree of automation at the same time. The greatest potential for increasing productivity lies essentially in increasing of the deposition rate for LMD. However special consideration of the cooling rates will be required to preserve the feasibility for local shielding. Finally, quality assurance measures based on continuous digitization of the processes are also required. In addition, various methods of in-line part inspection are also being considered, for example, the usage of high resolution camera systems to perform layer-by-layer inspection of the part top surface with regard to the detection of defects and the presence of annealing colours. Modern image processing algorithms will also enable a first analysis of geometric deviations by extracted structure features.

4. Acknowledgements

The projects presented were conducted in collaboration with the following colleagues: Alba Alegre Cubillo, Christian Melzer, Jan Richter (RUAG Space Germany GmbH), Stefan Lender, Andreas Ihl (INVENT GmbH), Elena Christina Paul, Paolo Zaltron, Ana Brandão, Laurent Pambaguian, A. Norman, J. Gumpinger, M. Bavdaz, T. Ghidini (European Space Research and Technology Center – ESTEC) and Vladislav Robiner, Samira Gruber, Lukas Stepien, Mirko Riede (Fraunhofer IWS).

5. References

1. C. Wilsnack, A.A. Cubillo, V. Robiner, C. Melzer, J. Richter, E.C. Paul, P. Zaltron, M. Riede L. Stepien, E. López, F. Brueckner, C. Leyens, ECSSMET 2021 (2021) “Realization and verification of a compliant mechanism produced by additive manufacturing”.
2. R.M. Fowler, L.L. Howell, S.P. Magleby, *Mechanical Sciences* 2 (2011) 205–215.
3. R. Willner, S. Lender, A. Ihl, C. Wilsnack, S. Gruber, A. Brandão, L. Pambaguian, M. Riede, E. López, F. Brueckner, C. Leyens, *Journal of Laser Applications* 32(3) (2020) p.32012.
4. J. Schneider, A. Norman, J. Gumpinger, F. Brückner, M. Bavdaz, C. Leyens, T. Ghidini, *CEAS Space Journal* 15(1) (2023) 55-68.

Please note that the manuscript presented here is a compilation of results from references [1], [3] and [4].

MICROSTRUCTURE AND CRYSTALLOGRAPHIC TEXTURE OF A NEAR-BETA TITANIUM ALLOY FABRICATED BY LASER POWDER BED FUSION WITH A FLAT-TOP LASER BEAM

Tomonori Kitashima[1,2], Dennis Edgard Jodi[1,2], Makoto Watanabe[1]

1 National Institute for Materials Science, 1-2-1 Sengen, Tsukuba, Ibaraki, 305-0047 Japan.
2 Department of Materials, Kyushu University, 744 Motooka Nishi-ku, Fukuoka, 819-0395 Japan.

A near-β Ti-6Al-2Sn-4Zr-6Mo alloy (Ti-6246) was fabricated by laser powder bed fusion using a flat-top laser beam, and its microstructure and texture were investigated. Fabrication was carried out using an SLM 280 HL equipped with a flat-top laser beam, 700 μm in diameter. A single fusion track was initially analyzed using a Ti-6246 plate without powder. The melt-pool depth decreased with increasing laser scan speed under constant laser power, and the melt-pool geometry shifted from super-Gaussian to planar. However, a smaller melt-pool depth led to a less stable melt-pool geometry. By using optimized parameters to achieve a planar melt pool geometry via fusion track analysis, grain growth occurred parallel to the build direction in the powder bed fusion. This resulted in a near-{001}<100> β texture formation on the plane perpendicular to the build direction. This could be because the direction of local thermal gradients at the solid–liquid interface of the bottom of the melt pool was aligned parallel to the build direction. Very thin grain α phases and fine grain interior acicular α phases were formed. The melt-pool geometry and texture formation can be controlled by combining flat-top laser and Gaussian beams in laser powder bed fusion.

Keywords: Laser powder bed fusion, flat-top laser beam, titanium, texture, grain growth, melt pool.

1. Introduction

Additive manufacturing is an effective process for manufacturing jet engine parts. Controlling the grain structure and microstructure of engine parts during manufacturing is crucial for achieving high performance. There have been various reports on the effects of fabrication parameters and scan strategies on the grain structure and defect formation in laser powder bed fusion (LPBF) for Ti alloys [1–5]. Previous reports adopted a Gaussian laser beam that possesses a Gaussian profile intensity on the irradiated plane (Figure 1(a)). This results in a large temperature gradient from the center to the edge across the irradiated surface. Researchers have been able to control the crystallographic textures with a Gaussian laser beam by adopting different scan strategies. For example, Ishimoto *et al.* demonstrated that bidirectional scanning with and without a 90° rotation between layers led to different textures with preferential orientations of <001> and <011> along the building direction, respectively, in the Ti-15Mo-5Zr-3Al alloy [1]. Jodi *et al.* recently demonstrated the feasibility of producing a single-crystal structure of pure Ni using a flat-top laser beam profile with a uniform intensity on the irradiated surface (Figure 1(b)) [6]. The optimization of the fabrication parameters allowed the formation of a planar melt pool, which promoted the growth of <001>-oriented solidification grains almost parallel to the build direction (BD). Gradually, <001>-oriented grains become dominant over grains grown in other orientations, leading to the suppression of high-angle grain boundaries (HAGBs) formation. Finally, a single-crystal structure with homogeneous <001> texture was obtained. However, it contained low-angle grain boundaries (LAGBs) and sub grains. Thus, obtaining a planar melt pool using a flat-top laser beam is a useful approach for aligning the grain structure in a way that differs from conventional methods. However, there have been few reports on the texture formation of near-β Ti alloys with α precipitates fabricated using a flat-top laser beam [7]. In this study, a near-β Ti-6Al-2Sn-4Zr-6Mo alloy (Ti-6246) was fabricated by LPBF using a flat-top laser beam, and its microstructure and crystallographic texture were investigated and compared with those obtained using a Gaussian laser beam instead of a flat-top laser beam.

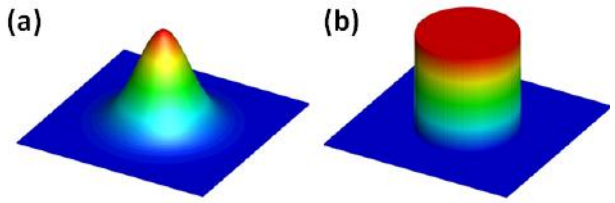

Figure 1. Schematics of the intensity distribution on the plane perpendicular to the laser irradiated direction for (a) Gaussian and (b) flat-top laser beams.

2. Experimental procedures

The fabrication was performed in an Ar atmosphere using an SLM 280 HL (SLM Solutions, Germany). The SLM apparatus comprised flat-top laser and Gaussian lasers with beam diameters (d_b) of 700 and 80 μm, respectively. Single tracks were analyzed to observe the melt pool geometry using Ti-6246 plates (TIMET, USA) without a powder layer coating. The power (P) and scan speed (v) of the laser in the single-track analysis varied between 250–350 W, 600–1500

mm/s, respectively, for the Gaussian beam. For the flat-top beam, the scan speed ranged from 100–550 mm/s. The melt-pool geometry was observed on the build direction (BD)–hatch direction (HD) plane, which is perpendicular to the scanning direction (SD). Multilayers were fabricated in the powder bed fusion using the *P*–*v* combination of the observed melt pool geometry. The energy density (E_M) was obtained for multiple multi-layers using the following equation [8]:

$$E_M = \frac{\beta P}{h\sqrt{4\alpha d_b v}}, \quad (1)$$

where, β and α represent absorption factor (~0.8) and thermal diffusivity (~2.55 mm^2/s), respectively. The parameters used for fabricating the multilayers and the energy densities calculated from these parameters are listed in Table 1. The layer thickness was maintained at 30 µm during fabrication. Plasma-atomized Ti-6246 powder (Advanced Powders & Coatings, Inc., Canada) was used. D_{10}, D_{50}, and D_{90} values of the powder were ~25.3, ~41.1, and ~63.7 µm, respectively. The laser was used to scan in a zigzag manner, with a 90° rotation for each layer, during the multilayer fabrication. Cylindrical specimens (12 mm in diameter and 30 mm in height) were fabricated on pure Ti plates, as shown in Figure 2. In this study, the powder stage was not heated. All specimens were sectioned and ground with abrasive paper (#320 and #600) and mechanically polished using diamond (9, 3, and 1 µm) and colloidal silica suspensions. Scanning electron microscopy (SEM; JEOL JSM-7001F) and electron backscatter diffraction (EBSD) were used to characterize the microstructure of the specimens. The EBSD analysis was conducted on the HD–BD cross-section with minimum measuring areas of 800×1200 µm and a step size of 4 µm. The EBSD data were analyzed using TSL OIM 8. In this study, LAGBs and HAGBs were classified based on misorientations, with LAGBs and HAGBs having misorientations ranging from 5°–15° and >15°, respectively. The constituent phases were identified by X-ray diffraction (XRD) analysis using a SmartLab diffractometer (Rigaku, Japan) with Cu Kα (λ = 1.5418 A) radiation generated at 45 kV and 200 mA.

3. Results and discussion

3.1. Single-fusion track analysis

Single-fusion tracks were initially analyzed to investigate the correlation between the fabrication parameters, particularly the laser scan speed and melt-pool geometry. Figure 3 shows the backscattered electron (BSE) images of the cross-section of the fusion tracks scanned by the Gaussian laser beam. As the laser scan speed increased, the melt pool became shallower and narrower because of the decreased energy density.

Table 1: Fabrication parameters in this study.

	Laser power (W)	Laser scan speed (mm/s)	Hatch space (µm)	Energy density (J/mm^3)
G1	300	1500	90	76.22
FT1	300	350	110	43.65
FT2	300	250	120	47.34

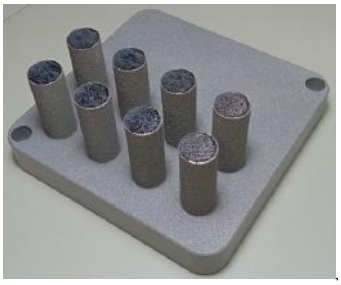

Figure 2. Fabricated cylindrical specimens. Diameter: 12 mm and height: 30 mm.

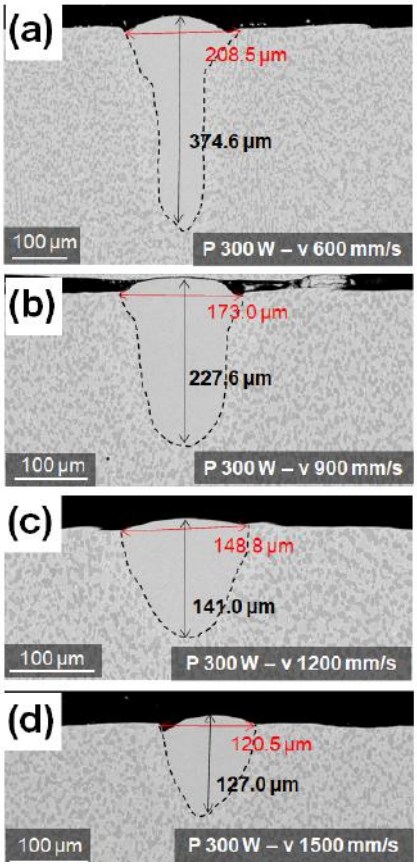

Figure 3. Cross sections of the plate fusion tracks scanned by Gaussian beam.

At 600 mm/s, the melt pool was deep, whereas at 1500 mm/s, the geometry was semi-elliptical. In contrast, when the flat-top laser beam was used to scan for a single track, the melt pool became shallower and narrower as the laser scan speed increased, as shown in Figure 4. This trend is similar to that observed with the Gaussian laser beam, although the melt pool geometry with the flat-top laser beam was significantly shallower than that obtained with the Gaussian laser beam. The geometry of the planar melt pool caused by the flat-top laser beam becomes unstable and asymmetric at scan speeds greater than 350 mm/s (Figure 4(c)–(e)). Different ranges of the laser scan speed were adopted for the Gaussian and flat-top laser beams as shown in Figures 3 and 4. Because these beam diameters are different, the energy densities are different for the same fabrication parameters. For example, when the laser scan speed was set to 1500 mm/s with a laser power of 300 W on a single track using a flat-top laser, the plate melted partially.

3.2. Multi-layer fabrication

Figure 5 shows the BSE images of the cross section parallel to the BD at the center, specifically at the height of 29.5 mm, for the multilayered specimens of G1 (a, c) and FT2 (b, d).

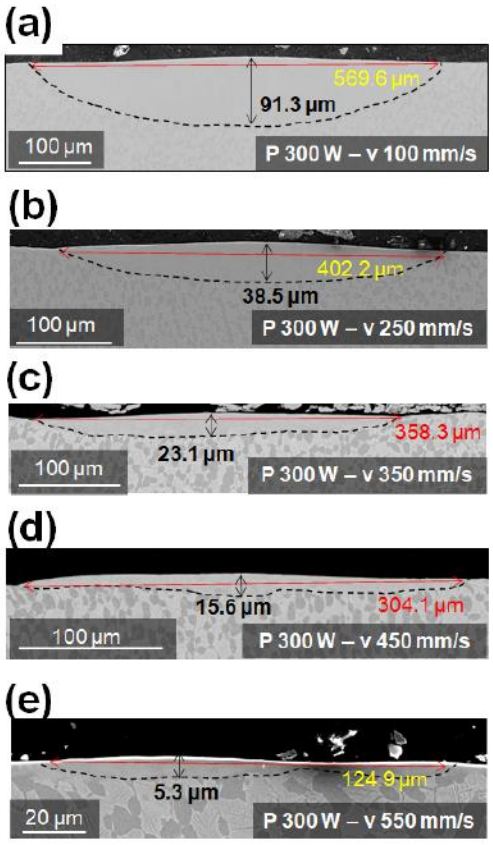

Figure 4. Cross sections of the plate fusion tracks scanned by flat-top beam.

The laser power and scan speed of G1 and FT2 were the same as those used in the semi-elliptical and planar melt pools, respectively, as shown in Figures 3(d) and 4(b). The grain boundaries are indicated by the dashed lines in Figures 5(a) and (b). Figures 5(c) and (d) show the magnified grain boundary (GB) α in Figures 5(a) and (b), respectively. For both G1 and FT2, columnar grains grew in the BD. However, the widths of the grown grains were relatively uniform in G1, but not in FT2. This is because during the solidification of the melt pool, due to the Gaussian laser beam, the grains grew toward the melt pool center and upward from the semi-elliptical fusion line in the direction perpendicular to the fusion line on the HD–BD plane. The HAGBs then formed at the center line as a "laser trail." However, in FT2, such "laser trails" were not observed because the <001>-oriented growth, parallel to the BD, caused negligible angle differences between grain growth directions on the fusion line on the HD–BD plane. This will be discussed later using the EBSD results. In the XRD analysis, the peaks of α–α" and α–β were detected for G1 and FT2, respectively. This is because the cooling rate during the fabrication of G1 was very high, and martensitic α" was transformed from the β phase soon after solidification. In contrast, the cooling rate of FT2 may be slower, and/or the layer-by-layer heat cycles during the shallow-melt-pool formation continued to heat the solidified layers during fabrication. This resulted in the transformations of β to α" and α–β after solidification [9]. For both G1 and FT2, the GB α was formed with a thickness of less than 100 nm, as shown in Figure 5. However, the thickness of GB α was thinner in G1, which has a lower cooling rate than FT2. In addition, very fine acicular phases precipitated in grains of both G1 and FT2 although the grain-interior α in FT2 was more distinguishable with larger sizes.

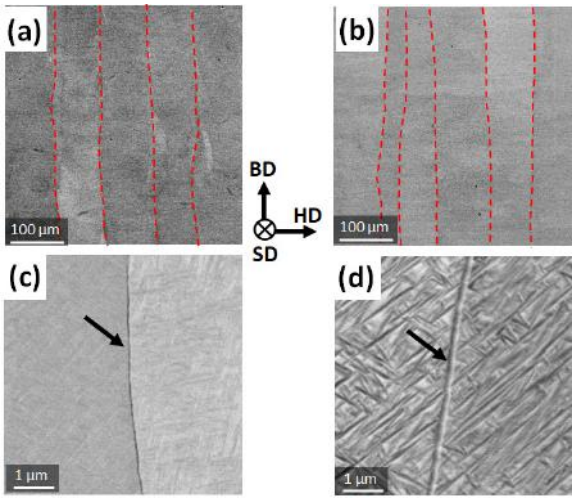

Figure 5. Cross sections perpendicular to the build direction for multi-layered specimens fabricated using (a, c) Gaussian and (b, d) flat top laser beams. (a) and (c): G1; (b) and (d): FT2.

Figures 6(a–c) and (d–f) show the inverse pole figure (IPF) maps for β phase and phase maps for α/β phases, respectively, on the cross-section parallel to the BD for G1, FT1 and FT2 at the center, specifically at the height of 29.5 mm. The β-phase IPF maps (Figures 6 (a–c)) were obtained as IPF-Z for the texture perpendicular to the BD. The atomic positions in the orthorhombic α" phase are close to those in the cubic β phase, leading to similarly indexed EBSD patterns. Therefore, the α" texture was characterized using the crystal parameters of β-Ti in the EBSD analysis [10]. In G1 and FT1, the <001>–<111> texture was observed as shown in Figures 6(a) and (b). However, the "laser trails" were clearly observed in G1. In FT2, A homogeneous <001>β-texture was obtained (Figure 6(c)), although the α phase was dominant in the as-fabricated microstructure, as shown in Figure 6(f). The α phase fractions were 0.47, 0.60, and 0.77 for G1, FT1, and FT2, respectively.

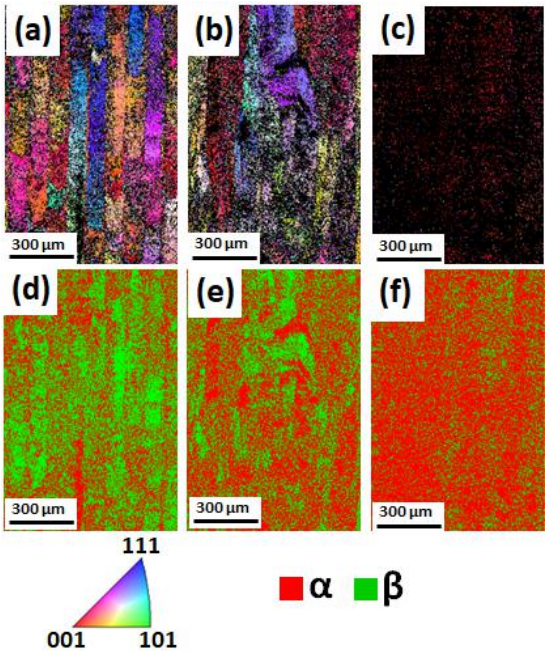

Figure 6. (a–c) β-phase IPF map and (d–f) α/β-phase map on the cross-section parallel to the BD. The β-phase IPF map shows the texture perpendicular to the BD (IPF-Z). (a) and (d): G1, (b), (e): FT1, (c) and (f): FT2.

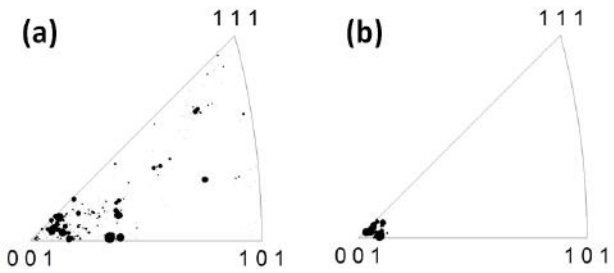

Figure 7. β-phase-grain orientations and sizes for (a) G1 and (b) FT2. These were obtained from the areas of Figure 6(a) and (c), respectively.

Figures 7(a) and (b) shows maps of each β-phase grain orientation and size for G1 and FT2, respectively. These were obtained from the areas shown in Figures 6(a) and (c), respectively. The G1 grains exhibited various orientations on the plane perpendicular to the BD, whereas FT2 exhibited <001>-oriented grains. One reason for this difference is that the texture formation depends on the melt pool geometry. In the melt pool caused by the Gaussian laser beam, the grains grew in the direction of the highest temperature gradient from the semi-elliptical fusion line, that is, perpendicular to the fusion line on the HD–BD plane, as mentioned previously.

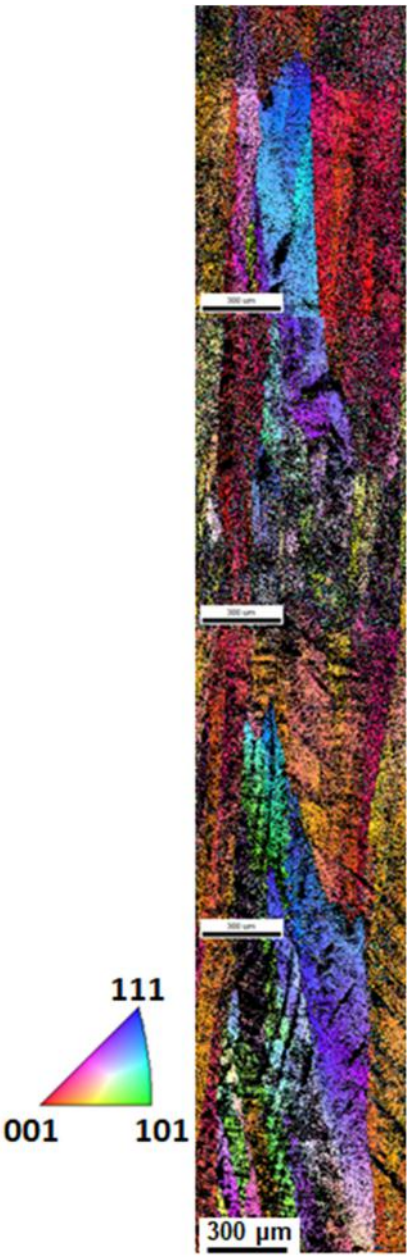

Figure 8. The β-phase IPF map of FT1 on the cross-section parallel to the build direction, which shows the texture perpendicular to the BD.

In contrast, for the flat-top-laser-derived melt pool, the grains grew in a direction close to the BD on the HD–BD plane because of the planar melt pool geometry. However, the β-texture for FT1 was composed of grains of various orientations, as shown in Figure 6(b), although the melt pool geometry was planar in Figure 4(c) in the fusion track analysis. As the energy density of the flat-top laser beam decreased, the melt pool became increasingly shallower and narrower. In addition, the geometry became unstable and asymmetric. This asymmetry may be unfavorable for controlling the grain growth in the direction aligned to the fusion line.

The LPBF process generates a high thermal gradient-to-cooling rate (G/R) ratio owing to the smaller melt pool size in comparison to the surrounding powder bed. In addition, the small distance between the melt-pool bottom and melt-pool surface prevents significant undercooling, particularly for melt pools with small depths. Moreover, equiaxed grains do not form from bulk homogeneous nucleation without a high density of solid particles or partially unmelted powder. Therefore, in LPBF, epitaxial growth predominantly occurs from the melt-pool fusion line, taking on the crystal structure and orientation of the lower layer. The <001>orientation of cubic crystals, such as body-centered cubic (bcc) and face-centered cubic (fcc) crystals, preferentially grows along the direction of the highest temperature gradient at the fusion line. Figure 8 shows the IPF map of FT1 for the HD–BD cross-section at the center top of the specimen. The texture on the plane perpendicular to the BD is shown here. The EBSD analysis area in Figure 8 is 800×4800 μm with a step size of 4 μm. In FT1, grains grew upward epitaxially even though each layer thickness was 30 μm. The <001>–<111> textures appear asymmetrically and periodically. To obtain a homogeneous <001>-texture on the HD–scanning direction (SD) plane, it is important to optimize the fabrication parameters and render the planar and symmetrical melt pool geometry.

Previous studies have demonstrated that the as-fabricated texture can be altered by changing the scan strategy of a Gaussian laser beam, as described in Section 1. The combination of a flat-top laser beam with a Gaussian beam in the LPBF allows for greater control over the melt-pool geometry and texture formation.

4. Acknowledgments

The authors thank Dr. Takanobu Hiroto, Dr. Miwako Takano, Mr. Masaru Suzuki, Ms. Chiho Togashi, Mr. Koji Nakazato, and Mr. Masahiko Kawasaki of the National Institute for Materials Science for their assistance. This study was supported in part by Amada Foundation (AF-2022215-B3).

5. References

1. T. Ishimoto, H. Hagihara, K. Hisamoto, S.H. Sun, T. Nakano, *Scripta Materialia* 132 (2017) 34–38.
2. L. Thijs, F. Verhaeghe, T. Craeghs, J.V. Humbeek, J.P. Kruth, *Acta Materialia* 58 (2010) 3303–3312.
3. C.M. Cepeda-Jiménez, F. Potenza, E. Magalini, V. Luchin, A. Molinari, M.T. Pérez-Prado, *Materials Characterization* 163 (2020) 110238.
4. A. Carrozza, A. Aversa, P. Fino, M. Lombardi, *Journal of Alloys and Compounds* 870 (2021) 159329.
5. H. Hassanin, Y. Zweiri, L. Finet, K. Essa, C. Qiu, M. Attallah, *Materials* 14 (2021) 2056.
6. D.E. Jodi, T. Kitashima, Y. Koizumi, T. Nakano, M. Watanabe, *Additive Manufacturing Letters* 3 (2022) 100066.
7. S. Pilz, T. Gustmann, F. Günther, M. Zimmermann, U. Kühn, A. Gebert, *Materials and Design* 216 (2022) 110516.
8. P. Ferro, R. Meneghello, G. Savio, F. Berto, *The International Journal of Advanced Manufacturing Technology* 110 (2020) 1911–1921.
9. L. Zeng, T.R. Bieler, *Materials Science and Engineering A* 392 (2005) 403–414.
10. E. Bertrand, P. Castany, T. Gloriant, *Scripta Materialia* 83 (2014) 41–44.

INVESTIGATION OF THE DWELL FATIGUE CRACK INITIATION MECHANISM IN A NEAR A TITANIUM ALLOY TI6321

Wenyuan Zhang [1], Jiangkun Fan [1, 2], Xiangyi Xue [1], Hongchao Kou [1], Jinshan Li [1]

1 State Key Laboratory of Solidification Processing, Northwestern Polytechnical University, Xi'an 710072, China.

2 National & Local Joint Engineering Research Center for Precision Thermoforming Technology of Advanced Metal Materials, Xi'an 710072, Chin.

The crack initiation mechanism of dwell fatigue has always been a key problem in rationalizing the dwell effect and is still not fully understood. In this work, stress-controlled low-cycle fatigue and dwell fatigue tests were performed on Ti-6Al-3Nb-2Zr-1Mo alloy with bimodal microstructure to reveal the microstructural characteristic and crack initiation mechanism. The study revealed that the faceted cracking occurred at (0001) basal plane with the maximum Schmid factor value, through a special cracking mode referred to as (0001) twist boundary cracking. The criterion of the parameter C demonstrated that grain combining a moderately high Schmid factor for basal slip and Burgers vector well-orientated out-of-surface plane, is the preferable site for (0001) twist boundary crack initiation. Based on this, phenomenological models were proposed to explain the (0001) twist boundary cracking mechanism from the perspective of surface extrusion-intrusion-induced micro-notches.

Keywords: Titanium alloy; Dwell fatigue; Fatigue crack initiation; Crystallographic orientation.

1. Introduction

Near α titanium alloys have been widely used in key equipment components such as aviation, aerospace, and navigation due to their high strength-weight ratio, corrosion resistance, and excellent high/low temperature mechanical properties and welding properties [1,2]. In the 1970s, dwell fatigue failure was first reported in an aviation accident with a fan disk made of the near α titanium alloy IMI685 for Rolls-Royce's RB211 engine [3]. This has drawn extensive attention to the dwell fatigue behavior of titanium alloys [4–6]. It turns out that taking a simplified triangle-wave or sine-wave load spectrum to design and predict material life under actual operating conditions has significant drawbacks, while trapezoidal wave fatigue that remains loaded for a period (dwell fatigue) of time at peak stress is comparable to actual flight/diving conditions closer (Takeoff-cruise-landing/dive-cruising-surfacing) [3]. Cold creep is common in near α titanium alloys [7–9], and a significant creep-fatigue interaction occurs during the dwell fatigue process [3,6]. Even under the same stress conditions, the obvious creep strain accumulation leads to a significantly lower holding fatigue life than conventional fatigue (dwell fatigue effect), which has seriously endangered the safety and reliability of titanium alloy components and equipment.

There is considerable evidence shows that dwell fatigue failure initiation is related to the occurrence of facet crack nucleation in α nodules, it was also evidence that the facet plane formed on the basal plane of hexagonal-closed-packed (HCP) structure with maximum misorientation less than 15° [6,10–12]. It is argued that a comprehensive understanding of the mechanism of facet cracking is the key to reveal the dwell effect [13]. However, due to the variation of chemical composition, dwell loading, and microstructure configuration. There has not reached a common sense of the mechanism of crack initiation, and systematic investigation combining the crack morphology and microscale deformation behaviors is needed.

In the current study, the crystallographic crack-initiation mechanism of fatigue and dwell fatigue of Ti-6Al-3Nb-2Zr-1Mo with a bimodal microstructure, a representative near α titanium alloy for marine engineering, is systematically studied. The dominating crack initiation mode as (0001) twist boundary cracking were thoroughly revealed using scanning electron microscope (SEM) and Electron-back-scattered-diffraction (EBSD). Phenomenological models were

proposed to describe the (0001) twist boundary cracking mechanism.

2. Titanium manufacturing titanium

Ti6321 alloy plates with bimodal microstructure were investigated in the present study, the chemical composition is illustrated in Table 1. The microstructure results from two passes of rolling and one pass of reversing rolling in the α+β phase field followed by annealing at 970 ℃ for one hour with air cooling (the β transition temperature is 985 ℃[14]). The microstructure is presented in Figure 1 which is composed of equiaxed primary α (α_p, size~15μm) and lamellar secondary α (α_s, thickness~2μm) within the transformed β matrix (β_t). Flat dog-bone-shaped specimens with a 2 mm gauge width and a 1.8 mm thickness were machined from the Ti6321 plate along the TD direction. Both faces were ground finished with 4000 grades SiC paper, a polishing step is then applied on one face using a 9 μm diamond suspension along with an additional electrolytic polishing step using a solution compounded of 60% methanol, 35% N-butanol, and 5% perchloric to remove the layer of imperfection and residual stress. The above processing was aimed to acquire a gauge section that is suitable for direct SEM/EBSD detection.

Dwell fatigue experiments were performed in tension-tension fatigue (R=0.1) under stress-controlled loading. Loading and unloading were achieved in 1 second. The minimum stress (σ_{min}) was held for 1 second. Tests were carried out with maximum stress (σ_{max}) values of the 95% of yield strength (YS), and the load holding period values were selected ranging from 1 s to 120 s.

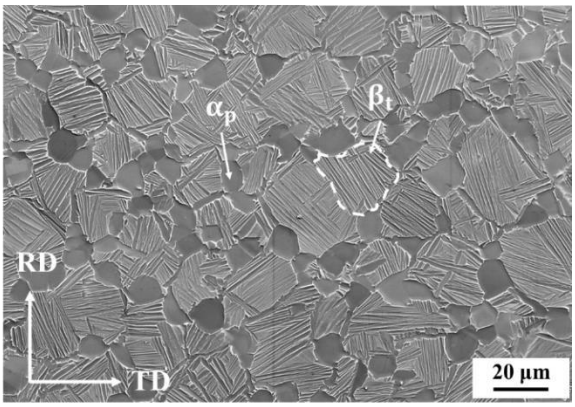

Figure 1. (a) SEM/SE image of microstructure of bimodal Ti6321 alloy

Table 1: Chemical composition of Ti6321 alloy.

Element	Ti	Al	Nb	Zr	Mo	Fe
Wt.%	Bal.	6.08	2.94	2.02	1.02	0.03

After dwell loading, the entire 2×2 mm gauge section of flat specimens was observed on SEM to locate the initiated cracks. The local crystallographic orientation nearby the crack was characterized using the same microscope with the EBSD detector. For certain crack sites, an atomic force microscope (AFM) was used to depict the morphology of the crack on the *z*-axis.

3. Results and discussion

3.1 Microstructural and crystallographic features of TB cracks

The loading conditions along with the corresponding results were illustrated in Table 2**.** These tests involved: specimens dwell loaded at 785MPa (0.95YS) for 1 s, 10 s, 30 s, and 120 s, and interrupted until fatigue life reached 1000 cycles. Gauge sections (2×2 mm) of these specimens in Table 2 were fully analyzed using SEM observation to find out all the surface cracks. A total of 52 cracks have been detected and four major crack-initiation modes were concluded. The (0001) twist boundary cracking was found as the predominant crack initiation mode, judging by the “number and proportion of (0001) cracks” in Table 2 which indicates the ratio of the number of cracks originating at (0001) twist boundaries (TB) to the total number of cracks. In addition, the number and proportion of (0001) TB cracks show no apparent relevance to the loading conditions, even at the same loading as dwell holding 30 s at 785 MPa, the numbers of (0001) TB cracks are significantly different between different them which reached maximum as 21 in DF30-1000-1.

Table 2. The dwell fatigue test conditions and the summary of the corresponding results.

Specimen tag	Dwell time/ s	Number and proportion of (0001) TB cracks
DF1-1000	1	6/7
785-DF10-1000	10	3/4
785-DF30-1000-1	30	21/23
785-DF30-1000-2	30	4/5
785-DF30-1000-3	30	4/6
785-DF120-1000	120	4/7

Figure 2(a-l) illustrates the SEM/SE micrographs, EBSD-derived IPF maps and KAM maps of typical (0001) TB cracks in DF1-1000, DF10-1000, DF30-1000-1, and DF120-1000 specimens, which shows that all cracks were located and initiated within α_p nodules, and propagated across the entire α_p phase until arrested at the grain boundaries. On the other hand, the (0001) plane trace of HCP structure in SEM/SE images is parallel to the cracks, along with the crystallographic orientation maps suggesting that crack initiation may occur at (0001) twist boundaries between two α_p nodules. The twist angle **ω** values (the misorientation angle around the *c*-axis between grains) of cracked TBs varied mostly from 10° to 30°, as illustrated in **Figure 3(a)**.

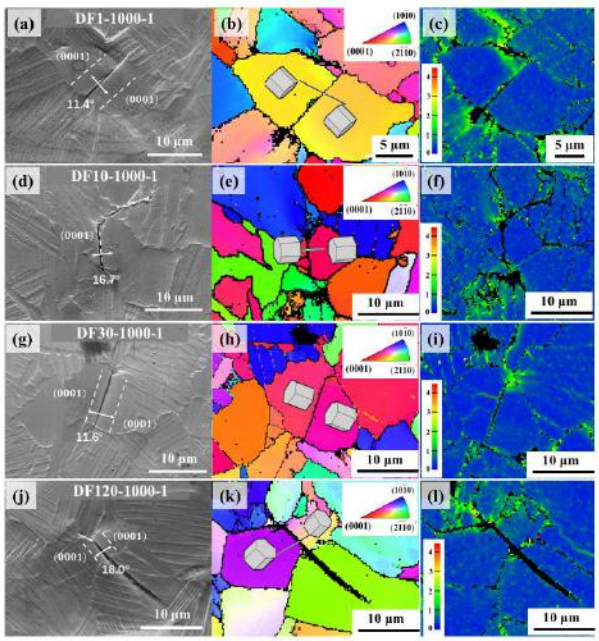

Figure 2. The SEM/SE micrographs and corresponding EBSD-derived IPF maps along the LD. The (0001) TB cracks in: (a) 785-DF1-1000; (b) 785-DF10-1000; (c) 785-DF30-1000-1; (d) 785-DF120-1000. Other types of twist boundary crack: (f) $(\bar{2}110)$ TB cracks in 785-DF1-1000; (g) $(0\bar{1}10)$ TB cracks in 785-DF30-1000-1.

Take Figure 2(a) as an example, crack was found at a (0001) TB with twist angles **ω** of 11.4° according to the EBSD-derived IPF map. Subsequently, the crack tips were arrested at the β_t regions leading to an obvious lattice distortion on the neighboring β_t as shown in Figure 2(c). Deformation patterns were also widely observed on both sides of the crack, the slip traces analysis indicates the existence of intense basal slip activities, which can be further confirmed by the crystallographic orientation distribution of twist grain pairs. As shown in Figure 3(b), it depicted the crystalline orientation of the TB cracked nodules which are annotated by different colors for different samples. Easy to find that most facets were oriented from 20° to 60°, which means they were favorably oriented for basal <a> slip in this crystallographic orientation domain. Such distribution indicated that most twist cracked grains were located on the domain with the SF value higher than 0.4. Hence, it seems the crack initiation can be easily associate with the basal slip activities.

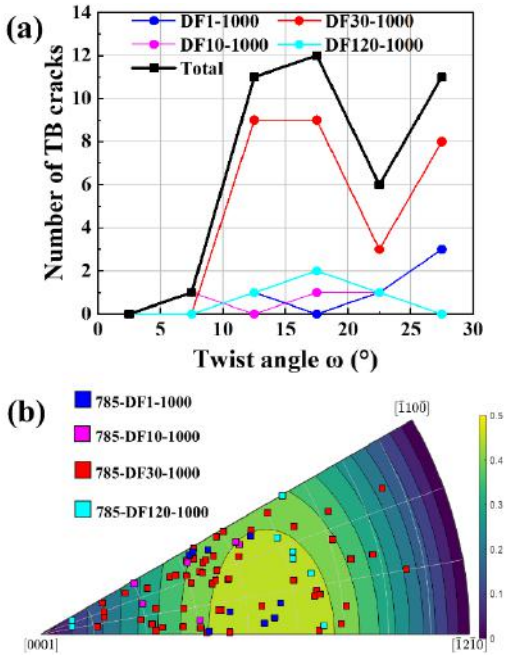

Figure 3. (a) A schematic illustration of twist boundary, the twist angle is annotated by ω. (c) Crystallographic orientation distribution with respect to the tensile axis of twist boundary cracked grains. The iso-

curves indicate the maximum Schmid factor iso-contour of the basal systems with the interval of 0.05.

3.2 Morphological features of TB cracks

Another important aspect to attention in the cross-sectional views in Figure 4(b)(d)(f) is the height difference between two sides of the crack, as annotated in red dash lines. AFM measurement was conducted to acquire the surface morphology across the crack region. Here, the surface height profiles along with the corresponding 3D views of two typical (0001) TB cracks were presented in Figure 4(c) and (g), interestingly, altitude differences were also evident between the two sides of TB cracks. The surface roughness was measured along 'AB' and 'CD' lines as plotted in Figure 4(d) and (h), an extrusion plane with the height of 80 nm and 100 nm was observed at those two TBs, also an intrusion with the height of near 20 nm was annotated in Figure 4(h), which suggests the slip extrusion and intrusion on the surface and formation of a step-like surface morphology might be necessary for the TB cracking.

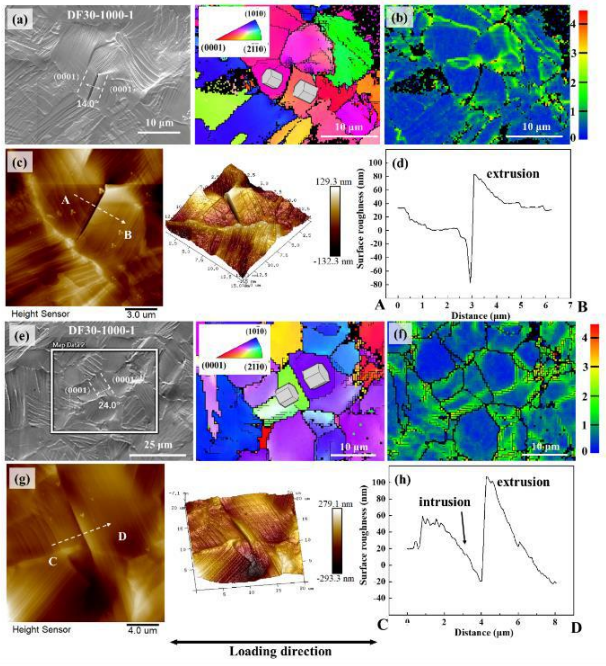

Figure 4. (a)(e) SEM/SE micrographs and EBSD-derived orientation maps (IPF//LD) at the TB crack region; (b)(f) the corresponding KAM value distribution maps; (c)(g) The 2D and 3D views of surface roughness maps obtained using AFM measurement; (d)(h) the surface roughness distribution along 'AB' and 'CD' directions.

On the other hand, the KAM maps in Figure 4(b) and (f) reveal relatively large local misorientation distributed at crack ends where the crack tip is arrested by adjacent grains. Such a strain localization was possibly due to the shear stress performed on (0001) TB due to basal slip activities [15]. Since the plastic deformation induced by tensile stress normal to the basal plane is absent, it can be speculated that shear stress along the basal plane is more related to crack-initiation.

3.3 Phenomenological models for twist boundary crack formation

The extrusions and intrusions formed at the specimen surface in PSBs were considered as the ideal fatigue crack initiation site [16–19], the above discussion also highlights the role of extrusion/intrusion as a prerequisite for (0001) TB crack initiation. Therefore, phenomenological models for extrusion/intrusion crack initiation among a pair of twist nodules were proposed in Figure 5. Normally, during cyclic loading, dislocations were generated at the specimen surface and move to the interior of the grain [16]. Take Figure 5 (a) as an example, supposing forward loading could cause a pile-up of dislocation with a positive sign on the right side of the extrusion slice, the reverse loading flow is expected to take up by the dislocation with a negative sign moving on the left side of the slice. In such a way, the accumulation of vacancy of interstitial dipoles was accumulated thus building up an extrusion (Figure 5(a)) or an intrusion (Figure 5(b)) [19]. Although in the present study, a load ratio R=0.1 was conducted, which means the reverse loading flow is absent, it is expected the back stress caused by dislocation pile-up is not entirely reversed, leaving irreversible dislocation dipoles which were also amplified with the number of stress cycles. Once the extrusion/intrusion was formed, a micro-notch morphology was built up (Figure 5(d)(h)), caused a stress concentration under the applied stress, and formed the crack embryo [19]. As the local normal stress is sufficient to overcome the cohesive strength of the material, the following growth of the crack embryo would easily occur along the flat TB boundary which poorly accommodated the accumulated strain resulting from crack opening, thus formed a sharp facet along basal plane. Among all the three cracking modes, the extrusion-intrusion cracking mode is expected to be the preferable and most common

crack initiation mode in (0001) TB cracking. Due to the different Burgers vector directions among the twist-grain pair, the angle between them was equal to the twist angle (the angle between the same slip directions), or equal to the angle between different activated basal slip system. This leads to extrusion/intrusion building up in different directions, consequently, positive shear stress and negative shear stress confront along the (0001) TB interface, greatly pushing forward the crack-initiation.

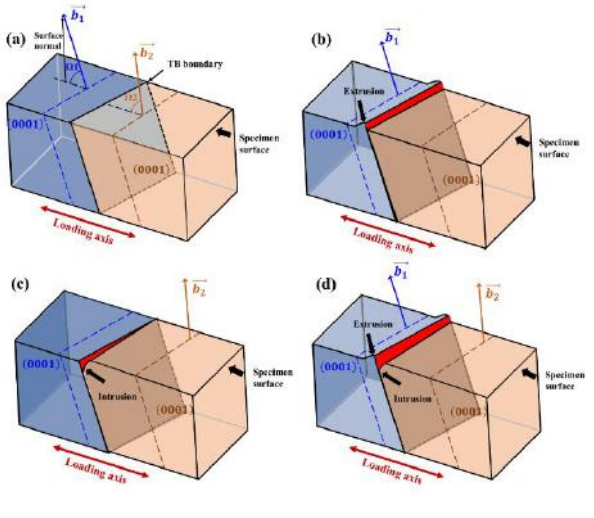

Figure 5. Schematics for phenomenological models for twist boundary crack initiation: (a) A schematic illustration of angle Ω, the angle between Burgers vector and specimen surface; (b) the crack formed at an extrusion site; (c) the crack formed at an intrusion site; (d) the crack formed at an extrusion-intrusion site;

4. Conclusions

In this work, the fatigue and dwell fatigue tests of Ti6321 alloy were performed at room temperature. Quantitative characterizations were performed to reveal the fatigue crack initiation mode. Phenomenological models were proposed to explain the mechanism of crack initiation. The following conclusions were drawn from this study:

(1) Among them, (0001) twist boundary cracking mode was considered as a common mode to initiate faceted cracks for both fatigue and dwell fatigue loading.

(2) The characteristics of (0001) twist boundary cracks were thoroughly investigated. Most of TB cracks were formed on α_p nodules with orientation angle ranging from 20~60°, and twist angle ranging from 10~30°.

(3) Phenomenological models were proposed, which indicated the formation of micro-notch morphology resulting from the effect of surface extrusion/intrusion is a prerequisite for (0001) twist boundary cracking.

5. Acknowledgment

The authors gratefully acknowledge the National Natural Science Foundation of China (Nos. 52074231 and 52001258) and the Chongqing Natural Science Foundation (No. cstc2020jcyj-msxmX1056) for the financial support to this work.

6. References

[1] S. Yan, G.-L. Song, Z. Li, H. Wang, D. Zheng, F. Cao, M. Horynova, M.S. Dargusch, L. Zhou, Journal of Materials Science & Technology 34 (2018) 421–435.

[2] D. Banerjee, J.C. Williams, Acta Materialia 61 (2013) 844–879.

[3] J. Qiu, Y. Ma, J. Lei, Y. Liu, A. Huang, D. Rugg, R. Yang, Metallurgical and Materials Transactions A 45 (2014) 6075–6087.

[4] R.W. Evans, R.J. Hull, B. Wilshire, Journal of Materials Processing Technology 56 (1996) 492–501.

[5] M.R. Bache, W.J. Evans, Journal of Engineering for Gas Turbines and Power 125 (2003) 241–245.

[6] M.R. Bache, M. Cope, H.M. Davies, W.J. Evans, G. Harrison, International Journal of Fatigue 19 (1997) 83–88.

[7] W. Shen, W.O. Soboyejo, A.B.O. Soboyejo, Mechanics of Materials 36 (2004) 117–140.

[8] K.U. Yazar, S. Mishra, A. Karmakar, A. Bhattacharjee, S. Suwas, Metall Mater Trans A 51 (2020) 5036–5042.

[9] J. Peng, C.-Y. Zhou, Q. Dai, X.-H. He, Materials & Design 71 (2015) 1–16.

[10] M. Bache, International Journal of Fatigue 25 (2003) 1079–1087.

[11] V. Sinha, M.J. Mills, J.C. Williams, Metallurgical and Materials Transactions A 37 (2006) 2015–2026.

[12] V. Sinha, M.J. Mills, J.C. Williams, J.E. Spowart,

Metallurgical and Materials Transactions A 37 (2006) 1507–1518.

[13] A.L. Pilchak, Scripta Materialia 68 (2013) 277–280.

[14] J. Fan, H. Huang, X. Xue, W. Zhang, Y. Wang, B. Zhang, B. Tang, R. Zhao, H. Kou, J. Li, Frontiers in Materials 7 (2020).

[15] S. Hémery, J.C. Stinville, F. Wang, M.A. Charpagne, M. Emigh, T.M. Pollock, V. Valle, Acta Materialia (2021).

[16] J. Man, K. Obrtlík, J. Polák, Philosophical Magazine 89 (2009) 1295–1336.

[17] J. Polák, J. Man, International Journal of Fatigue 91 (2016) 294–303.

[18] S. Sasaoka, J. Arakawa, H. Akebono, A. Sugeta, Y. Shirai, E. Nakayama, Y. Kimura, International Journal of Fatigue 117 (2018) 371–383.

[19] K. Tanaka, T. Mura, Journal of Applied Mechanics 48 (1981) 97–103.

THEORETICAL INVESTIGATION OF OXIDATION MECHANISM IN Ti AND ITS ALLOYS

Ryoji Sahara[1], Somesh Kr. Bhattacharya[1], Kanika Kohli[2], Prasenjit Ghosh[2], Kyosuke Ueda[3], and Takayuki Narushima[3]

1 1 National Institute for Materials Science (NIMS), Tsukuba 305-0047, Japan
2 Indian Institute of Science Education and Research, Pune 411008, India
3 Department of Materials Processing, Tohoku University, Sendai 980-8579, Japan

In the study, the mechanism of oxidation of Ti and its alloys are clarified using both of first principles calculations and machine learning. First, using first-principles calculations, we identified the mechanisms of the oxidation of α-Ti surfaces. In addition to the case of pure Ti case, the effect of alloying elements was also systematically analyzed. It is shown that the result of oxidation resistivity of alloys can be analyzed with their electronegativity. Next, we built a machine learning model to predict the parabolic rate constant, k_p, for high temperature oxidation of Ti alloys. Exploring the experimental studies on high-temperature oxidation of Ti alloys, the dataset for machine learning was built. It is shown that the model can predict k_p well.

Keywords: high temperature oxidation, parabolic rate constant, first principles calculations, machine learning, electronegativity.

1. Introduction

Titanium (Ti) and its alloys are used for high-temperature components of jet engines, implants and sports equipment because of their superior mechanical properties with being light weight [1]. Their high affinity for oxygen, particularly at elevated temperatures, severely limits their application above 650℃. Therefore, it is important to develop oxidation-resistant Ti alloys. There are many basic researches through experiments to understand the effect of alloys elements in Ti alloys. For example, the oxidative behavior of Si-containing Ti-6Al-4V alloys in air was studied by Maeda *et al*. [2], and the effect of different alloying elements on the tensile strength and oxidation properties of α- and near α-Ti alloys has been outlined by Kitashima *et al*. [3]. While, it is important to perform theoretical investigation of oxidation mechanism in Ti and its alloys. In the study, the mechanism of oxidation of Ti and its alloys are clarified using both of first principles calculations based on density functional theory (DFT) and machine learning models.

2. Calculation

2.1. First principles calculation

To identify the mechanisms of the oxidation of α-Ti surfaces, first-principles calculations were performed [4-7] using the Vienna Ab initio Simulation Package [8] and Quantum Espresso [9]. We constructed an asymmetric 11-layer Ti slab to represent the α-Ti(0001) surface as shown in Fig. 1. Typically, each layer is constructed by 4×4 atoms. The four bottom layers of the slab were kept fixed at the bulk distance while other atoms were allowed to relax. A sufficient vacuum region (16-20 Å) was introduced in the [0001] direction to avoid any spurious interaction. In addition to the case of pure Ti case, the effect of alloying elements was also systematically analyzed considering their electronegativity. In the study, we considered alloying with Zr, Hf, Nb, and Mo (d-block) as well as Al, Ga, Si, and Ge (p-block) elements, which are most widely studied alloying elements for Ti. The segregation of alloying elements was studied by substituting Ti with alloying elements. They were substituted at different layers to understand the preferred substitution sites.

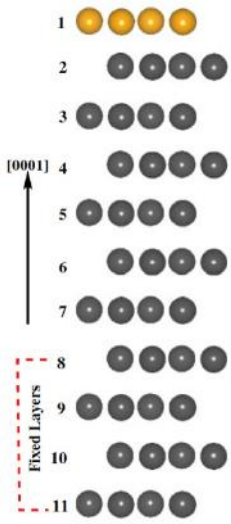

Figure 1. Side view of the α-Ti(0001) slab model [4-7].

To understand the stability of the adsorbed oxygen atom on the pure and alloyed Ti surface, the adsorption energies (E_{ads}) were estimated using the Eq. (1),

$$E_{\mathrm{ads}} = E_{\mathrm{O+surf}} - E_{\mathrm{surf}} - \frac{1}{2}E_{\mathrm{O_2}} \quad (1)$$

where $E_{\mathrm{O+surf}}$, E_{surf}, and E_{surf} are the total energies of the system containing the surface and the adsorbed species, the clean surface, and the O_2 molecule in the gas phase, respectively. To compute the minimum energy path and barriers for the diffusion of O atoms from the

surface to the subsurface layer, the climbing image based nudged elastic band (CI-NEB) method [10] was performed. Results were analyzed using the electronegativity difference between Ti and alloying element.

2.2. *Machine learning model*

We built a machine learning model to predict the parabolic rate constant, k_p , for high temperature oxidation of Ti alloys [11-12]. Here, k_p is defined by Eq. (2) in the unit of $g^2cm^{-4}s^{-1}$,

$$(\Delta M/A)^2 = k_p \times t \quad (2)$$

where $\Delta M/A$ is the mass gain per unit area during oxidation and t is the time during which the oxidation was performed. Exploring the experimental studies on high-temperature oxidation of Ti alloys, we built our dataset for machine learning. Apart from the alloy composition, we included the constituent phase of the alloy, temperature of oxidation, time for oxidation, oxygen and moisture content, remaining atmosphere, and mode of oxidation testing as the independent features, while k_p was predicted as the target feature.

3. Results and Discussion

3.1. *First principles calculation*

At first, by analyzing the segregation energy, it is found that all the alloying elements prefer to be present on the surface. Therefore, we constructed models where the alloying element is segregated at the surface. Then, Fig. 2 [7] shows the finally obtained relationship between diffusion barrier of oxygen atom from the surface to subsurface, E_{act} , and ΔEN, the electronegativity difference between Ti and the alloying element, at different oxygen coverages θ = 0.06, 0.50, and 1.00 ML (mono layer).

Figs. 2(a) and (b) show the case of d- and p-block elements, respectively. Generally, it is observed that E_{act} reduces when θ increases. The lowering of the barrier as a function of ΔEN is due to the stronger (weaker) binding of the surface O atom in the presence of alloying elements that are less (more) electronegative than Ti, which suggest a stronger driving force for the diffusion process. This means that the results suggest that doping Ti with a more electropositive element will be more effective to hinder the early oxidation. It is shown that the relationship almost reproduces the experimental observation of the alloying element dependence of mass increase due to oxidation [3].

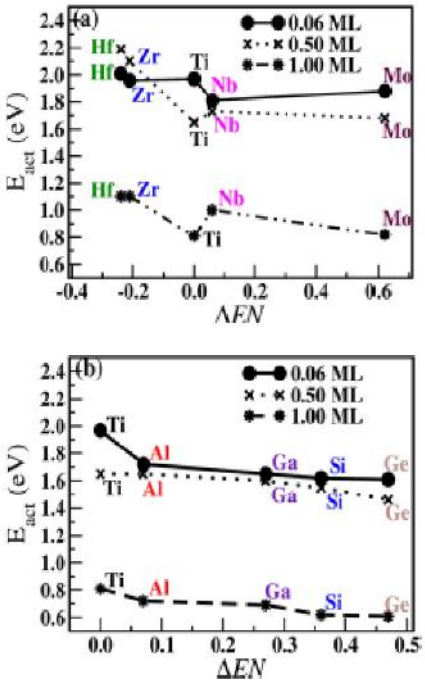

Figure 2. Relationship between diffusion barrier and ΔEN at different oxygen coverage. Plots for (a) d- and (b)p-block elements. [7].

3.2. *Machine learning model*

Fig. 3 shows the relationship between the experimental and predicted values of k_p in the case of Gradient Boosting (GB) model [11], where the coefficient of determination R^2 of 0.92.

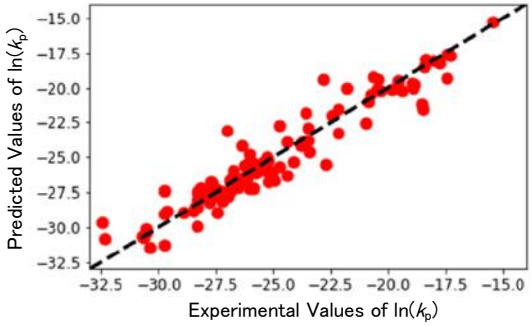

Figure 3. Relationship between the experimental and predicted values of k_p for the Gradient Boosting (GB) [11].

Fig. 4 and 5 show the Pearson's correlation coefficient (PCC), which measures the statistical relationship between two continuous variables and provide the information about the magnitude of the association. These Figs. indicate that alloying elements with a negative PCC such as Al, Zr, Si, Nb, and Ta increases the oxidation resistance while elements such as Fe, Cr, V show positive PCC showing that they have detrimental effect on the oxidation. It is shown that the predicted k_p values for some Ti alloys using the model

qualitatively agrees well with the corresponding experimental values [12].

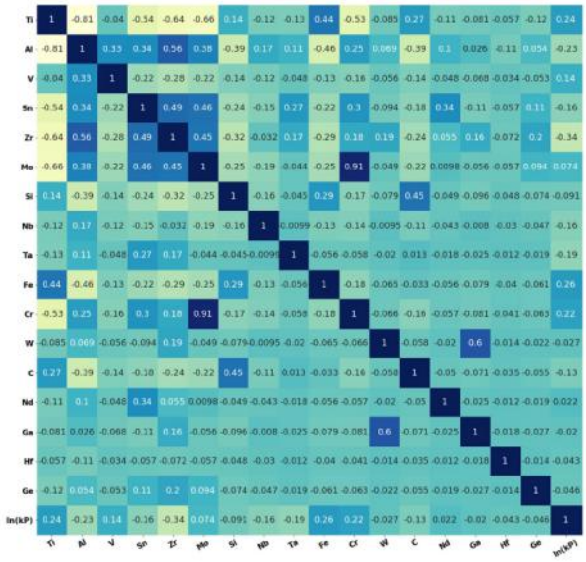

Figure 4. Graphical representation of the PCC between the alloying elements and ln(k_p) [11].

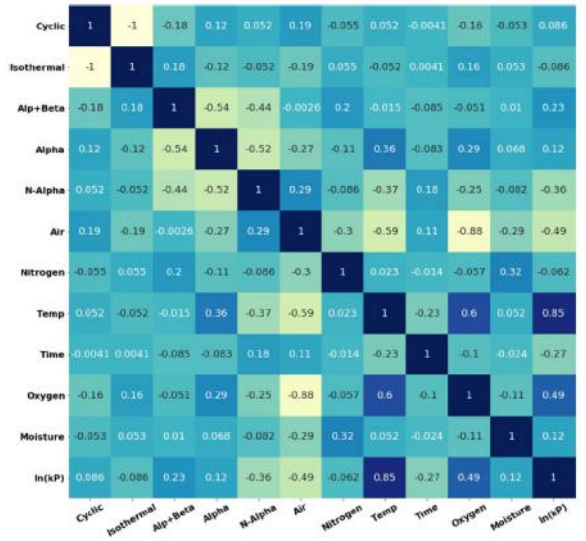

Figure 5. Graphical representation of the PCC between the different remaining features and ln(k_p) [11].

4. Summary

In the study, the mechanism of oxidation of Ti and its alloys are clarified using both of first principles calculations and machine learning model. The effect of alloying elements was systematically analyzed and showed that electronegativity can be used as a good indicator to oxidation resistance. Furthermore, it is shown that our machine learning model reproduces the experimental value well. The knowledge gained from the study can be used to design novel Ti alloys with excellent resistance towards high-temperature oxidation.

5. Acknowledgements

The calculations in the study were performed at the Numerical Materials Simulator at the National Institute for Materials Science (NIMS), the supercomputing system at the Institute for Materials Research (IMR), Tohoku University (Proposal No. 202012-SCKXX-0506), and the ITO system at Kyushu University under the HPCI system project (Project IDs: hp190014, hp190059, hp200040, hp210019, hp220017). The work was partially supported by the Japan Society for the promotion of Science KAKENHI grant (numbers 21H01607 and 21H04603).

6. References

1. M. M. Klinger, F. Rahemtulla, C. W. Prince, L. C. Lucas, and J. E. Lemons, Crit. Rev. Oral Biol. Med. 9, 449-463 (1998).
2. Kodai Maeda, Satoshi Suzuki, Kyosuke Ueda, Tomonori Kitashima, Somesh Kr. Bhattacharya, Ryoji Sahara, and Takayuki Narushima, *J. Alloys Compd*. 776 (2019) 519-528.
3. T. Kitashima, Y. Yamabe-Mtarai, S. Iwasaki, and S. Kuroda, *Proceedings of the 13th World Conference on Titanium*; The Minerals, Metals & Materials Society, (2016) 479−483.
4. Somesh Kr. Bhattacharya, Ryoji Sahara, Tomonori Kitashima, Kyosuke Ueda, and Takayuki Narushima, *Jpn. J. Appl. Phys*. 56 (2017) 125701.
5. Somesh Kr. Bhattacharya, Ryoji Sahara, Kyosuke Ueda, and Takayuki Narushima, *Sci. Tech. Adv. Mater.* 18 (2017) 998-1004.
6. Somesh Kr. Bhattacharya, Ryoji Sahara, Satoshi Suzuki, Kyosuke Ueda, and Takayuki Narushima, *Appl. Surf. Sci.* 463 (2019) 686-692.
7. Kanika Kohli, Somesh Kr. Bhattacharya, Kyosuke Ueda, Takayuki Narushima, Ryoji Sahara, and Prasenjit Ghosh, *Langmuir* 38 (2022) 1448-1457.
8. G. Kresse and J. Furthmüller, *Comput. Mater. Sci.* 6, (1996) 15-50.
9. P. Giannozzi *et al*., *J. Phys. Condens. Matter.* 21 (2009) 395502.
10. G. Henkelman and H. Jónsson, *J. Chem. Phys.* 111 (1999) 7010−7022.
11. Somesh Kr. Bhattacharya, Ryoji Sahara, and Takayuki Narushima, *Oxidation of Metals* 94 (2020) 205-218.
12. Takayuki Narushima, Satoshi Suzuki, Kyosuke Ueda, Somesh Kr. Bhattacharya, and Ryoji Sahara, *ISIJ International* 62 1512-1521.

DEVELOPMENT OF COLD-ROLLED STRIPS OF V-FREE α+β TITANIUM ALLOY TI–5AL–1FE

Tomonori KUNIEDA[1], Yoshiki KOIKE[1], Genki TSUKAMOTO[1] and Ryotaro MIYOSHI[1]

1 Nippon Steel Corporation, 20-1 Shintomi, Futtsu, Chiba, 293-8510, Japan.

Ti–5Al–1Fe (mass%) is an α+β-type titanium alloy developed as a low-cost alternative to Ti–6Al–4V extra low interstitial (ELI) alloy, in which the expensive β-stabilizing V is replaced with low-cost Fe. Ti–5Al–1Fe has high strength (equivalent to that of Ti–6Al–4V ELI), excellent hot-workability, and high a Young's modulus, making it suitable for use in applications such as golf clubs and connecting rods for automobiles. Notably, it also has excellent room-temperature workability because of its reduced Al content (5 mass% compared to 6 mass% for Ti–6Al–4V), enabling the fabrication of cold-rolled Ti–5Al–1Fe strip in production mills. Cold-rolled Ti–5Al–1Fe strip (0.4 mm thick) has an extremely fine and equiaxed grain structure, and its room-temperature tensile properties are equivalent to those of Ti–6Al–4V ELI. Its in-plane anisotropy is also significantly lower than that of hot-rolled strip. Cold-rolled Ti–5Al–1Fe strip exhibits better room-temperature bendability than Ti–6Al–4V sheet in both the longitudinal and transverse directions, with no surface cracks forming even at the testing limit (120°) during transverse bending. Additionally, no cracks form at the shoulder sections during deep drawing at room temperature. These results demonstrate the excellent room-temperature formability of cold-rolled Ti–5Al–1Fe strip. Furthermore, cold-rolled Ti–5Al–1Fe strip undergoes 200% elongation before fracture in high-temperature tensile tests (800 °C), with strain rate sensitivity (m values) of 0.3 or higher at a low strain rate, demonstrating its superplasticity. In conclusion, cold-rolled Ti–5Al–1Fe strip can be manufactured using production mills and has excellent formability at both room and elevated temperatures. Hot- and cold-rolled Ti–5Al–1Fe strip were registered as Aerospace Material Specifications (AMS) standards in 2022 (AMS4948 and AMS4947, respectively).

Keywords: Ti-5Al-1Fe, cold-rolled strip, α+β titanium alloy.

1. Introduction

High-strength α+β-type titanium alloys typically contain α-stabilizing elements such as Al and O and β-stabilizing elements such as V and Mo. A representative alloy is Ti–6Al–4V (mass%), which is widely used in aerospace applications [1]. However, the high cost of V, which is a β-stabilizing element, considerably increases the alloy cost. In addition, there are political and geographical concerns around the use of V because most V deposits are distributed in China, Russia, and South Africa. To overcome these challenges, various V-free alloys have been developed, in which V is replaced with a more readily available and inexpensive β-stabilizing element such as Fe [2]. One such alloy is Ti–5Al–1Fe, an α+β-type titanium alloy that was developed in the 1990s and features inexpensive Fe as a β-stabilizing element instead of expensive V and Mo. This alloy has high hardness and comparable strength to that of Ti–6Al–4V extra low interstitial (ELI) alloy at the standard O concentration of 0.15mass%. Moreover, by increasing the O concentration to 0.2mass% or higher, the strength of Ti–5Al–1Fe reaches that of ordinary Ti–6Al–4V [3–5]. In addition, Ti–5Al–1Fe has excellent hot workability and a high Young's modulus, and is currently mass-produced as round bar and hot-rolled strip for the fabrication of connecting rods and golf clubs [4,6,7].

In general, when an α+β-type titanium alloy is heated to the β-region and unidirectionally hot-rolled, it develops a transverse ("T") texture, in which the [0001] direction of the hexagonal close-packed structure is oriented in the sheet width (transverse (T)) direction. This texture leads to strong in-plane anisotropy, resulting in high strength, high Young's modulus, and low ductility in the T-direction. Ti–5Al–1Fe also develops a strong T-texture (Figure 1) in hot strip mills, where it is heated to the β-phase region and unidirectionally rolled. Hot-rolled Ti–5Al–1Fe has a particularly high Young's modulus in the T-direction, at approximately 140 GPa. This makes the alloy well-suited for use in golf clubs, and currently, several tens of tons of hot-rolled Ti–5Al–1Fe strip are produced annually [4,6,7].

In contrast, the production of cold-rolled strip from high-strength α+β-type titanium alloys is uncommon. Usually, such alloys are formed into thin sheets by sheet or pack rolling, in which several titanium

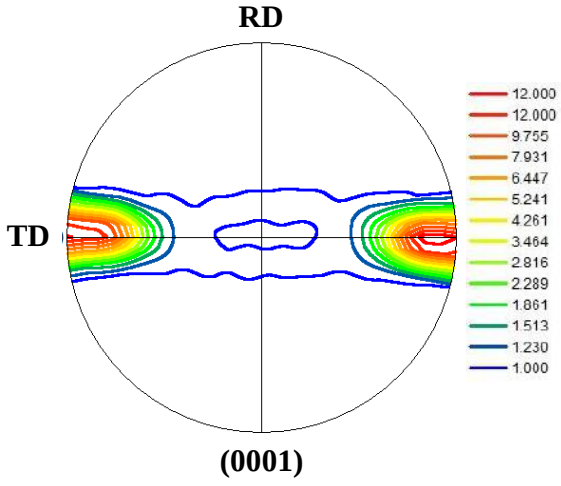

Figure 1 (0001) pole figure of hot-rolled Ti–5Al–1Fe strip manufactured at a production mill.

sheets are stacked and enclosed (packed) with steel and then hot-rolled at elevated temperature. However, this method is expensive and has low productivity. Owing to its lower Al content compared to that in Ti–6Al–4V, Ti–5Al–1Fe has excellent workability at both elevated and room temperatures [4–7], making it a promising candidate for cold-rolling. In this study, we investigate the production and properties of cold-rolled Ti–5Al–1Fe strip.

2. Results

2.1 Cold -rolled Ti–5Al–1Fe strip

Figure 2 shows the appearance of cold-rolled Ti–5Al–1Fe strip produced in an actual production mill [6, 7]. The Ti–5Al–1Fe alloy was successfully produced in the form of cold-rolled strip owing to its excellent cold-rolling workability.

Figure 2 Photographs of cold-rolled Ti–5Al–1Fe strip manufactured at a production mill [6, 7].

2.2 Microstructure

The microstructure of the mill-manufactured cold-rolled strip and laboratory-manufactured cold-rolled sheet with a thickness of 0.4 mm was investigated. Figure 3 shows inverse pole figure (IPF) maps in the normal direction (ND) and (0001) pole figures. In both cases, the grains were fine and equiaxed with sizes of about 3–5 μm [6]. While the texture was exclusively T-texture after hot-rolling, as shown in Figure 1, after cold-rolling and subsequent annealing, the T-texture of the mill-manufactured cold-rolled strip diminished, and a split-TD-texture emerged (Figure 3(a)). In addition, in the laboratory-manufactured cold-rolled sheet produced under optimized cold-rolling conditions, the T-texture almost completely disappeared and the split-TD-texture developed more strongly (Figure 3(b)).

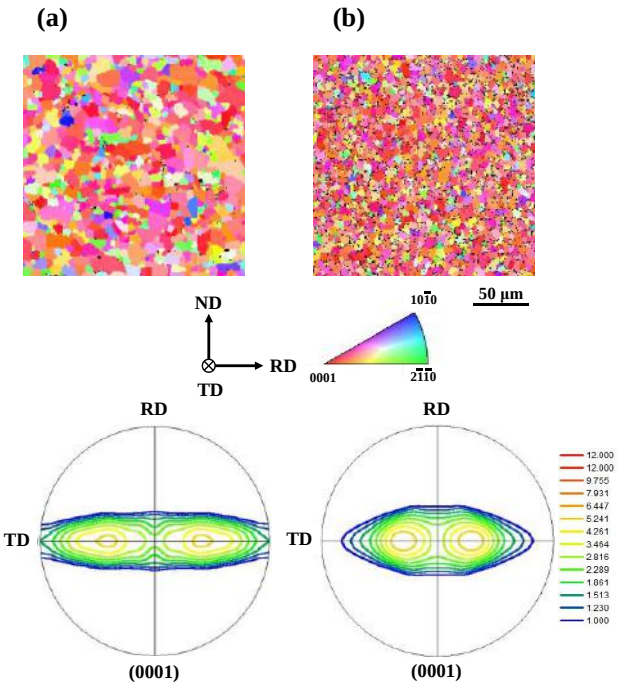

Figure 3 IPF maps in the normal direction (ND) (top) and (0001) pole figures (bottom) of (a) mill-manufactured cold-rolled Ti–5Al–1Fe strip and (b) laboratory-manufactured cold-rolled Ti–5Al–1Fe sheet.

2.3 Room-temperature properties

Table 1 lists the room-temperature mechanical properties of the hot-rolled strip, mill-manufactured cold-rolled strip, and laboratory-manufactured cold-rolled sheet. The ratio of 0.2% proof stress between the width and length directions (T/L ratio) was approximately 1.26 for the hot-rolled strip, indicating that it had high in-plane anisotropy. In contrast, the T/L ratio of the mill-manufactured cold-rolled strip was approximately 1.15, demonstrating that it had much lower in-plane anisotropy. The laboratory-manufactured cold-rolled sheet produced under the optimum cold-rolling conditions had even lower in-plane anisotropy with a T/L ratio of approximately 1.07.

The cold-rolling process led to a change in the texture of the Ti–5Al–1Fe alloy from T-texture (Figure 1) to split-TD-texture (Figure 3). Moreover, optimizing the cold-rolling conditions meant the T-texture disappeared almost entirely. This texture change to split-TD-texture is thought to have significantly reduced the in-plane anisotropy.

Next, the room-temperature formability was investigated. For aerospace applications, Ti–6Al–4V must withstand a bending angle of 105°, as specified in AMS4911. Notably, the cold-rolled Ti–5Al–1Fe strip had excellent room-temperature workability, with no cracking

Table 1 Room-temperature mechanical properties of hot- and cold-rolled Ti–5Al–1Fe strip.

	Thickness (mm)	Direction	0.2% proof stress (MPa)	Tensile strength (MPa)	Total elongation (%)
Hot-rolled strip	**3.7**	**Longitudinal**	**767**	**910**	**14.6**
		Transverse	**967**	**1038**	**14.8**
Mill-manufactured cold-rolled strip	**0.4**	**Longitudinal**	**770**	**929**	**14.7**
		Transverse	**885**	**935**	**14.9**
Laboratory-manufactured cold-rolled sheet	**0.4**	**Longitudinal**	**773**	**916**	**17.4**
		Transverse	**829**	**900**	**17.7**

observed after bending at 105°. Therefore, three-point bending and deep drawing tests were performed to further elucidate the room-temperature formability.

Figure 4 shows the maximum bending angles of the mill-manufactured cold-rolled strip and laboratory-manufactured cold-rolled sheet in the three-point bending tests [6]. The tests were conducted on test pieces with dimensions of 60 × 30 mm that were cut from the cold-rolled strip and sheet. The test pieces were pushed up to a maximum distance of approximately 10 mm using a punch with a radius of 0.4 mm, clearance of 2 mm, and pushing speed of 10 mm/min. The maximum bending angle was taken as the angle at which a crack formed on the surface during bending, or as 120° (i.e., the maximum bending angle used in the tests) if no cracks formed during the test. The mill-manufactured cold-rolled strip and laboratory-manufactured cold-rolled sheet both had maximum bending angles of about 100° in the longitudinal (L)-direction (with the long side of the specimen in the L-direction) and 120° (i.e., the test limit) in the T-direction (with the long side of the specimen in the T-direction). In comparison, a commercially available Ti–6Al–4V sheet had a maximum bending angle of 90°. This highlights the excellent bendability of the cold-rolled Ti–5Al–1Fe strip and sheet. The lower Al content of Ti–5Al–1Fe (5 mass%), as compared to that of Ti–6Al–4V (6 mass%), makes it easier to deform. Moreover, as shown in Figure 3, the cold-rolled Ti–5Al–1Fe strip and sheet both have a split-TD-texture, enabling them to be bent in the T-direction by activating only the basal slip system. These features resulted in the excellent bendability of the cold-rolled Ti–5Al–1Fe strip and sheet.

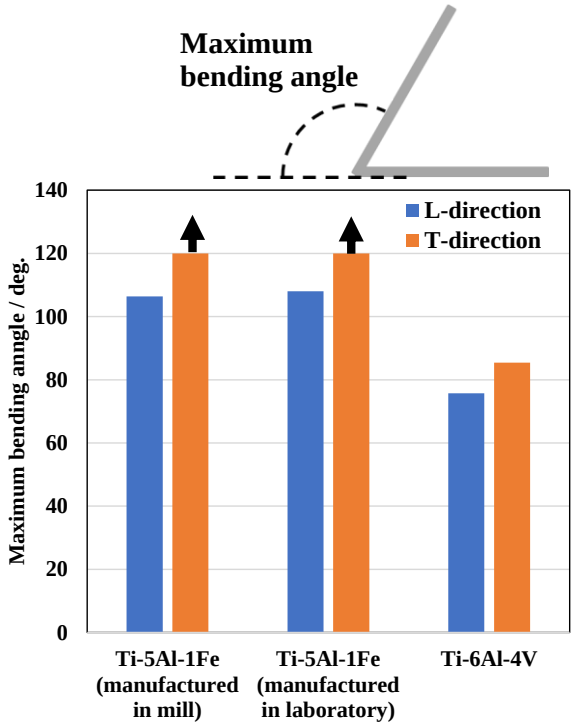

Figure 4 Maximum bending angles of 0.4 mm thick Ti–5Al–1Fe strip, Ti–5Al–1Fe sheet, and Ti–6Al–4V sheet in three-point bending tests [6].

The performance of the cold-rolled strip in the deep drawing test is shown in Figure 5 [6]. The test was performed at room temperature using a punch with a diameter of 40 mm, wrinkle suppression force of 2.8 tons, and sheet lubrication. Room-temperature deep drawing without shoulder cracks and similar defects was possible up to a specimen diameter of 80 mm.

2.4 High-temperature properties

High-temperature tensile tests were performed on 1 mm thick laboratory-prepared cold-rolled sheet. The manufacturing process was the same as that of the cold-rolled strip, except that the conditions were controlled to reduce the effects of atmospheric oxidation. Figure 6 shows the temperature dependence of the tensile properties from room temperature to 500 °C. Both the 0.2% proof stress and tensile strength linearly decreased with increasing temperature. Nevertheless, a high tensile strength of 600 MPa was achieved even at 400 °C. In addition, the difference in strength between the L- and T-directions decreased with increasing temperature, with

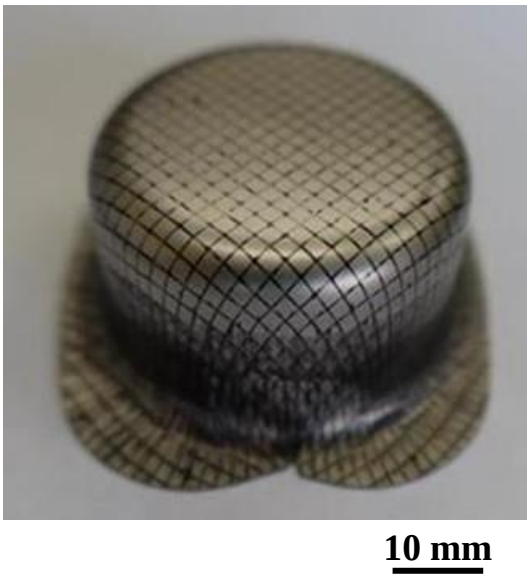

Figure 5 Deep-drawing test of 0.4 mm thick cold-rolled Ti–5Al–1Fe strip [6].

almost no difference between them at 400 °C. Although lower than that of Ti–6Al–4V, Ti–5Al–1Fe still has a relatively high Al content of 5 mass%; therefore, we considered that high strength can be maintained even at high temperatures. The elongation decreased slightly with increasing temperature up to 400 °C; however, the minimum elongation was nearly 15%, indicating that this alloy has high ductility.

We next investigated the superplasticity of the cold-rolled Ti–5Al–1Fe alloy. Titanium alloys such as Ti–6Al–4V exhibit superplasticity and elongation of several hundred percent under tension in the α+β two-phase region. A special test piece with a short parallel length (6 mm) was used so that the parallel portion of the test piece could fit in the soaking section of the tester. Figure 7 shows the appearance of the test pieces before and after high-temperature tensile tests at 800 and 900 °C at a strain rate of 10^{-3} s^{-1}. Table 2 shows the strain rate sensitivity (m values) at a strain of 0.2 during high-temperature tensile tests [6]. At a strain rate of 10^{-3} s^{-1}, a very large elongation of 400–600% was observed. Moreover, the m value was 0.3 or more at 800 °C or higher. Generally, the criteria for superplasticity are an elongation of 200% or more and an m value of 0.3 or higher; thus, the cold-rolled Ti–5Al–1Fe sheet exhibited superplasticity at 800-900 °C.

In general, Ti–6Al–4V exhibits superplasticity at about 900 °C, where the phase fractions of the α and β phases are almost equal, and at a low strain rate (10^{-4} s^{-1}) [8]. In contrast, the cold-rolled Ti–5Al–1Fe sheet in this study exhibited extremely large superplastic elongation

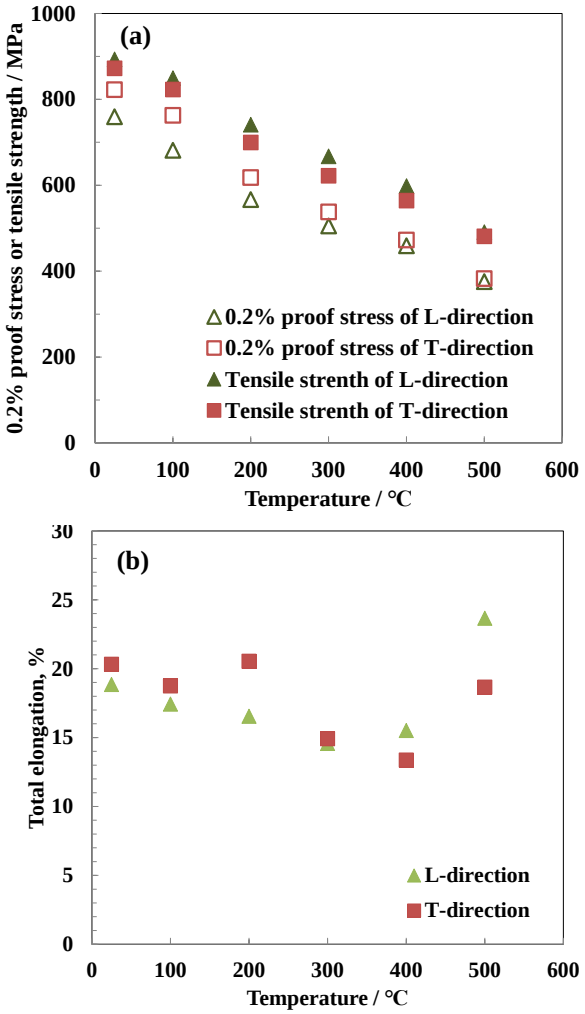

Figure 6 Temperature dependence of tensile properties of cold-rolled Ti–5Al–1Fe sheet: (a) 0.2% proof stress and tensile strength and (b) total elongation.

Figure 7 Specimens before and after high-temperature tensile test (Strain rate: 10^{-3} s^{-1}).

Table 2 *m* value of cold-rolled Ti–5Al–1Fe sheet at a strain of 0.2 [6].

Temperature (°C)	Strain rate	
	10^{-2} to 10^{-3} s^{-1}	10^{-3} to 10 s^{-1}
800	0.31	0.35
900	0.35	0.22

of several hundred percent even at a relatively low temperature of 800 °C and relatively high strain rate of 10^{-3} s^{-1}. Typically, the finer the grains, the more likely superplasticity is to occur [9]. In the cold-rolled Ti–5Al–1Fe sheet, the grain size after recrystallization was as small as 3–5 μm. Therefore, superplasticity occurred at the relatively low temperature of 800 °C. We concluded that cold-rolled Ti–5Al–1Fe sheet can be formed into complex shapes by processes that require superplasticity.

2.5 Aircraft standards

The hot-rolled Ti–5Al–1Fe strip is already mass-produced for consumer. However, this study revealed the potential of cold-rolled Ti–5Al–1Fe strip. These products were registered as Aerospace Material Specifications (AMS) standards in 2022 (hot-rolled strip: AMS4948, cold-rolled strip: AMS4947). Therefore, cold-rolled Ti–5Al–1Fe strip is expected to be used in aerospace applications in the future.

3. Conclusion

In this study, we investigated the production and characteristics of cold-rolled Ti–5Al–1Fe strip. The results are summarized as follows.

1) The mill-manufactured cold-rolled Ti–5Al–1Fe strip had a fine equiaxed grain structure and split-TD-texture that developed during the cold-rolling and subsequent annealing processes.

2) The in-plane anisotropy of the mill-manufactured cold-rolled Ti–5Al–1Fe strip was approximately 1.15, while that of laboratory-manufactured cold-rolled sheet (produced under the optimum conditions) was approximately 1.07.

3) The cold-rolled Ti–5Al–1Fe sheet had excellent room-temperature formability, including in bending and deep drawing.

4) The cold-rolled Ti‐5Al‐1Fe sheet exhibited superplasticity at 800‐900 ℃, making it suitable for the formation of complex shapes by processes that require superplasticity.

5) Hot-rolled Ti–5Al–1Fe strip (AMS4948) and cold-rolled Ti–5Al–1Fe strip (AMS4947) are both registered AMS standards (2022).

4. References

1. Inagaki, T. Takechi Y. Shirai and N. Ariyasu, *Nippon Steel & Sumitomo Metals Technical Report*. 396, (2013), 23-28.
2. H. Fujii and T. Maeda, *Nippon Steel & Sumitomo Metals Technical Report*, 396, (2013) 16-22.
3. H. Fujii and K. Takahasi, *Nippon Steel Technical Report*, 375, (2001), 100-103.
4. H. Fujii, Y. Yamashita, Y. Hatta and K. Matsuhashi, *Titanium*, 49, (2001), 171-176.
5. A. Kawakami and H. Fujii, *Nippon Steel & Sumitomo Metals Technical Report*, 396, (2013), 69-75.
6. T. Kunieda, Y. Koike and G. Tsukamoto, *Nippon Steel Technical Report*, 418, (2021), 38-42.
7. T. Kunieda and G. Tsukamoto, *The Japan Titanium Society 70th Anniversary Book*, (2023), 81-83.
8. N. E. Paton and C. H. Hamiltion.: *Metallurgical Transactions A*, 10A, (1979), 241-250.
9. T. Lee, D. S. Shih, Y. Lee and C. S. Lee, *Metals*, 5, (2015), 777-789.

EVALUATION OF THE ROLE OF MTR ON COLD DWELL FATIGUE IN TI-6AL-4V ALLOYS BY DIC MEASUREMENT

Shigeru Yasuda[1], Itsuki Kawata[2], Yuta Kitamura[1], Yoshihiro Otani[1], Kenta Kikuchi[2], Masayuki Tsukada[2], Shinya Miyazaki[1]

1 Technology & Intelligence Integration, IHI Co., Ltd, Yokohama, Japan
2 Aero engine space & Defense business area, IHI Co., Ltd, Tokyo, Japan

Ti-6Al-4V (Ti-64) alloys are widely used in aeroengine components. It is known that micro texture regions (MTRs) in titanium alloys causes a life degradation against cold dwell fatigue (CDF). In previous studies, the size of the MTR has been considered an important factor in life degradation. However, the orientation of the MTR and the direction of loading are also considered to be significant factors. In order to predict the degree of life degradation in the presence of such complex MTR parameter, it is desirable to define the criteria for CDF fracture and evaluate them by analytical methods such as crystal plasticity FEM (CPFEM). In this study, in-situ digital image correlation (DIC) measurements under dwell loading were performed to understand the effect of MTR on fracture and to define the criteria for CPFEM. To evaluate the effect of MTR, two types of Ti-64 specimens were prepared: "Low-MTR material" with a homogeneous crystallographic orientation distribution and " High-MTR material " that contains large MTRs. The fracture life of the High-MTR material was significantly lower than that of the Low-MTR material. In the strain distribution of the High-MTR material by DIC measurement showed strain concentration around the MTR, which was a hard MTR and not easily deformed in the loading direction. The facets that initiated failure were located near this strain concentration area. The results support that the orientation of the MTR with respect to the load axis is also important. In addition to elaborate experimental approach, we performed CPFEM, in which the crystal morphology of High-MTR material was reproduced. The analysis simulated the strain concentration around the hard MTR as in the DIC measurement. In addition, high c-axial stress was observed in the hard MTR. These experimental results and CPFEM help to construct the CDF life modelling.

Keywords: Ti-6Al-4V, Cold dwell fatigue, Micro texture regions, Crystal plasticity FEM, Digital image correlation measurements

1. Introduction

Titanium alloys are widely used in aeroengine components due to their lightweight advantages. However, Micro Texture Regions (MTRs), where the crystalline orientation is locally concentrated in a particular direction, occur during the forging process. There have been cases of in-service failures of forged Ti64 disc, and failure investigations [1] have shown the presence of MTRs at the crack initiation site. Therefore, there is concern about strength deterioration due to MTRs. Titanium alloys are also known to have a shorter fatigue life in dwell loading at peak stress than under normal cyclic loading [2], such as the loading pattern in aeroengines. This strength deterioration is due to the superposition of creep strain at room temperature, which accumulates during the dwell period, and fatigue. Therefore, load forms that include dwell period are referred to as cold dwell fatigue (CDF). The effect of MTRs on CDF has been studied because of its importance [3]. The effect of MTR for the CDF life is highly dependent on the grain distribution [4]. Therefore, Cristal Plasticity Finite Element Method (CPFEM) is expected to be utilised to predict the effect of MTRs on CDF by considering the slip system of each grain and analyses the stress and strain distributions. In this study, the deformation behaviour of MTRs and surrounding grains was experimentally obtained by Digital Image Correlation (DIC) measurement, and a CDF life prediction model was constructed by using of CPFEM.

2. CDF testing using in-situ DIC measurement

2.1. Test specimen

Ti-6Al-4V (Ti-64) material containing almost no MTR (here after referred to as Low-MTR material) and Ti-64 material containing a large amount of coarse MTRs (here after referred to as High-MTR material) were prepared. One specimen of each material was machined into flat specimen shapes with the dimensions shown in fig. 1. The results of electron beam backscatter diffraction (EBSD) observations for the evaluation area of each specimen are shown in fig. 2 and fig. 3. Fig. 2 shows the IPF in the ND direction and fig. 3 shows the map in the direction of the C-axis of the hcp. High-MTR material show the presence of coarse MTRs of several in the specimen with aligned C-axis directions. On the other hand, Low-MTR material are homogeneous.

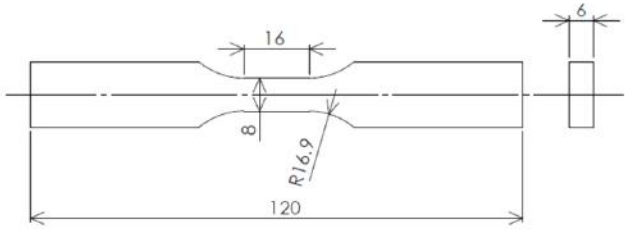

Figure 1. Shape of the test specimen (Unit: mm)

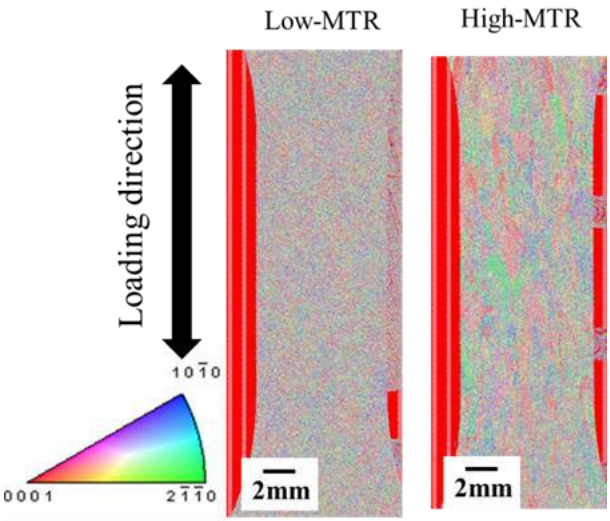

Figure 2. IPF map ND direction

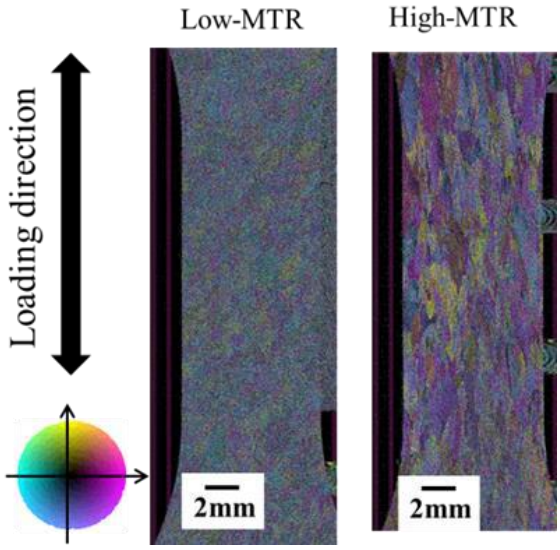

Figure 3. C-axis map of hcp

2.2. *DIC measurement methods and CDF test methods*

Random patterns consisting of fine dots were deployed to the surface of the specimen to perform DIC measurements. CDF tests were carried out using a hydraulic uniaxial fatigue testing machine and subjected to loading waveforms shown in fig.4. The maximum stress was set at 0.9 x 0.2% yield stress, with stress ratio of 0.01. The dwell time at maximum load was 120 s. In each cycle, images for DIC were captured during the dwell time.

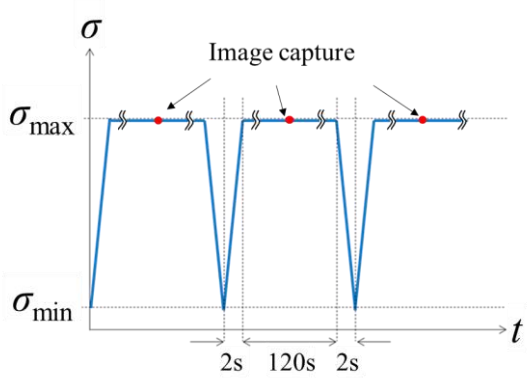

Figure 4. CDF test waveform

2.3. *Test results*

The fracture life was 21,889 cycles for the Low-MTR material and 1,042 cycles for the High-MTR material. Low-MTR material showed a life span 20 times longer than High-MTR material. Fig. 5 shows a fracture specimen of Low-MTR material and the positions measured by DIC. The result of the DIC analysis of strain was obtained at 21,800 cycles. The result for High-MTR material is shown in fig. 6. The strain distribution was obtained by DIC analysis at 1,040 cycles just before rupture. In High-MTR material, strain concentration occurred. The strain concentration occurs around a “hard MTR“ which is difficult to deform plastically because its lower Schmid factors on basal slip systems. In the High-MTR material, cracks initiated at the location of the strain concentration, as shown in fig. 7. The fracture surface was examined in scanning electron microscope (SEM) and facets were identified as crack initiation points. In the High-MTR material, the presence of coarse hard MTR is thought to cause strain concentrations around the hard MTR, resulting in fracture with facets and a shorter life than in the Low-MTR material.

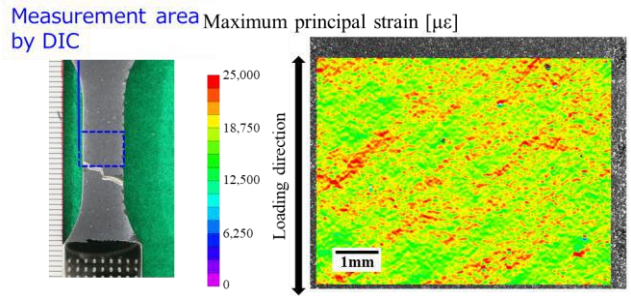

Figure 5. DIC analysis result of Low-MTR material

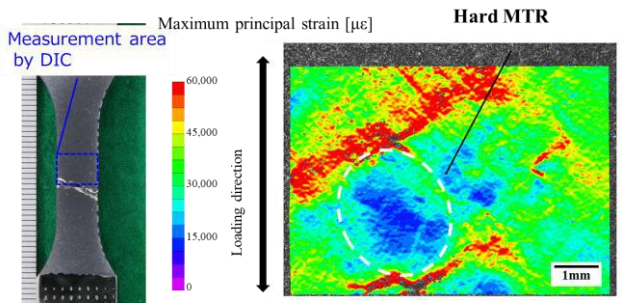

Figure 6. DIC analysis result of High-MTR material

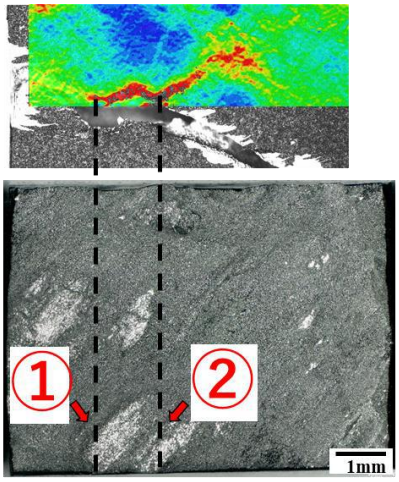

Figure 7. Fracture surface and crack initiation location of High-MTR material

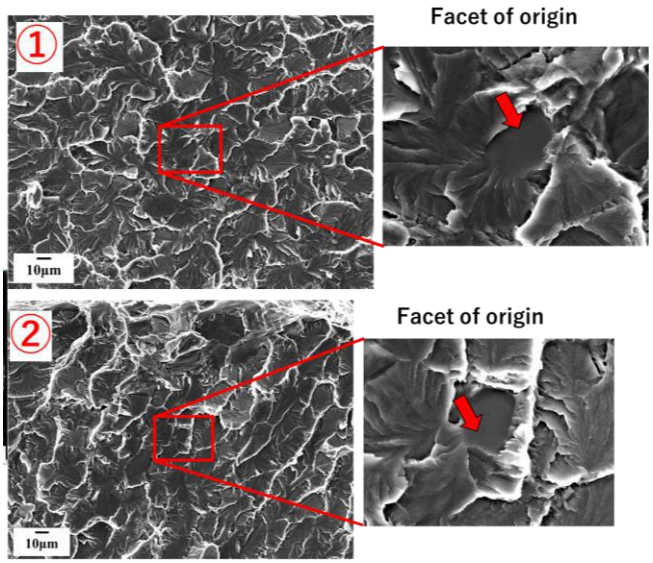

Figure 8. Images of crack initiation location by SEM

3. Life prediction by CPFEM

3.1. Crystal plasticity model

3.1.1. Constitutive equations

Ti-64 consists of α phase with HCP structure and β phase with BCC structure. Since the volume fraction of the β phase is small, only the α phase was modeled in this study. As a model expressing the relationship between the slip velocity $\dot{\gamma}^i$ and the resolved shear stress τ^i of the slip system i, the following viscoelastic constitutive equation proposed by Cuddihy [5] was used.

$$\dot{\gamma}^i = \begin{cases} 0, & |\tau^i| < \tau_c^i \\ \rho_{SSD}^m b^i v \exp\left(-\frac{\Delta F}{kT}\right) \sinh\left(\frac{(|\tau^i| - \tau_c^i)\Delta V^i}{kT}\right), & |\tau^i| \geq \tau_c^i \end{cases} \quad (1)$$

Where ρ_{SSD}^m is the density of mobile dislocations, b^i is the magnitude of the Burgers vector, v is the dislocation jump frequency, ΔF is the activation energy, k is the Boltzmann constant, T is the absolute temperature, and ΔV^i is the activation volume. τ_c^i is the critical resolved shear stress, which is described as follows using the initial critical resolved shear stress τ_0^i.

$$\tau_c^i = \tau_0^i + \chi^i \quad (2)$$

Here, the back stress χ is a function of the statistically stored dislocations density ρ_{SSD} and the geometrically necessary dislocations density ρ_{GND}. Also, ρ_{GND} was calculated from the strain gradient.

3.1.2. Calibration

Material constants of the crystal plasticity constitutive equations were determined from the results of a set of tensile tests in several strain rates. Two types of Ti-64 forged materials were used in the tensile tests; Low-MTR and High-MTR material. Polycrystalline grains were modeled by voxel mesh. Grain sizes of the Low-MTR and High-MTR materials were obtained by EBSD, and the average grain size of each was reflected in the analysis model. In addition, the crystal orientations were given based on the orientation distributions obtained by EBSD.

Fig. 9 shows the stress-strain curve obtained by the tensile tests and CPFEM analyses. In the analyses, although transition from the elastic region to the plastic region occurred more gently than in the tests, the stress-strain curve after yielding could be accurately reproduced, including the grain size dependency and strain rate dependency of the curve. The slowly yielding behaviour in the analysis was due to the sequential activation of slip systems of many grains with various orientations at different times. Since the stress-strain curve after yielding is extremely important for reproducing room temperature creep behaviour, which has a large effect on CDF with load holding, this crystal plasticity model was adopted in this paper.

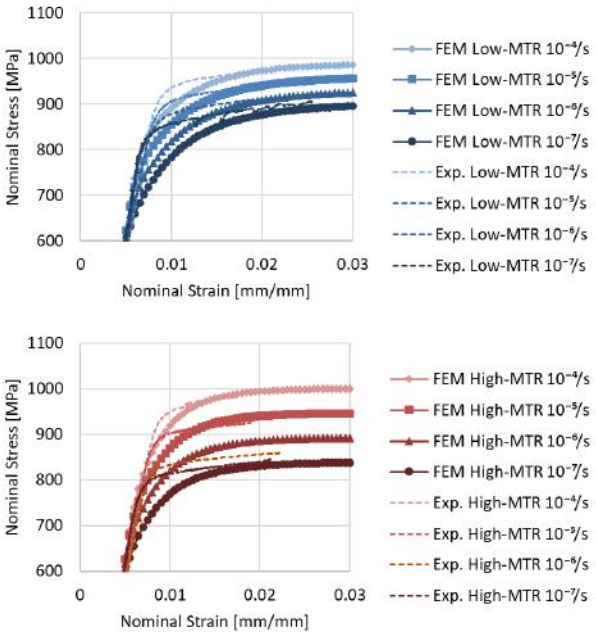

Figure 9. Stress-strain curve obtained by the tensile tests and CPFEM. (Top: Low-MTR／Bottom: High-MTR)

3.1.3. Validation

Analyses that reproduce room temperature creep tests of the Low-MTR and High-MTR materials were performed and compared with test results. Fig. 10 shows the relationship between load holding time and strain. It was found that the trend of room temperature creep behaviour can be reproduced by using the crystal plasticity model that qualitatively predict the stress-strain curve.

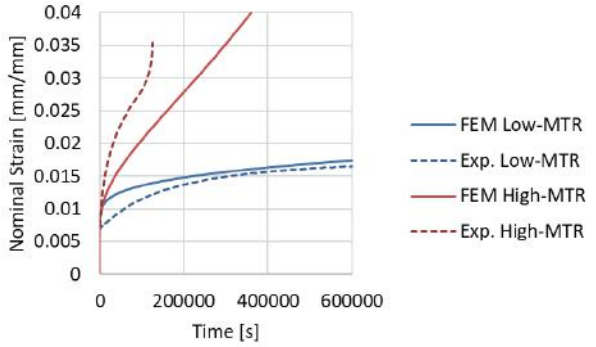

Figure 10. Results of room temperature creep tests and CPFEM.

3.2. CDF life prediction

3.2.1. CDF fracture criteria

Fracture criteria in CDF were investigated using CPFEM and in-situ DIC. In the analysis model, the grain shape and crystal orientation were reproduced using the EBSD measurement results of the observed area in in-situ DIC, including hard MTR. Fig. 11 shows the maximum principal strain distribution in the analysis at the time when macroscopic deformation equivalent to that at fracture occurred in the test. Comparing Fig. 11 to Fig. 6, it was found that the principal strain was smaller in the hard MTR both in the analysis and test. This is attributed to the fact that the Schmid factor of $\{0001\}\langle 11\bar{2}0\rangle$, which is the easiest active slip system in the Ti-64 α phase, becomes smaller in hard MTR. Fig. 12 shows the distribution of normal stress in c-axis direction. High c-axis stress was generated in hard MTR. In addition, it was clarified that stress redistribution occurred due to the plastic strain increase in the grains around the hard MTR during load holding, and the c-axis stress in the hard MTR was increased, which was difficult to deform plastically. Considering the above-mentioned fracture surface observation results of the specimens, the normal stress in c-axis direction was considered to be a factor which greatly affected the CDF fracture. Therefore, magnitude of the normal stress in c-axis direction obtained by CPFEM was adopted as the CDF fracture criterion.

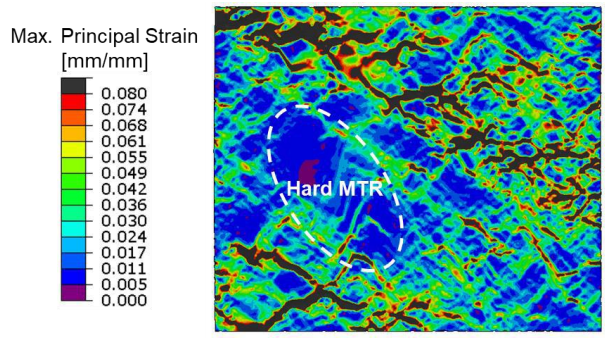

Figure 11. Distribution of maximum principal strain obtained by CPFEM.

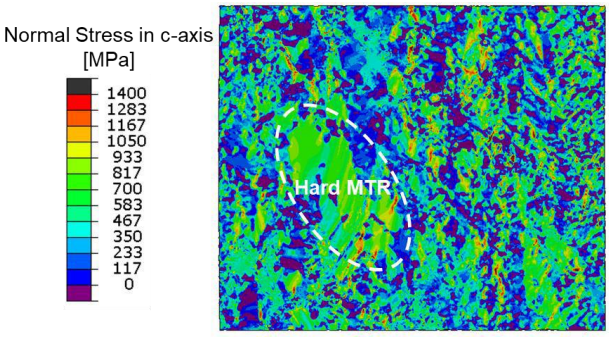

Figure 12. Distribution of normal stress in c-axis obtained by CPFEM.

3.2.2. CDF life prediction results

CDF tests were performed, and the CDF life was predicted by CPFEM using the fracture criteria described above. In the CDF tests, five types of Ti-64 forged materials, Low-MTR-A and -B, Middle-MTR and High-MTR-A and -B, were used. Each material was also tested with multiple holding loads. In the analyses, voxel meshes with 1000 grains were used as the polycrystalline models.

The average grain size and crystal orientation of the models reflected the EBSD measurement results.

Fig. 13 compares the CDF life obtained by the tests and the predicted results by CPFEM. From this figure, it was found that the magnitude relationship of the CDF life of each material could be qualitatively predicted. The prediction accuracy was approximately factor of 10. In the future, improving the quantitative accuracy will be an issue.

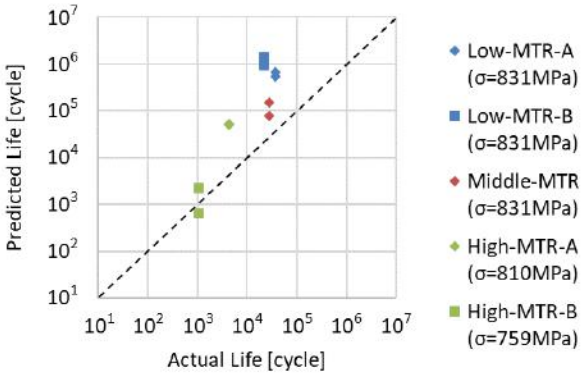

Figure 13. CDF life prediction results.

4. Conclusions

In this study, the effect of MTRs on CDF was experimentally confirmed, and the CDF life modelling was constructed by CPFEM. The following conclusions are presented.

1. Ti-64 materials containing a large amount of coarse MTRs significantly reduced the life of the CDF. The DIC observations suggest that the concentration of strain around the hard MTR has resulted in a reduced lifetime.

2. A method for predicting the CDF life by CPFEM were investigated. It was shown that life can be predicted with a certain degree of accuracy by using the normal stress in c-axis that increases while load holding.

5. References

1. Investigation report, BEA2017-0568, September 2020.
2. M.R. Bache, *International Journal of Fatigue* 25 (2003) 1079–1087.
3. V. Venkatesh, R. Noraas, A. Pilchak, S. Tamirisa, K. Calvert, A. Salem, T. Broderick, M.G. Glavicic, I. Dempster, V. Saraf, *MATEC Web of Conferences* 321 (2020) 11091.
4. J. Li, H.M. Davies, K. Fox, M. Mulyadi, M.G. Glavicic, M.R. Bache, *International Journal of Fatigue* 171 (2023) 107589
5. M.A. Cuddihy, A. Stapleton, S. Williams, F.P.E. Dunne, *International Journal of Fatigue* 97 (2017) 177–189.

INFLUENCE OF CHEMICAL COMPOSITION AND FORGING PROCESS ON MECHANICAL PROPERTIES AND MICROSTRUTURE OF TA15 ALLOY

Jinfeng Shu[1], Enen Xu[1]

1 Western Superconducting Technologies Co., Ltd., Xi'an 710018, China.

The forging process and chemical composition are important aspects that determine the organization and properties of titanium alloys. In this paper, the effects of forging process, forging equipment and chemical composition on the microstructure and mechanical properties on TA15 alloy were studied. The results show that increasing the forging heating temperature, the content of the primary α phase is reduced and the secondary α phase is lamellar. Meanwhile, the endurance performance is significantly improved. For 80mm diameter bars, rolling results in a flatter, less-thick secondary alpha phase， and the endurance performance is increased by 80h compared to radial forging. The content of Si element has little effect on the microstructure. The endurance performance shows a clear trend of improvement with the increase of Si content. However, the addition of more silicon elements leads to a reduction in impact toughness of about 24 J/cm^2.

Keywords: TA15 alloy, Forging Process, Chemical composition, Microstructure, Mechanical properties.

1. Introduction

Titanium alloys have been widely used in various military fields due to their high-temperature strength, fatigue performance, corrosion resistance and oxidation resistance[1]. Among them, the TA15 titanium alloy is similar to an α titanium alloy. Its nominal composition is Ti-6Al-2Zr-1Mo-1V. TA15 titanium alloy has medium room temperature strength, excellent high temperature properties and welding performance[2-4]. It has, therefore, been widely used in the manufacturing of aeroengine load-carrying constructions.

The chemical composition and microstructure of titanium alloys have a significant impact on mechanical properties[5-8]. Barboza M.J.R.[9] studied the creep behavior of Ti–6Al–4V is investigated at 500℃and 600℃ under constant load. The correlation between the values of activation energy and stress exponents indicates that the primary creep, as well as the steady-state creep, was controlled by dislocation climb in the hexagonal phase. The increase in tertiary creep rate was related to the necking development and to nucleation and coalescence of microvoids. Sahoo, R.[10] investigated systematically the effects of microstructure types and microstructural parameters on creep properties through an analysis of microstructure and properties of Ti-6Al-4V alloys The results indicated that the creep properties of the Ti-6Al-4V alloy are strongly dependent on microstructure type. Creep resistance of Ti-6Al-4V alloys is better in lamellar microstructure followed by bimodal and equiaxed microstructure respectively.

The influence of chemical elements on the microstructure and properties of titanium alloys has also been widely studied. The evolution of intergranular lattice strain in the α titanium alloy Ti–7Al wt% was characterised using in situ time-of-flight (TOF) neutron diffraction during room temperature tensile loading. Samples were aged to promote ordering and the formation of nanometre-scale α2 (Ti3Al). On ageing, at 550 °C and 625 °C, dislocations were observed to travel in pairs, which is beneficial for the strengthening of the alloy[11]。 The effect of Mo on microstructure and mechanical properties of high temperature titanium alloy at 650℃ was studied. The results show that Mo can refine the microstructure of the alloy, and can significantly increase the room temperature strength of the material. However but it has no significant effect on the elevated temperature strength and ductility at 650℃ [12]. There were finer dimple structures on the tensile rupture fracture surface of the alloy with high element V than the alloy with low element V under the high temperature conditions[13]. In addition， It is found The increase of Zr content will result in silicide coarsening, silicide volume fraction increasing and precipitation position changing[14]. The influence of Si content on the mechanical properties of Ti-6Al-2Zr-1Mo-1V titanium alloy at room temperature and 500 °C also was studied. the tensile strength and high-temperature strengthening performance are improved when 0.04 wt%~0.14 wt% Si is added to the Ti-6Al-2Zr-1Mo-1V alloy; the plasticity is less changed; the impact toughness and plane strain fracture toughness are decreased[15].

However, there is a lack of the impact of the composition of Si and corresponding processing parameters on the mechanical properties of TA15 alloy. Here in this work, the influence of the TA15 alloys with different Si composition processed with diverse forging temperatures on the tensile properties, impact energy, endurance properties, were comprehensively studies. The microstructures were revealed by using OM, SEM.

2. Experimental procedure

In this study, the TA15 alloy 80mm and 300mm diameter bar prepared by Western Superconducting Technology Co., Ltd were used. The bars were prepared by deformation of the ingot through a single phase zone and a two phase zone.

The corresponding forging processes and chemical compositions of the two bars are shown in Tables 1 and 2. Only the forging equipment and forging heating temperature are changed to compare the impacts of various forging equipment and temperature on the microstructure and properties of the bars with diameters of 80mm from I to III in Table 1. Table 2 compares the microstructure and mechanical properties of bars with varying Si content, with Si content steadily increasing from 1# to 4# 300mm diameter bars. The remainder of the chemical composition are essentially the same. In addition, the chemical composition of 5# bar is basically the same as 2# bar, only the forging heating temperature is 10°C lower, comparing the changes in the organization and properties of bars with different forging processes.

A section of 80 mm long specimen was intercepted from the 80 mm diameter bar, held at 840°C for 2 h and then air-cooled, and then 14×14×72mm and 11×11×60mm blanks were taken at R/2. The blanks were machined into room temperature tensile, enduring and impact specimens. Blanks of size 14×14×72mm and 11×11×60mm were taken from the R/2 position of the 300mm diameter bar, held at 850°C for 2h and then air cooled. The heat-treated blanks were processed into room temperature tensile, endurance and impact specimens. Observe the change pattern of mechanical properties through mechanical property testing. At the same time, the metallographic specimen of 10×10×12mm were intercepted on the R-state bar, and the microstructure morphology were observed by OM and SEM.

Table 1: Chemical composition (wt.%) and forging process of TA15 alloy 80mm diameter bars

Bar No.	Ti	Al	Mo	V	Zr	Si	Fe	C	Forging equipment	Heating temperature
I	Bal.	6.76	1.80	2.31	2.29	0.01	0.03	0.006	Radial forging	T_β-50°C
II	Bal.	6.78	1.78	2.32	2.32	0.01	0.02	0.009	Radial forging	T_β-40°C
III	Bal.	6.76	1.79	2.30	2.30	0.012	0.03	0.007	Rolling	T_β-50°C

Table 2: Chemical composition (wt.%) and forging process of TA15 alloy 300mm diameter bars

Bar No.	Ti	Al	Mo	V	Zr	Si	Fe	C	Heating temperature
1#	Bal.	6.75	1.80	2.30	2.27	0.01%	0.029	0.005	T_β-30°C
2#	Bal.	6.78	1.81	2.32	2.30	0.03%	0.025	0.005	T_β-30°C
3#	Bal.	6.80	1.83	2.31	2.27	0.05%	0.028	0.005	T_β-30°C
4#	Bal.	6.81	1.78	2.28	2.29	0.08%	0.030	0.006	T_β-30°C
5#	Bal.	6.79	1.83	2.28	2.31	0.03%	0.023	0.006	T_β-40°C

3. Results and discussion

3.1. Effect of forging process on microstructure and properties

3.1.1. Effect of forging process on microstructure and properties of 80mm diameter bars

Figure 1 shows the microstructure and endurance fracture of 80mm diameter bar prepared at different radial forging heating temperatures. It can be seen from Figure 1 that most of the secondary α phases are in a fine equiaxed shape when the radial heating temperature is Tβ-50°C, as shown in Figure 1(a) and (b). However, when the radial heating temperature is Tβ-40°C, the secondary α-phase is distributed in a lamellar shape, as shown in Figure 1(e) and (f). Besides that, it can also be found that the higher the heating temperature of radial forging, the less the content of primary α phase. The bars prepared at the two heating temperatures were tested for endurance performance. The forging heating temperature was 10°C higher and the endurance time was higher (about 26h

higher). This means that the higher the forging heating temperature, the better the endurance performance. The main reason is that the dislocation slip deformation first starts in the primary α-phase, being fixed in the α/β-phase interface, and the α/β-phase interface dislocation enters the adjacent primary α-phase by climbing. When the secondary α phase is lamellar, it can effectively increase the dislocation slip resistance and improve the high-temperature endurance performance[5]. From Figure 1(c) and (g), it can be seen that the endurance fracture is mainly divided into two regions, namely the dimple area and the shear area. There are a large number of fine t dimple in the dimple area, and the shear area is relatively smooth. Meanwhile, the dimple area of fracture with poor endurance performance is smaller, and the dimple is relatively large and shallow (as shown in Figure1(c) and (d)). However, fractures with relatively good endurance properties have a larger dimple area, and the dimple is small and deep.

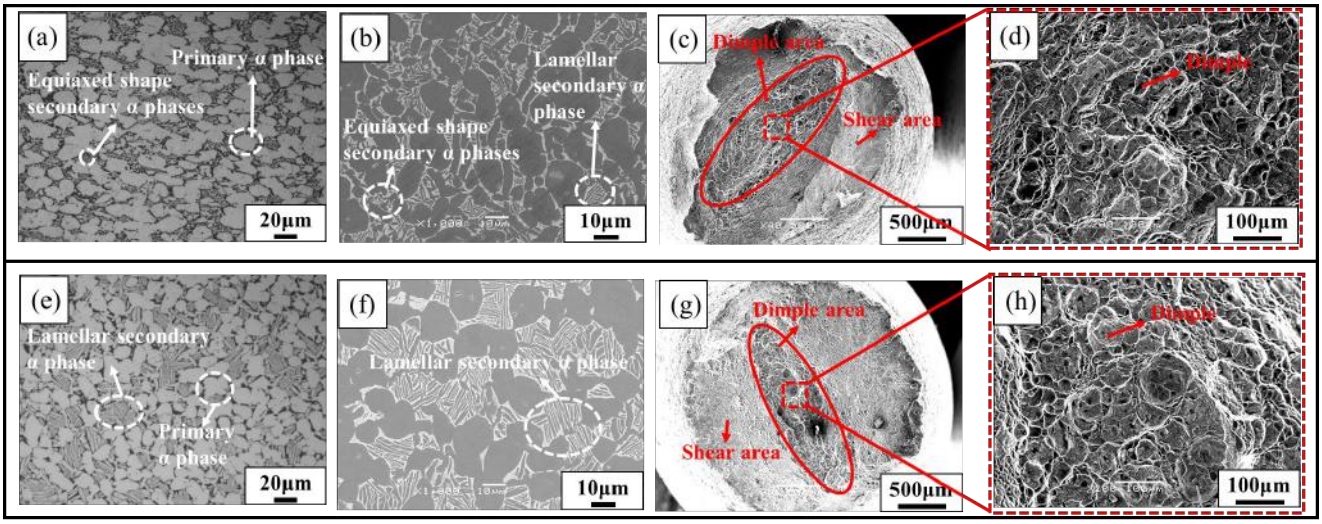

Figure 1. (a), (b) and (c), (d) are the microstructures and endurance fractures of radial forging at Tβ-50°C, and (e), (f) and (g), (h) are the microstructures and persistent fractures of radial forging at Tβ-40°C.

Figure 2 and 3 show the microstructure of 80 mm diameter bars prepared by different forging equipment. From Figure 2, the degree of primary α equiaxialization of the bars prepared by radial forging and rolling is close, and the content of primary α phase is also comparable. However, the bars prepared by rolling have a flatter secondary α-phase of the lamellae and a smaller lamellae thickness. This is mainly due to the greater deformation of rolling compared to radial forging, which increases the deformation storage energy as well as the number of crystal defects such as dislocations, resulting in more nucleation locations. And the formation of lamellar α phase within the residual β phase maintains a Bergs-site relationship with the β phase. Due to the limitation of this relationship, it is difficult to further coarsen the lamellar α phase after it is formed, resulting in a smaller lamellar thickness of the secondary α phase of the rolling bar[16].

Figure 3 shows the mechanical properties of the 80 mm diameter bars prepared by different forging equipment. From figure3, the room temperature tensile strength of the 80 mm diameter bars prepared by rolling is about 10-20 MPa lower, and the impact toughness is about 10 J/cm^2 higher. Meanwhile, the endurance time is about 80h longer and the elongation (denoted as A) and reduction of area (denoted as Z) are close. Compared to radial forging, the endurance performance of the 80mm diameter bars prepared by rolling was significantly improved.

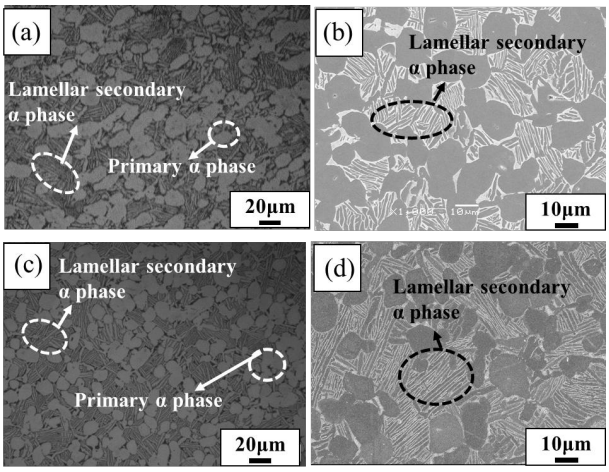

Figure 2. The microstructure of the 80 mm diameter bars prepared by different forging equipment: (a)(b) radial forging, (c)(d) Rolling.

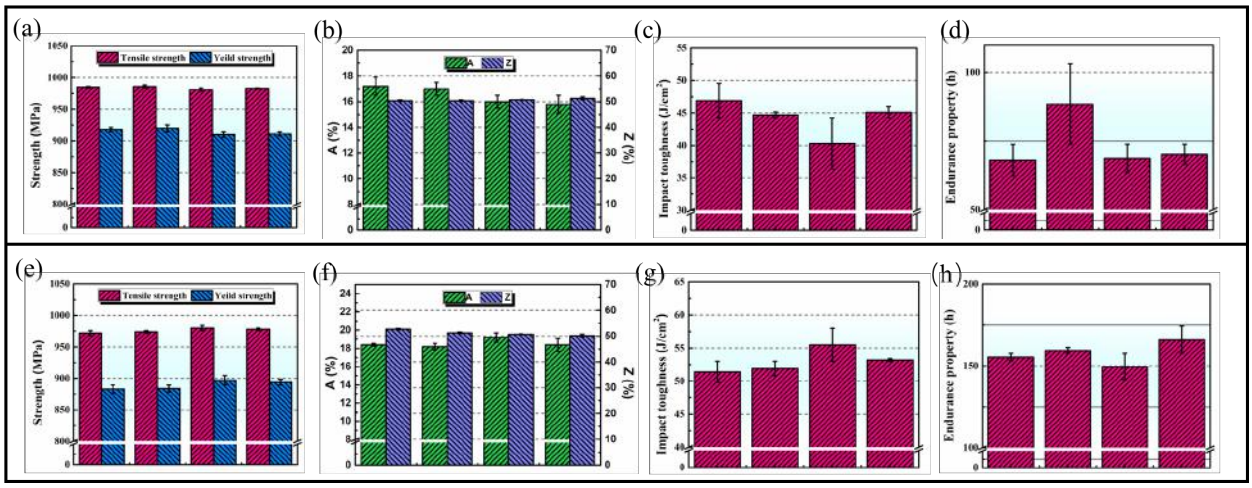

Figure 3. The mechanical properties of the 80 mm diameter bars prepared by different forging equipment: (a)(b)(c)(d) radial forging, (e)(f)(g)(h) Rolling.

3.1.2. Effect of forging process on microstructure and properties of 300mm diameter bars

The microstructure of 300 mm diameter bars prepared at different forging heating temperatures is shown in Figure 4. As can be seen from Figure 4, the secondary α-phase is lamellar and close in thickness at both forging heating temperatures. Compared to Tβ-40°C, bars forged with a higher heating temperature of Tβ-30°C have about 10% lower content of primary α phase, more lamellar structure and about 20h higher endurance time. The main reason is that the higher the heating temperature, the lower the content of primary α phase. Moreover, the higher the final forging temperature is, the higher the precipitation of flatter secondary α phase with the same forging time. Accordingly, more lamellar structure can effectively increase the dislocation slip resistance and improve the endurance performance[5].

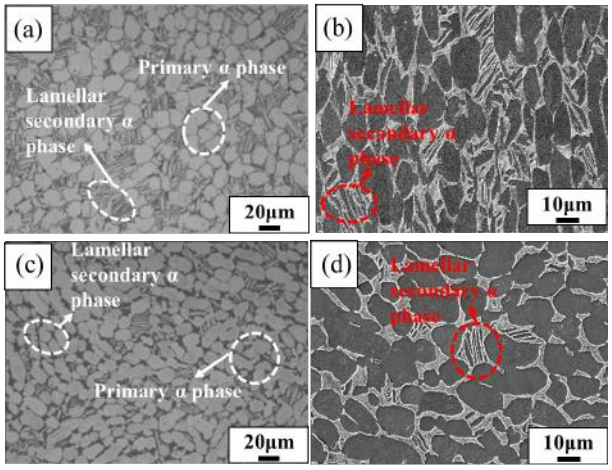

Figure 4. The microstructure of 300 mm diameter bars prepared at different forging heating temperatures: (a)(b) Tβ-30°C, (c)(d) Tβ-40°C.

3.2. Effect of chemical composition on microstructure and properties

The microstructure of 300mm diameter bars with different Si contents from 1# to 4# is shown in Figure 5，As shown in Figure 5, the microstructures of different Si contents are close to each other, and the primary α phases are all equiaxed and the secondary phases are lamellar. The primary α phase content is about 47%, and the cluster width and the thickness of the secondary α phase are 17.52 μm and 2.88 μm, respectively. It indicates that the content of Si element has little effect on the microstructure. The primary α phase content, cluster width and lamella thickness of secondary α-phase for 300mm diameter bars with different Si content are statistically shown in Table 3.

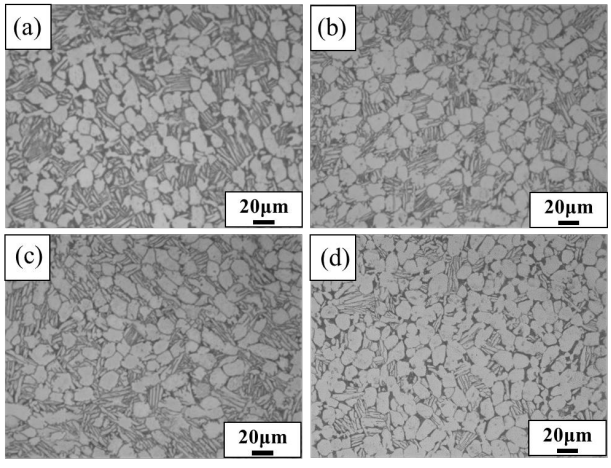

Figure 5. The microstructure of 300mm diameter bars with different Si contents：(a) 1# Bar, (b) 2# Bar, (c) 3# Bar, (d) 4# Bar

Table 3: The primary α phase content, cluster width and lamella thickness of secondary α-phase for 300mm diameter bars with different Si content

No.	primary α phase content /%	cluster width /μm	lamella thickness of secondary α-phase /μm
1#	45	17.04	2.78
2#	48	18.68	3.05
3#	46	17.62	2.92
4#	49	16.72	2.77

Figures 6-9 show the comparison of room temperature tensile strength, elongation, reduction of area, impact toughness and endurance performance of 300mm diameter bars with different Si contents from. It can be seen from Fig.6 that the room temperature tensile strength and yield strength of the bars from 1# to 3# did not fluctuate significantly with the increase of Si content. However, when the Si content was further increased, the room temperature tensile strength and yield strength of 4# bars increased by 7 MPa and 14 MPa, respectively. The strength level of the 4# bars is slightly increased due to the slightly higher content of primary α phase and slightly smaller cluster width. With the increase of Si content, there are fluctuations in elongation and reduction of area, which did not show an obvious regularity, as shown in Figure 7. From Figure 8, the impact toughness of the bars from 1# to 3# did not change significantly as the Si content increased. However, when the Si content further increases, the impact toughness decreases significantly, with a decrease of about 24 J/cm^2.

It can be seen from Figure 9 that the endurance performance shows a clear trend of improvement with the increase of Si content. The main reason for the improved endurance performance is the addition of Si elements, which are attracted to the dislocations and cause elemental polarization, thus forming Cottrell gas clusters to impede the dislocation movement. Meanwhile, the nanoscale silicides precipitated at grain and phase boundaries act as a strong pegging effect on the dislocations[15]. However, interfacial silicide precipitation above a certain amount leads to a reduction in impact toughness, as shown in Figure 8.

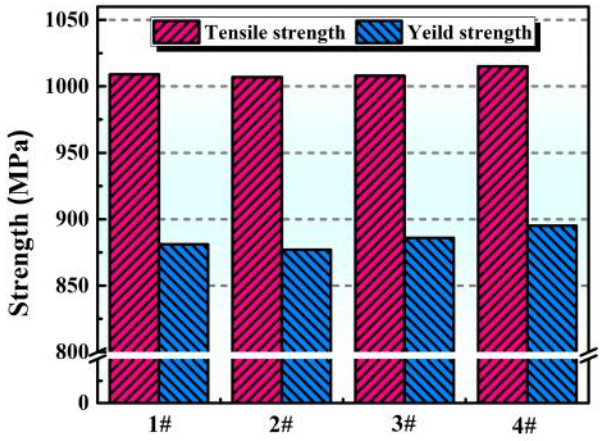

Figure 6. the comparison of room temperature tensile strength of 300mm diameter bars with different Si contents from 1# to 4#.

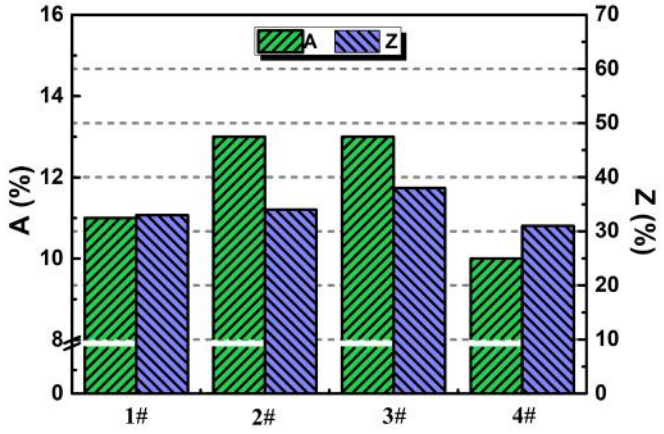

Figure 7. The comparison of elongation and reduction of area of 300mm diameter bars with different Si contents from 1# to 4#.

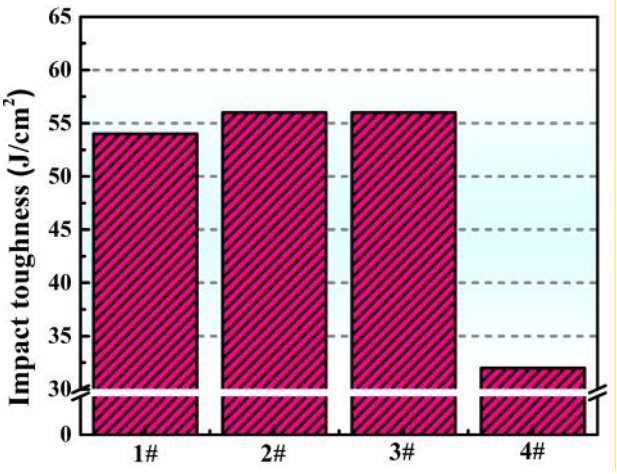

Figure 8. The comparison of impact toughness of 300mm diameter bars with different Si contents from 1# to 4#.

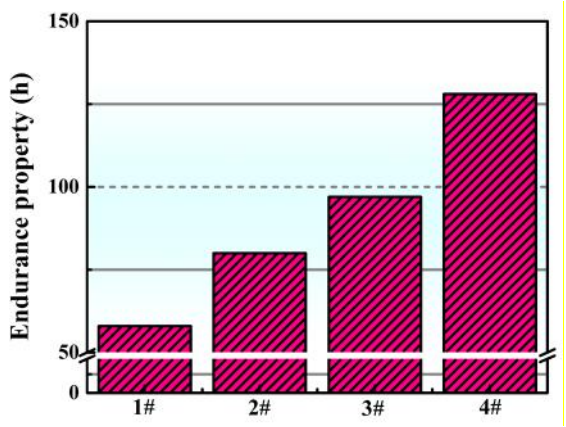

Figure 9. The comparison of endurance performance of 300mm diameter bars with different Si contents from 1# to 4#.

4. Conclusions

In this paper, the effects of forging process, forging equipment and chemical composition on the microstructure and mechanical properties on TA15 alloy were studied. The achieved results can be summarized as follows:

(1) For 80 mm diameter bars, increasing the radial forging heating temperature to Tβ-40°C, the content of the primary α phase is reduced and the secondary α phase is lamellar. Compared with the forging heating temperature of Tβ-50°C, the endurance time was increased by 26h. The dimple area of the endurance fracture was relatively large, and the dimple was small and deep.

(2) Compared with radial forging, the secondary α phase in the microstructure of 80mm diameter bar prepared by rolling is flatter and the thickness of the lamellae is smaller. Its room temperature tensile strength is about 10-20MPa lower, and the impact toughness is about 10J/cm^2 higher. Meanwhile, the endurance time is about 80h longer, and the elongation and reduction of area are close.

(3) Compared to Tβ-40°C, the incipient α-phase content of the 300 mm diameter bars prepared by forging heating temperature of Tβ-30°C is 10% less. Meanwhile, because of the higher final forging temperature, it is conducive to the precipitation of a more straight secondary α phase, and the endurance performance is improved by about 20h.

(4) The content of Si element has little effect on the microstructure, and the microstructure of 300 mm diameter bars with different Si content is close. The endurance performance shows a clear trend of improvement with the increase of Si content. The main reason for the improved endurance performance is the addition of Si elements, which are attracted to the dislocations and cause elemental polarization, thus forming Cottrell gas clusters to impede the dislocation movement. Meanwhile, the nanoscale silicides precipitated at grain and phase boundaries act as a strong pegging effect on the dislocations. However, the addition of more silicon elements leads to a reduction in impact toughness of about 24 J/cm^2.

5. Acknowledgements

This research was financially supported by the independent research project of Western Superconducting Technologies Co., Ltd. (ZX2022010).

6. References

1. D. Ren, Y. Jiang, X. Hu, et al. *Intermetallics* 132 (2021):107-115.
2. W. Xu, Z. Zhang. *Transactions of Nonferrous Metals Society of China* 26(2016) 3135-3146.
3. A.M. Zhao, H. Yang, X.G. Fan, et al. *Materials & Design* 109 (2016) 112-122.
4. M. Rizwan, J. Lu, F. Chen, et al. *Acta Metallurgica Sinica (English Letters)* 34 (2021) 1201-1212.
5. Yi Gu, et al. *Materials Science & Engineering A*. 575 (2013) 575 74-85.
6. J. Guo, B. Fang, X. Huang, et al. *Chinese Journal of Rare Metals* 28 (2004): 362-364.
7. N.E. Paton, M.W. Mahoney. *Metallurgical Transactions A* 7 (1976) 1685-1694.
8. S. Gollapudi, et al. *Materials Science & Engineering A* 556 (2012) 510-518.
9. M.J.R. Barboza, C. Moura Neto. C.R.M. Silva. *Materials Science & Engineering A* 369 (2004) 202–209.
10. R. Sahoo, B. B. Jha, T. K. Sahoo. *Transactions of the Indian Institute of Metals*, 71 (2018) 1573-1582.
11. Anna Radecka, James Coakley， Ian P. Jones, et al. *Materials Science & Engineering A* 650 (2016) 28-37.
12. J. Guo, Y. Dong, B. Chen, et al. *Nonferrous Metal Materials and Engineering* 39(2018) 6-11.
13. A. Huang, Y. Xing-Fu, Y. Wang, et al. *Foundry* 62 (2013) 448-455.
14. F. Xu, G.P. Li, R. Yang, *Acta Metallurgica Sinica* 48 (2019) 1749-1755.
15. J. Ju, Y. Wang, F. Hao, et al. *Rare Metal Materials and Engineering* 48 (2019) 1749-1755
16. Z. Sun, S. Guo, H. Yang, *Acta Materialia* 61 (2013) 2057-2064

ADVANCES IN THE DEVELOPMENT OF DIRECT ENERGY DEPOSITION FOR THE MANUFACTURING OF AERONAUTICAL ELEMENTARY PARTS

Nicolas Maury[1], Matthieu Sicre[1]

1 Airbus Operations SAS, Toulouse, France.

Additive manufacturing technologies are actively being developed within Airbus Research & Technology, in order to manufacture titanium structure components more sustainably and at a lower cost. In particular, Direct Energy Deposition (DED) enables the manufacturing, at a high deposition rate, of integrated blanks close to the dimensions of the final part, thus leading to a reduction in raw material consumption and assembly. Large and complex Ti-6Al-4V components, concentrating various geometrical design features, have been manufactured by an in-house electron beam fusion wire fed machine, and further characterised as per the industrial end-to-end process. Results show dimensional compliance as per the drawings, thus demonstrating the technological capability for these complexities. Also, dedicated non-destructive testing by ultrasound has shown to characterise potential internal defects in the volume manufactured. These indications can be correlated to the monitoring of the process parameters, thus indicating their origin and contributing to defining the key process parameters to master the technology.

Keywords: additive manufacturing, direct energy deposition, non-destructive testing, process monitoring.

1. Manufacturing Engineering Technologies Innovation within Airbus

Airbus is committed to pioneer sustainable aviation by decarbonizing the aeronautical industry. Decarbonization concerns the complete life cycle of an aircraft, starting at the manufacturing of structure components. These environmental goals involve technological and industrial challenges, for which the propulsive system is a key enabler. Within Research and Technology (R&T) at Airbus Commercial Aircraft, new buy-to-fly manufacturing technologies are actively developed to be introduced in future serial production, especially among the additive manufacturing family, in line with global developments in the aeronautical industry [1,2].

More precisely, Direct Energy Deposition (DED) technology has become, during the last few years, a promising technology under active development [3,4] for the future manufacturing of Titanium Ti-6Al-4V blanks, among which at Airbus Saint Eloi plant for a large range of aircrafts' structural components. This is in particular the case of pylons, which are assembled from large titanium parts that are relevant for DED. This component is key for the integration of the engines and the thrust, while being exposed to high thermo-mechanical loads in-service.

The technology maturation, continuously ongoing, is based on the Technology Readiness Level (TRL) criteria, requiring among others the manufacturing and characterization of multi-scale (non-flying) demonstrators. This activity is further detailed in the present study, applied to more and more complex design features and industrial end-to-end characterizations.

2. DED technology

2.1. Advantages and industrial challenges

DED technology enables the manufacturing, at a high deposition rate, of blanks close to the dimensions of the final part, thus leading in particular to a reduction in the raw material consumption and the environmental footprint. It opens the design field for more integrated and complex elementary part designs, leading to weight savings, while also benefiting of a high agility and short lead time for development (between a design trade and the manufacturing of a part). From an industrial perspective, the buy-to-fly and assembly build processes are even more optimised. Also, the less tooling and machining required enables to further reduce costs.

All these advantages still come with some technological challenges that need to be demonstrated compliant to the TRL requirements. On the manufacturing engineering side, one can mention the distortions of the blanks manufactured, as near-net-shape as possible, that affect the tolerancing rules. Also, these blanks need to be characterised by non-destructive testing methods, in order to identify potential internal defects that could affect the mechanical properties. To do so, a specific ultrasonic technology was development particularly for DED.

These manufacturing trials come along with the mastering of the DED machine, the definition of its key process parameters and their surveillance in real time. Such data has to be monitored, acquired and post-processed to demonstrate quality and robustness. In particular, their correlation to the non-destructive characterisations is an enabler.

2.2. Manufacturing cycle

The technology developed in-house by Airbus is electron-beam fusion, wire fed. It uses a plate of titanium Ti-6Al-4V as a substrate, on which the wire of the same material is deposited and melted by the heat generated by the focused electron beam (under vacuum), to generate a geometric feature. The melt pool solidifies when cooling to form a layer of metal deposited on the substrate, then a complete first layer (Fig. 1). This operation is repeated by stacking the layers on top of each other, eventually building the blank of a part. The machine operating at Saint Eloi plant is a Sciaky EBAM 110 (electron gun power of 60 kV at 700 mA (30 kW)), fed with a wire of 3.2 mm in diameter.

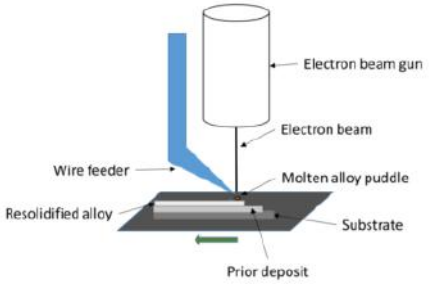

Figure 1. Illustration of the DED electron beam wire fed technology to deposit a bead.

Fig. 2 illustrates a typical part design relevant for DED technology. From the design of the final part, the DED blank is drawn and then manufactured, before machining of the final part. It can be clearly seen the savings of raw material and machined chips, compared to machining the part entirely from a thick plate (blue). The weight of the initial blank/plate is thus reduced from more than 26 kg to 4.4 kg in this example.

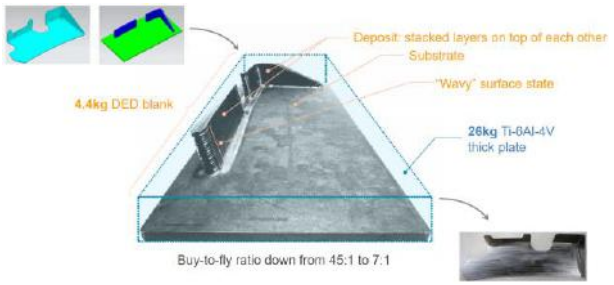

Figure 2. Illustration of the manufacturing of a DED blank compared to a thick plate.

The typical manufacturing end-to-end sequence is:

1. Deposition preparation: definition of trajectories and operating parameters, programming;
2. Deposition (manufacturing of the blank);
3. Stress-relieving heat treatment (reduction of internal stresses in the blank);
4. Non-Destructive Testing (NDT): 3D dimensional scan of the blank;
5. Machining of the blank to obtain the finished part according to the 3D drawing;
6. NDT: characterization of internal defects by ultrasound, characterization of post-machining surface cracks by dye penetrant;
7. Final dimensional check and marking of the part.

3. Demonstrators

3.1. Blank manufacturing

DED is a clear enabler for the design of more complex and non-linear geometric features, while achieving greater precision and control over the final product. One example of this is the use of a spiral geometry, which involves the continuous deposition of material in a spiral pattern around the substrate, with a high degree of accuracy and precision.

A notable example of such of near-net shape complex curved geometries is the manufacturing of the blank of an Occitan Cross shown in Fig. 3, with the substrate still clamped onto the tooling. This demonstrator, of about 450 x 450 x 600 mm, is obtained by the combined 2D movement of the wire head and the substrate. The symmetrical quarter spiral geometry consists in the succession and repetition of no less than 5 different trajectories, linear or spiral. The “wavy” surface state is typical of a DED deposition, although still quite regular.

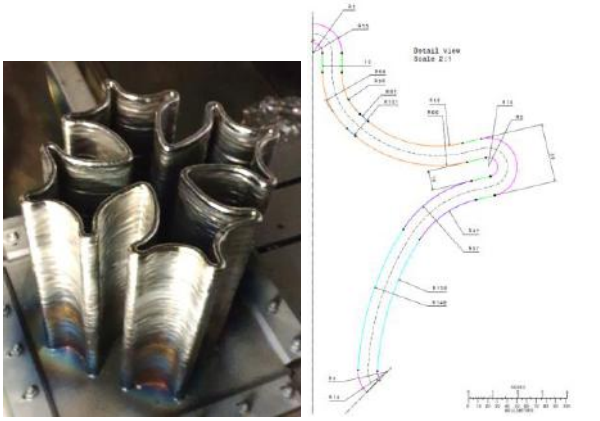

Figure 3. Occitan Cross geometry DED blank manufacturing (left) and detail drawing illustrating the succession of 5 linear and spiral geometrical features (right)

Considering geometries closer to typical aeronautical parts, Fig. 4 shows the design and blank manufacturing of a 600 x 600 mm demonstrator of an integrated panel with stiffeners and an attachment. More precisely, these stiffeners exhibit various geometrical complexities: variations in height (80 to 100 mm) and thickness (6 to 14 mm), tilts (12° from the deposition axis), angles (90°, 40° closed, 115° opened), 360° circular deposition and 4 intersections.

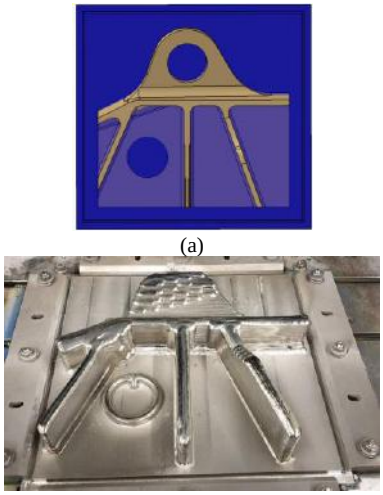

Figure 4. (a) Design and (b) blank manufacturing of an integrated demonstrator.

3.2. *Dimensional characterization*

As part of the R&T manufacturing activities, a systematic 3D dimensional scan is performed on the blank, after stress-relief heat-treatment. This allows to confirm that within the blank volume, the finished part can be machined to its dimensions and within tolerances. A "best fit" is thus performed to determine the machining coordinates of the final part.

Fig. 5 shows the 3D map of the blank of the integrated demonstrator (Fig. 4). This was achieved with a calibrated LEICA AT960 means, using the Polyworks V2020 IR7.1 software. It appears globally some extra material deposited, especially for the stiffeners and the attachment. There is only a reduced overthickness on the substrate, which is the base of the panel.

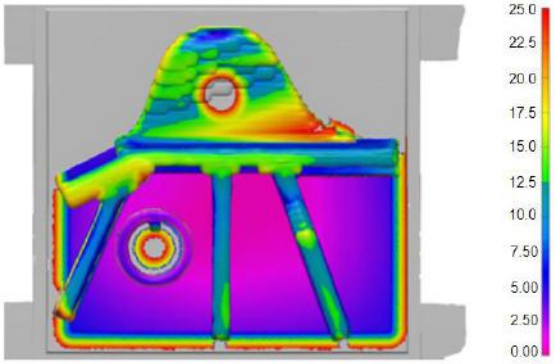

Figure 5. 3D dimensional scan of the blank of the integrated demonstrator. Best fit compared to the 3D drawing of the finished part.

Following the confirmation of the best fit from the 3D scan of the blank, the part is machined to its final dimensions. Fig. 6 shows the machined demonstrator, hence the finished part, in accordance with the 3D drawing (Fig. 4(a)). It can be noted that at this stage, it is impossible to distinguish visually which was the initial plate from the wire raw material.

Figure 6. Machining of the integrated demonstrator to its final dimensions according to the drawing.

Post-machining 3D scan of the finished part was then performed to confirm the geometrical and dimensional compliance compared to the 3D drawing (Fig. 4(a)). The resulting map, shown in Fig. 7, demonstrates the compliance of the machined demonstrator to the theoretical drawing. Indeed, considering the dimensional tolerance of ± 0.2 mm, against ± 0.3 mm for the machined radii, it appears the dimensions of this finished part are compliant to the general tolerances of aeronautical parts.

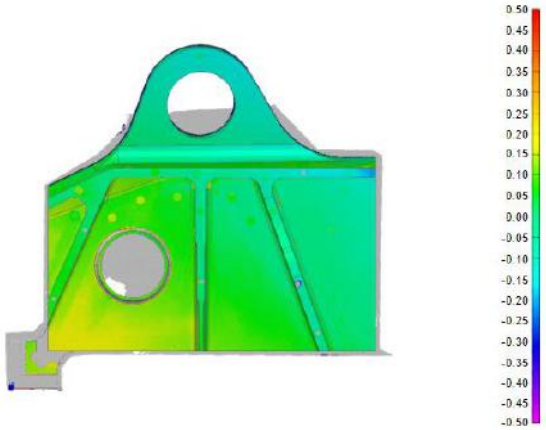

Figure 7. 3D dimensional scan of the machined part, compared to the 3D drawing of the part.

3.3. *Internal defects characterisation*

The characterisation of the deposited material internal defects is one of the most critical steps of the end-to-end manufacturing sequence, linked to strict requirements of the design office. To guarantee this inspection, the Ultrasonic phased array pulse-echo (non-destructive) inspection technology, using Total Focusing Method (TFM), has been developed for Titanium DED components [5].

The physical principle behind the ultrasonic TFM (USTFM) defect detection method is based on the propagation of acoustic waves through the material. When these waves encounter a discontinuity, some of the energy is reflected back to the transducer, while the rest

of the energy continues to propagate through the material. By using complex image processing algorithms, USTFM allows for the complete image reconstruction of the tested object using all recorded acoustic information. This method enables to localise and characterise rounded or linear indications (i.e. porosities, inclusions, lacks of fusion…), whatever their orientation and with a high spatial resolution.

Fig. 8 shows an example of Ultrasonic TFM characterisation of the machined integrated demonstrator (Fig. 6). This was performed with a calibrated GEKKO means, linked to a 12 MHz 64 elements probe. In this example, on one of the stiffeners (Fig. 8(a)), an indication of about 1.5 mm in length was locally identified and reported: size, Cartesian coordinates (X, Y, Z). This operation is then repeated to cover all the deposited volume. The surrounding material, appearing in blue, illustrates "healthy" material with no indication in the volume analysed.

Such data on the material health has to be precisely localised, in order to be further compared to the process parameters and trajectories programmed in these specific areas and then determine the origin of these potential non compliances.

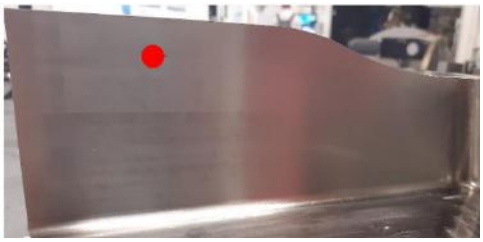

(a)

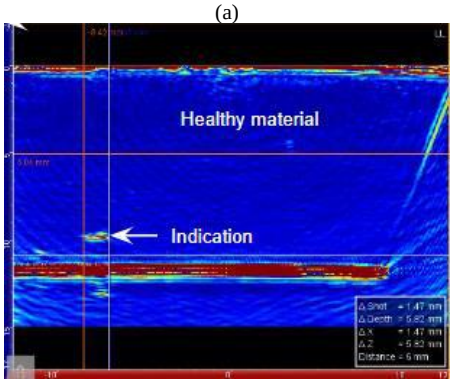

(b)

Figure 8. Ultrasonic TFM testing of the machined integrated demonstrator: (a) stiffener with location of the inspected area (red circle) and (b) identification and quantification of an indication (defect).

4. Monitoring of process parameters

The monitoring and analysis of data, applied to the programmed process parameters, is key for the mastering of the technology. In particular, as part of these R&T developments, they allow to globally assess the deposition quality and repeatability from one blank to another. Also, as introduced previously, these data can be correlated to the properties of the material characterised, in particular the internal defects, and thus determine the origin of these potential non compliances.

Regarding future production, such data is to be used in manufacturing reports, for quality and further parametric optimization. Additionally, the use of predictive maintenance based on this real-time monitoring can help to prevent costly equipment failures and minimise downtime in manufacturing operations.

Furthermore, the use of a high-resolution camera during the welding process provides valuable insight into the behaviour of the molten pool and the wire feed. By capturing images of the bead deposition at a high frequency, it is possible to monitor the shape and stability of the molten pool, as well as the feed rate and positioning of the wire, as shown in Fig.9. This information can then be used to identify potential defects or quality issues, and to optimise the welding parameters for improved performance and efficiency.

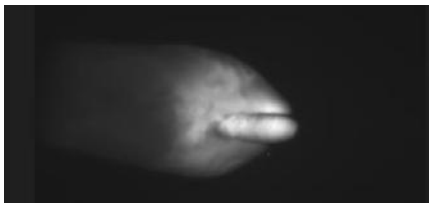

Figure 9. Observation of the melt pool (wire feed) and prior bead deposit via a camera.

4.1. Methodology

During deposition, about 10 process parameters of the EBAM 110 machine are monitored in real time, thanks to digital tools that have been developed. From this data acquired, a statistical analysis approach can easily be carried out to give an overview of the stability of the process parameters. In the case of the electron gun beam current (BC) key process parameter, during the blank manufacturing of the Occitan Cross (Fig. 3) and the integrated demonstrator (Fig. 4(b)), these statistics (median, 1st quartile, 3rd quartile) did not show any dispersion in the process parameters and thus a satisfactory stability.

Nevertheless, such averaged data does not reveal punctual precisely punctual fluctuations, such as peaks,

that can occur during deposition. These peaks, referred to as “flash”, generate an instability of the melted pool and can typically be at the origin of internal defects such as the one shown in Fig. 8(b). The origin of these flash is still uncertain, but the best hypothesis considered is the effect of the metallisation of the cathode of the electron beam gun and/or the instability of the electronic and mechanical compounds of the industrial means itself. These flash occurrences generate the stop the deposition in order to protect the integrity of the means and are therefore not acceptable in terms of manufacturing operability. Also, such stop and re-start can impact locally the material performance and generate non compliances.

The definition of the range of stability of the parameter (target, minimum and maximum tolerance interval) is therefore a key step. The methodology developed was to count the occurrence of each value of the parameter and classify them by range, from a population of about 1.4 M data in the present study. The range of accepted value of the parameter is then defined considering that 99% of the data is within this range, against 1% considered instable outside of this range. This is illustrated in Fig. 10 for the manufacturing of the Occitan Cross. In this case, the range of stability defined is at 39 ± 2% of the maximal operable beam current considered.

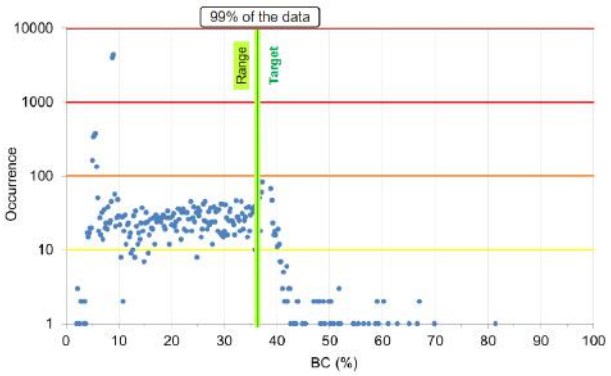

Figure 10. Definition of the stability range of the beam current process parameter, considering 99% of the data monitored within the range, during the blank manufacturing of the Occitan Cross.

4.2. Correlation with ultrasonic indications

The definition of the parameter range allows to identify all the localisations of deposition at risk where a flash, or any beam current out of the range, has occurred. In the case of the Occitan Cross demonstrator (Fig. 3), the mapping of the values of the beam current outside of the range of 39 ± 2% (Fig. 10), is shown in Fig. 11(a) and Fig. 11(b) in 2D, for values below and above the range respectively. Also the total amount of data outside of the range is shown in 3D in Fig 11(c). It can be seen that there is no direct link and consequence between a trajectory and stability of the parameter. This demonstrates that one single range of process parameter can be used on multiple geometrical features of a same layer deposited.

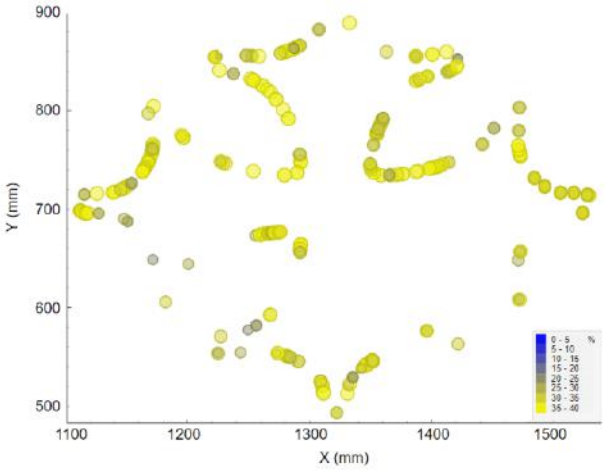

(a)

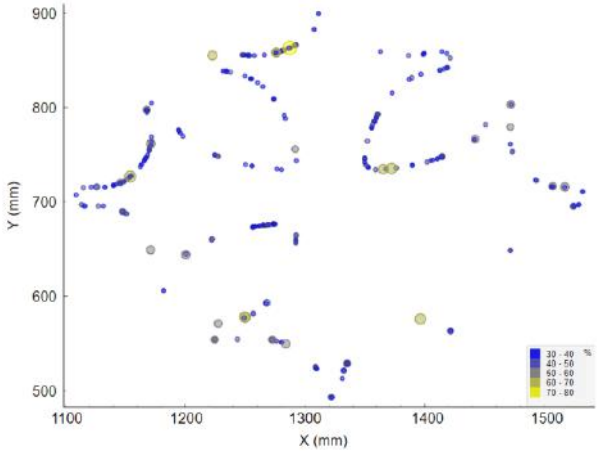

(b)

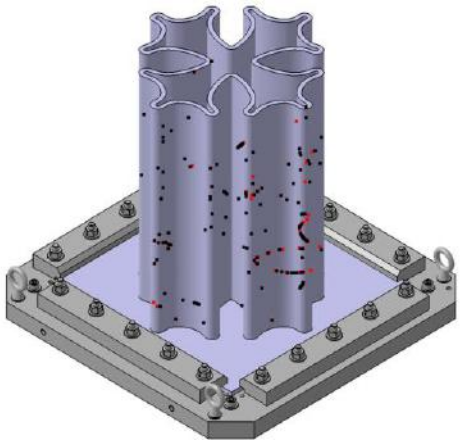

(c)

Figure 11. 2D mapping of the beam current values (a) below and (b) above the range defined (the size of the font increases with its value). (c) 3D mapping of all the beam current values below (black) and above (red) the range defined.

All these points, of Cartesian coordinates known, are then compared to those of the indications detected during the non-destructive testing, as in Fig. 8(b). If correlated, the analysis can conclude that the occurrence

of a flash due to a peak of beam current has generated the material internal defect, with a high confidence. Depending on these results, a design of experiment is implemented in order to study the impact of a flash on the material properties and further validate the range of the parameter defined.

Preventing the occurrence of any flash during deposition appears to be necessary to guarantee the stability of the process parameters and the quality of manufacturing. An "anti-flash" system has thus been developed [6] that allows to monitor automatically the intensity of the controlled beam current, compare it to a given range, and stopping the deposition when the intensity of this controlled beam current is greater than the given range. The ranges of stability defined are then applied in the anti-flash system to avoid any peaks, and subsequent deposition start and re-stop, in all further blank manufacturing.

5. Conclusion and perspectives

Large and complex Ti-6Al-4V demonstrators have been manufactured by an in-house EBAM110 DED machine and further characterised as per the industrial end-to-end sequence. By combining advanced geometric modelling tools with innovative deposition techniques, it is now possible to create highly complex and functional components with a wide range of applications, in the aerospace field or even automotive and biomedical.

- The feasibility, dimensional and geometrical compliance, as per the drawing, has been demonstrated on several complex geometrical demonstrators;
- The geometries demonstrated enable to open the design field and provide solutions for function integration in the design of future parts for structure components, while benefiting from the savings of this technology (cost, environmental footprint, short manufacturing lead time);
- NDT Ultrasonic TFM inspection technology, developed in particular for DED parts, has been successfully used to characterise internal defects in the deposited volume;
- Mastering the technology requires to identify and quantify the key process parameters and their impact of the operability, the blank and material properties. The anti-flash system developed, applied to the beam current, is a key enabler to guarantee manufacturing quality, repeatability and means integrity. The implementation of design of experiments to investigate these impacts shall fill databases and catalogues of defects;

As DED technology continues to advance, targeting future serial applications, one of the key areas of development is the automation of the correlation methodology between variations in process parameters and non-destructive testing. By applying the methodology developed to all key process parameters, it will be possible to achieve greater quality, precision and robustness over the final product, while also reducing the need for time-consuming post-processing and inspection procedures. This will help to streamline the production process and make it more cost-effective and competitive, enabling manufacturers to produce high-quality components and products on a larger scale. Furthermore, the use of advanced design techniques, such as topology optimization and lattice structures, will enable the creation of even lighter components, with a wide range of applications in the aerospace and industrial sectors.

6. Acknowledgements

The authors thank the DED team at Saint Eloi plant, as well as the R&T design office, for contributing to the development of DED technology. The authors also thank internal sponsors for their support and funding.

7. References

1. D. Herzog, V. Seyda, E. Wycisk, C. Emmelmann, Additive manufacturing of metals, Acta Mater. 117 (2016) 371–392.
2. T. Sharon Tshephe, S. Olukayode Akinwamide, E. Olevsky, P. Apata Olubambi, Additive manufacturing of titanium-based alloys- A review of methods, properties, challenges, and prospects, Heliyon. 8 (2022) e09041.
3. P. Wanjara et al., Titanium Alloy Repair with Wire-Feed Electron Beam Additive Manufacturing Technology, Advances in Materials Science and Engineering, 2019:1-23.
4. F. Pixner et al., Wire-Based Additive Manufacturing of Ti-6Al-4V Using Electron Beam Technique, 2020 13(15): 3310.
5. European Patent n° EP4095527A1, Method and system for an ultrasonic detection of defects of a component, in particular for an aircraft, November 2022.
6. European Patent n° EP4129560A1, Additive manufacturing process using a focused energy source, said method being regulated as a function of the intensity of a control current of said focused energy, February 2023.

EXPLORING THE STRUCTURE AND PROPERTIES OF NANOSCALE PRECIPITATES IN A HIGH-STRENGTH TITANIUM-BASED SYSTEM

RFL Mellor[1], P Vacek[1], NG Jones[1], PA Midgley[1], HJ Stone[1]

[1]*Department of Materials Science and Metallurgy, University of Cambridge, 27 Charles Babbage Road, Cambridge, CB3 0FS, UK*

Many high-strength titanium alloys rely on complex processing routes to achieve a balance between α and β phases, and alternative strengthening by intermetallic precipitate reinforcement has not been widely explored. In this research, a TiFeAl alloy has been produced which exhibits high hardness associated with finescale intermetallic features after just one heat treatment. The features exhibit a lenticular morphology and have a well-defined orientation relationship with the β-matrix. This alloy demonstrates the exciting potential of intermetallic precipitate reinforcement in titanium alloys and highlights the need to explore alloy design concepts beyond those traditionally exploited.

Keywords: microstructure, alloy design, superlattice SED

1. Introduction

Metastable β-titanium alloys offer the highest strength-to-weight ratios of titanium alloys [1], however the optimisation of thermomechanical processing routes is critical as they exhibit a wide range of microstructural morphologies depending on small changes in processing [2]. Generally, their high strength and toughness is derived from a well-controlled dispersion of α-phase in a retained β matrix, however, the inclusion of additional intermetallic phases is now being explored. Investigation of the O-phase in the Ti-Al-Nb system is the most widely-researched example [3,4].

A further development to the inclusion of intermetallic phases is to consider addition of a phase which adopts a bcc superlattice crystal structure. This could lead to synergistic benefits relating to the additional hardening from the ordered structure [5]. The best example of exploiting superlattice structured precipitates is the nickel-based superalloys [6], from which a range of FCC analogues have additionally been explored [7–9].

It is interesting to consider the application of superalloy design strategies to a titanium-based system owing to its much lower density than alternative matrix metals. This could lead to entirely novel microstructures in such alloys which is of interest for the development of more sustainable, lightweight metals for the future.

2. Experimental Methods

The Ti-20Fe-10Al (at.%) alloy was produced by arc melting elemental metals (with purity >99.9%) together under a Ti-gettered Ar atmosphere. The 40 g ingot was re-melted five times to enhance the compositional homogeneity. The solidus and B2 solvus temperatures were measured by differential scanning calorimetry to determine a sensible homogenisation heat treatment temperature. A Netzsch DSC 404 calorimeter was used under flowing Ar, with a heating rate of 10 °C/min.

An as-cast section of the bar was cut for characterisation, and the remainder was wrapped in Ta foil and sealed in an Ar-backfilled fused silica tube for the homogenisation heat treatment of 24h at 1115 °C. The sample was quenched into ice water while contained within the tube. Later, individual 10 mm sections of material were prepared in the same way for 100h heat treatments at 400 °C, 600 °C, 800 °C and 1000 °C.

Samples for observation by scanning electron microscopy (SEM) were cut and mounted in conductive bakelite. The surfaces were ground with SiC papers up to 4000 grit, before being polished using a buffered colloidal silica solution. A Zeiss GeminiSEM 300 operating at 15 kV was used for backscattered electron (BSE) imaging and an Oxford Instruments X-Max^N 50 detector was used for energy dispersive X-ray spectroscopy (EDX).

X-ray diffraction was performed at the I12 beamline at the Diamond Light Source using a transmission Debye-Scherrer geometry [10]. A monochromatic 100 keV beam was used to record diffraction patterns using a Pilatus 2M CdTe 2D area detector with a sample-detector distance of 867 mm. The 2D patterns were dimensionally reduced using the DAWN software [11,12]. The powder specimens were produced by grinding in a pestle and mortar. Lattice parameters were determined by individual peak fitting.

Specimens for examination by transmission electron microscopy (TEM) were produced by electropolishing 120 μm thick discs of material at 17 V and -35 °C in 8% perchloric acid in methanol. The TEM DPs were recorded using an FEI Tecnai Osiris with a 200 kV operating voltage. The same machine was also used for scanning transmission electron microscopy (STEM) high-angle annular dark field (HAADF) imaging. High resolution STEM-HAADF images were recorded using a ThermoFisher Spectra with a 300 kV operating voltage, and scanning electron diffraction (SED) was performed using an FEI Tecnai F20 with a 200kV operating voltage. The data was analysed using the Hyperspy and Pyxem python libraries [13,14].

Vickers hardness measurements were conducted using a 5 kg load and 15 s dwell time on a Laizhou Huayin machine. Thermodynamic calculations were made using the TCTI2 database in the Thermo-Calc software [15].

3. Alloy Design

The Fe-Ti binary system contains a eutectic reaction between bcc-Ti and B2-FeTi phases, where the Fe solubility in the bcc-Ti phase decreases with temperature, which allows for an age-hardening production route. The microstructure of Fe-Ti binary alloys has been explored previously and a Ti-20Fe (at.%) alloy heat treated for 50 hours at 600 °C was reported to contain bcc-Ti, B2, α and ω phases [16]. The presence of α at this temperature suggests that additional β-stabilisation could be of interest. There has been some work investigating similar alloys in the Fe-Mo-Ti system, which indeed shows the additional β-stabilisation from Mo results in no α phase at 750 °C [17].

Here, Al was added to Fe-Ti as although it is an α-stabiliser, it has the potential to dramatically improve the oxidation resistance. Furthermore, since a range of B2 compounds form with Al, it could lead to stabilisation of the B2 phase, and a range of interesting microstructures involving B2 phases have previously been reported in similar aluminium-containing systems [18,19].

To achieve an age-hardened microstructure, it was necessary to select a composition where it is possible to achieve a single phase field at high temperature and a two-phase bcc+B2 field below this for a subsequent precipitate ageing step. In the binary system, the maximum Fe content which can be added before the single phase field at high temperature is lost is 22 at.%. Based on the ternary Ti-Fe-Al diagram of Palm [20], almost 14 at.% Al can be added into a Fe-Ti alloy whilst still maintaining the bcc-B2 two-phase field at 1000 °C. Thermodynamic predictions using the TCTI2 database in ThermoCalc show that the addition of 10% Al to Fe-Ti leads to very little change in the maximum potential Fe addition, and causes a shift of the phase boundaries to higher temperatures, Figure 1. As a result, an alloy composition of Ti-20Fe-10Al (at.%) was selected as it should allow production of an age-hardened alloy with a large B2 volume fraction. The higher the Fe content, the higher the predicted precipitate volume fraction, Figure 1.

4. Results and Discussion

4.1. Characterisation of as-cast microstructure

The average composition of the alloy after arc melting was measured as (69.4±0.2)Ti-(20.2±0.3)Fe-(10.5±0.1)Al at.% by averaging five 500 μm × 500 μm EDX area measurements. In the as-cast state, the alloy contained bcc and B2 phases, as identified from the XRD scan in Figure 2 (top), though the first set of bcc peaks appears to be split in two; with lattice parameters measuring 3.15 Å and 3.19 Å. The lattice parameter of the B2 phase is 3.01 Å. Since the alloy exhibited a dendritic morphology, it is suggested that the two sets of bcc peaks relate to bcc-Ti in the dendritic cores and in the interdendritic regions, respectively, which would be expected to have different compositions, leading to two different lattice parameters, according to Vegard's Law [21].

From the SEM micrograph, also in Figure 2, the bcc matrix contains B2 precipitates of two different morphologies; fine cube-shaped precipitates less than a micron in size, and larger irregular precipitates which are up to 10 μm across. The B2 precipitates have a bright contrast as they are richer in Fe than the matrix.

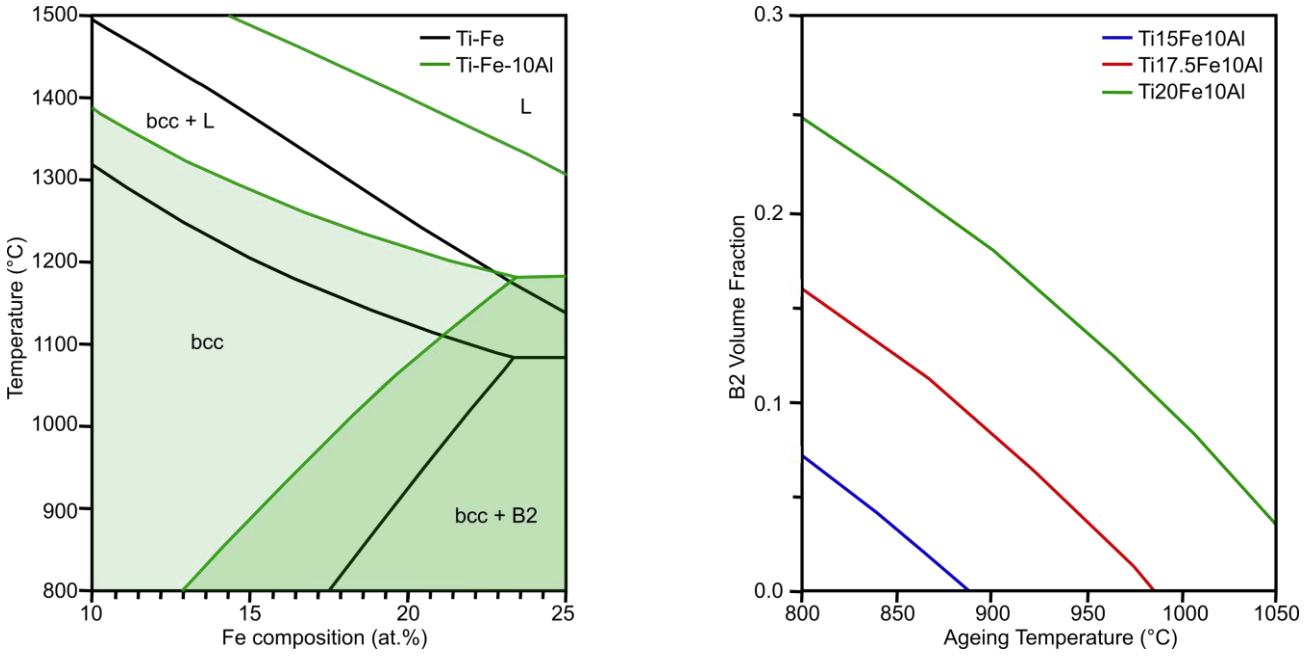

Figure 1 Thermodynamic predictions produced using ThermoCalc software [15]. Left - Effect of Al addition on the phase boundaries in the Fe-Ti system. Right - Effect of Fe composition on the volume fraction of B2 FeTi phase.

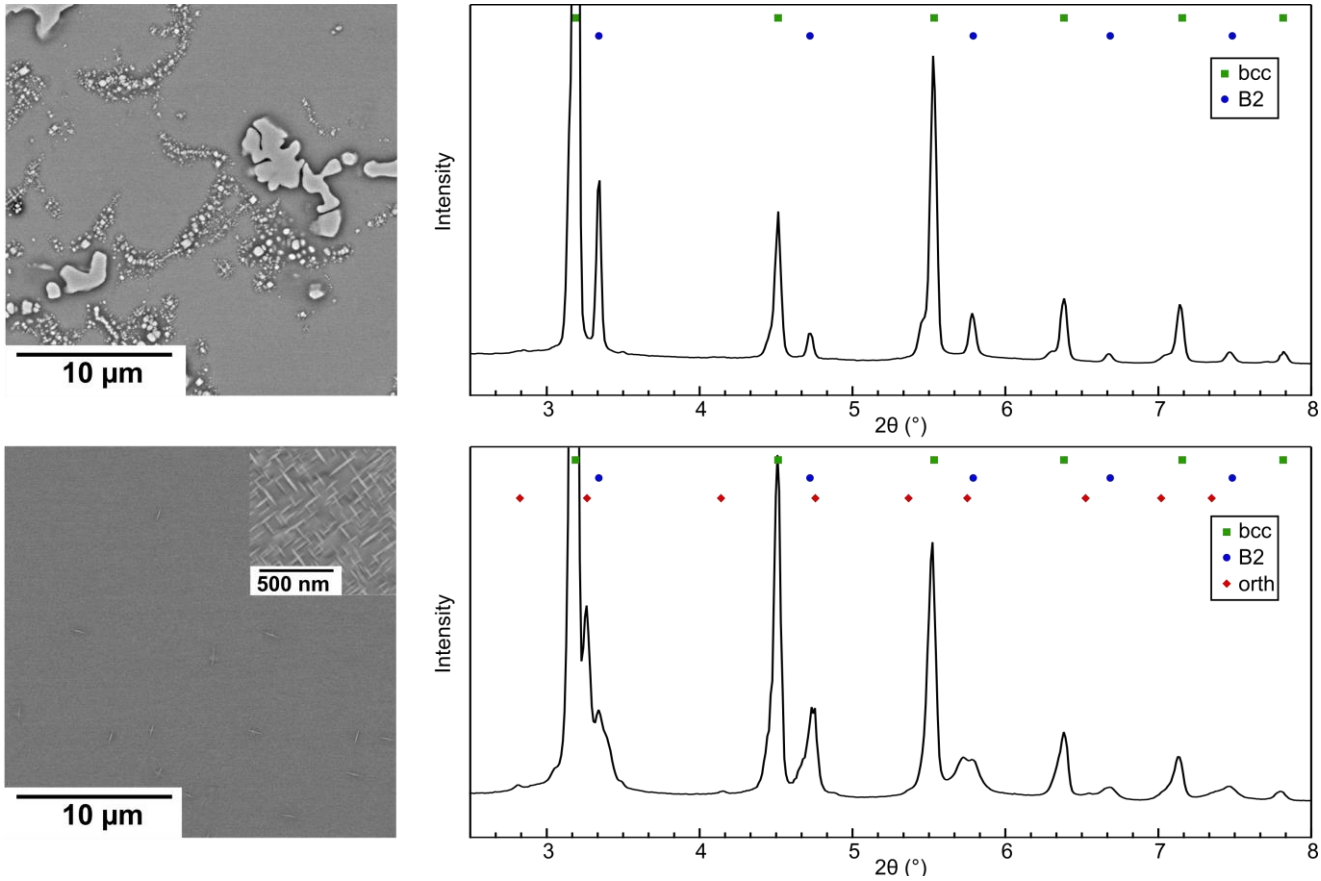

Figure 2 Top - Data recorded for the alloy after arc melting; Left – SEM BSE micrograph, Right – XRD scan. Bottom - Data recorded for the alloy after the homogenisation heat treatment and quench; Left – SEM BSE micrograph, Right – XRD scan.

4.2. Characterisation of homogenised microstructure

After the 24h heat treatment at 1115 °C, the alloy was expected to be single phase bcc-Ti to allow for formation of a bcc-B2 microstructure by a subsequent lower temperature age. However, as can be seen in Figure 2 (bottom), after heat treatment, the alloy was not single-phase. In fact, there are more reflections present in the XRD pattern after homogenisation than in the as-cast state. The bcc and B2 phases can again be identified, as well as additional reflections. The lower magnification SEM BSE image indicates that there are no largescale features present in the microstructure, which suggests that it was indeed in the single-phase field at 1115 °C. However, observation at higher magnification indicates the presence of lenticular precipitates which appear to have a well-defined orientation relationship with the matrix. Two perpendicular sets of precipitates can be seen in cross-section, and circular features with lower contrast can also be identified, which are thought to be lenticular precipitates in plan view.

4.3. Identification of finescale microstructure and orthorhombic phase

TEM was used to investigate the microstructure at higher magnification. Figure 3 (top) shows a STEM-HAADF image of the microstructure. This reveals that the lenses themselves contain a finer substructure. The lenses in cross section contain channels of alternating bright and dark contrast, whilst those in plan view, as can be seen in the lower right corner of the image, consist of a grid of approximately square bright features with darker channels between them.

A high resolution STEM-HAADF image was recorded of a lens in plan view, Figure 3 (bottom). It is now possible to distinguish the bright and dark features within the lens. Since this HAADF image was recorded with a high collection angle (65-200 mrad), the contrast is dominated by compositional differences. Thus, the larger square-shaped features have a higher average atomic number than the channels between them.

The corresponding DP in Figure 4 can be used to identify the phases present. It was not possible to obtain selected area DPs of the individual phases owing to their fine scale, so instead the DP has been recorded down a $<100>_{BCC}$ zone axis in an area which includes the matrix and multiple precipitates. It is along this zone axis that the HAADF images in Figure 3 were also recorded. This demonstrates that the lenses have a fixed alignment relative to the $<100>_{BCC}$ zone axis. The DP fits well to a combination of bcc, B2 and orthorhombic phases (here termed ‘orth’). The bcc and B2 phases exhibit the expected cube-cube orientation relationship and the lattice misfit between them (-5.2% as calculated from the lattice parameters determined by XRD) leads to a splitting

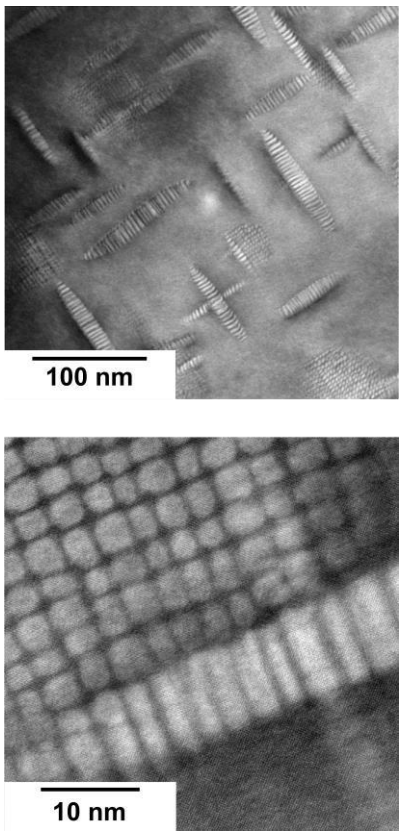

Figure 3 STEM-HAADF images of the alloy after homogenisation heat treatment.

of the reflections. This is not entirely visible in the DP as the fundamental reflections have been over-exposed so that the additional reflections can be clearly observed. Two variants of a disordered orthorhombic phase were identified, which have been labelled 'orth1' and 'orth2'. It is the orthorhombic phase that leads to the additional reflections identified in Figure 2 (bottom).

A DP has also been recorded along a $<110>_{BCC}$ zone axis, Figure 5. A grid of bcc reflections with additional B2 superlattice reflections can be seen, and the splitting of the fundamentals owing to both bcc and B2 phases can be seen far away from the direct beam. The presence of reflections relating to an orthorhombic phase is less clear in this DP, and there is additional intensity present which is consistent with the ω phase [22].

The STEM-HAADF image recorded down this direction further establishes the orientation of the lenses; two sets of the lenses are now blurred out across the microstructure as they have lens normals at 45° to the viewing direction, whilst the final set remain as thin lenses in cross-section.

The identified phases were located within the microstructure using SED. This method involves scanning a probe across the specimen. At each pixel position, a DP is recorded. Virtual dark field images can be produced by mapping the real space origin of intensity in specific regions of the DP. This process was carried out

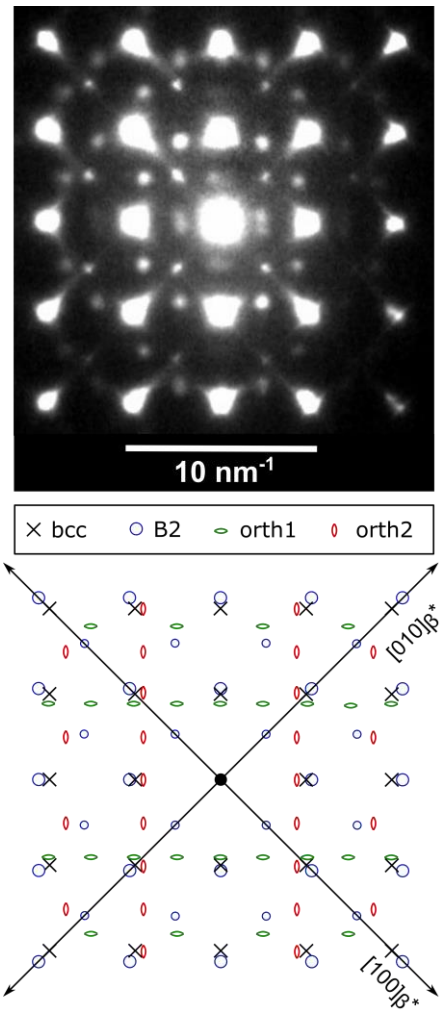

Figure 4 Top - $<100>_{BCC}$ DP recorded for the alloy after the homogenisation heat treatment. Bottom – schematic simulated DP for bcc, B2 and two variants of orthorhombic phase.

down the $<100>_{BCC}$ zone axis for reflections relating to both orthorhombic orientations, as well as for the B2 superlattice reflection.

Figure 6 depicts the results for the two orthorhombic orientations. In each case, the virtual dark field image is shown, as well as a characteristic DP from an individual pixel. If the intensity from both virtual dark

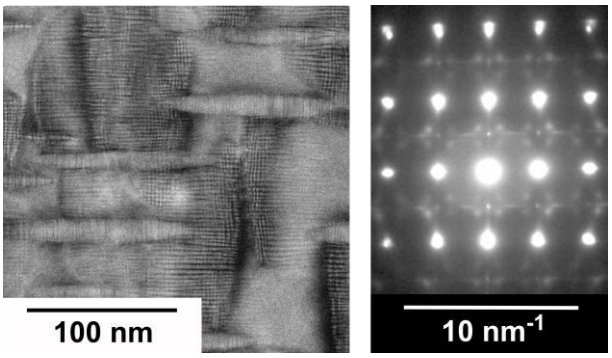

Figure 5 Data recorded along the $<110>_{BCC}$ zone axis for the alloy after homogenisation heat treatment. Left – STEM-HAADF image, Right – TEM DP.

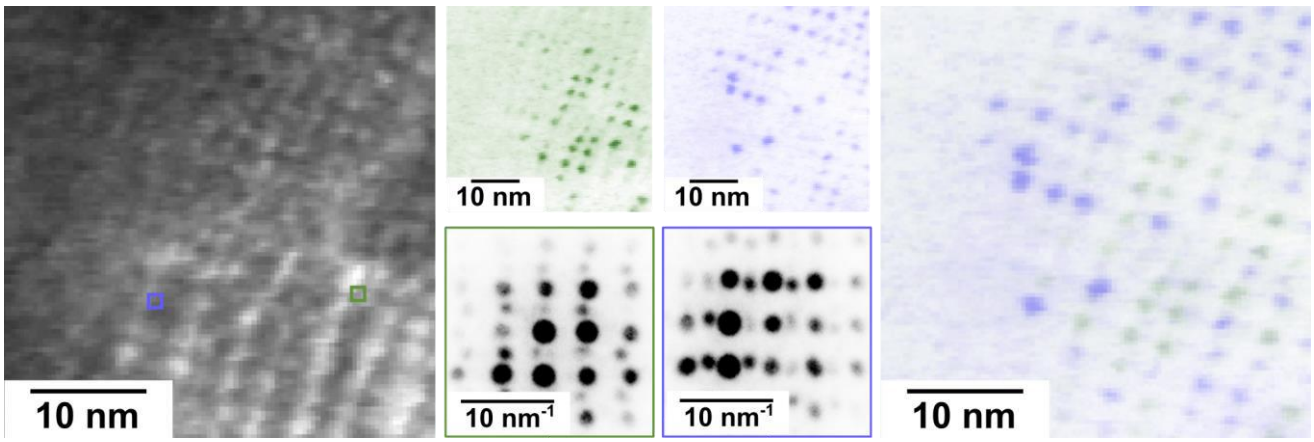

Figure 6 SED recorded for the alloy in the homogenised condition. Left – virtual STEM-HAADF image generated by using a virtual aperture to capture intensity diffracted to large collection angles. Right – overlaid virtual dark field images produced from the two orthorhombic variants, Middle – virtual dark field images produced for two different orthorhombic variants (green and blue) and characteristic DPs associated with each.

field images are overlaid, it can be seen that the two variants make up an entire grid of precipitates within the lens. SED was utilised to identify that the B2 superlattice reflections also originate from within the lenses, although the specific position of this phase was less clear. Instead, a high-resolution STEM-HAADF image was recorded to locate the phase, Figure 7.

High-resolution STEM-HAADF imaging revealed that the bright square-shaped features are cubic B2 phase, whilst the darker grid network consists of the orthorhombic phase. It is hypothesised that the orthorhombic phase forms in order to minimise the overall misfit strain between the precipitates and the matrix, since the B2 lattice parameter is smaller than that of the parent bcc, and the orthorhombic phase leads to an expansion.

In order to initially assess the mechanical performance of this alloy, a Vickers hardness test was performed. The result, 590 HV5.0, is very high and corresponds to a yield strength of over 1500 MPa.

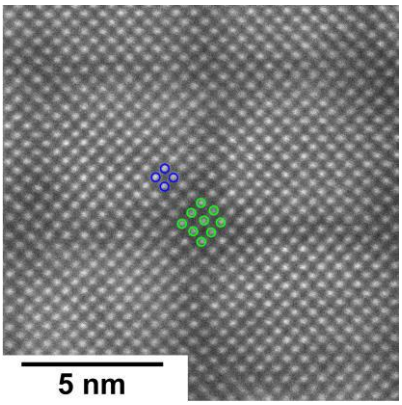

Figure 7 High resolution STEM-HAADF image depicting atomic columns within a plan view precipitate. Some atoms have been circled to highlight different structures: Dark blue – cubic B2 structure, Green – orthorhombic structure with characteristic zig-zag.

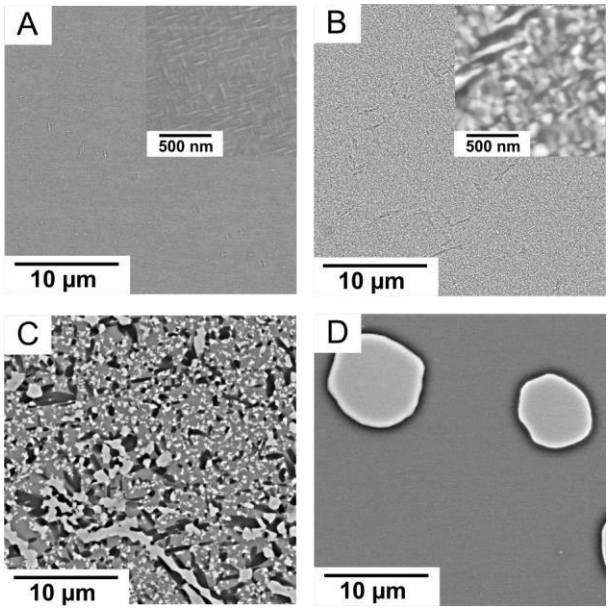

Figure 8 SEM BSE micrographs of the alloy after heat treatment at various temperatures for 100 hours. A – 400 °C, B – 600 °C, C- 800 °C, D – 1000 °C. A and B contain higher magnification sections.

5. Further Investigation

5.1. Effect of temperature

The effect of heat treatment at a range of higher temperatures was investigated to determine the elevated temperature phase behaviour of this alloy. A characteristic SEM BSE micrograph recorded after heat treatment at each temperature is included in Figure 8.

After a heat treatment at 400 °C for 100 hours, the microstructure appears very similar to that after the homogenisation heat treatment and quench. Lens-shaped precipitates were observed within the matrix and no further macroscale phases formed at temperature.

After heat treatment at 600 °C and 800°C, three phases are present. These have been identified by XRD and EDX to be bcc, B2 and α_2. The microstructure after the 600 °C heat treatment is much finer, as would be

expected from a lower temperature age. At 1000 °C the α_2 is no longer thermodynamically stable and only bcc and B2 phases are present.

5.2. Effect of composition

Two additional alloys were fabricated to explore the effect of small compositional changes in the vicinity of the alloy reported above. These were Ti-20Fe-15Al (at.%) and Ti-15Fe-10Al (at.%). Both alloys underwent the same homogenisation treatment (24 h at 1115 °C) and a subsequent ageing treatment of 100 h at 400 °C. The microstructures as reported in Figure 9 show that some finescale breakdown appears to occur in both alloys, and that they are morphologically different from each other.

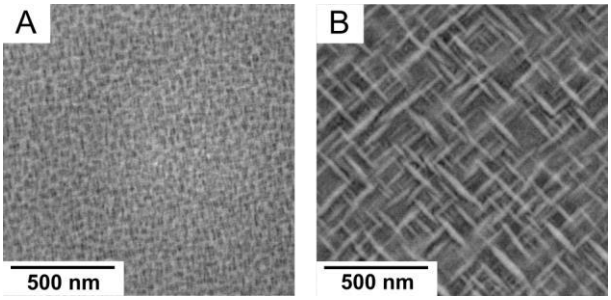

Figure 9 SEM BSE micrographs of two alloys with different compositions after homogenisation and subsequent ageing at 400 °C for 100 hours. A – Ti15Fe10Al (at.%), B – Ti20Fe15Al (at.%).

6. Conclusions

An alloy has been produced in the Ti-Fe-Al system which exhibits a hierarchical microstructure after a homogenisation heat treatment and quench. The microstructure consists of bcc, B2 and orthorhombic phases, where the latter two are assembled in a regular array within finescale lenticular precipitates. The orthorhombic phase is thought to reduce the misfit between the B2 precipitates and matrix. The alloy has a high hardness as a result. The thermal stability of the microstructure has been reported, which shows that bcc, B2 and α_2 phases are stable at higher temperatures, and the effect of compositional adjustment has briefly been reported, demonstrating that even small adjustments in Fe content may lead to morphological differences in the microstructure.

7. Acknowledgements

The authors would like to thank S. Michalik, N. L. Church and J. Hogg for their assistance with sample preparation and data collection at the I12 beamline, and N. L. Church for the dimensional reduction of the data.

8. References

1. R.P. Kolli, A. Devaraj, *Metals*, 8 (2018) 506.
2. N. Clément, A. Lenain, P.J. Jacques, *JOM* 59 (2007) 50–53.
3. D. Banerjee, A.K. Gogia, T.K. Nandi, V.A. Joshi, *Acta Metallurgica* 36 (1988) 871–882.
4. B. Mozer, L.A. Bendersky, W.J. Boettinger, R.G. Rowe, *Scripta Metallurgica et Materiala* 24 (1990) 2363–2368.
5. A.J. Ardell, V. Munjal, D.J. Chellman, *Metallurgical Transactions A* 7 (1976) 1263–1268.
6. R.C. Reed, The Superalloys, Cambridge University Press, Cambridge, 2006.
7. J. Sato, T. Omori, K. Oikawa, I. Ohnuma, R. Kainuma, K. Ishida, *American Association for the Advancement of Science* 312 (2006) 90–91.
8. G.M. Novotny, A.J. Ardell, *Materials Science and Engineering A* 318 (2001) 144–154.
9. L.A. Cornish, R. Süss, L.H. Chown, L. Glaner, *Platinum Metals Review* 53 (2009) 155–163.
10. M. Drakopoulos, T. Connolley, C. Reinhard, R. Atwood, O. Magdysyuk, N. Vo, M. Hart, L. Connor, B. Humphreys, G. Howell, S. Davies, T. Hill, G. Wilkin, U. Pedersen, A. Foster, N. De Maio, M. Basham, F. Yuan, K. Wanelik, *Journal of Synchrotron Radiation* 22 (2015) 828–838.
11. M.L. Hart, M. Drakopoulos, C. Reinhard, T. Connolley, *Journal of Applied Crystallography* 46 (2013) 1249–1260.
12. M. Basham, J. Filik, M.T. Wharmby, P.C.Y. Chang, B. El Kassaby, M. Gerring, J. Aishima, K. Levik, B.C.A. Pulford, I. Sikharulidze, D. Sneddon, M. Webber, S.S. Dhesi, F. Maccherozzi, O. Svensson, S. Brockhauser, G. Náray, A.W. Ashton, *Journal of Synchrotron Radiation* 22 (2015) 853–858.
13. Hyperspy software, 10.5281/zenodo.592838
14. Pyxem software, 10.5281/zenodo.2649351
15. J.O. Andersson, T. Helander, L. Höglund, P.F. Shi, B. Sundman, *Calphad* 26 (2002) 273–312.
16. R.D. Jones, A.J. Knowles, W.J. Clegg, *Scripta Materialia* 200 (2021) 113905.
17. A.J. Knowles, N.G. Jones, C.N. Jones, H.J. Stone, *Metallurgical and Materials Transactions A* 48 (2017) 4334–4341.
18. R. Strychor, J.C. Williams, W.A. Soffa, *Metallurgical and Materials Transactions A* 19A (1988) 225-234.
19. X.M. Huang, L.L. Zhu, G.M. Cai, H.S. Liu, Z.P. Jin, *Journal of Materials Science* 52 (2017) 2270–2284.
20. M. Palm, J. Lacaze, *Intermetallics* 14 (2006) 1291–1303.
21. L. Vegard, *Zeitschrift Für Physik* 5 (1921) 17–26.
22. D. De Fontaine, N.E. Paton, J.C. Williams, *Acta Metallurgica* 19 (1971) 1153–1162.

EFFECTS OF ALLOYING ON SLIP INTERMITTENCY AND LOCALISATION IN α-Ti

Felicity F. Worsnop[1,2], Rachel E. Lim[3,4], Joel V. Bernier[3], Darren C. Pagan[4], Yilun Xu[2], Thomas P. McAuliffe[2], David Rugg[5], David Dye[2]

1 Department of Materials Science and Engineering, Massachusetts Institute of Technology, 77 Massachusetts Avenue, Cambridge, MA 20139, USA.
2 Department of Materials, Royal School of Mines, Imperial College London, Prince Consort Road, London SW7 2AZ, UK.34 Lawrence Livermore National Laboratory, 7000 East Avenue, Livermore, CA 94550, USA.
4 Department of Materials Science and Engineering, Pennsylvania State University, 221 Steidle Building, University Park, PA 16802, USA.
5 Formerly with Rolls-Royce plc., Elton Road, Derby DE24 8BJ, UK.

Cold dwell fatigue exemplifies the importance of time-dependent, spatially localised slip in understanding the performance of α+β titanium alloys for jet engine applications. Typically present in the hcp α phase of such alloys are interstitial oxygen (at a few hundred wppm) and aluminium (at a few wt.%). Both are known to promote spatial localisation of slip within α grains, through strong oxygen–dislocation core interactions and due to crystallographic ordering of Al to form Ti_3Al α_2 domains. The effects of these solutes on the time intermittency of slip have not been well established, however, leaving an open question regarding their contributions to dwell fatigue crack initiation. Here, we study model alloys Ti–7Al–0.05O and Ti–7Al–0.25O (wt.%) in crystallographically disordered and ordered states to isolate the effects of interstitial O and ordering of Al. Using in situ high-energy X-ray diffraction microscopy, the time-dependent behaviours of different slip systems in hundreds of grains were tracked during creep loading. Post-deformation dislocation configurations were characterised to provide complementary spatial and temporal pictures of slip phenomena. Our results demonstrate that, despite superficially similar effects on spatial localisation of slip at the grain scale, oxygen and aluminium have notably dissimilar effects on time intermittency of slip in hcp titanium.

Keywords: Dwell fatigue, slip intermittency, creep, high-energy X-ray diffraction microscopy.

1. Introduction

Critical rotating parts of jet engines require predictive capability regarding their failure mechanisms in order to safely manage component lifetimes in service. For cold dwell fatigue, in which cyclic lifetimes can be reduced by over an order of magnitude by holds at the peak stress [1], it has been established that crack nucleation is encouraged by long slip bands imposing a localised stress on regions of microstructure unable to co-deform [2].

Two microstructural features contributing to slip band formation are the ordered α_2 Ti_3Al phase and high concentrations of interstitial oxygen in the hcp α phase of alloys containing several wt.% Al. [3,4]. The presence of α_2 has been linked with reductions in dwell fatigue resistance [5], but the mechanistic basis for oxygen's influence on dwell fatigue cracking is less well understood. Recent progress in the understanding of O interstitials' interactions with dislocations [6] enables further progress towards mechanistic understanding of spatial localisation as well as time intermittency of slip in these alloys, crucial to enabling predictive capability and dwell-resistant alloy design.

2. Slip localisation and intermittency in α-Ti

In this work [7], model alloys Ti–7Al–0.05O and Ti–7Al–0.25O (wt.%) were used to represent the hcp α phase of commercial α+β alloys such as Ti–6Al–4V (wt.%) with oxygen concentrations at the lower and upper bounds of industrial relevance, respectively. Heat treatments were applied to produce fine, uniform dispersions of the ordered Ti_3Al α_2 phase, giving a set of four conditions that were tested in stress relaxation and creep in order to determine the independent and combined effects of O and α_2 on plasticity.

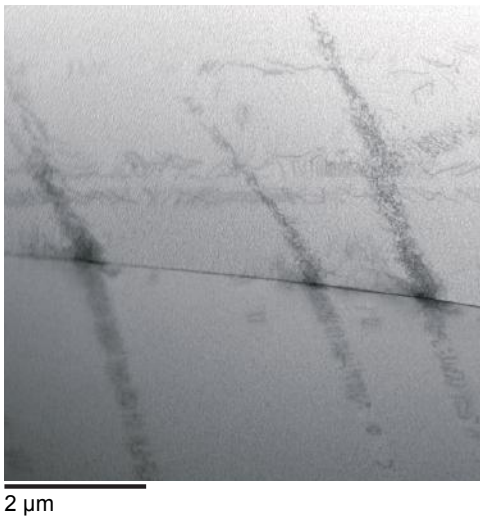

Figure 1. Slip bands impinging on a grain boundary in Ti–7Al–0.05O containing Ti_3Al α_2 precipitates (visible as mottled contrast in the image). The ordered precipitates cause restriction of slip to narrow bands, as well as preferential movement of dislocations in pairs.

Stress relaxation experiments demonstrated that while the rate of relaxation varied with α_2 precipitation, the influence of interstitial oxygen content was subtler. Post mortem TEM inspection of dislocation structures produced by stress relaxation from 1.5% plastic strain

showed that both α_2 precipitates and a raised O content caused slip to occur in confined bands, Fig. 1.

In situ far-field high energy X-ray diffraction microscopy (ff-HEDM) experiments were conducted to investigate the time intermittency of slip during creep. In these experiments, grain-scale information is captured for a mesoscopic volume of microstructure, enabling time-resolved tracking of the position, orientation and strain for each grain during deformation. As such, the occurrence of dislocation avalanches in individual grains can be analysed statistically. Direct observations were also made of individual load-shedding events between neighbouring soft–hard grain pairs, supporting the proposed crack nucleation mechanism.

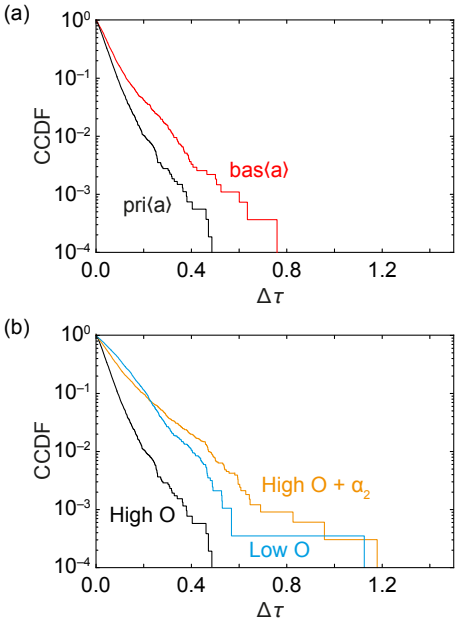

Figure 2. Complementary cumulative distribution functions of grain-scale stress drop magnitudes observed during creep of Ti–7Al–O alloys. Larger $\Delta\tau$ corresponds to larger slip avalanches, undesirable from a dwell fatigue crack initiation perspective. (a) Comparison of pri⟨a⟩ and bas⟨a⟩ behaviour for quenched Ti–7Al–0.25O. (b) Effects of O content and ageing to produce ordered α_2 Ti_3Al precipitates.

Distributions of stress drop event magnitudes, $\Delta\tau$, were obtained for the high and low oxygen alloys in the quenched (α) and aged ($\alpha+\alpha_2$) conditions, for each of the pri⟨a⟩, bas⟨a⟩ and pyr⟨c+a⟩ slip system families. In each case, pri⟨a⟩ slip was found to proceed by a larger number of smaller avalanches than bas⟨a⟩ slip, Fig. 2(a). Varying oxygen content showed that with increasing interstitial O concentration, slip intermittency is smoother, while the introduction of α_2 ordered domains causes dislocation motion to proceed by larger, more infrequent avalanches, Fig. 2(b).

Further investigation of the mechanistic basis for the effects of oxygen was conducted using discrete dislocation plasticity (DDP) modelling. This study, presented in [8], explains the relationship between interstitial solute atom density and thermally activated processes, contributing to recent progress towards predictive capability of dwell fatigue cracking susceptibility for $\alpha+\beta$ Ti alloys.

In summary, our results show that, despite both O and α_2 encouraging planar slip, they have opposite effects on the time intermittency of slip. This adds to the evidence that high concentrations of α_2-forming solutes and large slip lengths should be avoided when designing titanium alloys against dwell fatigue crack initiation.

3. Acknowledgements

F.F.W. was funded by Rolls-Royce plc and by the EPSRC Centre for Doctoral Training in the Advanced Characterisation of Materials (EP/L015277/1). F.F.W. wishes to thank Dr Thomas J. Kwok for his assistance in preparing the alloys. Much of this work was initiated and funded through the Hexmat EPSRC program grant EP/K034332/1. D.D. also acknowledges the provision of a Royal Society Industry Fellowship. Y.X. acknowledges the financial support by the Engineering and Physical Sciences Research Council for funding through the grant EP/R018863/1. J.V.B. acknowledges this work was performed under the auspices of the U.S. Department of Energy by Lawrence Livermore National Laboratory under Contract DE-AC52-07NA27344, and LDRD grant #20-ERD-044 (LLNL-JRNL-835496). This work is based upon research conducted at the Center for High Energy X-ray Sciences (CHEXS) which is supported by the National Science Foundation under award DMR-1829070.

4. References

1. A.L. Pilchak. Fatigue crack growth rates in alpha titanium: faceted vs. striation growth. *Scripta Mater.*, 68(5):277–280, 2013.
2. F.P.E. Dunne and D. Rugg. On the mechanisms of fatigue facet nucleation in titanium alloys. *Fatigue Fract. Eng. M.*, 31(11):949–958, 2008.
3. J.C. Williams et al. Deformation behavior of HCP Ti–Al alloy single crystals. *Metall. Mater. Trans. A*, 33(3):837–850, 2002.
4. J.C. Williams et al. The influence of oxygen concentration on the internal stress and dislocation arrangements in α titanium. *Metall. Mater. Trans. B*, 3(11):2979– 2984, 1972
5. M.C. Brandes et al. The influence of slip character on the creep and fatigue fracture of an α Ti-Al alloy. *Mat. Sci. Eng. A–Struct.*, 41(13):3463–3472, 2010.
6. Yu, Q. et al. Origin of dramatic oxygen solute strengthening effect in titanium. *Science* 347, 635–639 (2015).
7. Worsnop. F.F. et al. The influence of alloying on slip intermittency and the implications for dwell fatigue in titanium. *Nat. Commun.* 13, 5949 (2022).
8. Xu, Y. et al., Slip intermittency and dwell fatigue in titanium alloys: a discrete dislocation plasticity analysis (under review).

NEAR-TO-NET TITANIUM EXTRUSIONS AS A SUBSTITUTE FOR AEROSPACE PLATE AND FORGINGS

Steven James[1], Phani Gudipati[1], Anton Kantor[1], Josh Phillips[1]

[1] *Plymouth Tube Company, 29W150 Warrenville Rd, Warrenville, IL 60555, USA.*

Global supply chain conditions have disrupted traditional aerospace part production methods, and it is becoming increasingly difficult to source large aerospace parts produced from Ti-6Al-4V (Ti-64) plate and forgings. A potential solution to aid in meeting post-pandemic re-emerging demand is to explore alternative manufacturing solutions to existing production parts. Plymouth Engineered Shapes (PES) has developed advanced manufacturing techniques to produce near-to-net extrusions that replicate the required plate properties for parts that have traditionally been manufactured from rolled plate. While the primary objective of this development was to have an alternative manufacturing source for these products, utilizing shaped extrusions also has enabled other benefits. Parts that have historically required welding to join multiple plates together now can be made of a single shaped extrusion. This simplifying of the design improves the overall integrity of the part and reduces manufacturing time. Also, the required amount of machining to achieve the final part can be significantly reduced utilizing near-net shaped extrusions improving yield amongst other aspects of manufacturing. This paper will cover an in-depth exploration of extrusion properties and compare them to aerospace specifications. In addition, considerations for potential applications and details of this manufacturing methodology will be given.

Keywords: Ti-64, Near-to-net, Extrusions, Applications of extrusions, Substitute to aerospace plates and forgings,

1. Background and motivation

Titanium alloys have a unique combination of properties that are very enticing to aerospace design engineers. They are strong, lightweight, corrosion resistant, and are compatible with many composites. However, the biggest drawback of titanium has always been its high cost of production and machining / fabrication. [1]

Over the years there have been many attempts to reduce the cost of titanium. Specific examples of this include, lowering the cost of feedstock and replacement of subtractive manufacturing with additive manufacturing processes. While some of these methods have shown much promise, a significant and viable solution is still very far from being widely implemented in aircraft design.

It is well known that in the aerospace industry, there are limited number of internationally qualified producers of Ti-6Al-4V (Ti-64) plate and an even smaller number of producers capable of making specialized plates with low residual stress and very good flatness in alpha + beta or beta annealed condition. The recent war in the Eastern parts of the world has significantly disrupted the global supply chain conditions and thus has further limited the qualified producers of titanium plate and forgings. However, continued growth in demand and shortage of skilled labour, resources, and global manufacturing capacity has now led to significant increase in price for titanium. This includes aerospace plate and forgings. All these factors have caused lead-times to be greatly extended, and it is becoming increasingly difficult to source large aerospace parts produced from Ti-64 plate. [2]

A potential solution to aid in reducing the cost of titanium and meeting post-pandemic re-emerging demand is to explore alternative manufacturing solutions to existing production parts. Near-to-net extrusion technology is one such manufacturing process that provides a solution to the current global supply chain issues and futuristic approach to reduction in overall production costs of titanium.

This paper will cover an in-depth exploration of extrusion properties and compare them to aerospace specifications for plate and forgings of like heat treatment conditions. In addition, considerations for potential applications and details of this manufacturing methodology will be given.

2. Materials, Manufacturing Process, and Testing

To achieve industry adoption, any alternative manufacturing solutions must adhere as much as possible to standard materials and manufacturing processes. With that in mind, this work has been focused around using typical materials and methods commonly used in the aerospace industry. This includes utilizing NADCAP certified testing facilities and adhering to the appropriate ASTM testing standards.

2.1. Materials

The current study focusses on the mainstay titanium alloy, Ti-64, which is an α–β alloy with a standard composition per ASTM B265 Grade 5 (Table 1). Ti-64 makes up more than 50% of all global titanium alloy production and is extensively used in aerospace. For this study, the alloy was sourced as 150mm to 230mm diameter billet with an alpha + beta microstructure (Figure 1). Grain size of the billet is measured to be around ASTM #8. [3]

Table 1: Chemistry specification for ASTM B265 Grade 5, Titanium Sheet & Plate [3]

Element	Min (Wt. %)	Max (Wt. %)
Aluminum	5.5	6.75
Vanadium	3.5	4.5
Carbon		0.08
Oxygen		0.20
Nitrogen		0.03
Hydrogen		0.015
Iron		0.40

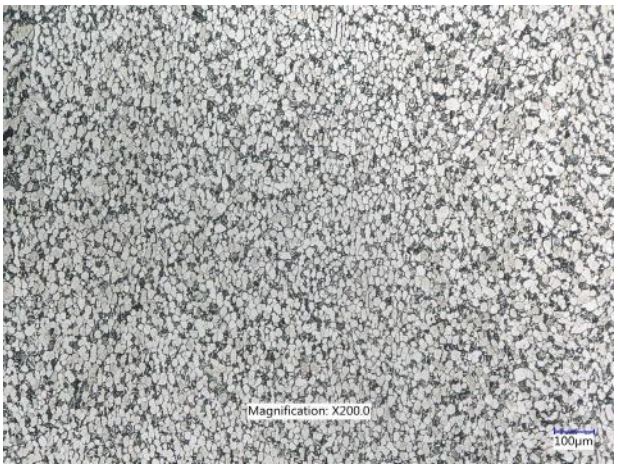

Figure 1. Ti-64 alpha/beta billet microstructure. 200x optical micrograph. Scale bar is 100µm.

2.2. Manufacturing Methods

As part of this study, Ti-64 billets of the varying diameters previously mentioned were extruded in the beta region (generally >1030°C depending on calculated beta transus temperature) to produce selected geometrical profiles. Two distinctive manufacturing routes, to be described below, were adopted to achieve a wide range of properties that could distinctly cater to different applications.

2.2.1. Standard Extrusions

These profiles were extruded above the beta transus temperature. They do not undergo any additional heat treatment before a hot stretch straightening process. The hot stretch straightening can also act as a below beta transus temperature stress relief anneal heat treatment. These extrusions are then chemically treated to remove the surface alpha case.

2.2.2. Beta Annealed Extrusions

Like standard extrusions, these profiles are extruded above the beta transus temperature. They then undergo a proprietary beta heat treatment before a hot stretch straightening process. Similar to the standard extrusions, these are also chemically treated to remove surface alpha case. [4]

2.3. Testing

Further to the production of these extruded profiles, material properties have been evaluated by excising test coupons off the front and the back, in the L, T and ST directions. ASTM and customer standards were adhered to while performing room temperature mechanical testing, fracture toughness, high cycle fatigue, and crack growth studies. Optical microscopy was performed to evaluate the grain structure and size.

3. Properties of Plymouth Ti-64 extrusions

3.1. Properties of standard extrusions

A standard PES Ti-64 aerospace extrusion adheres to the requirements of aerospace specification standards or similar customer specifications. For Ti-64, an aerospace specification requires a minimum yield strength of 830 MPa, ultimate tensile strength of 900 MPa, elongation of 10%, and reduction of area of 20%. It is to be noted that the standard extrusions exceed strength requirements by 10%, and ductility requirements by 50%. Fracture toughness of standard Ti-64 extrusions typically fall in the range of 55 to 90 MPa √m depending on extrusion ratio. [5]

3.2. Properties of beta annealed extrusions

To further improve toughness, extrusions can be heat treated above the beta transus temperature (beta annealed). This can increase fracture toughness above 100 MPa √m, but usually comes with a sacrifice of mechanical strength. An additional stress relief heat treatment after beta anneal can recover some of the lost strength (~5%) with a ~10% reduction in ductility. There is only a slight decrease in high cycle fatigue between standard and beta annealed extrusions. Detail of all mechanical property results is shared in section 4.1 & 4.2.

Table 2 represents typical mechanical properties from standard and beta annealed PES extrusions. In addition to these typical values, Figure 2 demonstrates typical strength ranges of both standard and beta annealed Ti-64 extrusions which can be influenced by many factors of production, material, and sample orientation.

Table 2: Typical properties of Ti-64 extrusions

Condition	YS (MPa)	UTS (MPa)	5D El (%)	RA (%)
Standard	838	954	16.4	34.5
Beta Anneal	807	958	10.0	25.4
Beta Anneal + Stress Relieve	850	974	9.1	16.4

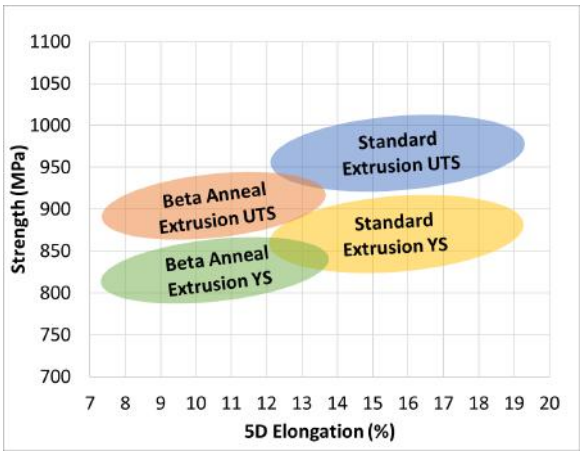

Figure 2. Extruded Ti-64 - Tensile Range

4. Comparison to plate and forgings

For extrusions to be a suitable substitute for aerospace plate and forgings, they will need to meet industry specifications. In addition to helping solve supply chain challenges, utilizing near-to-net extrusions can offer other design benefits, such as weight reduction and tighter tolerances. It also influences cost considerations such as total material use, reduced machining time, and less production steps.

To evaluate suitability, extrusion properties were compared to specifications for an aircraft OEM in both a standard hot rolled / forged condition, and a beta annealed condition. [6][7]

4.1. Comparison to standard extrusions

Key properties assessed include strength (0.2% yield strength, ultimate tensile strength), ductility (5D elongation, reduction of area), fracture toughness, high cycle fatigue strength, and fatigue crack growth. All testing was done at room temperature in air. Figures 3-8 demonstrate standard extrusions exceeding the strength, ductility, fracture toughness, and fatigue requirements in all sample orientations when measured against aerospace plate that was alpha/beta hot rolled, then annealed. [8]

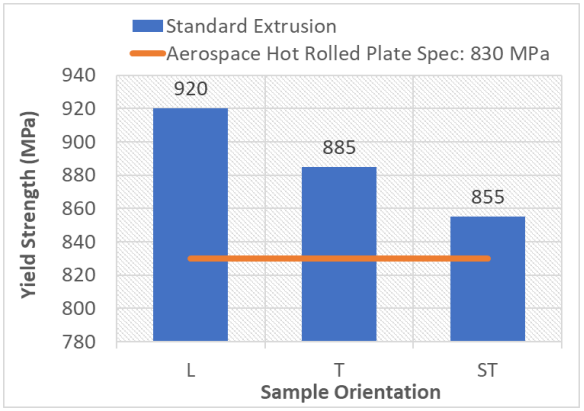

Figure 3. Yield strength of standard extrusions in longitudinal, transverse, and short transverse orientations versus a typical requirement for aerospace plate that has been alpha/beta hot rolled, then annealed.

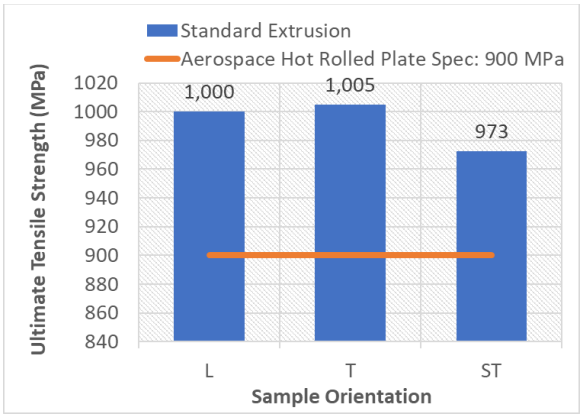

Figure 4. Ultimate tensile strength of standard extrusions in longitudinal, transverse, and short transverse orientations versus a typical requirement for aerospace plate that has been alpha/beta hot rolled, then annealed.

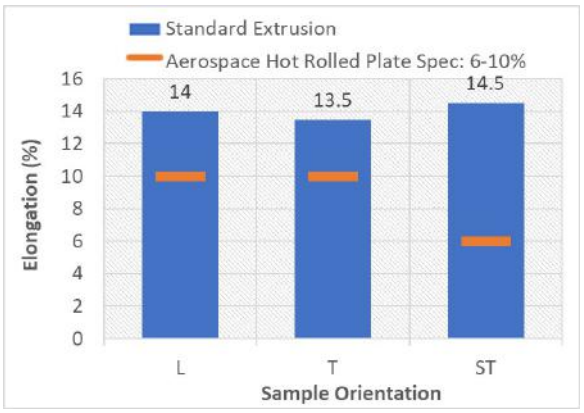

Figure 5. 5D elongation of standard extrusions in longitudinal, transverse, and short transverse orientations versus a typical requirement for aerospace plate that has been alpha/beta hot rolled, then annealed.

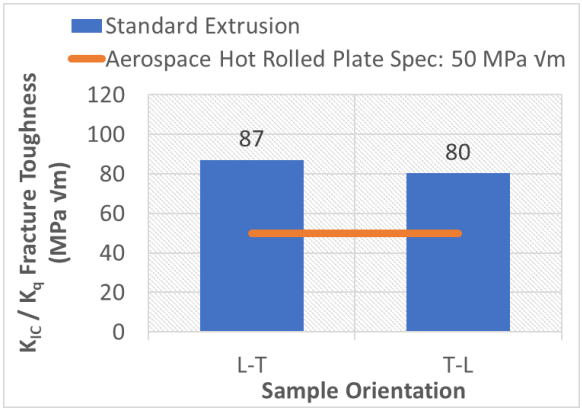

Figure 6. Fracture toughness of standard extrusions in longitudinal-transverse and transverse-longitudinal orientations versus a typical requirement for aerospace plate that has been alpha/beta hot rolled, then annealed.

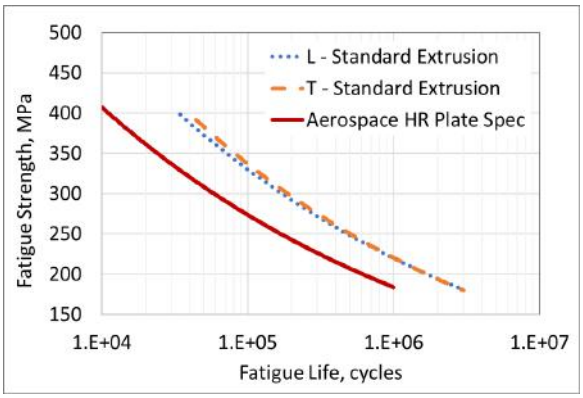

Figure 7. High cycle fatigue life of standard extrusions in longitudinal and transverse orientations versus a typical requirement for aerospace plate that has been alpha/beta hot rolled (HR), then annealed.

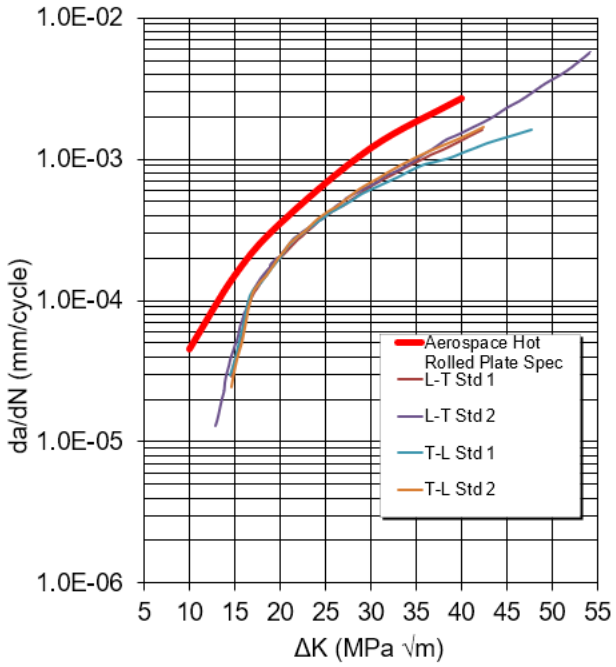

Figure 8. Fatigue crack growth of standard annealed extrusions in L-T and T-L orientations versus a typical requirement for aerospace plate that has been alpha/beta hot rolled, then annealed. Stress ratio: 0.10, Frequency: 20 Hz, Constant amplitude

4.2. Comparison to extrusions after beta anneal

A similar comparison was made for beta annealed extrusions versus beta annealed alpha/beta hot rolled aerospace plate and beta annealed alpha/beta hot forged forgings. Again, properties were evaluated for strength (0.2% yield strength, ultimate tensile strength), ductility (elongation, reduction of area), fracture toughness, high cycle fatigue strength, and fatigue crack growth. All testing was done at room temperature in air. These comparisons against aerospace specification requirements are represented by Figures 9-14. By most metrics, dependant on orientation and size requirements, beta annealed Ti-64 extrusions can meet aerospace requirements for beta annealed plate and forgings. For situations where requirements are not met, an additional stress relief heat treatment can be applied post beta anneal to increase strength approximately 5% with around a 10% reduction in ductility. Following the stress relief, all requirements evaluated can be met. Fatigue life is largely unaffected by the beta heat treatment of beta extruded products. [9]

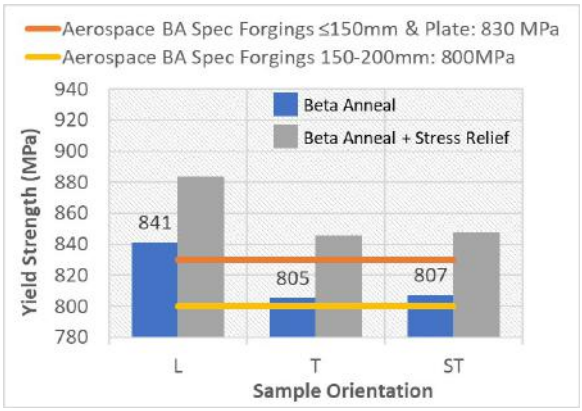

Figure 9. Yield strength of beta annealed (BA) extrusions in longitudinal, transverse, and short transverse orientations versus a typical requirement for aerospace plate/forgings that has been alpha/beta hot rolled/forged, then beta annealed. Also illustrated is the increase of yield strength associated with adding a stress relief heat treatment after the beta anneal.

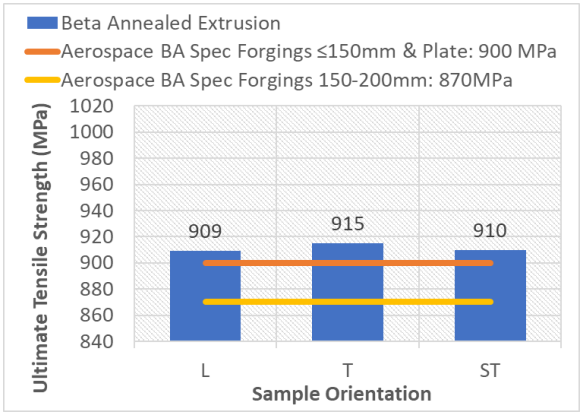

Figure 10. Ultimate tensile strength of beta annealed (BA) extrusions in longitudinal, transverse, and short transverse orientations versus a typical requirement for aerospace plate/forgings that has been alpha/beta hot rolled/forged, then beta annealed.

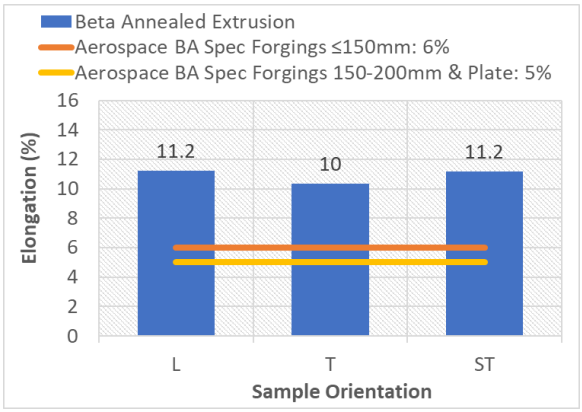

Figure 11. 5D elongation of beta annealed (BA) extrusions in longitudinal, transverse, and short transverse orientations versus a typical requirement for aerospace plate/forgings that has been alpha/beta hot rolled/forged, then beta annealed. Reduction of area exceeded requirements by similar margins.

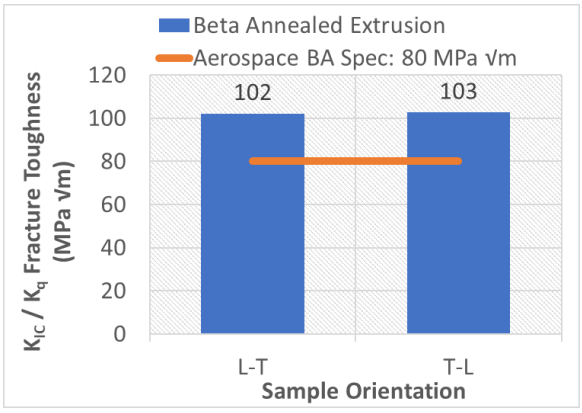

Figure 12. Fracture toughness of beta annealed (BA) extrusions in longitudinal-transverse and transverse-longitudinal orientations versus a typical requirement for aerospace plate/forgings that has been alpha/beta hot rolled/forged, then beta annealed.

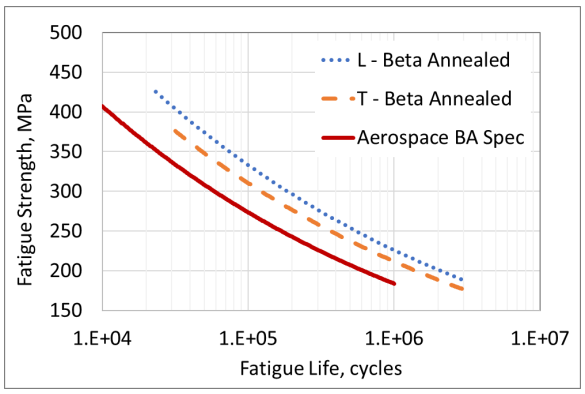

Figure 13. High cycle fatigue life of beta annealed (BA) extrusions in longitudinal and transverse orientations versus a typical requirement for aerospace plate/forgings that has been alpha/beta hot rolled/forged, then beta annealed.

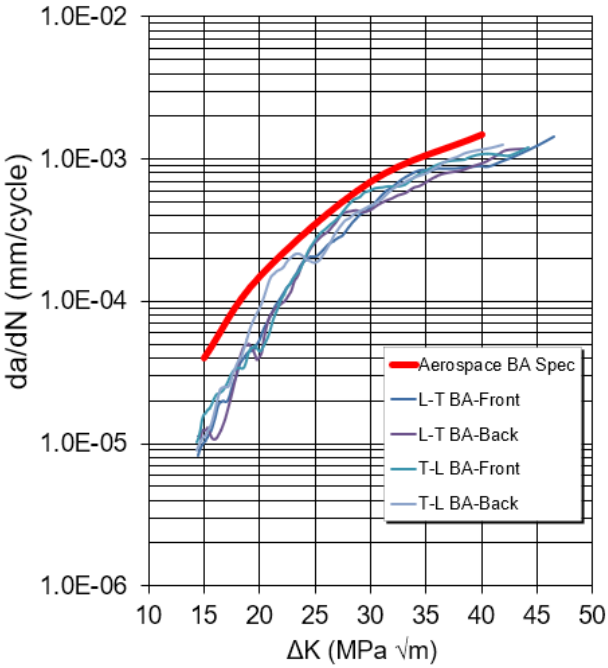

Figure 14. Fatigue crack growth of beta annealed (BA) extrusions in L-T and T-L orientations versus a typical requirement for aerospace plate/forgings that has been alpha/beta hot rolled/forged, then beta annealed. Stress ratio: 0.10, Frequency: 20 Hz, Constant amplitude

5. Discussion

In all cases, it has been shown that extrusions produced can meet or exceed aerospace customer mechanical property requirements for similarly heat-treated plate and forgings. To further the evaluation of the mechanical property results, micrographs were taken in each condition (Figures 15-16).

The standard process exhibits recrystallized prior beta grains with colony alpha structure. For the beta annealed extrusions, a coarse beta grain structure is observed. These resulting microstructures were both

expected given the processing conditions and material history.

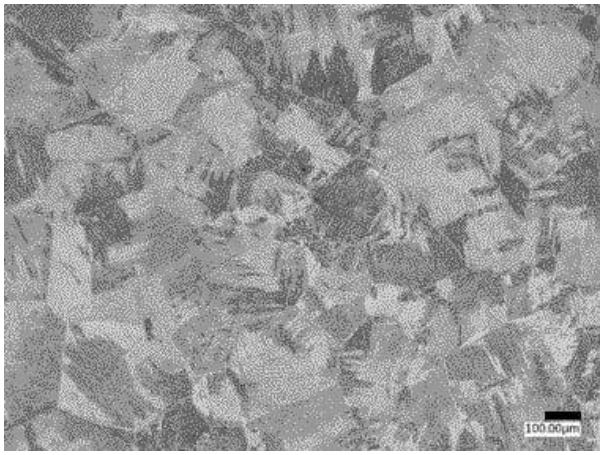

Figure 15. Standard Ti-64 extrusion microstructure. 200x optical micrograph. Scale bar is 100µm.

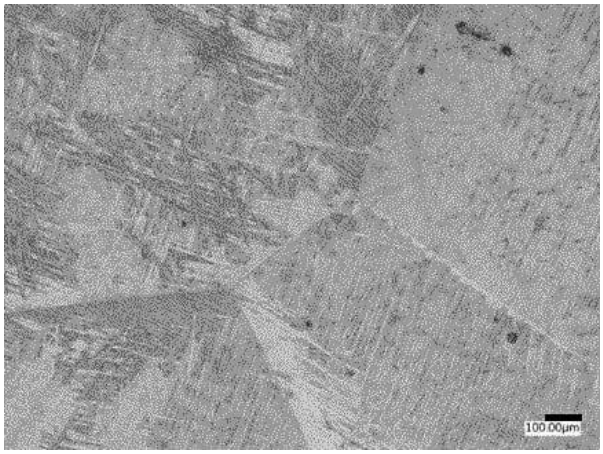

Figure 16. Ti-64 extrusion microstructure after beta anneal. 200x optical micrograph. Scale bar is 100µm.

6. Summary

A thorough review of the data suggests that standard and beta annealed extrusions have great potential to help relieve the aerospace plate and forging shortage. When appropriate heat treatments are compared, Plymouth extrusions can meet or exceed existing aerospace specification requirements for plate and forgings. This indicates a real opportunity for extrusions as a substitute for plate and forgings in many applications.

Furthermore, there are significant benefits that can be realized when making the transition to extrusions. For instance, the ability to produce more complex shapes requiring less welding and near-net shapes with reduced machining necessary to make the final part could be enough to offset any increased cost that may be associated with the substitution.

7. References

1. R. A Wood, R. J. Favor, *Titanium Alloys Handbook,* December 1972
2. Ivasyshyn, O.M., Aleksandrov, A.V. *Status of the titanium production, research, and applications in the CIS*, Mater Sci 44, 311–327 (2008).
3. Campanella, D., Buffa, G., El Hassanin, A. et al. Mechanical and microstructural characterization of titanium gr.5 parts produced by different manufacturing routes. Int J Adv Manuf Technol 122, 741–759 (2022).
4. "Standard Specification for Titanium and Titanium Alloy Strip, Sheet, and Plate," ASTM F1045-07, in Annual Book of ASTM Standards, vol. 15.07
5. "Titanium Alloy Extrusions and Flash Welded Rings 6Al - 4V Annealed Beta Processed AMS4935M", SAE International, Rev. M, 2022-08-17
6. P. Gudipati, M. Campbell, *Near-to-Net Shaped Aerospace Extrusions,* AeroMat (2018)
7. P. Gudipati, M. Campbell, B. Rogers, *Technological advancements in the manufacture of near-to-net extrusions for aerospace applications,* 15th World Conference on Titanium (Ti-2023), June 12-16, 2023, Edinburgh, UK.
8. Task Committee on Materials of the Committee on Aerospace Structures and Materials of the Aerospace Division, *Structural Materials in Aerospace Applications,* Transportation Engineering Journal of ASCE 108.5 (1982): 484-494.
9. R.J.H. Wanhill, S.A. Barter, *Fatigue of β processed and β heat-treated titanium alloys*, (2009)

TECHNOLOGICAL ADVANCEMENTS IN MANUFACTURE OF NEAR-TO-NET EXTRUSIONS FOR AEROSPACE APPLICATIONS

Phani Gudipati[1], Michael Campbell[2], and Brandon Rogers[1]

[1] *Plymouth Tube Company, 29W150 Warrenville Rd, Warrenville, IL 60555, USA*
[2] *Plymouth Engineered Shapes, 201 Commerce Ct, Hopkinsville, KY 42240, USA*

Extruded shapes generally are considered for the manufacture of long members of the aircraft that require constant cross-sectional areas. While titanium extrusions are used in a variety of applications ranging from sub-sonic systems to un-manned submarines, most common aerospace applications are limited to seat tracks using the work horse grade Ti-6Al-4V (Ti-64). Utilizing some of the favourable characteristics of Ti-64, such as flow stress above beta transus, Plymouth Engineered Shapes has developed advanced manufacturing techniques to produce near-to-net extrusions which can be utilized in various aero-engine applications alongside standard products. The gross titanium extrusion produces substantial material yield savings because of closer shape approximation and requires less machining to achieve the finished product. This paper will discuss various Ti-64 profiles extruded at Plymouth and demonstrate the improvement in buy-to-fly ratio due to the use of near-to-net shapes. In addition, it will present an overview of relevant mechanical properties, microstructural characterization, and the dimensional tolerances held over the length of the extrusion. Residual stresses that play an important role in the performance, machining, and structural stability of the extruded product will also be discussed.

Keywords: Ti-64, Near-to-net, Extrusions, Buy-to-fly, Aerospace applications.

1. Introduction

Extrusion is a compressive deformation process in which a billet is 'forced' (extruded) through a die to obtain a reduction in its cross-section and converted to the desired shape. The length of the extruded part will vary, dependent upon the initial dimensions of the billet and the profile extruded. The extrusion process produces profile cross sections that are uniform over the entire length of the product and hence, is ideally suited for fabrication of long members. Currently, the extrusion process is capable of manufacturing innumerable shapes and profiles that are widely utilized in the aerospace industry. Superior strength to weight ratio, and electrochemical compatibility with graphite in graphite-reinforced organic-matrix composites, make it convenient to employ titanium alloy extrusions for aerospace applications [1].

It is well known that each preform process such as forging, casting and plate stock incurs a considerable loss of material during machining due to the excessive material envelope built around the finished product. Extrusions reduce the buy-to-fly ratio by a significant amount and provide advantages not offered by alternative preform processes. Economic advantages include minimal tooling costs, reduced material usage, lower parts count resulting from the ability to extrude complex shapes over length in a single operation and less downstream machining and finishing [2]. The quality benefits of extrusions include improved surface finish, fine tolerances, superior flatness, and straightness that is critical for long-length structural operations [3]. Proven applications for titanium extrusions in the aerospace industry include floor beams, seat tracks, engine pylons, pylon attachment beams, chords, stiffeners, stringers, spars, flap and slat tracks, hinges, mounting brackets, jet engine rings, and space vehicle components.

To further reduce overall manufacturing costs and improve the buy-to-fly ratio, Plymouth Engineered Shapes has successfully developed an innovative process and manufactured near-to-net shaped Ti-64 extrusions of various geometries, approximately 8-14 meters long. This paper presents different near-to-net shaped extruded profiles and provides an overview of the weight savings, mechanical properties, microstructure, and stability in dimensional tolerances along the full length of the extrusion.

2. Extrusion Process

The extrusion process creates tremendous amount of geometric change and deformation of the work piece, more than any other metal forming processes such as forging, rolling etc. This process takes into consideration a variety of factors, many of which will be specific to each operation. The type of alloy, size of the original billet, geometric cross section of the extruded part, ram speed, and temperature of the billet are all important elements in the design and analysis of an extrusion operation. Typically, commercially available titanium extrusion presses are water hydraulic and have remarkably high strain rates in the range of $10s^{-1}$ or higher [4]. A vast majority of titanium extrusions are performed above the beta transus to allow for lower flow stresses and the ability to form near-to-net products. A beta extruded titanium billet will yield in products with an elongated grain structure that is often recrystallized by hot stretch straightening and annealing. The resultant structure consists of recrystallized prior beta grains with colony

alpha, which offers excellent combination of strength, fracture toughness and fatigue life [5].

The current work employs a direct or forward extrusion process, where the die and the ram are in the opposite ends and the billet travels in the same direction as the ram (Figure 1). Typically, the cross section of the work billet is much larger than the cross section of the extruded part. To relate the cross section of the work piece to that of the extruded product, a value commonly termed as “extrusion ratio” was established that is defined as the ratio of the area of the original billet cross section (A_o) to that of the extruded product (A_f). The extrusion ratio, or reduction ratio, can be expressed as (A_o/A_f). Depending on the final geometry of the part, there exists a wide range of extrusion ratios for extruding different titanium products.

Figure 1. Forward extrusion process where the ram pushes the hot billet through the die.

3. Manufacturing and Evaluation

3.1. Materials and processing

Various grades of titanium alloys can be produced by the extrusion process, but the majority of the commercial aerospace industry commonly utilizes Ti-64 for a large number of its applications. Therefore, the primary focus for this paper is limited to Ti-64 extrusions and related characteristics. Ti-64 billets, ranging from 150mm to 230mm in diameter, were induction heated to a temperature above beta transus and extruded to different geometric profiles. The dies used for the extrusion process were designed and manufactured in-house using modified tool steel. The parameters for the extrusion process are selected based on the billet size, extrusion ratio, and the profile to be extruded. The resultant extruded product is typically about 8-14 meters long, depending on the initial size of the billet. The extruded products are then subjected to hot straightening and annealing to achieve the mechanical properties and key characteristics such as flatness across the width of the part, straightness (bow/camber) and twist along the full length of the extrusion. To enhance the machinability, the finished extrusions are chemically treated to remove the thin layer of the surface alpha case.

3.2. Evaluation

Following the post processing operations on the extrusions, test coupons have been excised and evaluated for room temperature mechanical properties, microstructure characterization, dimensional stability, and residual stresses. In-house machining was performed on a selected sample to analyse the savings realized due to the use of near-to-net extrusions in comparison to ‘standard’ products.

4. Results

Five different profiles (Figure 2) with varying degrees of complexity in their respective geometries were selected for the purpose of this work. These profiles are used in structural aerospace and engine applications and produced from various product forms as indicated in Table 4.

Figure 2. Ti-64 near-to-net, as-extruded profiles, approximately 8-14 meters long, produced at Plymouth Engineered Shapes in Hopkinsville, KY.

4.1. Room temperature mechanical properties

Room temperature tensile testing was performed in accordance with ASTM E8 and various other customer specifications. The results, presented in Table 1, indicate that the mechanical properties conform to both industry standard [6] and certain customer specific requirements.

Table 1 also presents the extrusion ratios and the final lengths extruded for each profile.

Table 1. Mechanical properties of the near-to-net extruded profiles

Profile	Extrusion Ratio, %	Extruded Length, m	YS, MPa	UTS, MPa	El, %	RA, %
ES # 1	37.9	13.7	896	1006	19	38
ES # 2	27.6	10.3	848	965	20	30
ES # 3	16.6	8.1	927	998	15	35
ES # 4*	25.6	10.1	-	-	-	-
ES # 5	13.5	8.4	910	1013	16	31
Spec.	-	-	830	900	10	20

**** Testing is in progress, at this time of this paper***

4.2. Microstructure and surface roughness

Optical microscopy, performed using a Keyence digital microscope, revealed results as expected. The microstructure observed was resultant from a beta processed Ti-64, with colony alpha along the recrystallized beta grain boundaries (Figure 3). Average grain size, measured in accordance with ASTM E112, was found to be ~100µm. Longitudinal and transverse surface roughness was also measured using a standard profilometer that resulted in a range of 80-130 Ra for all the near-to-net extruded profiles. All results are tabulated and presented in Table 2.

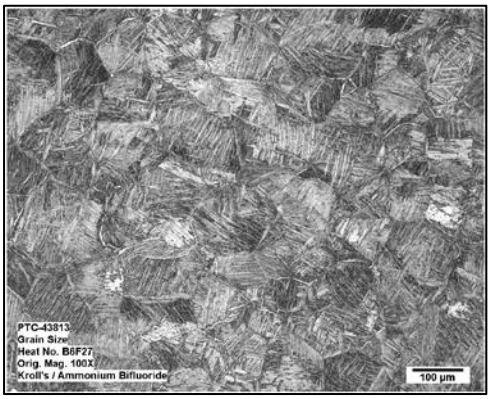

Figure 3. Optical micrograph from the near-to-net shaped extrusion profile, ES # 5, indicates lamellar alpha along the recrystallized beta grains. Samples were etched with Kroll's reagent after polishing. Similar microstructure was observed on all extruded profiles.

4.3. Dimensional Tolerances and Stability

4.3.1. Dimensions

Maintaining stable dimensions along the full length of the extrusion is extremely crucial for ensuring functionality, quality, and cost-effectiveness of the final product. Uniform dimensions with minimal variation, and straightness of the extrusions play a major role in the machining of the finished product. Due to limitations on space, data from two selected profiles (ES # 1 and ES # 5) is presented in this paper. Figure 4 shows the different dimensions measured for each profile. Results of dimensional measurements and variation to nominal planned dimensions for both profiles are shown in Figures 5 and 6. While aerospace standard specifications [7] allow for a deviation of ± 1.5mm on a given feature, it is to be noted that the near-to-net extrusions have outperformed the specification by presenting a variation less than 50% of the total permissible limit from the nominal.

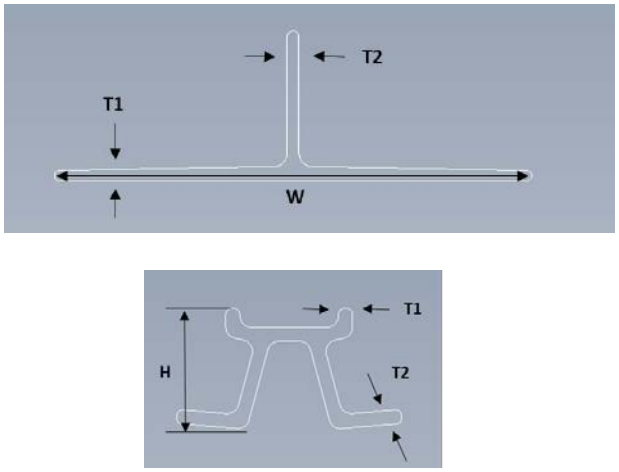

Figure 4. Thickness, height, and width of the various extruded profiles, as indicated, are measured along the full length of the extrusion at an interval of approximately 30cm, from end to end.

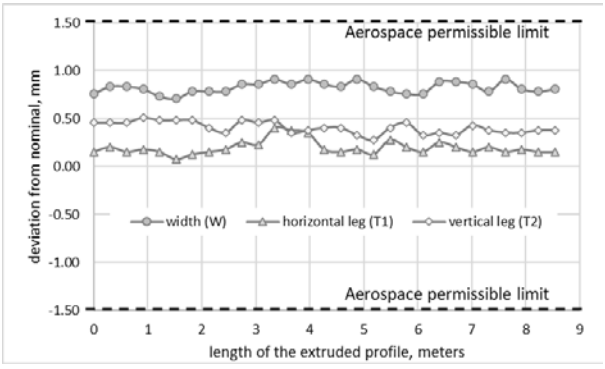

Figure 5. Deviation in dimensional tolerances, from nominal for near-to-net extruded profile ES # 1.

4.3.2. Straightness

Machining of titanium extrusions requires extreme control of tolerances on key characteristics such as transverse flatness, straightness, twist, and angularity along the full length of the extruded part. With reduction in the envelope due to near-to-net shaped profiles, holding

these tolerances along the length of the extrusion is critical to successfully machine the final part. Transverse flatness tolerances on both ends of the near-to-net shaped extrusions on the selected profiles are presented in Table 3. It can be observed that the average values of critical characteristics are not only well within allowable limits, but the near-to-net extrusions also offer much tighter tolerance limits than specified in the aerospace specifications, thus making them exceptionally favourable for machining.

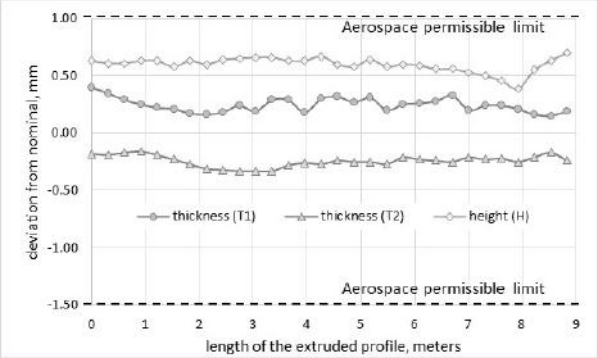

Figure 6. Deviation in dimensional tolerances, from nominal for near-to-net extruded profile ES # 5.

Table 2. Average tolerances on key characteristics of the near-to-net extruded profiles

Profile	Location	Flatness, mm	Max. Bow, mm	Max, Twist, deg.
ES # 1	North	0.33	1.4	0.3
	South	0.20		
ES # 5	North	0.00	0.25	0.7
	South	0.00		

4.3.3. Residual Stresses

Residual stresses can be present in any component as a result of both its thermal history and deformation history [8, 9]. They are produced because of a strain accommodation mechanism due to inhomogeneous plastic deformation of the work piece, as well as non-uniform expansion and contraction of the work piece during thermal processing. It was also found that the strain-rate at which the work piece is processed, also influences the residual stresses generated in a component [10]. As explained earlier, the Ti-64 billet undergoes significant reduction in beta region, at very high strain rates during the extrusion process.

A product with internal residual stresses can lead to material distortion or warping, which can make it more difficult to machine accurately. Additionally, the stresses can cause the material to deform or shift during the machining process, leading to increased tool wear, surface finish issues, and even damage to the machine tool and the finished product. It is therefore extremely important to manufacture the extrusions with minimal residual stresses to effectively machine the part. Proprietary techniques were developed to ensure that the extruded parts are free of residual stresses and do not indicate any distortion during the machining process. Residual stresses are measured on the extruded profile ES # 1, according to the hole-drilling strain-gage method of stress relaxation per ASTM E837. Results, as seen in Figure 7 and Table 3 indicate a max. and min. stress of –0.04 MPa and -0.16 MPa respectively. Although negligible, there are negative or compressive type of residual stresses measured from the near-to-net extruded profiles, which make the machining process much simpler. It is also to be noted that residual compressive stresses are generally helpful because they reduce the effects of applied tensile stresses and contribute to the improvement of fatigue strength in the material [11].

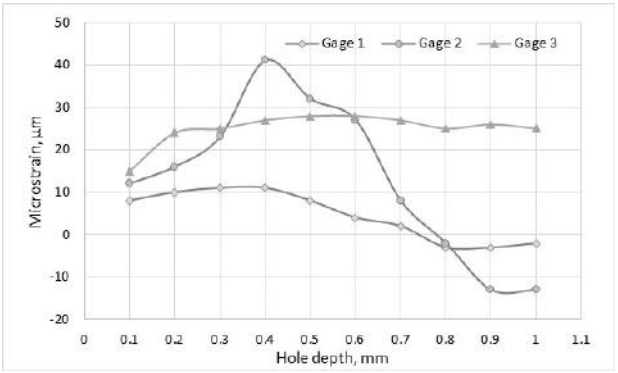

Figure 7. Measured micro strains from residual stress analysis of the near-to-net shaped extruded profile ES # 1. Type A rosette (0-45-90 configuration) was utilized for testing purposes.

Table 3. Maximum and minimum residual stresses calculated per ASTM E837 standards, on near-to-net shaped extruded profile ES # 1. Cartesian stresses are used for calculation purposes per the specification.

Max stress, MPa	Min stress, MPa	Angle β, deg.	Cartesian stresses (MPa)		
			σ_x	σ_y	σ_z
-0.04	-0.16	15	-0.05	-0.15	-0.03

5. Discussion

5.1. Buy-To-Fly

Each preform process such as forging, casting and plate stock incurs a considerable loss of material during machining due to the excessive material envelope built around the finished product. This can result in higher costs for both the manufacturers and the customers. In addition, excess material waste can have environmental impacts. Extrusions reduce the buy-to-fly ratio (BTF) by significant amount and provide advantages not offered by the alternative preform processes. With the advancements in the near-to-net extrusion technology, the BTF ratio is further reduced, which significantly reduces the costs associated with machining of the final product.

Tables 4 and 5 provide the BTF of the selected profiles from their existing product form and compares it to the improvement provided by the near-to-net shaped extrusions. As observed from Figure 8, utilizing near-to-net shaped extrusions provide at least 50-80% savings in raw material consumption to produce the same finished part. Considering the significant disruptions in the global titanium supply chain [12, 13] in the current geo-political scenario, near-to-net extrusions provide an optimum solution for titanium sourcing needs for the aerospace industry along with reducing the overall manufacturing costs.

Table 4. Buy-to-Fly (BTF) of various profiles, when machined from their current product forms.

Profile	Current product form	Weight/meter, kg	BTF
ES # 1	Standard extrusion	6.43	3.14
ES # 2	Standard extrusion	8.04	4.13
ES # 3	Standard extrusion	11.52	5.84
ES # 4	Sheet	1.96	1.48
ES # 5	Plate	10.54	7.00

Table 5. Buy-to-Fly (BTF) of various profiles, when machined from near-to-net extrusions.

Profile	Proposed product form	Weight/meter, kg	BTF
ES # 1	Near-to-net extrusion	2.14	1.10
ES # 2	Near-to-net extrusion	2.86	1.47
ES # 3	Near-to-net extrusion	5.23	2.65
ES # 4	Near-to-net extrusion	1.96	1.48
ES # 5	Near-to-net extrusion	1.96	1.34

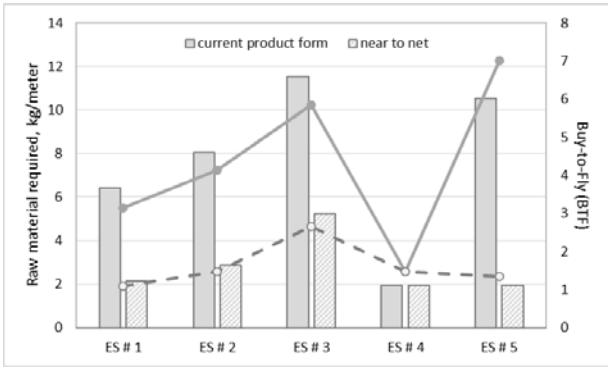

Figure 8. Comparison of raw material requirement and BTF for the selected profiles in their current supply condition vs. near-to-net extrusions.

5.2. Conversion from Sheet

ES # 4 is a prime example of the advancements made in the near-to-net extrusion technology. This product usually produced from a sheet material (~4mm thick) posed a challenge to the manufacturer in terms of thinning (underfill) in the inner radii during the hot forming process. While the buy-to-fly ratio was not really changed, the proprietary die design for the near-to-net extruded profile was able to accommodate and aid in successful production and machining of the product. This unique ability and enhancements in extrusion technology can not only provide savings in terms yield improvements but also should lead to considering near-to-net extrusions as a viable alternative to the products produced from the aerospace sheet & strip.

5.3. Machining Benefits – A Case Study

A case study was conducted to best estimate and compare the benefits of machining near-to-net extruded profiles with that of a standard extrusion. Machining was performed on an in-house CNC machine (Haas VF-6 vertical 3-axis mill) and the near-to-net extruded profile ES # 2 was selected to be machined for this study. Since the in-house equipment is limited by the amount of tool travel, approximately 20mm of the finished part was machined from the extruded profile, for analysis and comparison. Figures 9 and 10 show the finished part being machined out of a standard and a near-to-net extrusion, respectively. As shown in Table 6, with all machine settings remaining constant, about 0.5kg of machined scrap was generated when machining the finished part from the standard extrusion. In comparison, a near-to-net

extrusion only resulted in 0.1kg of scrap, approximately one-fifth compared to that of a standard extrusion.

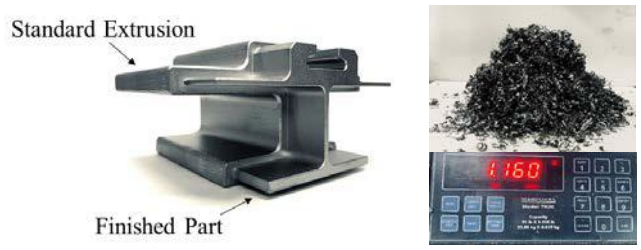

Figure 9. A finished part (20mm long) was machined out of a standard extrusion using the in-house equipment, that resulted in approximately 0.5kg of machined waste.

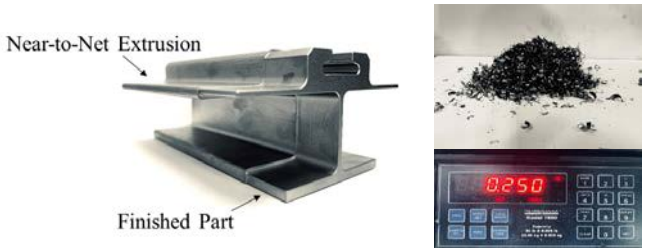

Figure 10. A finished part (20mm long) was machined out of a near-to-net extrusion using the in-house equipment, which resulted in approximately 0.1kg of machined waste.

Table 6. Comparison of machining results for standard and near-to-net extruded profiles

Product form	Machined Scrap, kg	Machine time, min	Tool life estimate
Standard Extrusion	0.5	26.2	X
Near-to-net	0.1	14.2	2.5X

6. Summary

Near-to-net extrusions provide significant economic advantages by reducing the buy-to-fly ratio. This results in further reduction of raw material usage, and tooling costs. Various near-to-net shaped profiles were extruded successfully to reduce the buy-to-fly ratio and to provide an optimal solution for the current and future disruptions in the global titanium supply chain. Microstructure, room temperature mechanical properties, and extrusion-critical characteristics such as straightness conformed to the available aerospace and customer specifications. Compressive residual stresses which are known to aid in improving the fatigue properties, were observed on the near-to-net extrusions. Machining of a finished product from near-to-net extrusions resulted in approximately one-fifth the scrap and reduced the machining time by more than 50% when compared to a standard extrusion. Considering the merits of the titanium alloys coupled with the advantages of the properties that extrusions can offer [14], it is strongly believed that aerospace industry could significantly benefit by the advancements in the manufacture of near-to-net shaped extrusions.

7. References

1. R.R. Boyer, E.R. Barta and J.W. Henderson, Journal of Materials, March 1989, 36-39.
2. P. Gudipati and M. Campbell, Advanced Materials and Processes, April 2021, 19-22.
3. J. Phillips and T. Esposito, AeroMat 2007, June 25-28, 2007, Baltimore, Maryland, USA.
4. G. Legate, Titanium 2013, Oct 6 – 9, 2013, Las Vegas, Nevada, USA.
5. Russell Wanhill and Simon Barter, Springer Briefs in Applied Sciences and Technology.
6. *Titanium Alloy Extrusions and Flash Welded Rings*, Ti-6Al-4V Annealed, Beta Processed, AMS 4935 Rev. L, issued 1959-06, Revised 2022-08.
7. *Tolerances, Titanium and Titanium Alloy Extruded Bars, Rods, and Shapes*, AMS 2245 Rev. C, issued 1973-12, Revised 2021-09.
8. James J.D. Pollard, Salah Rahimi, A. Watford, Martin Jackson and B.P. Wayne, Proceedings of the 13th World Conference on Titanium, Ti-2015, August 16-20, 2015, San Diego, USA.
9. P.J. Withers, Reports Prog. Phys. 70 (2007), 2211-2264.
10. A.K. Tiwari, A.R. Patel and N. Kumar, Mater. Des. 65 (2015), 1041-1047.
11. George E. Dieter, Mechanical Metallurgy (McGraw-Hill, 1988).
12. Valius Venckunas, *"The titanium supply chain crisis: how it began and what it means for aerospace"*, Aerotime Hub, October 2022.
13. Willy Shih, "*The titanium supply chain for the aerospace industry goes through Russia*", Forbes, March 06, 2022.
14. S. James, P. Gudipati, A. Kantor and J. Phillips, in this conference proceedings, Ti-2023, June 12-16, 2023, Edinburgh, UK.

METALLURGICAL INVESTIGATION OF A TI6242 DISK WITH FATIGUE PROGRESSION FROM SUBSURFACE MICROVOIDS

Philip Sherer[1]

1 Pratt & Whitney, East Hartford, CT 06118, USA.

Ti-6Al-2Sn-4Zr-2Mo is a titanium alloy commonly used in the manufacture of static and rotating hardware in aerospace engine applications. This paper will present the results of an investigation into the cracking of a Ti6242 component emanating from an atypical microstructural feature. The observed crack was due to fatigue with an origin at a cluster of subsurface micro-voids containing internal alkaline earth metal deposits. This paper presents the results of this investigation, as well as details of a root cause investigation into possible sources of the micro-voids and deposits.

Keywords: Fatigue, micro-voids, Ti-6Al-2Sn-4Zr-2Mo, Ti-2023.

1. Introduction

In 2007, fatigue cracking that had initiated from a linear array of subsurface micro-voids was detected in the bore of a Ti-6Al-2Sn-4Zr-2Mo high pressure compressor (HPC) disk. The cracking was found during routine overhaul of a commercial engine (fig 1). Pratt & Whitney conducted a metallurgical investigation of this part as well as several others found during an inspection campaign, all of which involved micro-void-initiated fatigue cracking. These parts were all associated with one heat of MRAL[1] plus 3x VAR titanium produced in 1987. The following provides the findings of the destructive evaluation of two of these parts.

2. Destructive Evaluation Results – Overhaul Find

The HPC disk was dis-assembled and sent to the lab. An evaluation of the bore surface was performed, after which the crack was broken open for fractographic examination (fig 2). Examination of the crack surface in the scanning electron microscope (SEM) found a large area of striated fatigue progression, which had progressed from the perimeter of a subsurface origin region (fig 3). Within the crack origin region, the crack mode was predominantly low ΔK faceted growth [2].

Figure 1. View of the inside of an HPC rotor assembly, which exhibited a crack in the bore of an HPC disk.

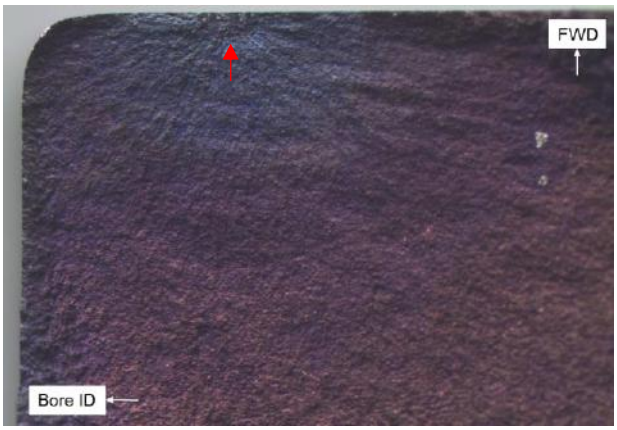

Figure 2. An overall view of the fatigue origin and vicinity.

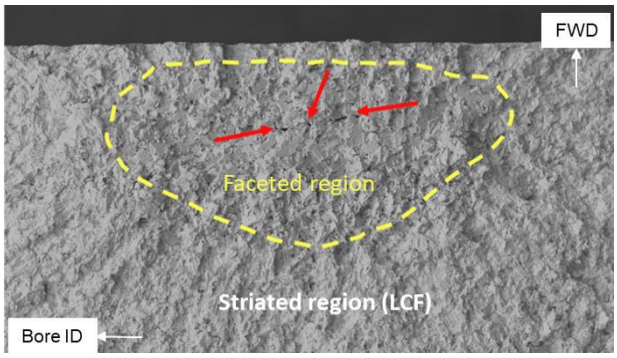

Figure 3. SEM image of the fatigue origin area.

The size of the faceted growth region was 0.56 by 1.2 mm. The faceted fatigue progression within this region could be traced to a series of centrally located micro-voids that were from 0.18 to 0.25mm subsurface from the bore forward face. The micro-voids were distributed along a linear path that was inclined at a shallow angle relative to the forward bore face (figs 3 and 4). An adjacent area of the HPC disk bore was sectioned to create a planar surface through the bore with the same orientation as the crack origin. This sample was macro-etched to reveal forging flow lines. The linear distribution of the micro-voids was found to be consistent with the direction of forging flow.

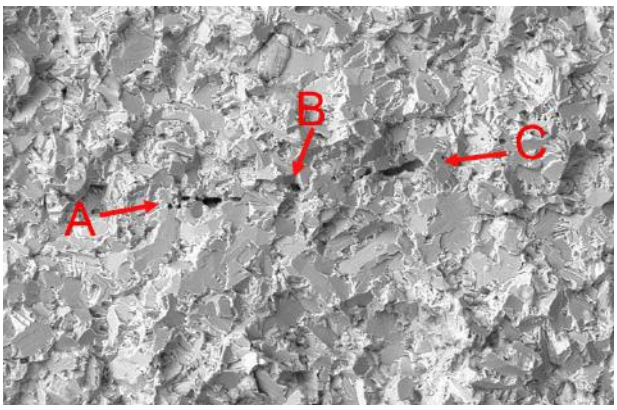

Figure 4. SEM image showing multiple micro-voids that extended along a linear path. The micro-voids appeared to be unfilled.

The SEM examination found that individual micro-voids appeared to be unfilled (fig 5) and were less than ~30um in length. Both halves of the crack origin area were sectioned from the disk bore and mounted in epoxy. The initial plane of polish for each was adjacent to the micro-voided origin area. These samples were then serial polished into the micro-void region.

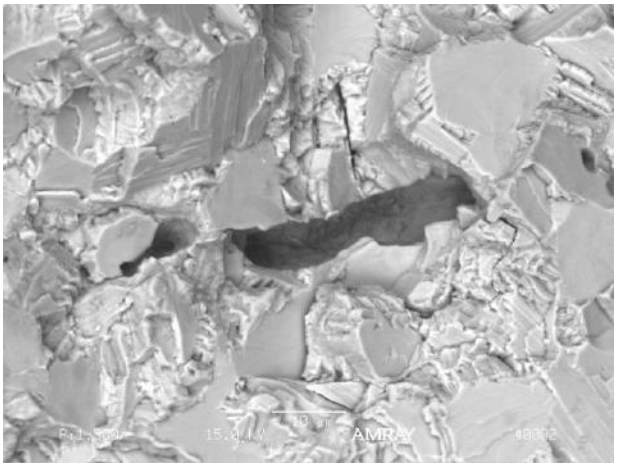

Figure 5. Close up SEM image of micro-void area C.

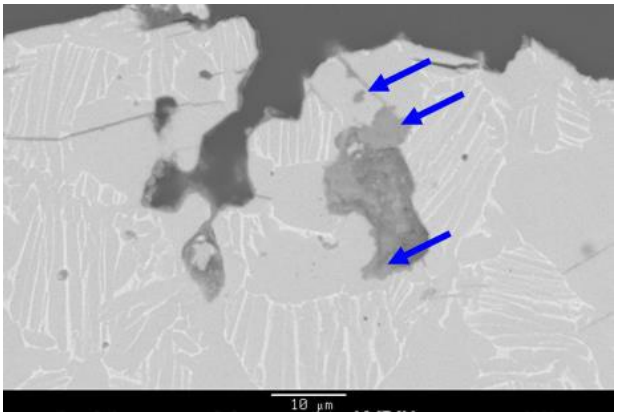

Figure 6. SEM BSE image of a side A plane of polish that intersected a micro-void area. Micro-voids below the crack surface were filled.

The serial polishing consistently found a bimodal alpha plus beta microstructure in the disk bore, as expected. Micro-voids were intersected at the crack surface within several planes of polish. The microstructure local to micro-void areas did not show any stabilization of either the alpha or the beta phase. Micro-hardness surveys found no detectable change in hardness at or away from micro-void areas. The cross-sections also found micro-voids that appeared to be subsurface to the crack plane. Some of these micro-voids were filled, i.e. contained deposits. Polished sections exhibiting filled micro-voids were carbon coated and analysed via energy dispersive spectroscopy (SEM/EDS) to determine the composition of the deposits.

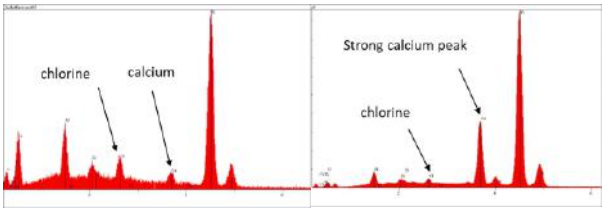

Figure 7. SEM/EDS analysis results for figure 6.

Typical SEM/EDS results for side A filled micro-voids found elevated levels of chlorine and calcium (fig 7). The elevated levels of chlorine could have been from the epoxy mount material, which had been potted in a mild vacuum to promote edge retention. The calcium and chlorine levels appeared significant but did not include other mineral content, notably no magnesium. These micro-void deposit compositions were not consistent with bore surface deposits, which tended to exhibit silicon aluminium and oxygen primarily, with sulphur, potassium, calcium, and sodium typically also present in small quantities.

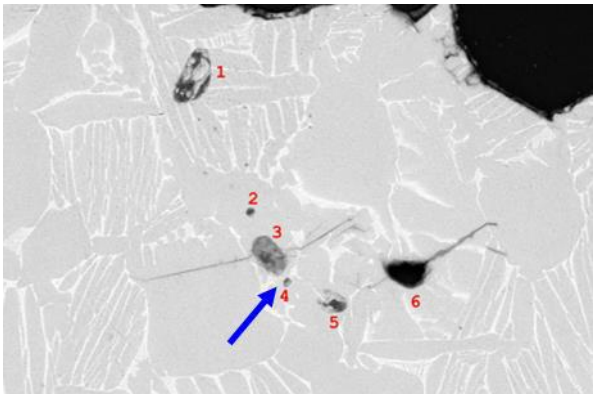

Figure 8. SEM BSE image of a side B plane of polish that intersected a micro-void area. Micro-voids below the crack surface were filled.

A similar SEM/EDS was conducted for filled micro-voids found associated with the side B crack origin area (fig 9). In this case excess zirconium, calcium,

oxygen, chlorine, and fluorine were noted. As a result of these findings, several test samples were prepared to assess the possibility of cross contamination from the lab polishing process. These samples were prepared using the same polishing techniques and equipment, and then the as polished surfaces were evaluated via SEM/EDS. This evaluation detected particles containing aluminium and silicon suggestive of residual polishing compounds. In other cases, surface deposits containing a mixture of silicon, aluminium, sodium, sulphur, chlorine, potassium, and phosphorus were found.

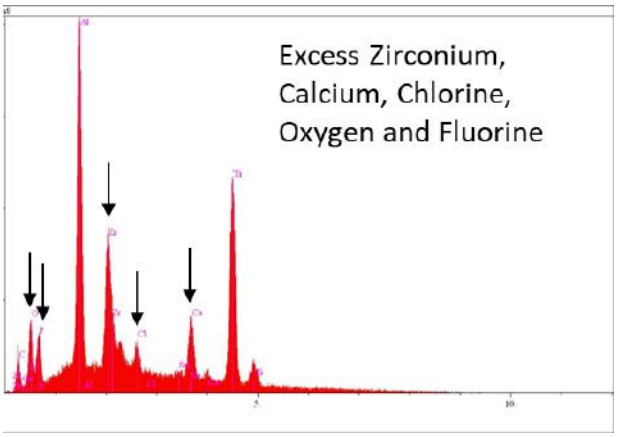

Figure 9. SEM/EDS analysis results for figure 8.

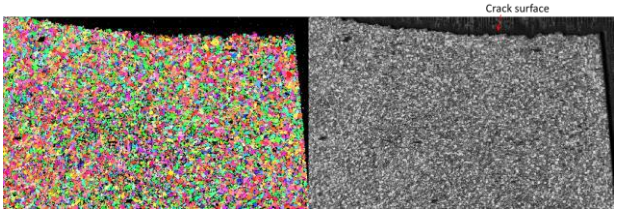

Figure 10. EBSD data for polish plane through micro-void origin. (source: EBSD analytical – used with permission)

During the assessment of the side B crack origin area, the serial polishing was paused near the mid-point of the origin area to collect grain orientation data via EBSD (fig 10). The EBSD data revealed a highly random structure, with no evidence of microtextured regions that could have caused or contributed to crack initiation.

3. Subsequent HPC Inspection Results

During subsequent inspections, another HPC disk from the same heat was found with two surface connected crack indications in the bore (fig 11). Both "disk 2" cracks were broken open for destructive evaluation. Both cracks exhibited a faceted nucleation region followed by striated fatigue progression similar to "disk 1" (fig12). Within the faceted growth region, both disk 2 cracks exhibited cracking that had initiated from micro-voids. The micro-voids appeared to be more of a singular cluster, rather than a linear array (fig 13). Individual micro-voids were similar in size compared to the previous event, but the overall size of the micro-void area was smaller in the disk 2 cracks vs. the disk 1 crack.

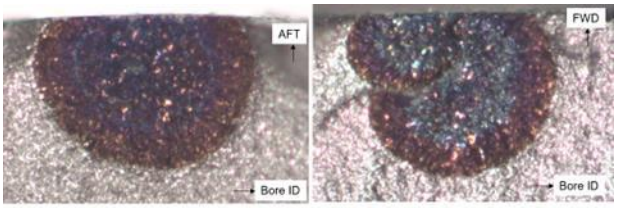

Figure 11. Disk 2 cracks A (right) and B (left).

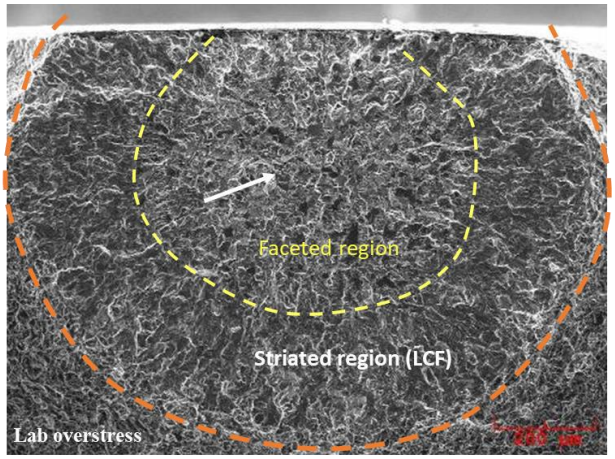

Figure 12. SEM image of disk 2 crack B, which exhibited striated growth from a faceted region containing a cluster of filled micro-voids.

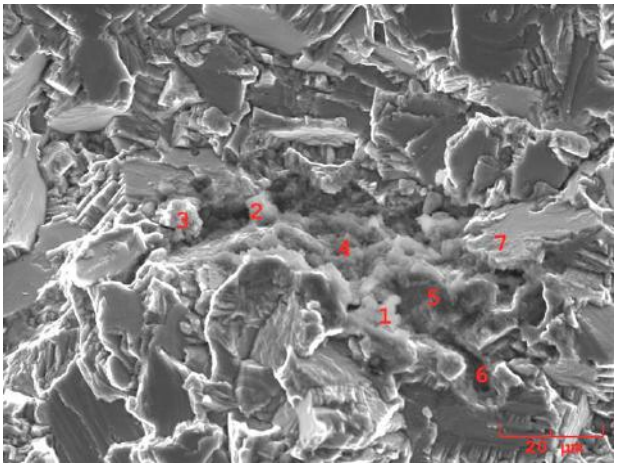

Figure 13. SEM image of micro-voids and deposits at the crack B internal origin site.

SEM examination of the crack B origin area again found micro-voids, most of which contained deposits. SEM/EDS of the deposits found predominantly calcium and sulfur, as well as areas exhibiting oxygen, fluorine, and traces of chlorine (fig 14). The relative absence of chlorine compared to the disk 1 deposits may reflect the fact that the disk 2 deposits were analyzed in-situ on the crack surface vs. disk 1 where metallographic samples mounted in epoxy were used.

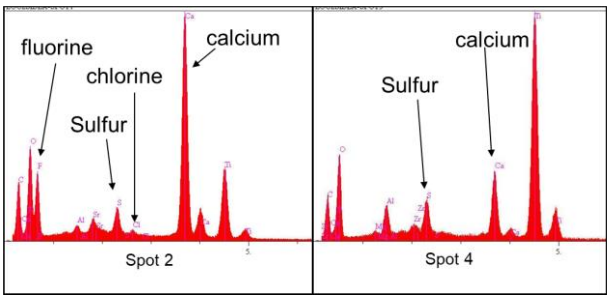

Figure 14. SEM/EDS analysis results for figure 13.

To evaluate whether smaller filled micro-voids were present just below the crack surface, a thin foil extraction into the origin voids was attempted via focused ion beam (FIB) milling. This was successfully completed, resulting in a thin foil section into the micro-void / deposit cluster (fig 15). The foil appeared to contain the edge of an internal inclusion containing deposits. The internal cavities that were exposed did not exhibit deposits.

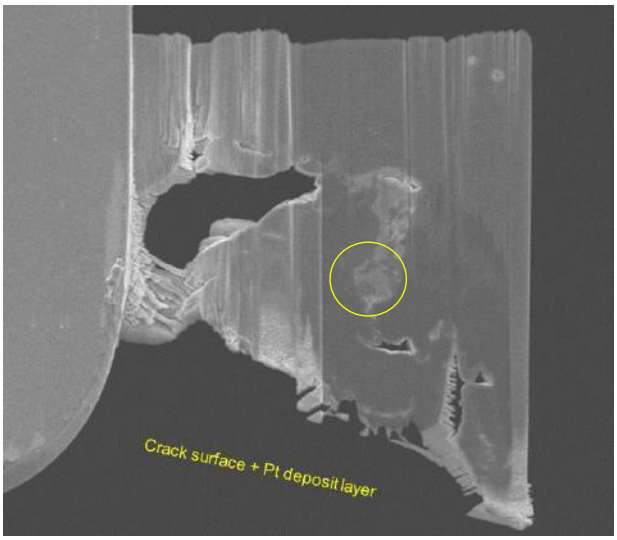

Figure 15. SEM image of thin foil section extracted from micro-void origin area of disk 2 crack B. internal deposit area is circled.

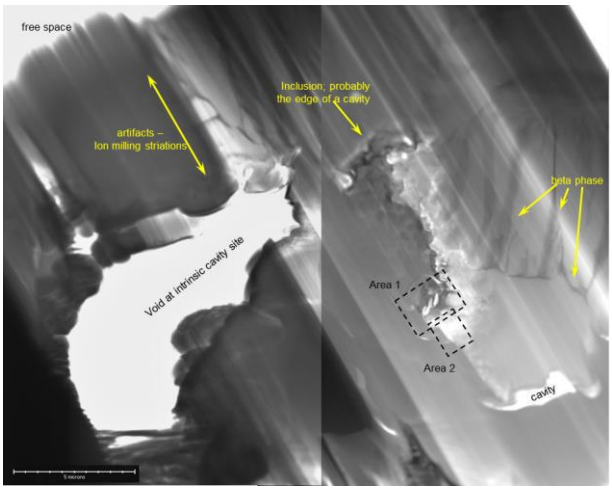

Figure 16. higher magnification view of foil. Analysis results for Area 1 are presented in figures 17-21, Area 2 in figure 22.

Further analysis of Area 1 (fig 16) identified a region of nanocrystalline CaO particles (fig 17). The evaluation of the selected are diffraction pattern (SADP) found spacings (fig 18) that compared favorably with the d-spacings for CaO (fig 19).

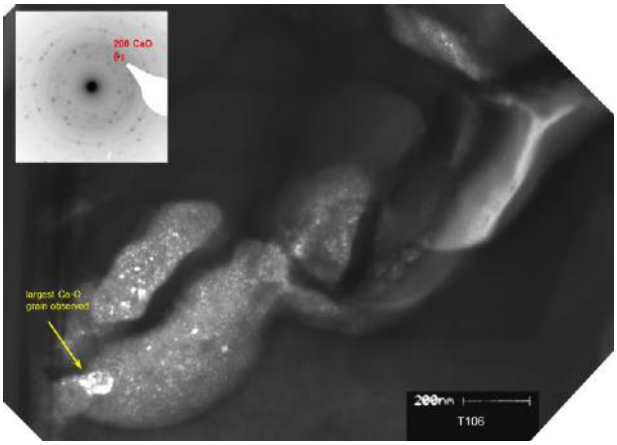

Figure 17. Dark field TEM image formed using the CaO spot identified in the inset SADP.

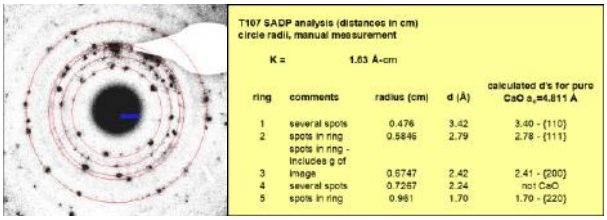

T107 SADP analysis (distances in cm)
circle radii, manual measurement

K = 1.63 Å-cm

ring	comments	radius (cm)	d (Å)	calculated d's for pure CaO a_o=4.811 Å
1	several spots	0.476	3.42	3.40 - {110}
2	spots in ring	0.5846	2.79	2.78 - {111}
3	spots in ring - includes g of image	0.6747	2.42	2.41 - {200}
4	several spots	0.7267	2.24	not CaO
5	spots in ring	0.961	1.70	1.70 - {220}

Figure 18. Diffraction spot measurement of SADP from fig 17, compared to d-spacings from pure CaO.

The CaO nanocrystals from Area 1 were also spot analyzed via EDS (fig 19), which detected calcium peaks at various intensities (fig 20).

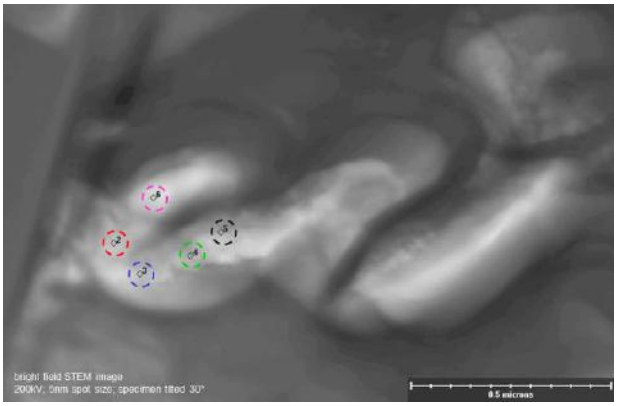

Figure 19. bright field STEM image of area 1 showing EDS spot analysis location.

A dark field image of area 2 from figure 16 provides a better view of the size and distribution of individual crystallites (fig 21). Overall, the evaluation of disk 2 confirmed fatigue cracking had initiated in the bore of a disk produced from the same heat of Ti-6Al-2Sn-4Zr-

2Mo material as disk 1. The cracking was found in the bore, which progressed from sub surface, non-reacted micro-voids. Individual micro-voids were similar in size to those from disk 1, however, the overall size of the micro-void area was smaller in disk 2.

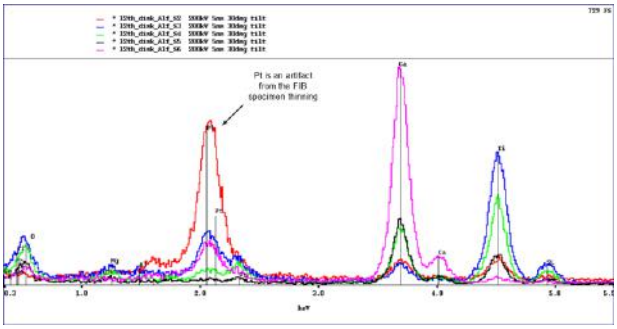

Figure 20.EDS analysis results from figure 20.

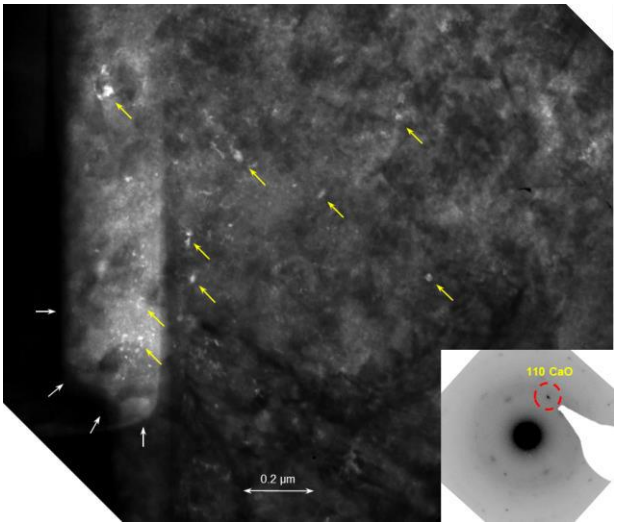

Figure 21. Dark field TEM image formed using the CaO spot identified by the inset SADP. CaO crystals were marked by yellow arrows.

4. Discussion

The micro-void origin areas did not exhibit evidence of micro/macro segregation or reaction zones at or near micro-void areas. There was no stabilization of either the alpha or beta phase associated with the micro-void areas. Internal micro-voids were found which included the presence of Ca rich compounds. The TEM thin foil from a micro-void origin confirmed calcium in sub-crack surface deposits. The measured d-spacings were consistent with Ca-O. Dark field images suggested the Ca-O particle size was extremely fine (nano scale).

A P&W team investigated the possible causes of the micro-voids. The conversion and forging processes were reviewed in detail based on the hypothesis that the micro-voids might have been strain induced porosity (SIP), that were later contaminated with deposits once the crack had become surface connected. However, these reviews effectively ruled out strain induced porosity (SIP). Also the Ca-O crystals found during the TEM examination suggested filled voids instead of SIP, i.e. an inclusion [3]. This type of inclusion was not consistent with either a high interstitial defect (HID), a high aluminum defect (HAD) or a high-density inclusion (HDI) [4]. The processes used in the production of this heat of material were also reviewed in detail. These evaluations identified several possible contamination opportunities involving calcium containing compounds, however, a singular cause could not be established. There is continued interest for the industry to evaluate and implement further controls for potential sources of charge material contamination including shop cleanliness, Ti sponge / master ally contamination as well as revert solid / chip contamination.

5. Acknowledgements

During this investigation, I was grateful for the support provided by a talented team of colleagues from the Materials and Processes Engineering department (MPE) at P&W. Cristal Chan for numerous contributions during the destructive evaluation and SEM/EDS characterization of the disks. Greg Levan and Fred Galli for support in advanced characterization of titanium. Dr. David Snow for his expertise in TEM analysis. Jon Bertus, Janet Stanley and Andy Haynes for their expertise in titanium alloys. Bruce Laube at United Technologies Research Center for advanced characterization support. Ron Witt at EBSD analytical for EBSD scans of crack origin and vicinity. Lastly, I'd like to thank John Moskito at the Evans Analytical Group, for the FIB extraction of a micro-voided area, as well as for advanced characterization support.

6. References

1. W. Kroll 1940 *Trans. Electrochem.* Soc. 78 35.
2. A .L. Pilchak, A . Bhattacharjee, A .H. Rosenberger, J.C. Williams, *Low _K faceted crack growth in titanium alloys,* Int. J. Fatigue 31 (5) (2009) 989–994 .
3. AC 33.15-1, *Manufacturing Process of Premium Quality Titanium Alloy Rotating Engine Components,* https://www.faa.gov/documentLibrary/media/Advisory_Circular/AC_33_15-1.pdf.
4. Woodfield A, Lemaitre G. *Aerospace Titanium Alloy Melt Process Quality Improvements.* InMATEC Web of Conferences 2020 (Vol. 321, p. 04008). EDP Sciences. Y. Tuo, T.B. Kroll, A.J. Titanium, *Scripta Materialia* 76 (2023) 1–15.

CONTINUOUS, INDUSTRY-WIDE EFFORTS TO IMPROVE THE SAFETY OF TITANIUM ALLOY TURBINE ENGINE ROTORS

Andrew Woodfield[1], David Furrer[2], Jamie Moschini[3], Adam Pilchak[2], Jean-Manuel Ruppert[4]

1 GE Aerospace, 1 Neumann Way, Cincinnati, OH 45215, USA.
2 Pratt & Whitney,400 Main Street, East Hartford, CT 06118, USA.
3 Rolls-Royce, plc., PO Box 31, Derby DE24 8BJ, United Kingdom.
4 Safran Helicopter Engines, Av. Joseph Szydlowski, 64510 Bordes, France.

In 1998, the Federal Aviation Administration (FAA) published Advisory Circular (AC) 33.15-1 in response to a major rotor failure due to a melt-related defect. This advisory circular has and continues to provide guidance and information related to the control of the manufacture of premium quality titanium for use in fracture critical rotating components in aircraft engines in support of industry-wide safety. This document summarizes extensive FAA and industry experience related to the introduction and detection of life-limiting anomalies (e.g., Type I, or hard alpha inclusions, high density inclusions, etc.)) that may occur during melting of titanium alloys. The document provides guidance to established industry best-practice manufacturing processes, in-process material and component inspections, and finished component inspections for all critical rotating titanium alloy parts. The FAA requested a team, consisting of members of the Jet Engine Titanium Quality Committee (JETQC), provide recommendations for updating AC 33.15-1 in response to the finding that a recent fan disk event was due to microtexture-related cold dwell fatigue of Ti-6Al-4V. The purpose of this paper is to report on continued industry quality and safety improvements related to (i) melt inclusions, and (ii) the development and control of microtexture that are recommended for incorporation into AC33.15-1.

Keywords: FAA, AC33.15-1, JETQC, Ti-6Al-4V, titanium, critical rotating parts, melt related anomalies, microtexture regions, cold dwell fatigue, MTR.

1. Introduction

United Airlines flight UAL292 crash-landed in Sioux City, USA on July 19, 1989 as a result of an uncontained engine fan disk failure due to a hard alpha inclusion in the Ti-6Al-4V material [1]. The resultant crash led to the loss of 112 lives as the aircraft tipped over on landing. The Ti-6Al-4V alloy was double vacuum arc remelted (VAR) in 1971 and the fan disk was close to its life limit. The Federal Aviation Administration (FAA) responded with the formation of the Jet Engine Titanium Quality Committee (JETQC) consisting of all the premium quality (PQ) titanium alloy suppliers for critical rotating parts, the engine original equipment manufacturers (OEMs) and the FAA. Since 1990, JETQC has been tracking the melt anomaly rates across all PQ titanium alloy suppliers, and there has been an impressive reduction in anomaly rates for both hard alpha and high-density inclusions (HDI) as described in references [2-4] and shown in Figure 1. In 1998, the FAA published Advisory Circular AC 33.15-1 [5], entitled "Manufacturing Process of Premium Quality Titanium Alloy Rotating Engine Components". This document covers best practices related to melting, conversion, forging, heat treatment, and inspection of PQ titanium alloy components. The document is mostly focused on melt anomalies since that was the focus following the Sioux City accident in 1989.

A recent uncontained Ti-6Al-4V fan disk failure in 2017 on AF066 occurred over Greenland and the aircraft was able to land safely with no injuries to passengers or crew. After an exhaustive search, portions of the fan disk were recovered from the ice and the origin of the failure was traced back to a cold dwell fatigue mechanism (CDF) linked to the presence of microtexture regions (MTRs), or macrozones, in the component [6]. As a result of this accident, the FAA tasked JETQC with recommending potential updates to AC 33.15-1 related to MTRs and CDF as well as updating the document for melt-related lessons learned since 1998.

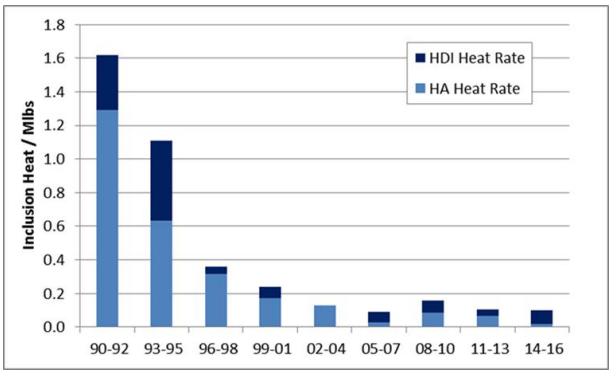

Figure 1. Reduction in PQ Ti melt anomalies since JETQC inception in 1990 [4].

As JETQC assessed the FAA's request, it became clear that incorporating high-level, MTR-related CDF guidance into AC 33.15-1 was a major task since a large amount of information has been published in the open literature on MTRs and CDF, in addition to individual engine OEMs having performed their own research on these topics, with that information being largely unpublished. JETQC undertook a comprehensive review of the open literature including a detailed FAA-sponsored report on CDF in Ti-6242 [7] and agreed to

share some of their unpublished research to highlight all the key scientific as well as practical engineering aspects of CDF and MTRs. This work was recently completed and is reported in [8], with a Journal report planned later in 2023. A high-level summary of this work is reported in a separate paper in this conference proceedings [9]. The focus of this paper is a set of high-level recommendations that JETQC has provided to the FAA for consideration in a future update to AC 33.15-1.

2. AC 33.15-1 Background

Figure 2 shows the cover page of the FAA advisory circular AC 33.15-1 relating to the manufacturing process of premium quality titanium alloy rotating engine components, taken from [5].

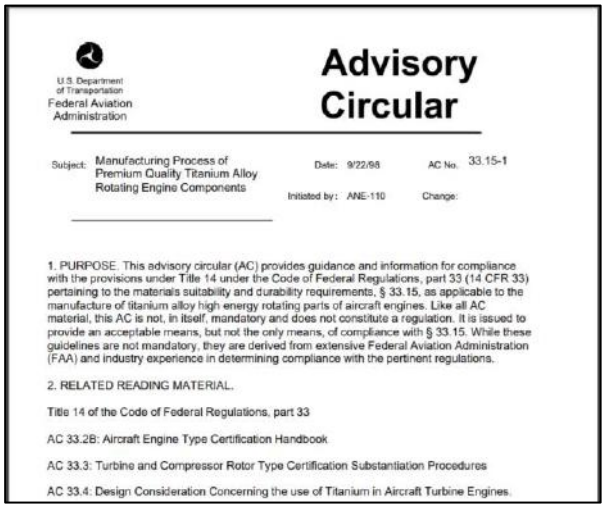

U.S. Department of Transportation
Federal Aviation Administration

Advisory Circular

Subject: Manufacturing Process of Premium Quality Titanium Alloy Rotating Engine Components

Date: 9/22/98 AC No. 33.15-1

Initiated by: ANE-110 Change:

1. PURPOSE. This advisory circular (AC) provides guidance and information for compliance with the provisions under Title 14 under the Code of Federal Regulations, part 33 (14 CFR 33) pertaining to the materials suitability and durability requirements, § 33.15, as applicable to the manufacture of titanium alloy high energy rotating parts of aircraft engines. Like all AC material, this AC is not, in itself, mandatory and does not constitute a regulation. It is issued to provide an acceptable means, but not the only means, of compliance with § 33.15. While these guidelines are not mandatory, they are derived from extensive Federal Aviation Administration (FAA) and industry experience in determining compliance with the pertinent regulations.

2. RELATED READING MATERIAL.

Title 14 of the Code of Federal Regulations, part 33

AC 33.2B: Aircraft Engine Type Certification Handbook

AC 33.3: Turbine and Compressor Rotor Type Certification Substantiation Procedures

AC 33.4: Design Consideration Concerning the use of Titanium in Aircraft Turbine Engines.

Figure 2. FAA AC 33.15-1 cover page showing the Advisory Circular purpose [5].

As noted in the advisory circular, Section 1, Purpose, the AC provides guidance and information for compliance with the provisions under Title 14 under the Code of Federal Regulations, part 33 (14 CFR 33) pertaining to the materials suitability and durability requirements, § 33.15, as applicable to the manufacture of titanium alloy high energy rotating parts of aircraft engines. Like all AC material, this AC is not, in itself, mandatory and does not constitute a regulation. It is issued to provide an acceptable means, but not the only means, of compliance with § 33.15. While these guidelines are not mandatory, they are derived from extensive Federal Aviation Administration (FAA) and industry experience in determining compliance with the pertinent regulations.

Section 4 Background in [5] notes that the manufacture of titanium alloy forged rotating components can introduce component life limiting anomalies at all stages of material processing, from sponge processing, through melting, billet conversion, component forging, and inspection of the finished component. Since optimum capability to detect these anomalies may vary according to their type and source in the manufacturing process, the manufacturing process should be established so that, at each stage, appropriate controls and inspections are in place to minimize the occurrence of and to maximize detection of, such anomalies based on the best available technologies.

Section 4 Background in [5] also notes that the conventional melting process for titanium alloys has been the triple VAR process was the current standard for critical rotating components. Improvements in VAR technology have resulted in a significant reduction in the occurrence of melt related defects since the mid 1980's. The newer cold hearth melt (CHM) technology virtually eliminates the risk of having HDI's survive through the melting cycle. Current cold hearth melting technology involves a CHM cycle using either plasma arc melt (PAM) or electron beam melt (EBM) followed by a final VAR cycle.

Sections 6 - 8 in [5] detail guidance relating to the various manufacturing stages of PQ titanium alloy components, with the major emphasis being on raw materials and storage (Section 6.0), consolidation and melting (Section 7.0), and billet conversion, disk forging and non-destructive testing (Section 8.0). Most of the AC 33.15-1 guidance issued in 1998 [5] relates to melting and the avoidance and detection of melt-related inclusions that were noted in [1] to be the root cause of the 1989 Sioux City accident.

3. Recommended AC 33.15-1 Updates

Following the issuance of the failure investigation report of the AF066 fan disk failure in 2017 attributed to CDF [6], FAA tasked JETQC to provide a series of recommended updates to AC 33.15-1 related to CDF and melting improvements that have occurred over the last ~25 years since the original AC was issued. These recommendations from JETQC to FAA are summarized below.

Section 3 is recommended to be updated with a series of new definitions relating to MTRs and specific features of MTR size, crystallographic alignment, etc., enabling a more consistent electron backscatter diffraction (EBSD) quantification method of MTR features between different organizations. The recommended MTR feature definitions are as follows:

Microtextured Region: A localized region in converted billet or a component forging where neighboring alpha grains have similar crystal orientations such that the feature may act as a larger structural unit during deformation. Size, Shape, Density, Intensity, Frequency, Orientation, Neighboring Region Characteristics, and Volume Fraction of Primary Alpha are important parameters when characterizing MTR features. These features are known to impact dwell-fatigue capabilities. MTRs are also sometimes referred to as "macrozones" or "primary alpha colonies". MTR regions were identified once electron backscatter diffraction methods were developed which allowed correlation of specific microstructural features with their underlying crystallographic orientation.

MTR Density: A measure of the area fraction of the alpha grains in an MTR that have a similar basal (0001) plane orientation. This factor includes contributions from both primary alpha and transformed beta crystallographic orientation.

MTR Size Frequency: The number of MTR features of a given size within a volume of titanium.

MTR Intensity: A measure of the range of variation of crystallographic orientations of all of the alpha grains within an MTR that includes weighted contributions from the fraction of well-aligned alpha grains as well as the fraction of not well-aligned grains. The weighting of contributions are a function of alignment and area (or volume) fraction. Low MTR orientation spread with high MTR density would be referred to as an intense MTR. A material having intense MTRs does not imply anything regarding the material's macrotexture, i.e. the macrotexture could be weak or strong in a material having intense MTRs.

MTR Neighboring Regions: The region surrounding MTR features. These could include MTR features of different character or regions of substantially randomly orientated alpha (average orientation regions). The neighborhood surrounding MTR features are critical to the potency of MTRs impact on dwell fatigue.

MTR Orientation: The dominant crystallographic orientation of the alpha grains within an MTR region. MTRs with the basal plane oriented nearly perpendicular to the principal stress direction are classified as "Hard MTRs". Combinations of other orientations that enable easy basal or prismatic slip relative to a stress axis are classified as "Soft MTRs". Both "hard" and "soft" MTRs influence dwell fatigue performance of titanium materials. The "soft" regions accumulate significant creep strain during dwell while the "hard" regions are potent crack nucleation sites and then offer very limited resistance to crack propagation. Electron Backscatter Diffraction or similar methods are needed to assess crystallographic orientations.

MTR Orientation Spread: A measure of the average crystallographic misorientations of the similarly aligned alpha phase grains within an MTR.

MTR Quantification: Methods to quantify MTR Size, Shape, Density, Intensity, Frequency, Orientation, Neighboring Region Characteristics, and Volume Fraction of Primary Alpha, are important parameters when characterizing MTR features. This characterization requires a means of discerning and measuring alpha grain orientations.

MTR Shape: The general geometric morphology of a contiguous area of similar alpha grain orientations, which may be expressed as the aspect ratio of longest and shortest dimensions, or the ratio of the axes of an ellipse fit to the MTR in 2D cross-section.

MTR Size: The size of a specific, connected area of similar alpha grain orientations plus all other grains internal to this region often expressed as an area or equivalent diameter in 2D cross-section. The JETQC committee and titanium community as a whole are continuing to work toward a commonly agreed upon criteria to establish specific MTR size.

MTR Volume Fraction: The summed area (or volume) of all MTR features, including all grains internal to the MTRs, divided by the total area (or volume) of titanium investigated.

Additional definitions recommended for Section 3 include other aspects related to CDF (dwell, residual stress, stressed volume), additional microstructural features (beta fleck, beta transus, colony, grain flow, macrotexture, primary alpha) and a melt-related definition (skull melting).

Section 4 Background is recommended to be updated with the note that CHM + VAR has become another standard melting process for premium quality titanium. A well-controlled CHM + VAR process has demonstrated the capability of reducing hard alpha and high-density inclusion rates compared with a well-controlled triple VAR process as shown in Figure 3 [4]. The presence of the hearth melt in a well-controlled CHM + VAR process allows for a significantly longer residence

time to allow inclusions to dissolve and HDIs to density-separate compared with a well-controlled VAR process.

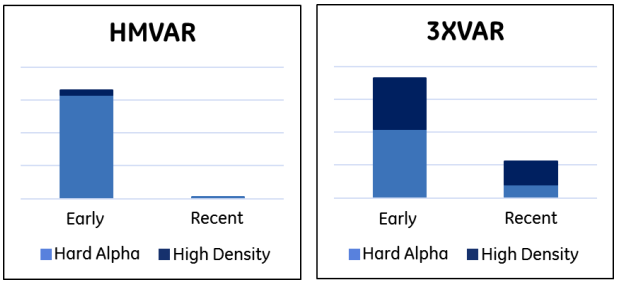

Figure 3. Significant reduction in inclusion rates in CHMVAR versus 3XVAR PQ Ti melt processes since JETQC inception [4].

Section 4 is also recommended to be updated noting that the manufacturing process used to produce titanium alloy forged rotating components will result in the presence of MTRs in the final part. Depending on the alloy, applied stress, stress-state, stressed volume, remaining bulk residual tensile stress, application temperature, hold-time, etc., the presence of MTRs might result in reduced component life, and the manufacturing process should be established so that, at each stage, appropriate controls are in place to minimize the severity of the MTRs. A significant amount of research has been performed related to MTRs, but much still has yet to be learned. Initial directional guidance related to billet conversion and component forging is provided in a later section, but it is recognized that this guidance may change as more research is conducted. Much of this detailed research is captured in [8] and at a higher level in [9].

Section 7 Consolidation and Melting is recommended to be updated to include a description of skull melting [4], minimizing the risk of primary electrode burning on exposure to air after melting, attachment of electrode stub via a chamber weld or a furnace plunge weld, a description of new CHM inclusion elimination process capability validation via use of seeded heats, and housekeeping. Housekeeping improvements are believed to have been a significant contributor to the overall melt anomaly rate reduction noted in Figures 1 and 3.

Section 8 Billet Conversion, Disk Forging and NDT has many recommended updates, primarily related to MTRs. The recommended updates to billet conversion are as follows:

Beta Recrystallization: Initial beta work combined with a subsequent alpha/beta pre-strain and a beta recrystallization step will set-up a smaller recrystallized prior beta grain size. A smaller prior beta grain size will minimize the size of the subsequent MTRs. A minimum deformation ratio is necessary in this temperature domain in order to break down the solidification structure and obtain a uniform, relatively small prior beta grain size. Minimizing the time at temperature for the beta recrystallization step results in a smaller recrystallized prior beta grain size.

Post-beta-recrystallization Cooling: Cooling after beta recrystallization results in the formation of alpha colonies; these colonies are the origin of MTRs. A faster cooling rate minimizes the alpha colony size and the thickness of the lamellae within the colonies; thinner alpha plates increases the ability of MTRs to be broken-up during subsequent billet and component forging processing. Metal temperature, transfer time and temperature of the water tank prior to quenching along with section size should be controlled to maximize cooling rate.

Final Alpha/beta Work: The degree of sub-beta-transus work imposed on the billet following the last quench from the beta phase field is important in reducing MTRs through the breaking up of colonies. Increased levels of final alpha/beta work generally lead to a reduction in MTR size and a decrease in MTR intensity.

Temperature of Final Alpha/beta Work: A higher final alpha/beta work temperature decreases the MTR intensity. The temperature for initial and reheating sequences should be controlled to mitigate variations in bar length, reduction per pass, and bites per pass with associated surface chilling and adiabatic heating.

Reheat Time for Final Alpha/beta Work: Longer reheat times between the final alpha/beta forge operations that have imparted a minimum level of strain may decrease the MTR intensity. This should be balanced with the need to retain a refined, spheroidized primary alpha structure.

Type of Press Work: Billet forging work should be conducted using a press that is capable of imparting strain through the entire billet cross-section enabling refinement of microstructure, including MTRs, through to the center of the billet.

Redundant Work for MTR Break-up: A combination of upset and draw should be conducted in order to improve work in the billet material to reduce MTRs. Working in multiple directions imparts strain on all MTR orientations and subsequently reduces the MTR size and intensity. In addition, intermediate billet cross-section shape should be considered to ensure uniformity of microstructure.

Billet End Effects: It is known that forging and conversion of cast ingots to converted billets results in strain variation between the near steady-state region and ingot/billet ends. The variation of strain within the ends of ingots and billets will influence the evolution of MTRs.

The recommended updates to disk forging and heat treatment are as follows:

MTR Levels in Billet Used to Manufacture Parts: Billet that has been processed to minimize MTR size, frequency and intensity is less susceptible to retaining MTRs in forgings.

Alpha/beta Versus Beta Forging Practice: Alpha/beta forged parts may retain MTRs from the billet processing, whereas beta-forged parts erase MTRs from the billet processing. Beta forging followed by cooling through the beta transus can lead to the generation of colonies, and if properly controlled, the size of these colonies should be smaller than MTRs retained after similarly processed alpha/beta forged material.

Forge Strain, Strain Rate, and Temperature: A sufficient level of strain and associated strain rate and temperature will reduce remnant MTRs carried over from billet for alpha/beta forged parts. Strain path should also be considered relative to modification of location-specific MTR characteristics within the final part. Note that high levels of strain along a consistent strain path may increase the macrotexture within the forging and that alpha/beta forge practice should avoid excessive adiabatic heating that may locally reduce primary alpha volume fraction in the overheated region leading to the formation of a beta fleck.

Number of Re-heats: Time at temperature associated with multiple re-heats should be minimized to retain a finer primary alpha grain size.

Post-forge Cooling Rate for Beta-processed Alloys: The post-forge cooling rate should be maximized to ensure refined alpha colonies and thinner alpha lamellae.

Heat Treatment Temperature for Alpha/beta-processed Alloys: Selecting a heat treatment temperature closer to the beta transus for alpha/beta-processed alloys will reduce the primary alpha volume fraction and size, resulting in a reduction in MTR size and intensity. Note, if the selected temperature is too close to the beta transus, areas of remaining local ingot segregation of beta stabilizing elements may result in the formation of a beta fleck.

Post-solution Cooling Rate for Alpha/beta-processed Alloys: Increasing the post-solution cooling rate for alpha/beta-processed alloys will reduce the primary alpha volume fraction and grain size. It will also reduce the secondary alpha plate thickness as well as increase the likelihood that the secondary alpha plate morphology will change from a colony to a basketweave morphology. These changes in microstructure will result in a reduction in MTR size and intensity.

Bulk Residual Tensile Stress: Manufactured-in tensile residual stresses are additive to application stress which make them important relative to component life. Bulk residual tensile stress present after heat treatment will be a function of: (i) size and geometry of heat-treated forging (ii) heat treatment solution temperature, (iii) cooling method and transfer time, where applicable, following solution heat treatment, (iv) aging/stress relief temperature and time, and (v) alloy composition, where creep-resistant near-alpha alloys (e.g. Ti-6242, Ti-834) have the greatest susceptibility to retaining residual stress, while increasing alloy beta stabilizer content that lowers creep strength (e.g. Ti-6246, Ti-17 and Ti-64) reduces the propensity to retain residual stress.

Ti Alloy Class and Cold Dwell Fatigue Sensitivity: It should be noted that different alloy classes are believed to have different tendencies to form MTRs, and so processes will need to be adjusted between alloy classes to minimize MTR formation, frequency, size, volume fraction, and intensity. The alloy classes believed to be susceptible to dwell fatigue are near-alpha alloys (e.g. Ti-6242, Ti-811, Ti-685, Ti-829 and Ti-834), and to a lesser extent alpha-beta alloys (e.g. Ti-64). Alpha-beta alloys with increased beta stabilization (e.g. Ti-6246 and Ti-17) are believed to have low sensitivity to cold-dwell fatigue debits.

The recommended ultrasonic inspection updates to non-destructive testing (NDT) are as follows:

Ultrasonic inspection relies on the transmission of elastic waves within the material. Discontinuities in the material with large differences in density or elastic properties, like cracks, voids, or inclusions, will result in discrete backscattered reflections of appreciable amplitude indicating the presence of an undesirable defect. These signals are relatively straightforward to detect in material with fine, uniform grain size without any MTRs (or with MTRs much smaller than the incidence wavelength), but the presence of MTRs diminishes the inspectability of bar, billet, and finished components.

Two distinct phenomena are observed depending on the size, shape, and orientation of the major axis of the MTR relative to the incident ultrasound. Significant attenuation, leading to decreased signal, occurs when the wavelength is much smaller than the MTR size in the direction of wave propagation. In contrast, significant backscattering, leading to enhanced noise, occurs when the wavelength is of the order of the MTR size. These phenomena are a result of the elastic anisotropy of the alpha phase. Enhanced attenuation occurs due to variations in local wave velocity inside different MTRs that distort the coherent incident wavefront.

Additionally, the shape of the MTRs resulting from metal flow during the forging process may cause the wave to mode convert, reflect/refract, or otherwise travel in a path away from the source. The additional backscattering occurs because of the elastic (impedance) mismatch at MTR boundaries. Either of these phenomena decrease the signal to noise ratio making it more difficult to detect real flaws. In some instances, when the MTR size is large relative to the wavelength, and also depending on the attributes of the specific MTR and its neighborhood, geometric scattering can occur resulting in a single, large, discrete reflection to be received.

In the same way that MTR can impede the inspectability of titanium alloys, the presence of MTRs can also be inferred from ultrasonic inspection. MTRs can produce both an increased average noise response, quantified by the average root-mean-square of the backscattered signal content, as well as single high amplitude reflections. Depending on size and aspect ratio relative to the incident sound wave, MTRs can also cause a measurable increase in attenuation or backscattering, and hence interrogation in multiple directions can be useful in determining preferred MTR orientation. The use of these effects requires the correlation of the ultrasonic parameters with levels of MTR severity, along with consideration of interactions between sound wavelength and microstructure.

Finally, the presence of macrotexture may also be inferred from the measurement of ultrasonic wave velocity. Because wave speed is proportional to elastic modulus, the velocity is highest along the c-axis of the unit cell, and slowest perpendicular to it.

4. Summary

The JETQC engine OEMs have collaborated with the FAA to develop a series of recommendations to update the FAA AC 33.15-1 to incorporate best practices related to manufacturing of PQ titanium alloys components and CDF, and update best practices related to melting based on the last ~25 years' experience.

5. Acknowledgements

The authors would like to thank Dr. Tim Mouzakis, FAA, for his encouragement and guidance as the team has worked to develop a series of recommendations for the FAA, and our JETQC colleagues from GE, specifically Dr. Rich Klaassen for the NDT section, Honeywell, IHI, MTU, PW, PWC, Rolls-Royce, SAE, SHE and Williams International for their input. The authors would also like to thank colleagues from ATI, TIMET and Howmet for their review of the draft recommendations.

6. References

1. Sioux City NTSB report – NTSB Office of Aviation Safety, Aircraft Accident Report AAR-90-06 NTIS No. PB90-910406.
2. A. Woodfield and G. Lemaitre, "Aerospace titanium alloy melt process quality improvements" presented at the *14th World Conference on Titanium,* 11 June 2019, La Cité Nantes Events Center, Nantes, France.
3. A. Woodfield and C. Shamblen, "Titanium Industry Quality Improvements", *Ti-2003: Science and Technology, Proceedings of the 10th World Conference on Titanium*, Hamburg, 2003, p2737.
4. A. Woodfield and C. Shamblen, "Titanium Alloy Melt Process Quality Improvements", *Ti-2007: Science and Technology, Proceedings of the 11th World Conference on Titanium*, Kyoto, 2007, p151.R. Titanium, J. Titanium, A.J. Titanium, I. P. Titanium, *Philosophical Magazine*, Vol. 105, Nos. 28–29, 1–21 May 2023, 3280–3314.
5. Advisory Circular AC 33.15-1, Manufacturing Process for Premium Quality Titanium Alloy Rotating Engine Components: https://www.faa.gov/documentLibrary/media/Advisory_Circular/AC_33_15-1.pdf.
6. Bureau d'Enquêtes et d'Analyses (BEA) Investigation Report, 2017-0568.en/2020 September, https://www.bea.aero /uploads/tx_elydbrapports/BEA2017-0568.en.pdf.
7. The evaluation of Cold Dwell Fatigue in Ti-6242, https://www.tc.faa.gov/its/worldpac/techrpt/tc17-57.pdf
8. A. Pilchak et al., Cold Dwell Fatigue of Titanium Alloys: History, Current State, and Aviation Industry Perspective, DOT/FAA/TC-23/40.
9. A. Pilchak et al., Industry-wide Learning and Perspectives on Management of Cold-Dwell Fatigue Capabilities, World Titanium Conference 2023.